Ceramic Composites of 3Y-TZP Doped With CuO:

Processing, microstructure and tribology

Shen Ran

Graduation committee:

Chairman:	Prof. dr. ir. J.A.M. Kuipers	University of Twente
Promotor:	Prof. dr. ing. D. H. A. Blank	University of Twente
Assistant promotor:	Dr. A. J. A. Winnubst	University of Twente
Members:	Prof. dr. G. J. Vancso	University of Twente
	Prof. dr. ir. D. J. Schipper	University of Twente
	Prof. dr. C. Chen	University of Science and Technology of China (China)
	Prof. dr. J. Vleugels	Katholieke Universiteit Leuven (Belgium)
	Prof. dr. ir. S. van der Zwaag	Delft University of Technology

CERAMIC COMPOSITES OF 3Y-TZP DOPED WITH CUO:

Processing, microstructure and tribology

DISSERTATION

to obtain

the doctor's degree at the University of Twente,

under the authority of the rector magnificus,

prof. dr. W.H.M. Zijm,

on account of the decision of the graduation committee,

to be publicly defended

on Friday 16th June 2006 at 13:15

by

Shen Ran

born on 26th January 1975

in Shanghai, China

This dissertation is approved by the promotor:

Prof. dr. ing. D. H. A. Blank

and the assistant promotor:

Dr. A. J. A. Winnubst

To my wife, Yanshu
and my beloved family in China

Summary

The work described in this thesis is about processing, microstructure and tribology of CuO doped 3Y-TZP (3 mol% yttria stabilised tetragonal zirconia polycrystals) composite ceramics. This group of materials has shown attractive properties such as superplastic behaviour at elevated temperature and a low friction coefficient under dry sliding conditions.

This thesis can be divided in two parts. The first part (chapter 2-7) describes investigations on the fabrication process, including powder preparation, compaction and sintering, and the relation between processing and microstructure. Major efforts were paid on fabrication of nanostructured composite ceramic in this part. The second part (chapter 8-9) deals with the tribological properties of the coarse-grained CuO doped 3Y-TZP composite ceramics under dry sliding conditions.

In chapter 2 the effect of addition of a small amount of coarse-grained CuO powder on the sintering behaviour of submicron 3Y-TZP is described. It is shown that in these coarse-grained systems the addition of CuO strongly retards densification of 3Y-TZP and results in a destabilisation of the tetragonal zirconia phase in the material. These phenomena are interpreted in terms of several reactions during sintering as stated in literature. Among these reactions, dissociation of CuO to Cu_2O at around 1030 °C is recognised to be very detrimental for densification. This reaction can be retarded by an increase in oxygen partial pressure. Sintering in flowing oxygen results in a remarkable higher density (96 % after sintering at 1400 °C) if compared to the case of sintering in air (86 % after sintering at 1400 °C).

Chapter 3 deals with preparations of nanocrystalline 3Y-TZP and CuO powders. A weakly agglomerated 3Y-TZP powder with an average particle size of 10 nm was prepared by a co-precipitation technique (CP). For CuO powder preparation, a copper oxalate complexation-precipitation technique was developed. A detailed description is given on influences of calcination process, precipitation/washing media on crystallite size, aggregation and agglomeration behaviour as well as phase composition of the produced CuO powder. Oxalate precipitation in ethanol followed by sequential drying and calcination at 250 °C in an open tubular furnace was found to be the optimal procedure for producing nanocrystalline CuO powder with small aggregates and weak agglomerates. By using this optimal procedure a CuO powder with crystallite diameter and BET equivalent particle diameter of respectively 12 and 20 nm was obtained. The compaction behaviour of composite powders of 3Y-TZP doped with CuO powders with different particle size is also presented in this chapter.

In chapter 4 investigations of reactions during sintering of CuO doped 3Y-TZP nano-powder composites are described. Nano-powder composites of 8 mol% CuO doped 3Y-TZP produced from the nanocrystalline powders prepared by the methods as described in chapter 3 were investigated by thermal analysis techniques (DTA, TGA), XPS and high-temperature XRD. It is revealed that a strong dissolution of CuO in the 3Y-TZP matrix occurs below 600 °C, resulting in significant enrichment of CuO in the 3Y-TZP grain boundaries with a grain-boundary layer thickness of several nanometres. Solid state reaction between CuO and yttria as segregated to the 3Y-TZP grain boundaries occurs at around 850 °C and forms $Y_2Cu_2O_5$.

Chapter 5 is focused on the influence of reactions, as described in chapter 4, on densification during sintering of CuO doped 3Y-TZP nano-powder composite compacts. It is shown that the dissolution of CuO in the 3Y-TZP grain boundaries, as occurs below 600 °C, increases grain boundary diffusivity and consequently promotes densification at a lower temperature if compared with undoped nanocrystalline 3Y-TZP. The formation of $Y_2Cu_2O_5$ at 800 - 950 °C however inhibits densification. These two reactions

are dependent on the CuO content as well as the CuO particle size. A solution for optimising sintering of the composites, i.e. by choosing proper content and particle size of added CuO powder is proposed. By adding 1.6 mol% of CuO with average particle size of 20 nm in the CP 3Y-TZP a very good sinterability is achieved.

In chapter 6 the microstructure evolution (grain growth and phase transformation) during sintering of CuO doped 3Y-TZP nano-powder composites is described. The microstructural changes were interpreted on the basis of reactions occurring while sintering. It is revealed that strong grain growth in the final sintering stage at 1130 °C is caused by the presence of CuO. The formation of $Y_2Cu_2O_5$ at around 850 °C leads to a t-m zirconia phase transformation during heating. A strong CuO enrichment on the sample surface was observed for the CuO doped 3Y-TZP nano-powder composites sintered at 1130 °C. This surface enrichment of CuO is related to the decrease in CuO solubility associated with grain growth. Finally it can be concluded from these results, that if the sintering procedure is well controlled, a dense 8 mol% CuO doped 3Y-TZP ceramic with an average grain size of 120 nm can be obtained.

In chapter 7 an advanced sintering method, namely spark plasma sintering (SPS), is employed for processing CuO doped 3Y-TZP nano-powder composites. SPS is proven to be a very efficient method for producing dense nanostructured ceramics of CuO doped 3Y-TZP. A 96 % dense composite ceramic with an average grain size of 70 nm was obtained by applying the SPS process at 1100 °C and 100 MPa for 1 min. The densification procedure (from starting of heating to end of dwell) takes only 7 min, whereas it normally takes at least several hours in the case pressureless sintering. CuO was reduced to metallic Cu after the SPS processing. Due to the suppression of reactions between CuO and 3Y-TZP, zirconia in the as-sintered material shows almost pure tetragonal phase. Annealing following the SPS process results in grain growth and formation of monoclinic zirconia. The grain size and m-ZrO_2 content are strongly dependent on the annealing temperature. By utilising different processing techniques, including pressureless sintering or SPS followed by annealing, properties of the composite ceramic can be tuned via manipulation of the microstructure. Tuning the mechanical properties of dense 8 mol% CuO doped 3Y-TZP composite ceramic by utilising different processing technique is shown as an example.

Chapter 8 describes the dependence of microstructure on the mechanical and tribological properties of the coarse-grained 8 mol% CuO doped 3Y-TZP composites. It is shown that only 50 °C difference in sintering temperature remarkably changes microstructure and consequently results in significant differences in mechanical and tribological properties. The material sintered at 1500 °C for 8 hours shows clean grain boundaries, whereas a ceramic sintered at 1550 °C contains a Cu-rich amorphous grain boundary layer. As revealed by pin-on-disc wear tests, the material sintered at 1500 ºC shows self-lubrication resulting in a low friction coefficient (*f*) of 0.2~0.3 and low specific wear rate (*k*) $<< 10^{-6}$ mm$^3 \cdot$N$^{-1} \cdot$m^{-1}. In contrast the material sintered at 1550 ºC showed poor tribological behaviour (*f* = 0.8~0.9; *k* $>> 10^{-6}$ mm$^3 \cdot$N$^{-1} \cdot$m^{-1}) under the same conditions. The difference in tribological behaviour of those two materials was interpreted on the basis of mechanical properties (strength and toughness) and microstructure characteristics.

Chapter 9 explores more insights of the reduction in friction coefficient of the tribosystem of CuO doped 3Y-TZP ceramic sliding against an alumina ball. The morphology of the wear track is investigated in detail and a deterministic model is involved to interpret the mechanism of reduction in coefficient of friction. It was recognised that a self-lubricating mechanism is the most contribution to the reduction of friction. During operation of the tribosystem, a Cu- and Al-rich soft oxide interfacial patchy layer is generated by deposition of wear debris in the contact area. Calculation based on a deterministic friction model confirms that this soft interfacial patchy layer reduces friction. However when this layer becomes too thick due to

accumulation of debris, detachment of top layer in the wear track occurs and a wear transition from mild to severe take place, resulting in significant increases in both friction coefficient and wear rate.

Finally in chapter 10 an evaluation of the results is given. Based on these results suggestions are given for the optimal microstructure for the best tribological properties i.e. low wear and low friction for a prolonged time. Also proposals are indicated for advanced ceramics processing in order to achieve this optimal microstructure.

Samenvatting

In dit proefschrift wordt een groep keramische materialen beschreven met bijzondere (structurele) eigenschappen. Zo zijn deze materialen (super)plastisch bij temperaturen van 1000 °C of meer, wat interessant is voor nauwkeurige vormgeving. Daarnaast vertonen deze systemen een lage wrijvingscoëfficiënt bij het over elkaar glijden zonder gebruik te maken van smeermiddelen; d.w.z. onder droge slijtage omstandigheden. Slijtage en wrijving is het onderzoeksgebied van de tribologie.

De fabricage van het keramiek en de wrijving en slijtage eigenschappen worden beschreven en verbanden worden gelegd tussen keramische microstructuur en fabricage proces en tussen microstructuur en tribologische eigenschappen van het materiaal. Het onderzochte keramiek is een zogenaamd twee-fasig materiaal. De hoofdfase (de matrix) bestaat yttrium oxide gedoteerd zircoon oxide met de tetragonale kristalstructuur (3Y-TZP) terwijl de tweede, minderheids-, fase uit koperoxide (CuO) bestaat en tot enkele mol procenten (0.8 – 8) aan de 3Y-TZP matrix is toegevoegd.

Het werk, zoals beschreven in dit proefschrift, kan in twee onderdelen worden gesplitst. Het eerste deel, zoals vermeld in de hoofdstukken 2 tot en met 7, geeft het onderzoek weer van het keramisch fabricage proces. Hier worden (nat-chemische) poederbereiding, vormgeving (compacteren) en sinterproces behandeld, waarbij relaties worden gelegd tussen de microstructuur (o.a. korrelgrootte en kristalfase) en de verschillende processen tijdens de fabricage. In het bijzonder wordt veel aandacht besteed aan de fabricage van zelfgemaakte nanogestructureerde poeders en composiet materialen, waarbij de uitgangspoeders een kristallietgrootte hebben van 8 tot 20 nanometer (hoofdstuk 3-7). In het tweede deel, zoals beschreven in de hoofdstukken 8 en 9 worden de tribologische (wrijving en slijtage) eigenschappen beschreven van grofkorrelig koperoxide gedoteerd 3Y-TZP. Hoofdstuk 10 geeft een evaluatie.

In hoofdstuk 2 worden commercieel verkrijgbare, relatief grofkorrelige, poeders gebruikt. Het toevoegen van CuO vertraagt de verdichting tijdens sinteren van 3Y-TZP. Daarnaast destabiliseert de tetragonale kristalstructuur onder vorming van monoklien zirconia. Deze verschijnselen worden verklaard aan de hand van de verschillende reacties, die tijdens het sinteren plaatsvinden. De dissociatie van CuO tot Cu_2O bij 1030 °C blijkt een sterk nadelig effect te hebben op de verdichting. Deze dissociatie vindt bij een hogere temperatuur plaats als een verhoogde hoeveelheid zuurstof aanwezig is. Sinteren onder een stromende zuurstofatmosfeer geeft een aanzienlijk hogere dichtheid in vergelijking met sinteren in lucht. De dichtheid na sinteren bij 1400 °C zijn respectievelijk 96 % en 86 % van de theoretische dichtheid.

De bereiding en eigenschappen van nanokristallijne 3Y-TZP en CuO poeders is gegeven in hoofdstuk 3. Zwak geagglomereerde 3Y-TZP poeders met een gemiddelde kristallietgrootte van 10 nm worden gemaakt via een co-precipitatie methode. Voor CuO is een complexatie-precipitatie techniek ontwikkeld. Voor dit laatste systeem is de invloed beschreven van precipitatie wijze, methode van wassen en temperatuur (calcineer) behandeling op kristallietgrootte en kristalstructuur. De optimale procedure voor het verkrijgen van een poeder met kristallietgrootte van 15 nm is complexatie-precipitatie in ethanol met vervolgens drogen en calcineren in een open buisoven. Tenslotte wordt in dit hoofdstuk het persgedrag beschreven van verschillende composiet poeders.

Hoofdstuk 4 beschrijft de verschillende reacties, die optreden tijdens het sinteren van de in hoofdstuk 3 beschreven poedercompacten. Gebruik wordt gemaakt van thermische analysetechnieken (DTA en TGA), X-ray Photoelectron Spectroscopy (XPS) en hoge temperatuur Röntgen diffractie (XRD). CuO lost op in de 3Y-TZP matrix bij een temperatuur < 600 °C. Dit resulteert in een sterke verrijking van CuO in de korrelgrenzen van 3Y-TZP.   Bij 850 °C vindt een vaste stof reactie plaats tussen CuO en Y_2O_3, welke door segregatie in relatief hoge concentratie aanwezig zijn in de korrelgrenzen van de 3Y-TZP matrix. Door deze reactie wordt een $Y_2Cu_2O_5$ fase gevormd.

In hoofdstuk 5 wordt de verdichting tijdens sinteren van deze nano-composieten verklaard aan de hand van de reacties, zoals beschreven in hoofdstuk 4. Het oplossen van CuO in de korrelgrenzen van 3Y-TZP, bij een temperatuur beneden 600 °C, verhoogt het materiaaltransport aan de korrelgrens (korrelgrensdiffusie) en bevordert daardoor verdichting bij lagere temperaturen. De vorming van de $Y_2Cu_2O_5$ fase vertraagt de verdichting bij 800 – 950 °C. Beide reacties zijn afhankelijk van zowel de hoeveelheid gedoteerd CuO als de deeltjesgrootte van het CuO. Het beste sinterresultaat (dicht materiaal bij de laagste temperatuur) wordt verkregen als 1.6 mol % CuO met een gemiddelde deeltjesgrootte van 20 nm toegevoegd wordt aan nanokristallijn 3Y-TZP.

Hoofdstuk 6 geeft de ontwikkeling van de microstructuur (korrelgroei en fase overgangen) tijdens sinteren van de nanokristallijne poeder compacten. Dit alles ook weer in relatie met de reacties die optreden tijdens sinteren. Er vindt een fase overgang van tetragonaal naar monoklien zirconia plaats bij ca. 850 °C als gevolg van de vorming van de $Y_2Cu_2O_5$ fase. Een sterke korrelgroei treedt op in deze composieten tijdens de eindfase van het sinterproces bij 1150 °C. Na deze sinterbehandeling is er een verrijking van CuO aangetoond aan het oppervlak van het keramiek, wat veroorzaakt wordt door afname in CuO oplosbaarheid in de 3Y-TZP matrix als gevolg van sterke korrelgroei. Het is mogelijk gebleken om een dicht 8 mol% CuO gedoteerd 3Y-TZP composiet te maken met een gemiddelde korrelgrootte van 120 nm.

In hoofdstuk 7 wordt een geavanceerde sintermethode gebruikt: Spark Plasma Sintering (SPS). Een dicht (96 %) CuO gedoteerd 3Y-TZP composiet met een korrelgrootte van 70 nm kan verkregen worden door SPS toe te passen bij 1100 °C en een druk van 100 MPa gedurende 1 minuut. Het gehele SPS proces neemt slechts 7 minuten in beslag, terwijl een normaal (drukloos) sinterproces tenminste enkele uren duurt. Na het SPS proces is het aanwezige CuO gereduceerd tot koper metaal, terwijl het uiteindelijke keramiek bijna volledig de tetragonale kristalstructuur heeft. Op deze manier zijn er methodes ontwikkeld om verschillende microstructuren te verkrijgen afhankelijk van de gebruikte techniek (drukloos sinteren of SPS) en eventuele temperatuur nabehandelingen.

De resultaten in hoofdstuk 8 geven de invloed weer van de keramische microstructuur op mechanische en tribologische eigenschappen van de grofkorrelige CuO-gedoteerde 3Y-YZP composieten, waarvan het fabricage proces beschreven is in hoofdstuk 2. Een verschil van 50 °C in sintertemperatuur geeft een opmerkelijke verandering in microstructuur en een duidelijk verschil in mechanische en tribologische eigenschappen. Een keramisch composiet gesinterd bij 1550 °C bevat een koper rijke amorfe fase om de keramische korrels en vertoont tijdens slijtage experimenten een hoge wrijvingscoëfficiënt *(f)* van 0.8-0.9 en een specifieke slijtagesnelheid *(k)* van $\gg 10^{-6}$ $mm^3.N^{-1}.m^{-1}$, hetgeen aantoont dat dit een materiaal is met slechte tribologische eigenschappen. Echter eenzelfde composiet maar dan gesinterd bij 1500 °C bezit geen amorfe fase en heeft tribologische waarden van f = 0.2-0.3 en een k-waarde $\ll 10^{-6}$ $mm^3.N^{-1}.m^{-1}$.

Hoofdstuk 9 geeft meer inzicht in het mechanisme, dat verantwoordelijk is voor de verlaging van de wrijvingscoëfficiënt van CuO gedoteerd 3Y-TZP glijdend tegen een aluminium oxide bal in vergelijking met het wrijvingsgedrag van ongedoteerd 3Y-TZP. De morfologie van het slijtagespoor is gedetailleerd onderzocht en een deterministisch model is gebruikt om het mechanisme te verklaren. Een zelf smerende laag wordt gevormd, doordat tijdens de slijtagetest een zachte, koper en aluminium oxide grenslaag ontstaat. Als deze laag echter te dik wordt door ophoping van slijtage resten, laat de toplaag van het slijtagespoor los, waardoor een ruw oppervlak ontstaat wat resulteert in een sterke toename van zowel wrijvingscoëfficiënt als slijtagesnelheid.

De evaluatie in hoofdstuk 10 geeft suggesties voor de meest optimale microstructuur voor de beste tribologische eigenschappen gedurende langere tijd. Tevens worden voorstellen gemaakt voor een keramisch proces voor het verkrijgen van deze optimale microstructuur.

Contents

Chapter 1

Introduction

1.1 General introduction to ceramic materials

Ceramics have been known by mankind since 30,000 years ago [1], and have played important roles in evolution and development of human civilisation. Nowadays ceramics are widely used in our daily life. Generally ceramics are defined as solid materials that have unique and varied properties and are composed of inorganic non-metallic materials [2]. Their specific characteristics, such as high melting point, high chemical inertness and low density make ceramic materials increasingly interesting in many applications.

Ceramic materials that are produced from modified and refined raw materials or even from chemically synthesised starting materials are often called advanced or technical ceramics [3]. Advanced ceramics can be divided into functional and structural regarding their special properties. Functional ceramics show special (di)electrical, optical or magnetic properties, while structural ceramics have potential engineering applications due to their advanced mechanical properties and high chemical and thermal stability. The latter group of materials consists mainly of oxides (e.g. Al_2O_3, ZrO_2), carbides (e.g. SiC, TiC), nitrides (e.g. Si_3N_4, Ti_3N_4), borides (e.g. TiB_2, ZrB_2), and their composites (e.g. ZTA, SiAlON). They can be further classified into oxide and non-oxide ceramics on the basis of chemical composition. In general oxide ceramics are oxidation-resistant and chemical inert. Non-oxide ceramics are less oxidation resistant but possess very high hardness and electric and thermal conductivities. At present, structural ceramics are widely used as i) cutting tools such as knives, scissors; ii) seal valves, chemical and slurry pumps, piston crowns, head face plates, piston liners; iii) drawing and hot extrusion dies; iv) biological implants [4]. Moreover, this group of materials have shown high potential for tribological applications [5].

1.2 Advanced ceramic processing

Usually processing of advanced ceramic materials consists of several steps, i.e. powder synthesis, forming/consolidation, sintering and post treatment [6, 7]. Each step can have significant influence on the properties and quality of the final products. Optimal properties require optimisation and good control of each of these steps in a coherent way.

1.2.1 Powder synthesis

For traditional ceramics such as pottery often natural clays are used as raw material. However the high requirements on composition, purity, particle morphology, particle size and agglomeration brought preparation of purely synthetic powders into the scope of advanced ceramics processing. In the past decades a large variety of powder synthesis techniques have been developed. These techniques can be approximately classified, based on matter states of the reactants, into the following categories:

- Solid state reactions, in which the desired powder is prepared by reaction of two or more solid components;

- Wet-chemical routes, in which the particles are formed from solutions or modified in with an aid of liquid media. This category includes, e.g. precipitation [8], sol-gel process [9], hydrothermal synthesis [10], citrate pyrolysis [11], EDTA synthesis [12], spray pyrolysis [13], etc.

- Vapour phase reaction and deposition, in which vapour particles are generated by vapour reaction and subsequent deposition. Some typical examples of this category are chemical vapour deposition (CVD) [14], microwave plasma synthesis [15], inert gas condensation [16], etc.

Among those powder synthesis techniques, wet-chemical routes such as complexation and precipitation are widely employed for the preparation of high quality, mostly nanocrystalline ceramic powders, due to a good control of particle growth combined with a large producing capability and relatively low cost. Practically several techniques are often combined to optimise the powder product. For instance, the reactants for a solid-state reaction may have been prepared by means of precipitation process. After precipitation often a hydrothermal treatment is applied for crystallisation for a better control of crystallite size and agglomeration morphology [17].

Ceramic powders always consist of clustered elements at different length scale, including primary crystallites, aggregates (in which the primary crystallites are held together by strong interactions) and agglomerates (in which the aggregates or the individual primary crystallites are held together by relatively weak attractive forces) [18-19]. The nature of these cluster elements, like morphology, size and strength, strongly influences the subsequent steps in the ceramic fabrication process and therefore as the final properties of the final ceramic as well. In general larger and stronger aggregates and/or agglomerates can give rise of large voids and significant non-uniformity, so that they should be avoided. After powder preparation post-treatment such as wet-milling, attrition milling and ultrasonic vibration are often used for deagglomeration or deaggregation. These post treatments are considered as a part of the powder synthesis route. Controlled granulation by e.g. spray drying is another method to improve powder morphology [20].

1.2.2 Compaction processing

Powder compaction transfers a powder feed material into a green product with a specific size, shape, strength and microstructure. The green compacts are formed by bringing the powder particles close to each other. The main compaction processing techniques for the fabrication of a "green" ceramic compact is briefly summarised by Winnubst [7], and shown in Table 1.1.

Table 1.1 Green compact forming methods[*]

Forming Method	Feed Material	Shape of green product
Dry or semi dry processing		
uniaxial pressing	powder or -free-flowing granules	Small simple shapes
isostatic pressing	powder or gragile granules	Larger, more complex shapes
Suspension/colloidal processing		
slip casting, colloidal filtration	suspension with low concentration of additives	Complex shapes
tape casting	suspension with relatively high binder content	Thin sheets
Paste processing		
extrusion	high visous mixture of powder and binder	Uniform cross section
injection moulding	mixture of powder and thermoplastic binders	Small complex shapes

* Table is taken from [7]

Dry pressing is the most straightforward compaction processing technique. However large voids and inhomogeneities can easily be created during dry pressing, especially when a nanocrystalline powder is used. In order to obtain a good quality dry-pressed green compact (high green density and homogeneity), the powder properties including morphology, aggregation and agglomeration have to be well optimised. Suspension and paste processing, in some cases, give better results of compaction. These techniques normally require various additives, including solvent, deflocculants, binders, lubricants and plasticisers. All additives must be removed prior to the pore-closure in the sintering process. Detailed information of additives can be found in [6].

1.2.3 Sintering

Sintering can generally be defined as a high-temperature process for consolidating and strengthening the powder compacts resulting in the ceramic [7]. During this step matter redistribution occurs as stimulated by a free energy change associated with the large free surface energy of fine particles in powder compacts [21]. Decrease in the interface energy is basically the driving force for sintering of a green compact.

Solid state sintering is commonly divided into initial, intermediate, and final stages [21]. However the boundaries between these stages are not clearly distinguishable. In the initial stage necks between particles forms and the density does not change much compared to the density of the green compact (normally in the range of 40 ~60 % of the theoretical density). In this stage particle rearrangement may occur. Most densification occurs in the intermediate sintering stage. After this stage the density has reached 85-90% of the theoretical density. Pore channels break up and the porosity type changes from open to closed pore. The crystallites (grains) are starting to grow in this intermediate sintering stage. In the final sintering stage only discrete close pores are present, which can only be eliminated by further grain growth.

In the past decades enormous efforts have been made on developing theoretical models for sintering [21-33]. Diffusion, including lattice, grain boundary and surface diffusion, is known as the most important mass transport mechanism in sintering [21, 24-28]. A commonly quoted model of densification during sintering can be expressed as [30]:

$$\frac{d\rho}{\rho dt} \propto \frac{\Omega \gamma \delta_b^m D_{eff}}{kTd^n} F(\rho) \qquad (Eq.1.1)$$

where ρ is density, t is time, Ω is atomic volume, γ is the surface free energy, δ_b is the boundary diffusion width, D_{eff} is the effective diffusion coefficient determined by the controlling diffusion mechanism, k is the Boltzmann constant, T is absolute temperature, d is the grain size, $F(\rho)$ is a dimensionless factor related to pore volume and its size and distribution, exponents m and n are determined by the controlling diffusion mechanism.

A large variety of microstructural parameters of powder and compact, including particle size, pore size and shape, etc., play profound roles in sintering. According to equation 1.1 a smaller particle size significantly enhances sintering. It is also recognised that in the initial stage of sintering a mixture of grain boundary and surface diffusion is present when particle size decreases from micron to nanometre scale [29]. The sintering model as developed by Kingery et al. [31] reveals that pores in the powder compact can not be removed by sintering when the pore/grain size ratio exerts a certain value. Additionally, according Lange's [32] coordination model of sintering, only the pores surrounding

particles less than a critical number (which is determined by the surface and grain boundary energies of these particles) can be eliminated by sintering. The work of Shi [29] revealed that the pore volume, size and distribution can give strong influence on sintering. Considering the influence of those mentioned factors, spherical particles with a uniformly and small (preferably nano) size and packed in a periodical arrangement through the compact would be the ideal for the best sintering results.

The evolution of the microstructure during sintering, including grain growth, phase transformation and sometimes chemical reactions, is one of the most important issues for ceramic processing as discussed in this thesis. Especially for processing of nanocrystalline ceramics, retention of the large fraction grain boundary region that is in metastable conditions, i.e. avoidance of significant grain growth during sintering, is critical for obtaining the special properties [33]. In general grain growth during sintering can be describe by an empirical equation [34]:

$$d_t^n - d_0^n = kt \qquad\qquad\qquad\text{(Eq. 1.2)}$$

where d_t and d_0 are the grain size at time of t and 0 respectively, and n and k are constants determined by the operative grain growth mechanism. Several models of grain-growth control were proposed in the past, e.g. impurity drag [35-36], phase partitioning [37], and micro-strain relaxation [38].

Sintering aids, which are actually small amounts of impurities introducing liquid phase during sintering are often added to improve the densification process [39-41]. The presence of this small amount of liquid phase facilitates mass diffusion and the process (which is known as liquid phase sintering) normally yields rather dense materials. However, addition of sintering aids can also lead to formation of a considerable amount of second phases as well as significant grain growth, which are undesired for several applications [40].

Several special sintering techniques involving non-thermal assistance for densification were developed to facilitate sintering process. These special sintering techniques can be generally divided into pressure-assisted and electrical/magnetic-field-assisted sintering. Pressure-assisted sintering includes hot pressing (HP) [42], hot isostatic pressing (HIP) [43] and sinter forging (SF) [44]. These pressure-assisted sintering techniques do not only enhance densification, but also remove processing flaws more effectively by generating creep deformation during sintering [44]. Microwave sintering [45] and spark plasma sintering [30, 46] are typical examples of electrical/magnetic-field-assisted sintering techniques. In these techniques heat can be generated by the material itself instead of external radiation heating unit, which implies more uniform heating of each part of the material. Additionally, engineering advantages such as very high heating rate (up to several hundreds °C·min^{-1}) [45-46], extra activation of mass transport due to non-thermal effect [47-30], are recognised to be generally associated with these electrical/magnetic- field-assisted sintering techniques. During spark plasma sintering an external pressure can be employed as well.

1.3 Tetragonal zirconia ceramics

Since the discovery of the transformation-toughening phenomenon in tetragonal zirconia based ceramics [48], these materials have gained extensive interests of research. Due to their excellent chemical inertness and mechanical properties, especially the very high fracture toughness [49], this group of ceramic materials is increasingly considered for a wide range of structural applications such as extrusion dies, cutting tools, valve guides, etc [50].

1.3.1 Crystal structure of zirconia

Pure zirconia exists in three well defined crystal structures: monoclinic, tetragonal and cubic. At room temperature zirconia shows a monoclinic structure which is stable up to about 1170 °C. At this temperature it transforms into the tetragonal structure. Upon further heating it transforms to the cubic structure at 2680 °C. By doping certain amount of metallic oxides, such as Y_2O_3 and CeO_4, the cubic structure can be stabilised to room temperature. An often quoted phase diagram of Y_2O_3-ZrO_2 system is given in [51].

The tetragonal structure can also be stabilised to room temperature if the free energy change associated with the t-m phase transformation ($\Delta G_{t \to m}$) remains positive [52]. This can be done by a combination of addition of stabiliser such as Y_2O_3, applying constraint stress, and reducing grain size below a critical value. More details of retention of tetragonal can be found in literature [52-54] and are also described in chapter 6.

1.3.2 Transformation toughening

Ceramic materials which contain tetragonal zirconia show much higher fracture toughness than other ceramics. The mechanism associated with a stress-induced tetragonal to monoclinic zirconia phase transformation is recognised to significantly contribute to this enhancement in toughness. This toughening mechanism is called phase transformation toughening [51, 55-57].

In a material containing tetragonal zirconia the metastable tetragonal phase of ZrO_2 may transform to the monoclinic phase, when the stress applied on the particle reaches a critical value. The unconstrained transformation yields a volume expansion of about 3-5% and a shear strain of 16%. As the crack grows, the high stress concentration at the crack tip will trigger the transformation of zirconia grains in a zone of surrounding the crack tip, resulting in a compressive stress layer around the crack. Consequently the fracture toughness of the material is enhanced, since a higher external stress must be applied to reach the critical conditions for the crack to propagate. This transformation toughening mechanism can be expressed as [57]:

$$K_{tip} = K_a - K_s \qquad\qquad\qquad\qquad \text{(Eq. 1.3)}$$

where K_{tip}, is the crack-tip stress intensity, K_a is the applied stress intensity factor and K_s is the stress intensity factor contributed by the transformed zone. The contribution of transformation toughening, i.e. K_a is determined by the transformation strain, volume and geometry of the transformation zone, and the fraction of the transformable tetragonal zirconia [57, 58].

1.3.3 CuO doped 3Y-TZP

CuO doped 3Y-TZP ceramics have attracted extensive research interest recently. It was reported that addition of small amounts of CuO (0.3 mol%) significantly enhances superplastic deformation of the 3Y-YZP system [59]. This gives the materials a great potential in near-net shape ceramic forming applications. It was also reported that an addition of 0.25 wt % Fe_2O_3 or 0.07 wt % (0.1 mol %) CuO results in significant strength retention of Y-TZP ceramics after ageing in water or humid environment [60]. Recently, tribological studies on 3 mol% yttria stabilized tetragonal zirconia polycrystalline (3Y-TZP) ceramics showed that the addition of 1.8 mol% of CuO leads to a reduction of friction coefficient from 0.6 to 0.2 under dry sliding conditions [61,62].

1.4 Tribology in ceramics

1.4.1 Theoretical background of tribology

Tribology is defined as the science and technology of interacting surfaces in relative motion, and embraces the study of friction, wear and lubrication. Friction and wear take place whenever two contacting bodies move over each other. Under some circumstances friction and wear make our life easy. For instance, without friction we could not walk or brake a car. However, in most engineering applications friction and wear have to be minimised to reduce energy consumption and to increase lifetime of device.

Friction

Friction is defined as the resistance to the motion of two contacting objectives. Leonardo Da Vinci (1452-1519) was one of the first scholars to study friction systematically. He found two empirical laws of friction: i) the apparent contact area has no effect on friction; and ii) friction force between two surfaces is proportional to the normal load. In 1699, Guillaume Amontons rediscovered the same laws based on his independent work. In 1785, Charles Austin Coulomb added the third law to the classic friction theory, i.e. iii) friction is independent of sliding velocity.

According to the first friction law, friction experienced by two moving bodies in contact can be quantified by the coefficient of friction (f), which is defined as:

$$f = \frac{F}{P} \qquad \text{(Eq. 1.4)}$$

where F is the friction force and P is the normal load.

Bowen and Tabor [63] gave a physical explanation for the laws of friction. They showed that the frictional force is dependent on the true contact area between the two surfaces. It was indicated that the frictional force arises from the adhesion force (F_{adh}), which is needed to break the contact between the surfaces, and the deformation force (F_{pl}), which is needed by asperities on one surface to plough through the other surface. The frictional force according to Bowden and Tabor [63] can be expressed as:

$$F = F_{adh} + F_{pl} = \tau_i A + HA' \qquad \text{(Eq. 1.5)}$$

Where τ_i is the interfacial shear force per unit area required to break the junction (i), H is the hardness of the softer material, A is the projected normal contact area and A' is the frontal contact area. This interfacial shear strength (τ_i) is the most difficult value to obtain. For a lubricated sliding contact, the shear strength is mostly related to the shear properties of the lubricant whereas for a dry sliding contact there is no direct relation between the interfacial shear strength and the bulk properties, and therefore it must be measured.

Wear

Wear can be defined as progressive loss of matter from the operating surface of a body as a result of relative motion at the surface. There are four basic mechanisms of wear, namely: adhesion, abrasion (wear associated with the presence of hard particles), fatigue and corrosion. Very often, more than one basic wear mechanism occurs in the operating tribosystem. Besides the wear mechanism, engineers

are also interested in quantifying the amount of material that is removed from the surface. In practice the specific wear rate, *k*, is a more useful parameter for evaluation of the tribosystems [64]:

$$k = \frac{V_W}{P \cdot x}$$
(Eq. 1.6)

where V_W is the worn volume, *P* is the normal load and *x* is the sliding distance. A unit of $mm^3 \cdot N^{-1} m^{-1}$ is normally used for this parameter. The specific wear rate is often referred to present the level of wear and, on the other hand, the wear-resistance of tribosystems. In practice the worn volume can linearly increase with sliding distance (at constant specific wear rate). But in some cases a sudden change in specific wear rate can occur, which implies a transition between different wear mechanisms.

1.4.2 Self-lubrication

In engineering applications minimising wear and friction is necessary in order to avoid large energy costs and fast damage of machine components. At present liquid lubricants, which are mainly organic substances, are widely used to reduce wear and friction. However, due to economic and environmental reasons, the usage of liquid lubricants is more and more unfavourable. Furthermore in some special circumstances, such as in high vacuum or at high temperatures, it is not possible to use such liquid lubricants. Therefore development of new materials that can be used in absence of lubricants, so called dry sliding conditions, is increasingly gaining attention. It is now generally recognised that materials suitable for unlubricated tribo-applications should fulfil the following two criteria [65]:

●   the specific rate, *k*, is less than 10^{-6} $mm^3 \cdot N^{-1} \cdot m^{-1}$;

●   the coefficient of friction, *f*, is lower than ≤ 0.2.

A model for reducing wear and friction in dry sliding conditions by means of self-lubrication is proposed by Alexeyev et al.[66]. According to this model, a soft second phase is uniformly dispersed in a matrix of hard materials during material processing. During sliding against the counter material, the soft phase will be squeezed out and smeared to form a soft thin film in the contact area between the sliding surfaces. This soft film can reduce wear and friction as a lubricant. Because the thin film is continuously generated during sliding, low wear and friction are expected to be sustainable for the tribosystem containing such a self-lubricating composite. Based on this self-lubricating idea, several promising tribological material systems have been developed in the past decade [61-62, 67].

1.4.3 Tribology study on tetragonal zirconia based ceramics

Specific properties of tetragonal zirconia based ceramics like high hardness, high toughness and high thermal stability, make these materials interesting for tribological applications. Intensive researches on tribological properties of various ceramic systems have been carried out in the past decades [68-76]. Most of the researches on tribology of zirconia based ceramics focused on their wear resistance, mechanism of wear and the dependency on microstructure and operation conditions.

High wear-resistance under dry sliding conditions (10^{-6} $mm^3 \cdot N^{-1} \cdot m^{-1}$) can often be obtained on the tribosystems where tetragonal zirconia ceramics are applied. He [68-69] observed a Hall-Petch type relationship between wear resistance and average grain size of the Y-TZP when the grain size is less than 0.7 μm. If the average grain size is larger than 0.9 μm the wear resistance of Y-TZP ceramics is proportional to the reciprocal of the average grain size. The transition between mild and severe wear

for zirconia ceramics is found to be a function of not only sliding velocity, normal load but also of microstructural parameters like grain size and crystal structure. Based on parameters like mechanical and thermal properties, Pasaribu [72] developed a wear model, which predicts the wear severity of the tribosystem under certain conditions.

In contrast to the low wear often obtained, the friction coefficient of tetragonal zirconia ceramics in tribosystem is normally unacceptably high (> 0.5) for dry sliding applications. Kerkwijk [70-71] used several oxide additives as a second phase in Y-TZP and alumina ceramics in order to obtain self-lubricating mechanism to reduce friction. Among those additives, CuO seems to be a very promising one. It was shown that addition of 1 wt% of CuO in the 3Y-TZP ceramic reduces the friction coefficient from 0.8 to 0.2 within several km of sliding distance.

1.5 Aim of this thesis

The major aims of the work described in this thesis are, on one hand to obtain a better control of processing of CuO doped 3Y-TZP ceramic materials, and on the other hand to explore their potential in tribological applications under unlubricated conditions. The former aim requires sound knowledge not only of 3Y-TZP and CuO powder synthesis, compaction and sintering behaviour of the composite powders, but also of microstructure evolution during sintering. With this knowledge it is possible to tune the properties of the CuO doped 3Y-TZP through manipulating microstructure by good control of processing or utilising different processing techniques. For the latter aim, more insight of the influence of the presence of CuO in 3Y-TZP on the tribological properties is necessary in order to obtain the optimal microstructure for low wear and friction in these systems. Chemical composition, sintering temperature as well as post-temperature treatments are parameters which influence the tribological properties.

1.6 Structure of this thesis

This thesis is divided into 10 chapters:

Chapter 2 deals with sintering behaviour of coarse-grained 0.8 mol% CuO doped 3Y-TZP composites prepared from commercial starting powders. The sintering behaviour is interpreted on the basis of several reactions, which occur during sintering. In this chapter it is shown that sintering in oxygen is beneficial for densification.

In chapter 3 synthesis and characterisation of nanocrystalline 3Y-TZP and CuO powders will be presented. Parameters for CuO powder preparation are optimised for minimising aggregation and agglomeration.

In chapter 4 investigations of reactions during sintering of CuO doped 3Y-TZP nano-powder composites are described. These reactions between CuO and the 3Y-TZP matrix are revealed by using techniques such as thermal analysis, XPS and high-temperature XRD.

Chapter 5 is focused on the influence of reactions, as described in chapter 4, on sintering behaviour of CuO doped 3Y-TZP nano-powder composites. A solution for optimising sintering of the composites by control of reaction is proposed. By doing so a very good sinterability is achieved.

In chapter 6 the microstructure evolution during sintering of CuO doped 3Y-TZP nano-powder composites is described. The influence of CuO addition on grain growth and tetragonal to monoclinic

zirconia phase transformation as well as CuO segregation are discussed on the basis of the reactions, which occur during sintering.

In chapter 7 an advanced processing technique, namely spark plasma sintering (SPS), is employed for processing CuO doped 3Y-TZP nano-powder composites. SPS is proven to be a very efficient method for producing dense nanostructured ceramics of CuO doped 3Y-TZP. The microstructure of the produced ceramic is adjusted by annealing after SPS process. It is also shown that tuning of material properties through manipulation of microstructure can be achieved by utilising different processing techniques.

Chapter 8 describes the dependence of microstructure on the mechanical and tribological properties of the coarse-grained 8 mol% CuO doped 3Y-TZP composites. It is shown that only 50 °C difference in sintering temperature remarkably changes microstructure and consequently results in totally different tribological properties. This tremendous difference in tribological properties is interpreted by the wear mechanism transition model as evaluated by Pasaribu [72].

Chapter 9 explores more insights of the reduction of friction coefficient, i.e. the self-lubrication effect in the tribosystem of CuO doped 3Y-TZP ceramic sliding against an alumina ball. The micromorphology of the wear track is investigated in detail and a deterministic model is involved to interpret the mechanism of reduction of friction coefficient.

Finally in chapter 10 evaluation of the presented work is given together with recommendations for future work.

References

1. Richerson, D.W., "The magic of ceramics", Westerville, American Ceramic Society, 2000.
2. Kingery, W.D., Bowen, H.K. and Uhlmann, D.R., "Introduction of Ceramics", Wiley, New York, 1976.
3. Brook, R.J., "Concise encyclopedia of advanced ceramic materials", Pergamon Press, Oxford, 1991.
4. Stevens, R. "An introduction to zirconia", Magnesium Elektron, Ltd. Sec. edition, Litho 2000, Twickenham, UK, 1986.
5. Kato, K., "Tribology of ceramics", *Wear*, 1990, **136**, 117-133.
6. Reed, J.S., "Principles of ceramics processing", second edition, Wiley, New York, 1994.
7. Winnubst, A.J.A., "Ceramic processing and microstructures", Lecture notes, University of Twente, The Netherlands, 2002.
8. Winnubst, A.J.A., Groot Zevert, W.F.M., Theunissen, G.S.A.M. and Burggraaf, A.J., "Microstructure characteristics of ultra-fine ZrO_2-Y_2O_3 ceramic powders", *Mat. Sci. Engr.*, 1989, **A109**, 215-219.
9. Rama, G.V., Ramakrishnan, K.N., Venkadesan, S., Mannan, S.L., "Synthesis of partially stabilized zirconia by a sol-gel process", *Mat. Lett.*, 1995, **22**, 71-75.
10. Shi, Y., Cao, C., Feng, S., "Hydrothermal synthesis and characterization of BiTiO", *Mat. Lett.*, 2000, **46**[5], 270-273.
11. Van den Graaf, M.A.C.G., Van Dijk, T., de Jongh, M.A., Burggraaf, A.J. "High Sinter Reactivity and Microstructure of Fine-Grained Substituted ZrO_2 Compacts", *Sci. Ceram.*, 1977, **9**, 75-83.

12. Sato, M., Tanji, T., Hara, H., Nishide, T., Sakashita, Y., "SrTiO$_3$ film fabrication and powder synthesis from a non-polymerized precursor system of a stable Ti(IV) complex and Sr(II) salt of EDTA", *J. Mat. Chem.*, 1999, **9**[7], 1539-1542.

13. Messing, G.L., Zhang, S.C., and Jayanthi, G.V., "Ceramic powder synthesis by spray pyrolysis", *J Am. Ceram. Soc.*, 1993, **76**[11], 2707-2726.

14. Wang, M.-C., Wu, N.-C., Tasi, M.-S., Liu, H.-S., "Preparation and characterization of AlN powders in the AlCl-NH-N system", *J. Crystal Growth*, 2000, **216**[1-4], 69-79.

15. Vollath, D., Sickafus, K.E., "Synthesis of nanosized ceramic oxide powders by microwave plasma reactions", *Nano. Mat.*, 1992, **1**, 427-437.

16. Skandan, G., "Processing of nanostructured zirconia ceramics", *Nano. Mat.*, 1995, **5**[2], 111-126.

17. Sagel-Ransijn, C.D., Winnubst, A.J.A., Burggraaf, A.J. and Verweij, H., "The Influence of Crystallization and Washing Medium on the Characteristics of Nanocrystalline Y-TZP", *J. Eur. Ceram. Soc.*, 1996, **16**[7], 759-766.

18. Van de Graaf, M.A.C.G., Ter Maat, J.H.H. and Burggraaf, A.J., "Microstructure and sintering kinetics of highly reactive ZrO$_2$-Y$_2$O$_3$ ceramics", *J. Mat. Sci.*, 1985, **20**[4], 1407-1418.

19. Groot Zevert, W.F.M., Winnubst, A.J.A., Theunissen, G.S.A.M. and Burggraaf, A.J., "Powder preparation and compaction behaviour of fine-grained Y-TZP," *J. Mater. Sci.*, 1990, **25** [11] 3449-3455.

20. Sagel-Ransijn, C.D., "Nanostructured zirconia ceramics by gel-precipitation, processing, microstructure and mechanical properties", PhD Thesis, University of Twente, The Netherlands, 1996.

21. Coble, R.L., "Sintering crystal solids, I. Intermediate and final state diffusion models", *J. App. Phys.*, 1960, **32**, 787-792.

22. Coble, R.L., "Sintering crystal solids, II. Experimental test of diffusion", *J. App. Phys.*, 1960, **32**, 793-799.

23. Kingery, W.D. and Berg, M., "Study of Initial Stages of Sintering Solids by Viscous Flow, Evaporation-Condensation, and Self-Diffusion," *J. Appl. Phys.*, 1955, **26**[10], 1205-1212.

24. Johnson, D.L., "New Method of Obtaining Volume, Grain-Boundary, and Surface Diffusion Coefficients from Sintering Data," *J. Appl. Phys.*, 1969, **40**[1], 192-200.

25. Ashby, M.F., "A First Report on Sintering Diagrams," *Acta Metall.,* 1974, 22[3], 275-289.

26. Hansen, J.D., Rusin, R.P., Teng, M.H., Johnson, D.L "Combined-Stage Sintering Model", *J. Am. Ceram. Soc.,* 1992, **75**[5] 1129-1135,

27. Zhao, J.J. and Harmer, M.P., "Sintering Kinetics for a Model Final-Stage Microstructure: A Study in A1$_2$O$_3$," *Philos. Mag. Lett*., 1991, **63** [l] 7-14.

28. Su, H.; Johnson, D.L., "Master sintering curve: a practical approach to sintering"; *J. Am. Ceram. Soc.*, 1996, **79**, 3211-3217.

29. Shi, J.L., "Thermodynamics and densification kinetics in solid-state sintering of ceramics", *J. Mat. Res.*, 1999, **14**[4], 1398-1408.

30. Shen, Z., Nygren, M., "Microstructural prototyping of ceramics by kinetic engineering: application of spark plasma sintering", *The Chem. Record*, 2005, **5**, 173-184.

31. Kingery, W.D. and Francois, B., "The sintering of crystalline oxides, I. Interactions between grain boundaries and pores", pp. 471-498 in Sintering and related phenomena. Ed. by G.C. Kuczynski, N.A. Hooton and C.F. Gibbon. Gordon Breach, New York, 1967.

32. Lange, F.F. and Davis, B.I., "Sinterability of ZrO$_2$ and Al$_2$O$_3$ powders: the role of pore coordination number distribution", *J. Am. Ceram. Soc.*, 1983, **66**, 699-713.

33. Groza, J.R., "Nanosintering", *NanoStructured Materials*, 1999, **12**, 987-992.

34. Brook, R.J., "Controlled grain growth", pp. 331-364, in: Treatise of Materials Science and Technology, **Vol. 9**, edited by F.F.Y. Wang, Academic Press, New York, 1976.

35. Lücke, K. and Detert, K., "A quantitative theory of grain-boundary motion and recrystallization in metals in the presence of impurities", *Acta Metall.*, 1957, **5**, 628-637.

36. Theunissen, G.S.A.M., Winnubst, A.J.A. and Burggraaf, A.J., "Sintering kinetics and microstructure development of nanoscale Y-TZP ceramics", *J. Eur. Cer. Soc.*, 1993, **11**, 315-324.

37. Lange, F.F., "Controlling grain growth", pp. 497-508 in: Ceramic microstructures '86: Role of interfaces, Materials Science Research Volume 21, Edited by J.A. Pask and A.G. Evans, Plenum Press, New York, 1987.

38. Rupp, J.L.M, Ludwig, A.I. and Gauckler, L.J., "Microstrain driven self-limited grain growth in nanocrystalline ceria ceramics", *in press.*

39. Boutz, M.M.R., Winnubst, A.J.A., Hartgers, F. and Burggraaf, A.J., "Effect of additives on densification and deformation of tetragonal zirconia", *J. Mater. Sci.*, 1994, **29** 5374-5382.

40. Kimura, N., Okamura, H. and Morishita, J., "Preparation of Low-Y_2O_3-TZP by low-temperature sintering", pp. 183-191 in Advances in Ceramics, vol 24: *Science and Technology of zirconia III*, The American Ceramic Society, 1988.

41. Lawson, S., Gill, C. and Dransfield, G.P., "The effects of copper and iron oxide additions on the sintering and properties of Y-TZP", *J. Mater. Sci.*, 1995, **30**[12] 3057-3060.

42. Mishra, R.S., Lesher, C.E. and Mukherjee, A.K., "High-pressure sintering of nanocrystalline γ-Al_2O_3", *J. Am. Ceram. Soc.*, 1996, **79**[11], 2989-2992.

43. Gao, L., Li, W., Wang, H.Z., Zhou, J.X., Chao, Z.J., Zai, Q.Z., "Fabrication of nano Y-TZP materials by superhigh pressure compaction", *J. Eur. Ceram. Soc.*, 2001, **21**, 135-138.

44. Winnubst, A.J.A. and Boutz M.M.R., "Sintering and densification; New techniques: sinter forging", *Key Engr. Mater.*, 1998, **153-154**, pp. 301-323.

45. Cheng, J., Agrawal, D., Zhang, Y., Roy, R., "Microwave sintering of transparent alumina", *Mat. Lett.*, 2002, **56**, 587-592.

46. Groza, J.R., Zavaliangos, A., "Sintering activation by external electrical field", *Mat. Sci. Eng.*, 2000, **A287**, 171-177.

47. Wroe, R., Rowley, A.T., "Evidence for a non-thermal microwave effect in the sintering of partially stabilized zirconia", *J. Mat. Sci.*, 1996, **31**, 2019-2026.

48. Garvie, R.C., Hannink, R.H.J. and Pascoe, R.T., "Ceramic Steel", *Nature*, 1975, **258,** 703-704.

49. Massaki, T., "Mechanical properties of toughened ZrO_2-Y_2O_3 ceramics", *J. Am. Ceram. Soc.*, 1986, **69**[8], 638-640.

50. Garvie, R.C., "Structural applications of ZrO_2-bearing materials", pp.465-479 in Advances in Ceramics, vol.12: *Science and Technology of Zirconia II*, ed. by Claussen, N., Ruhle, M., and Heuer, A.H., The American Ceramic Society, Columbus, Ohio, 1984.

51. Scott, H.G., "Phase relationships in the zirconia-yttria system", *J. Mat. Sci.*, 1975, **10**, 1527-1535.

52. Lange, F.F., "Transformation toughening: Part 1 Size effects associated with the thermodynamics of constrained transformations", *J. Mar. Sci.*, 1982, **17**, 225-234.

53. Garvie, R.C., "Stabilization of tetragonal structure in zirconia microcrystals", *J. Phy. Chem.*, 1978, **82**[2], 218-224.

54. Garvie, R.C. and Swain, M.V., "Thermodynamics of the tetragonal to monoclinic phase transformation in constrained zirconia microcrystals. Part I: In the absence of an applied stress field", *J. Mat. Sci.*, 1985, **20**[4], 1193-1200.

55. Evans, A.G., and Cannon, R.M., "Overview no. 48: Toughening of brittle solids by martensitic transformations", *Acta Metall.*, 1986, **34**[5], 761-800.

56. Heuer, A.H., "Transformation toughening in ZrO_2-containing ceramics", *J. Am. Ceram. Soc.*, 1987, **70**[1], 689-698.

57. Marshall, D.B., Shaw, M.C., Dauskardt, R.H., Ritchie, R.O., Readey, M.J. and Heuer, H., "Crack-tip transformation zones in toughened zirconia", *J. Am. Ceram. Soc.*, 1990, **73**[9], 2659-2666.

58. Evans, A.G., "Perspective on the development of high-toughness ceramics", *J. Am. Ceram. Soc.*, 1990, **73**[2], 187-206.

59. Hwang, C.M.J. and Chen, I.-W., "Effect of a liquid phase on superplasticity of 2-mol%-Y_2O_3-stabilized tetragonal zirconia polycrystals", *J. Am. Ceram. Soc.*, 1990, **73**[6], 1626-1632.

60. Lawson, S., Gill, C., Dransfield, G.P., "The effects of copper and iron oxide additions on the sintering and properties of Y-TZP", *J. Mater. Sci.*, 1995, **30**[12], 3057-3060.

61. Pasaribu, H.R., Sloetjes, J.W. and Schipper, D.J., "Friction reduction by adding copper oxide into alumina and zirconia ceramics", *Wear*, 2003, **255**[1-6], 699-707.

62. Kerkwijk, B., García, M., van Zyl, W.E., Winnubst, L., Mulder, E.J., Schipper, D.J. and Verweij, H., "Friction behaviour of solid oxide lubricants as second phase in α- Al_2O_3 and stabilised ZrO_2 composites", *Wear*, 2004, **256,** 182-189.

63. Bowden, F.P. and Tabor, D., "Friction and lubrication of solids", Clarendon Press, Oxford, 1950.

64. Hutchings, I.M., "Tribology: friction and wear of engineering materials", Edward Arnold, 1992.

65. Czhichos, H., Klaffke, D., Santner, E. and Woydt, M., "Advances in tribology: the material point of view", *Wear*, **190**, 1995, 151-161.

66. Alexeyev, N., Jahanmir, S., "Mechanics of friction in self-lubricating composite materials. Part I: Mechanics of second phase deformation and motion", *Wear*, 1993, **166**, 41-48.

67. Kumar, R., Sudarshan, S., "Self-lubricating composites: graphite-copper", *Mat. Tech.*, 1996, **11**, 191-194.

68. He, Y.J., "Tribological and mechanical properties of fine-grained zirconia and zirconia-alumina ceramics", Ph.D. thesis, University of Twente, the Netherlands, 1995.

69. He, Y.J., Winnubst, A.J.A., Schipper, D.J., Burggraaf, A.J. and Verweij, H., "Effects of a second phase on the tribological properties of Al_2O_3 and ZrO_2 ceramics", *Wear*, 1997, **210**, 178-187.

70. Kerkwijk, B., "Wear and friction of nanostructured zirconia and alumina ceramics and composites", Ph.D. thesis, University of Twente, the Netherlands, 1999.

71. Kerkwijk, B., Mulder, E., Verweij, H., "Zirconia–alumina ceramic composites with extremely high wear resistance", *Adv. Eng. Mater.*, 1999, **1,** 69-71.

72. Pasaribu, H.R., "Friction and wear of zirconia and alumina ceramics doped with CuO", Ph.D. thesis, University of Twente, the Netherlands, 2005.

73. Zum Gahr, K.-H., "Modeling and microstructural modification of alumina ceramic for improved tribological properties", *Wear*, 1996, **200,** 215-224.

74. Zum Gahr, K.-H., "Effect of grain size on friction and sliding wear of oxide ceramics", *Wear*, 1993, **162–164,** 269-279.

75. Woydt, M., Kadoori, J., Habig, K.-H., Hausner, H., "Unlubricated sliding behaviour of various zirconia-based ceramics", *J. Eur. Ceram. Soc.*, 1991, **7,** 135-145.

76. Kong, Y., Yang, Z., Zhang, G., Yuan, Q., "Sliding friction and wear of alumina-reinforced zirconia-toughened mullite composites", *Wear*, 2002, **252**, 607-613.

Chapter 2

Sintering behaviour of coarse-grained 0.8 mol% CuO doped 3Y-TZP ceramic

Abstract

In recent years, 3 mol% yttria stabilized tetragonal zirconia polycrystals (3Y-TZP) doped with copper oxide has obtained increasing interest due to its enhanced superplasticity and good potential in tribological applications. In this work, the effect of addition of small amounts (0.8 mol%) of CuO on the sintering behaviour of 3Y-TZP was studied using a dilatometer and high temperature X-ray diffraction. A qualitative sintering model was established based on several reactions during sintering as indicated by thermal analysis and XRD. Some of these reactions remarkably retard densification and consequently result in low final density (86%) of the sample sintered at 1400 ºC in air. The reaction between molten Cu_2O and yttria as segregated to the Y-TZP grain boundaries is recognised to result in a significant destabilisation of the tetragonal zirconia phase. A relatively higher oxygen partial pressure can inhibit the dissociation of CuO to Cu_2O. This inhibition in dissociation is one of the reasons why a dense (> 96%) 0.8 mol% CuO doped 3Y-TZP ceramic can be obtained after sintering at 1400 ºC in flowing oxygen.

2.1 Introduction

Since the discovery of the transformation-toughening phenomenon in tetragonal zirconia based ceramics, these materials have gained extensive interests in industrial applications [1]. It has been shown that yttria-doped tetragonal zirconia polycrystals (Y-TZP) ceramics display extremely high values of bending strength and fracture toughness [2-3]. Due to their excellent mechanical properties and chemical inertness Y-TZP ceramics are increasingly considered for a wide range of structural applications such as extrusion dies, cutting tools, valve guides, etc [4]. In addition, fine-grained Y-TZP also exhibits a superplastic deformation property, which has opened up the possibility of using ceramics in ductile near net shape forming operations [5].

In order to lower the sintering temperature, transition metal oxides like Fe_2O_3, Bi_2O_3 [6], or CuO [7] are often used as sintering additives. Moreover, addition of transition metal oxides also has important effects on physical properties of Y-TZP. It was reported that an addition of 0.25 wt % Fe_2O_3 or 0.07 wt % (0.1 mol %) CuO results in significant strength retention of Y-TZP ceramics after ageing in water or humid environment [8]. It is also well known that the addition of a small amount of CuO (< 1 mol %) to Y-TZP strongly enhances the superplastic performance of zirconia ceramics [9]. Recently, tribological studies on 3 mol% yttria stabilized tetragonal zirconia polycrystalline (3Y-TZP) ceramics showed that the addition of 1.8 mol% of CuO leads to a reduction of friction coefficient from 0.6 to 0.2 under dry sliding conditions [10,11].

For the CuO-doped Y-TZP system, the special tribological and superplastic properties are strongly dependent on the fabrication process. The whole process from powder preparation to sintering procedure has a significant influence on the final ceramic microstructure and consequently its properties. In order to optimize the fabrication process, it is important to have knowledge of the effect of CuO on the sintering behaviour. Detailed studies of the sintering behaviour of CuO-doped Y-TZP systems are not easy to be found in literature. A thermal analysis of a 3Y-TZP powder doped with copper oxide as performed by Seidensticker and Mayo has shown that several reactions occur in this system [12]. The contribution of these several reactions to the sintering behaviour of CuO-doped Y-TZP is not described yet.

In this work the sintering behaviour is studied of undoped and CuO-doped 3Y-TZP using a dilatometer. In order to investigate the influence of CuO as a second phase on the sintering of 3Y-TZP, such an amount of CuO (0.8 mol %) was chosen, which is slightly more than the solubility limit of CuO in the 3Y-TZP matrix (0.3 mol %, [12, 13]). The several effects of CuO addition to Y-TZP on sintering behaviour, microstructure development and zirconia phase evolution of these systems are discussed in terms of the several reactions, which may occur in the CuO Y-TZP system. These reactions during sintering are also interpreted by using among other things the thermal analysis experiments (DTA) as performed by Seidensticker and Mayo [12]. Furthermore, the influence of oxygen partial pressure on sintering behaviour is described.

2.2 Experimental procedure

Highly pure commercial 3Y-TZP (TZ3Y, Tosoh, Japan) and CuO powders (Aldrich Chemicals, Germany) were used as starting materials. The basic characteristics of the starting powders are listed in Table 2.1. A powder mixture of 3Y-TZP with CuO was prepared by ball milling in ethanol for 24 hours, using zirconia balls as milling medium. The CuO content was 0.8 mol% (0.5 wt%). The milled slurry was oven-dried at 80ºC for 24 hours and subsequently at 120ºC for 8 hours. The dry cake was ground slightly in a plastic mortar and sieved through a 180 μm sieve. Cylindrical compacts of the powder mixture and pure 3Y-TZP powder (milled in the same way as used for the mixture powder) were made by cold isostatic pressing at 400 MPa. The length and diameter of the compacts are 10 ~ 15 mm and 6 ~ 7 mm respectively. The green density of these compacts, measured by Archimedes technique in mercury, was 50~52% of the theoretical density of tetragonal zirconia (6.09 $g \cdot cm^{-3}$).

Table 2.1 Basic characteristics of commercial powders

Material	Molecular weight	Theoretical density	Particle size
3Y-TZP	126.3 $g \cdot mol^{-1}$	6.09 $g \cdot cm^{-3}$	30~40 nm
CuO	79.5 $g \cdot mol^{-1}$	6.31 $g \cdot cm^{-3}$	~5μm

The sintering behaviour was studied using a Netzsch 402E dilatometer, in stagnant air or in an oxygen flow. Linear shrinkage was recorded as a function of time while the samples were successively heated at 2 $ºC \cdot min^{-1}$, hold for 2 hours at 1400 ºC and finally cooled at 4 $ºC \cdot min^{-1}$. Assuming isotropy in densification of all the specimens, the density (ρ in $g \cdot cm^{-3}$) as a function of temperature during the dilatometer experiments was calculated from the green density and the observed linear shrinkage of the specimens and corrected for thermal expansion of the sample using:

$$\rho = \frac{\rho_G}{\{1 - \Delta L / L_0 + \alpha(T - T_R)\}^3} \qquad \text{(Eq.2.1)}$$

where ρ_G is the green density corrected for weight loss (due to removal of adsorbed water), $\Delta L / L_0$ is the observed linear relative shrinkage, T is the measured temperature, T_R is room temperature and α is the thermal expansion coefficient of the sintered body. α was determined using the linear shrinkage data during cooling assuming no densification during cooling. The final densities after the dilatometer experiment as calculated in this way were in good agreement with those measured by the Archimedes' technique (in mercury).

The zirconia phase evolution during sintering was investigated by X-ray diffraction (XRD, X'pert_APD, PANalytical) analysis on a green compact at various temperatures in air and oxygen flow. Prior to the XRD experiment the green compact was polished with abrasive paper (grade 1200) to a slice of 10×8×0.5 mm in dimensions. A heating rate of 5 ºC·min^{-1} was used during the XRD experiment. The volume fraction of the monoclinic zirconia phase was calculated from the (111) reflections using the relationship proposed by Toraya et al. [14]. Microstructures of the samples after dilatometer measurements were characterized using a scanning electron microscopy (SEM, JEOL-JSM5800, Japan). Gain sizes in the samples were determined by the linear intercept technique from SEM micrograph of polished, thermally etched (1100 ºC for 0.5h) surfaces. Elemental distribution of the sintered samples was analyzed by an EDX (Thermo-NORAN Instruments).

2.3 Results

2.3.1 Sintering behaviour in air

Fig. 2.1 shows the relative density as a function of temperature of undoped 3Y-TZP and 0.8 mol% CuO-doped 3Y-TZP during dilatometer tests in air. The relative density was calculated by using Eq. 2.1, while for the theoretical density the value of undoped 3Y-TZP (6.09 g cm^{-3}) was used. The undoped 3Y-TZP shows a gradual increase in density as a function of time/temperature. The
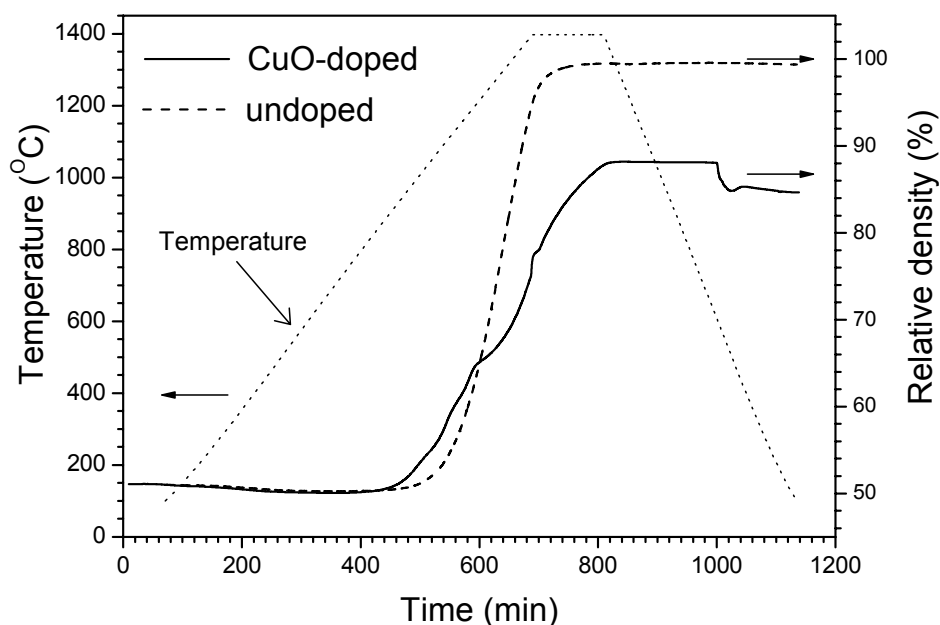
Fig. 2.1 Densification behaviour of pure 3Y-TZP and CuO-doped 3Y-TZP during sintering in air.

densification curve of CuO-doped system indicates large differences during sintering, if compared with the undoped 3Y-TZP. CuO-doped 3Y-TZP starts to densify at a lower temperature (850 ºC compared with 950 ºC for 3Y-TZP). During subsequent heating several changes in densification occur for the CuO-doped system among which the sudden change at about 1200 ºC is the most remarkable. At this temperature densification was retarded significantly. During cooling, a sudden decrease in relative density, which comes from a volume expansion, can be observed clearly at around 615 ºC for the CuO-doped system. This expansion is related to the zirconia phase transformation from tetragonal to monoclinic zirconia. XRD analysis of the surface of this CuO-doped 3Y-YZP ceramic after sintering shows about 55 vol % monoclinic zirconia, while the undoped 3Y-TZP sample contains 100 % tetragonal zirconia. This is in good agreement with the work of Lemaire [15] and Hayakawa [16], who observed that an addition of more than 0.3 mol% of CuO results in the formation of monoclinic zirconia after sintering.

In Fig. 2.1 it can be seen that the total shrinkage of the CuO-doped sample is much less than that of the undoped one. The relative densities of the samples after sintering are respectively 86% and 99 % of the theoretical one. For the case of CuO-doped 3Y-TZP the presence of monoclinic zirconia is taken into account for calculating the theoretical density (5.87 g·cm^{-3}).

For a better understanding of the differences in densification of undoped and CuO doped 3Y-TZP during heating, the densification rate is considered. A measure of the densification rate is the relative linear shrinkage rate as depicted in Fig. 2.2. The undoped 3Y-TZP sample exhibits only one maximum in densification rate at 1280 ºC indicating normal densification behaviour during the whole sintering process. For the CuO-doped sample several maximums in densification rate in heating are visible, respectively at 1010 ºC, 1105 ºC and 1185 ºC (Fig. 2.2). These variations in densification rate are caused by several reactions during heating and will be discussed in later sections.
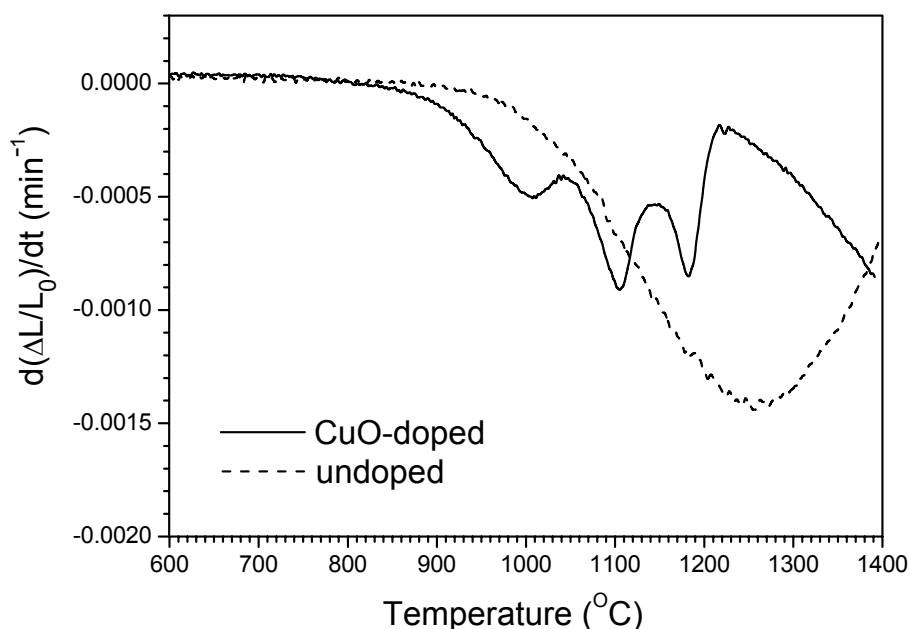
Fig. 2.2 Relative shrinkage rate of undoped 3Y-TZP and CuO-doped 3Y-TZP during sintering in air.

After the dilatometer experiment in air, several small cracks of a couple of millimetres in size were visible by eye on the surface of the CuO-doped sample. These large cracks are probably caused by stresses generated by the tetragonal to monoclinic phase transformation. Fig. 2.3 shows a scanning

electron microscope (SEM) image of a polished cross-section of the CuO-doped sample after the dilatometer experiment in air. It is clearly visible in the SEM picture that the sample contains many homogeneously distributed irregular pores with sizes up to 2 μm.
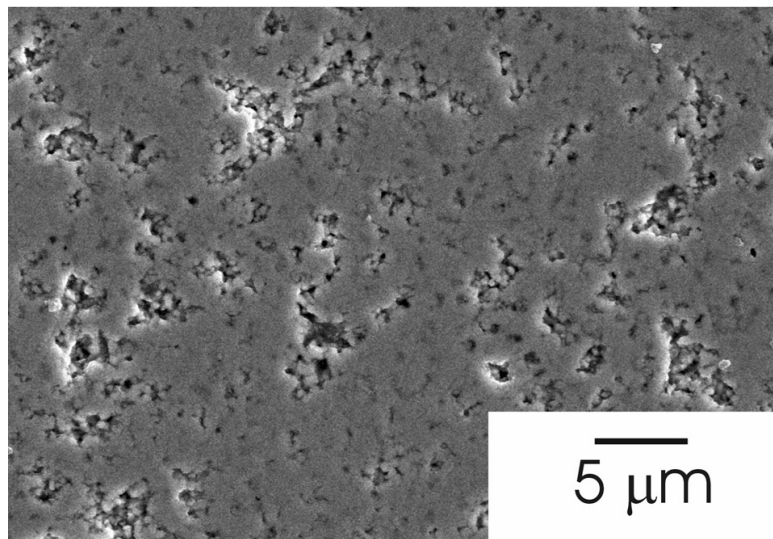
Fig. 2.3. Cross-section SEM image of a polished CuO-doped 3Y-TZP sintered in air.

2.3.2 Sintering behaviour in oxygen

Dilatometer measurements on undoped and 0.8 mol% CuO doped 3Y-TZP compacts were also conducted under a flowing oxygen stream. For the undoped 3Y-TZP, no remarkable difference in sintering behaviour between in air and in oxygen flow was found.
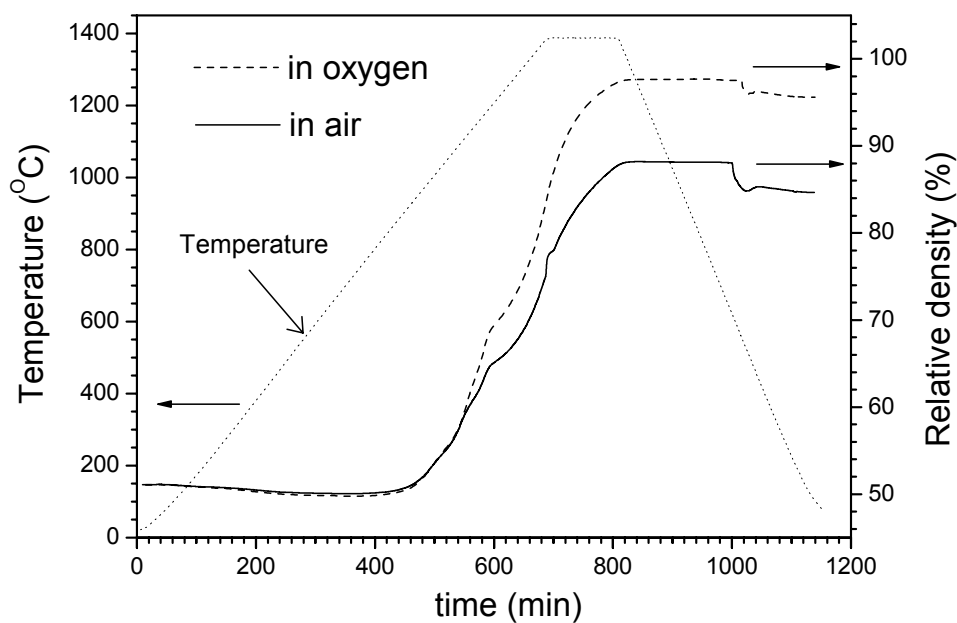
Fig. 2.4 Densification behaviour of CuO-doped 3Y-TZP during sintering in air and flowing oxygen.

For the CuO-doped sample, the relative density curve is shown in Fig. 2.4. If compared to the CuO-doped sample sintered in air, the sample sintered in oxygen showed similar changes in densification, but the total shrinkage is much higher. After the dilatometer experiment in oxygen, the sample achieved a relative density of 96 % (the presence of monoclinic zirconia is taken into account for calculating the theoretical density). During cooling of this sample an expansion can be observed, indicating again a phase transformation from tetragonal to monoclinic zirconia. The difference with the air-sintered sample is the shift of the expansion during cooling to 550 ºC (115 ºC lower). XRD analysis shows that the sample sintered in oxygen contains the same amount of monoclinic zirconia as the sample sintered in air (about 55 vol %).

The influence of oxygen partial pressure on the densification rate can be seen from Fig. 2.5. This figure shows the relative linear shrinkage rate of the CuO-doped 3Y-TZP samples during heating in stagnant air and flowing oxygen. Generally all 3 maximums in densification rate as appeared during sintering in air are also present while sintering in flowing oxygen. In both cases the temperature and intensity of the first maximum in densification rate (at 1000 ºC) are similar. However, the second maximum (at 1125 ºC in the case of oxygen) was delayed for 20 °C while sintering in oxygen, and has a relative stronger intensity as compared with the case in air. For the third maximum (at 1185 ºC) in densification rate, the influence of oxygen partial pressure was relatively less. After the dilatometer experiment in flowing oxygen, the sample looks good without visible cracks on the surface. Scanning electron microscope (SEM) analysis of a polished cross section of this sample showed a much denser structure if compared with the sample sintered in air (compare Figs. 2.6 and 2.3). Only few small pores with sizes less than 1 μm can be observed from the SEM picture in Fig. 2.6. Beside this, many homogeneously distributed dark spots can be observed on this cross-section. EDX analysis indicated that these dark spots consist of a Cu-rich phase, while in the lighter areas almost no copper was detected.
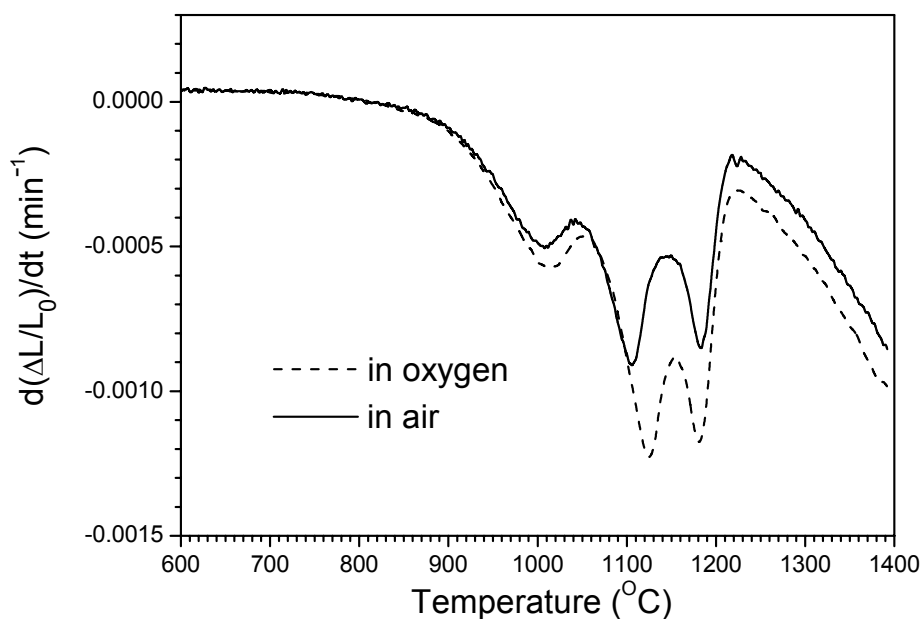
Fig. 2.5 Relative shrinkage rate of CuO-doped 3Y-TZP during sintering in air and flowing oxygen.
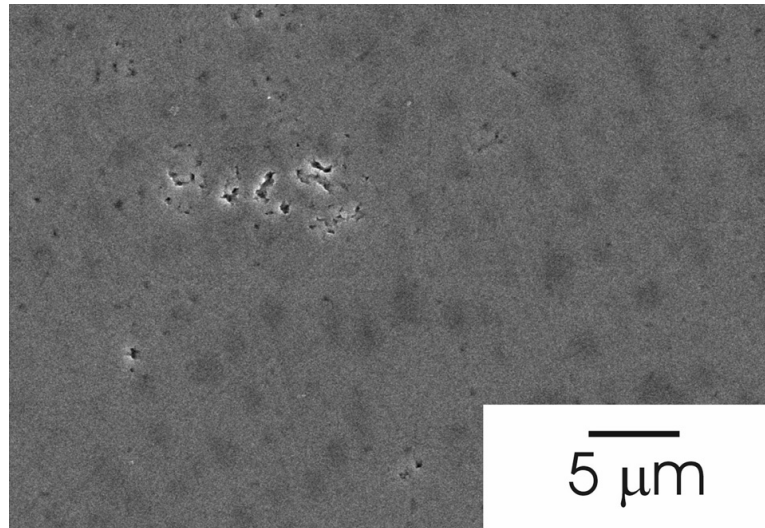
Fig. 2.6. Cross-section SEM image of a polished CuO-doped 3Y-TZP sintered in flowing oxygen.

2.3.3 Zirconia phase evolution during heating of the composite

XRD analysis at various temperatures in air and flowing oxygen showed that both tetragonal and monoclinic zirconia phases are present in the CuO-doped 3Y-TZP system and that phase transformations occur while heating. The XRD patterns obtained in air and oxygen are exactly the same at each temperature, indicating that the oxygen partial pressure has no influence on zirconia phase transformation in the present case. Based on the XRD patterns the volume fraction of these two phases can be calculated using the method as proposed by Toraya [14]. In Fig. 2.7 the volume fraction of monoclinic zirconia phase is plotted as a function of temperature. These results show that the green compact contains more than 35 vol. % of monoclinic zirconia although it was made from pure
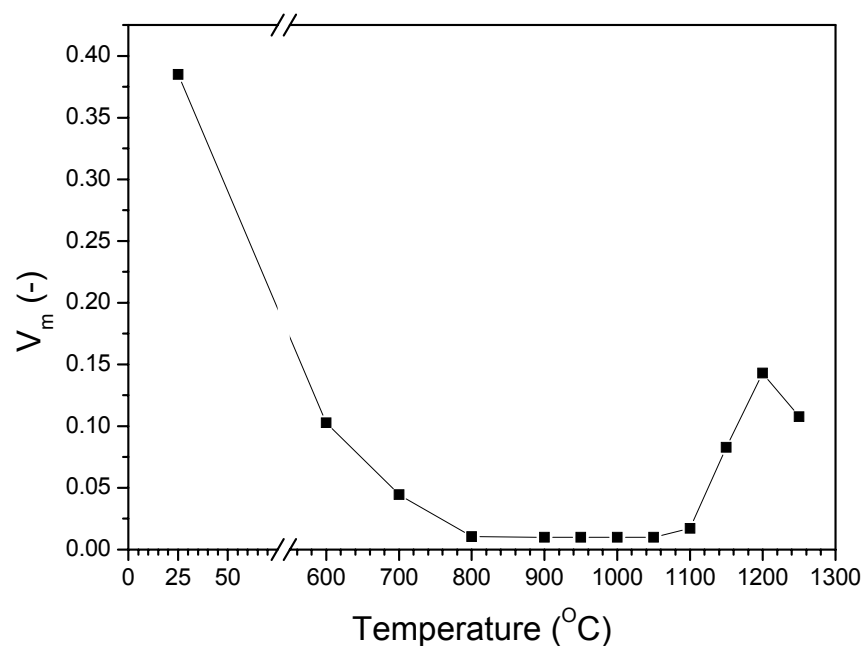
Fig. 2.7. Volume fraction of monoclinic zirconia in the CuO-doped 3Y-TZP as a function of temperature.

tetragonal 3Y-TZP powder. This presence of monoclinic zirconia was caused by the tensile stress applied on the sample during polishing prior to the XRD experiment. With increasing temperature monoclinic zirconia gradually transforms to tetragonal zirconia due to the relaxation of tensile stress until it almost disappears at 800 ºC. However, at around 1100 ºC the tetragonal zirconia starts to transform back to monoclinic phase, indicating a reaction, which destabilizes the tetragonal zirconia phase at this temperature. Above 1200 ºC monoclinic zirconia transforms to the tetragonal phase again because thermodynamically tetragonal zirconia becomes the stable phase in this temperature region.

2.4 Discussion

2.4.1 Effect of the addition of CuO on the densification behaviour of 3Y-TZP

It is shown that addition of a relative small amount of CuO (0.8 mol%) leads to several sintering stages during densification of 3Y-TZP (see Figs. 2.2 and 2.5). Generally these changes in densification rate can be explained in terms of reactions between CuO and 3Y-TZP. These reactions will now be treated for the system sintered in air (see Fig. 2.2). First the onset for densification at lower temperature (850 ºC compared with 950 ºC for 3Y-TZP) will be discussed. It is known from literature that 0.3 mol% of CuO can dissolve in the Y-TZP matrix by forming a Cu-enriched grain-boundary layer of 1~2 nm in thickness [12, 13]. As will be described in chapter 4, the CuO dissolution reaction can occur at a rather low temperature (< 600 °C). As a result of this CuO dissolution, the ion mobility in the 3Y-TZP grains and especially in the grain boundary region increases. This high ion mobility or ion diffusivity can be related to a high grain-boundary diffusion, which results in a higher densification rate [17], and consequently leads to a start of densification at a lower temperature. If the dissolution proceeded completely, 0.3 mol% of CuO would have been dissolved in the Y-TZP matrix while 0.5 mol% of CuO remained as a separate phase.

At 1010 °C the densification rate slows down slightly. Differential thermal analysis (DTA) as performed by Seidensticker et al. on a 3 mol % CuO doped 3Y-TZP powder showed an exothermic peak at around 1000 ºC during the first round of heating which is not present on reheating [12]. The authors did not explain what reaction happens here. According to the pseudo-binary phase diagram of the Y_2O_3-CuO system in air [18] a solid-state reaction between Y_2O_3 and CuO can take place above 900 ºC, and a solid $Y_2Cu_2O_5$ phase is formed in this temperature regime. Another phenomenon is that after a temperature treatment around 900 ºC yttrium segregates to the grain boundaries of Y-TZP [19, 20]. As can be speculated, the solid state reaction mentioned above occurs in the contacting region between Y-TZP grains and CuO grains. The formation of $Y_2Cu_2O_5$ was confirmed by Lemaire et al. [15]. It seems that the exothermal peak at around 1000 ºC on the DTA curve as given by Seidensticker [12] is attributed to this solid-state reaction. This solid-state reaction is likely to be corresponding to the slight decrease in densification rate observed at 1010 °C.

After the first decrease in densification rate further solid-state sintering starts at 1040 ºC as indicted by the increase in shrinkage rate (Fig.2.2). However at around 1100ºC the densification rate drops rapidly. High-temperature X-ray diffraction analysis shows that a phase transformation from tetragonal to monoclinic zirconia starts at this temperature (see Fig. 2.7). The cause of this phase transformation will be discussed later. At first sight one might expect that the decrease in densification rate in this temperature region is simply caused by the volume expansion of zirconia grains (i.e. expansion of the zirconia lattice) resulted from the phase transformation. However, calculations based on the volume fraction of monoclinic zirconia indicate that the contribution of phase transformation to the overall

sample volume change is less than 0.2 % and therefore negligible if compared to the sintering process in the corresponding temperature range (1100 – 1150 ºC). Furthermore, high partial pressure (sintering in flowing oxygen flow) clearly inhibits this decrease in densification rate but does not at all affect the t-m zirconia phase transformation. There must be another reaction, which contributes to the strong decrease in densification in this sintering stage. We propose that this phenomenon is caused by the dissociation of CuO.

It is shown that at 1030 ºC CuO starts to dissociate to Cu_2O while O_2 is released [12]. From the molecular weight and theoretical densities of CuO and Cu_2O it can be calculated that the volume of a formed Cu_2O particle is 12 % less than that of a CuO particle. As a result of this shrinkage of the copper oxide particles, pores are formed or grow rapidly. Considering the relative large particle size of CuO in the starting powder (~ 5μm), one can see that large pores with diameter up to 200 nm could be formed due to the rapid volume shrinkage of the copper oxide particles. The grain size of Y-TZP after this sintering stage is only around 60 nm [21]. So the pores generated by the dissociation of CuO are about 3 times larger than the zirconia grains (the main phase in the composite), meaning a pore/grain size ratio of 3. It has been shown that pores tend to grow instead of to shrink when the pore/grain size ratio exerts a certain value [22]. This critical ratio normally is less than 1. Subsequently, those large pores are difficult to be removed by normal solid-state sintering. The presence of the large pores with sizes up to several micrometers in the sample after sintering in air, as shown in the SEM picture (Fig.2.3), is an evidence of pore growth during sintering. In conclusion, the reduction in densification, which starts at 1100 °C, can likely be ascribed more to a mechanism related to CuO dissociation and not to the t-m zirconia phase transformation, which also occurs in this temperature regime.

Pure Y-TZP does not exhibit a phase transformation from tetragonal to monoclinic zirconia while heating at these temperatures. The effect of CuO on this phase transformation will now be discussed. As discussed above a solid-state reaction between CuO and yttria as segregated to the 3Y-TZP grain boundaries occurs at around 1000 °C and results to a formation of $Y_2Cu_2O_5$. It was confirmed by Lemaire et al. [15] that the formation of $Y_2Cu_2O_5$ is corresponding to the tetragonal to monoclinic phase transformation of zirconia. The correlation between the formation of $Y_2Cu_2O_5$ and destabilisation of tetragonal zirconia was also evidenced by our study on an 8 mol% CuO doped 3Y-TZP nano-powder composite, as will be described in chapter 6. Due to the few number of contact zones between Y-TZP and CuO grains in this temperature range (less than 1 % of the 3Y-TZP grains are in contact with CuO), the formation of $Y_2Cu_2O_5$ via solid-state reaction as described here proceeds rather limited so that only small amounts of tetragonal zirconia (< 10%) transforms to monoclinic at a temperature below 1130 °C.

Above 1130 ºC Cu_2O starts to melt [12] resulting in a drastic change in sintering behaviour. The first phenomenon observed is the increase in densification rate at this temperature as shown in Fig. 2.2. Liquid-phase sintering results in an enhancement in densification if the molten Cu_2O wets the Y-TZP grains well. On the other hand, the redistribution of molten copper oxide results in a larger contact area between Y-TZP and copper oxide. This increase in contact area leads to a more intensive reaction between copper oxide and yttria as segregated to Y-TZP grain boundaries. Moreover, after melting of Cu_2O the reaction proceeds in a solid-liquid manner, while the reaction product also exists in a liquid form. It is expected that this solid-liquid reaction (>1130°C) proceeds much faster if compared to the solid-solid reaction between Cu_2O grains and yttria on the Y-TZP grain boundaries (<1130°C). DTA experiments as performed by Seidensticker and Mayo [12] showed an intensive broad endothermic peak above the melting temperature of Cu_2O, which they ascribed to the solid-liquid reaction as also

discussed here. As a result of the further reaction between molten Cu_2O and yttria as segregated to the grain boundaries, more tetragonal zirconia is destabilized and transforms to a monoclinic phase in this temperature range (1150 ~1200 °C, see Fig. 2.7). Above 1200 °C the solid-liquid reaction can still proceed and more tetragonal Y-TZP grains get destabilised. The amount of monoclinic zirconia however decreases above 1200 ºC (Fig. 2.7) because tetragonal zirconia becomes the thermodynamically stable phase. During cooling all destabilised zirconia grains transform to the monoclinic phase as indicated by the sudden volume expansion at 615 ºC (see Fig. 2.1).

The solid-liquid reaction and/or its liquid products (an yttria-copper oxide phase) seem to be detrimental for densification and result in a drastic decrease in densification rate at around 1180 °C. One of the possible explanations for this phenomenon is that the newly formed liquid yttria-copper-oxide phase wets the Y-TZP grains less than molten Cu_2O.

2.4.2 Effect of oxygen partial pressure

All three densification rate maximums as appeared in the case of sintering in air are also present in the case of sintering in flowing oxygen (Fig 2.5). This is an indication that all reactions, which occur during sintering in air also take place during sintering under a higher oxygen partial pressure. The most obvious effect of a higher oxygen partial pressure on sintering is the fact that the second decrease in densification rate starts at 1125 ºC, while during sintering in air densification in this temperature regime retards at 1100 ºC (see Fig. 2.5). It is stated in the discussion, as given above, that dissociation of CuO to Cu_2O starts at 1040 ºC. This reaction can be expressed as follows:

$$4CuO(s) \Leftrightarrow 2Cu_2O(s) + O_2(g) \hspace{3cm} \text{(Eq. 2.2)}$$

Judging from this equilibrium reaction, it is clear that this reaction proceeds slower to the right as a function of temperature under a higher oxygen partial pressure (oxygen flow compared with air). Obviously, the formation or evolution of pores due to this reaction takes place slower too. Additionally, because the temperature of this dissociation reaction is close to the melting point of copper oxide, mechanisms like rearrangement of Y-TZP grains and especially viscous flow can take place. The delay of dissociation of CuO allows the Y-TZP grains rearrangement and viscous flow to proceed more effectively to fill the pores. As a result, the size of the pores formed in this sintering stage can be significantly smaller if compared with the case of sintering in air. Although the pores size was still sufficiently large to inhibit densification as indicated by the second decrease in densification rate (Fig. 2.5), probably most of those pores were able to be removed in further sintering, especially while a liquid phase is present (above 1130 ºC). This is confirmed by the SEM picture of the sample after sintering in flowing oxygen (Fig. 2.6), which only shows few small pores.

2.5 Conclusions

A small amount of CuO addition leads to a remarkable change in densification behaviour of 3Y-TZP. Several reactions occur during sintering which can be beneficial or detrimental for densification. The following sintering stages are discerned:

- − The starting temperature for densification is decreased due to the dissolution of CuO in the Y-TZP matrix.

- A solid-state reaction between CuO and yttria as segregated to the 3Y-TZP grain boundaries at around 1000 ºC retards densification slightly.

- Dissociation of CuO to Cu_2O starts at 1040 ºC. Large pores can be formed when this reaction proceeds too fast. The formation of large pores retards densification remarkably and consequently leads to a low density and a poor microstructure of the 0.8 mol% CuO-doped 3Y-TZP sample after sintering in air.

- A higher oxygen partial pressure can slow down this dissociation of CuO. The 0.8 mol% CuO-doped 3Y-TZP sintered under a relatively high oxygen partial pressure (in flowing oxygen) has a density of 96 %.

- While the Cu_2O starts to melt at 1130 ºC, densification is enhanced due to the presence of a liquid phase.

- After the melting of Cu_2O, a solid-liquid reaction between molten Cu_2O and yttria as segregated from the Y-TZP grains results in the decrease in densification rate at 1180 ºC. This reaction also leads to destabilisation of the tetragonal phase of zirconia.

- Both CuO-doped samples sintered in air and flowing oxygen contain 55 vol% of monoclinic zirconia while the undoped sample contains 100 % tetragonal zirconia after sintering.

References

1. Garvie, R.C., Hannink, R.H.J. and Pascoe, R.T., "Ceramic Steel", *Nature*, 1975, **258,** 703-704.

2. Massaki, T., "Mechanical properties of toughened ZrO_2-Y_2O_3 ceramics", *J. Am. Ceram. Soc.*, 1986, **69**[8], 638-640.

3. Tsukuma, K., Kubota, Y., Tsukidata, T., "Thermal stability and mechanical properties of Y_2O_3-stabilized tetragonal ZrO_2 polycrystals", pp. 382-390 in Advances in Ceramics, vol.12: *Science and Technology of Zirconia II*, ed. by Claussen N., Ruhle M., and Heuer A.H., The American Ceramic Society, Columbus, Ohio, 1984.

4. Garvie, R.C., "Structural applications of ZrO_2-bearing materials", pp.465-479 in Advances in Ceramics, vol.12: *Science and Technology of Zirconia II*, ed. by Claussen N., Ruhle M., and Heuer A.H., The American Ceramic Society, Columbus, Ohio, 1984.

5. Wakai, F., Sakaguchi, S. and Matsuno, Y., "Superplasticity of Yttria-Stabilized Tetragonal ZrO_2 Polycrystals", *Adv. Ceram. Mat.*, 1986, **1,** 259-263.

6. Boutz, M.M.R., Winnubst, A.J.A., Hartgers, F., Burggraaf, A.J., "Effect of additives on densification and deformation of tetragonal zirconia", *J. Mater. Sci.*, 1994, **29,** 5374-5382.

7. Kimura, N., Okamura, H. and Morishita, J., "Preparation of Low-Y_2O_3-TZP by low-temperature sintering", pp. 183-191 in Advances in Ceramics, vol 24: *Science and Technology of zirconia III*, The American Ceramic Society, 1988.

8. Lawson, S., Gill, C., Dransfield, G.P., "The effects of copper and iron oxide additions on the sintering and properties of Y-TZP", *J. Mater. Sci.*, 1995, **30**[12], 3057-3060.

9. Hwang, C.M.J. and Chen, I.-W., "Effect of a liquid phase on superplasticity of 2-mol%-Y_2O_3-stabilized tetragonal zirconia polycrystals", *J. Am. Ceram. Soc.*, 1990, **73**[6], 1626-1632.

10. Kerkwijk, B., García, M., van Zyl, W.E., Winnubst, L., Mulder, E.J., Schipper, D.J. and Verweij, H., "Friction behaviour of solid oxide lubricants as second phase in α- Al_2O_3 and stabilised ZrO_2 composites", *Wear*, 2004, **256,** 182-189.

11. Pasaribu, H.R., Sloetjes, J.W. and Schipper, D.J., "Friction reduction by adding copper oxide into alumina and zirconia ceramics", *Wear*, 2003, **255**[1-6], 699-707.

12. Seidensticker, J.R. and Mayo, M.J., "Thermal analysis of 3-mol%-yttria-stabilized tetragonal zirconia powder doped with copper oxide", *J. Am. Ceram. Soc.*, 1996, **79**[2], 401-406.

13. Mayo, M.J., Seidensticker, J.R., Hauge, D.C. and Carim, A.H., "Surface chemistry effects on the processing and superplastic properties of nanocrystalline oxide ceramics", *Nanostructured Mater.*, 1999, **11**[2], pp. 271-282.

14. Toraya, H., Yoshimura, M. and Somiya, S., "Calibration Curve for Quantitative Analysis of the Monoclinic-Tetragonal ZrO_2 System by X-Ray Diffraction", *J. Am. Ceram. Soc.*, 1984, **67**[6], C119-C121.

15. Lemaire, L., Scholz, S.M., Bowen, P., Dutta, J., Hofmeister, H. and Hofmann, H., "Effect of CuO additives on the reversibility of zirconia crystalline phase transitions", *J. Mater. Sci.*, 1999, **34,** 2207-2215.

16. Hayakawa, M., Inoue, T., Pee, J.-H., Suematsu, H. and Yamauchi, H., "Liquid phase sintering of Y-TZP with CuO and $Y_2Cu_2O_5$ dopants", *Mater. Sci. Forum*, 1999, **304-306**, pp.465-470.

17. Raming, T.P., Winnubst, A.J.A., van Zyl, W.E., Verweij, H., "Densification of zirconia-hematite nanopowders", *J. Eur. Ceram. Soc.*, 2003, **23**[7], p. 1053-1560.

18. Gadalla, A.M. and Kongkachuichay, P., "Compatible phases of the Y_2O_3–CuO–Cu_2O system in air", *J. Mater. Res.*, 1991, **6,** 450-454.

19. Theunissen, G.S.A.M., Winnubst, A.J.A. and Burggraaf, A.J., "Segregation aspects in the ZrO_2-Y_2O_3 ceramic system", *J. Mater. Sci. Lett.*, 1989, **8**[1], 55-57.

20. Burggraaf, A.J., Van Hemert, M., Scholten, D., Winnubst, A.J.A., "Chemical composition of oxidic interfaces in relation with electric and electrochemical properties", pp. 797-802 in Reaction of Solid, Ed. by P. Barret and L.C. Dufour, 1985.

21. Theunissen, G.S.A.M., Winnubst, A.J.A. and Burggraaf, A.J., "Sintering kinetics and microstructure development of nanoscale Y-TZP ceramics", *J. Eur. Ceram. Soc.*, 1993, **11**[4], 315-324.

22. Kingery, W.D. and Francois, B., "The sintering of crystalline oxides, I. Interactions between grain boundaries and pores", pp. 471-498 in Sintering and related phenomena. Ed. by G.C. Kuczynski, N.A. Hooton and C.F. Gibbon. Gordon Breach, New York, 1967.

Chapter 3

Fabrication of CuO and 3Y-TZP nano-powders as used for ceramic composites

Abstract

A weakly agglomerated 3Y-TZP powder with pure tetragonal crystal structure and a primary crystallite diameter of 8 nm was successfully prepared by means of co-precipitation of metal chlorides in an ammonia solution, followed by extensive washing with ethanol. A copper oxalate precipitation procedure for the preparation of nanocrystalline CuO powders was optimised in order to minimise aggregation and agglomeration. The influences of calcination procedure, synthesis medium and other parameters on characteristics of the CuO powders were investigated in detail. Oxalate precipitation in ethanol followed by sequential drying and calcination at 250 °C in an open tubular furnace was found to be the optimal procedure for producing nanocrystalline CuO powder with small aggregates and weak agglomerates. With this optimal procedure a CuO powder with crystallite diameter and BET equivalent particle diameter of respectively 12 and 20 nm was obtained. Compaction behaviour of composite powders of 3Y-TZP doped with CuO powders with different particle size was investigated.

3.1 Introduction

In the past two decades ceramic materials with grain size in nanometre range, so called nanostructured ceramics, have attracted great interest due to their special properties. As suggested by Burggraaf et al. [1,2] some of the characteristic features of nanostructured materials are:

• the constituting atomic domains (grains, phases, intra-crystalline domains) have a size less than 100 nm.

• a significant atom fraction is situated in the grain boundary region and/ or associated with interfacial effects.

Generally the grain boundary region shows metastabilities that can be classified into three categories: compositional (extended solution range), structural or topological (alternate crystal structure or amorphous phases) and morphological (finely divided structures) [3]. Special material properties can arise from the metastable conditions of the large fraction grain boundary region in nanostructured ceramics [4]. It has been shown in many papers that sintering temperature can be lowered by several hundred degrees by reducing the starting particle size to the nanometre range [5-7]. Nanostructured zirconia ceramics were also reported to possess very good mechanical properties [8, 9], strongly enhanced superplastic behaviour for e.g. near net-shape forming [10-12], and improved wear-resistance under dry sliding conditions [13]. It can also be used as interlayer for ceramic-ceramic bonding at lower temperature [14].

Coarse-grained CuO doped 3Y-TZP composite ceramics produced from submicron starting powders (Tosoh 3Y-TZP) have shown promisingly low friction coefficient under dry sliding conditions and enhanced superplastic behaviour [15-18]. It is of great interest to examine how the grain size influence the properties of the CuO doped 3Y-TZP composites, especially while the grain size is in the nanometre range.

In order to obtain a nanostructured composite ceramic with special properties ultra-fine starting powders are of course required. Currently a number of production techniques are available for the synthesis of nano-particles of oxides and non-oxides. These include laser ablation [19], microwave plasma synthesis [20], spray pyrolysis [21], flame pyrolysis [22], inert gas condensation [22], and wet-chemical synthesis [23-24]. These ultra-fine powders are not necessarily mono-dispersed but can also consist of larger, clustered microstructural elements [25-27]. These elements are

- primary crystallites, which are of course in the nanometre range;

- aggregates, in which the primary crystallites are held together by neck areas formed by strong interactions like chemical bonding;

- agglomerates, in which the aggregates or the individual primary crystallites are held together by relatively weak attractive forces.

The nature of these cluster elements strongly influences compaction behaviour, sinterability, microstructural evolution, and therefore the final quality of the product [8, 27]. The aggregates and agglomerates can give rise to different types of pores in a powder compact: intra-aggregate pores (pores between the crystallites), inter-aggregate or intra-agglomerate pores (first generation pores), and inter-agglomerate pores (second generation pores). During sintering all these pores must be eliminated from the compact for obtaining dense, defect-poor ceramics. However an inhomogeneous pore size distribution is present in powder compacts, which contain large aggregates or strong agglomerates. In such type of compacts pores larger than a critical size (which is normally smaller than the crystallite size) can be present and do not disappear but even grow during sintering [28]. These voids obviously lead to a poor quality of the final products. Moreover a non-uniform pore-size distribution across the powder compacts also causes inhomogeneous sintering behaviour and consequently an inhomogeneous microstructure evolution. A region of lower porosity will have less overall shrinkage during densification, resulting in distortion. Grains in this less porous region grow faster than the more porous regions, which can give rise of abnormal grain growth in part of the ceramic. Therefore precautions have to be taken to avoid the formation of hard agglomerates and large aggregates during powder synthesis.

Fabrication of nanocrystalline 3Y-TZP powders has been extensively investigated in past two decades [19-27]. It was reported that a weakly agglomerated 3Y-TZP powder with a primary crystallite diameter of 8 nm can be successfully synthesised by co-precipitation of chlorides in an ammonia solution followed by extensive washing with ethanol [24, 26-27]. The washing steps are critical for agglomeration control. In this thesis the 3Y-TZP nano-powders were all produced by this technique.

Doping CuO in 3Y-TZP nano-powder can be done by simply mixing CuO nano-powder with 3Y-TZP [29] or by an adsorption technique as reported by Mayo et al. [30]. The former method requires the synthesis of CuO nano-powders, which is not necessary for the latter method. However the adsorption technique has several drawbacks including the formation of strong agglomerates and a problem in composition control [31]. Thus mixing method is chosen in this thesis for producing nanocrystalline CuO doped 3Y-TZP composites.

A copper oxalate precipitation technique is often used to prepare CuO catalysts with crystallite sizes on the nanometre range as reported in [32-33]. However the important characteristics necessary for ceramic fabrication of this CuO powder, like degree of aggregation and agglomeration, can not be found in literature.

The work described in this chapter was undertaken to optimise the copper oxalate precipitation procedure from the ceramic fabrication point of view. Emphasis is laid on reduction of aggregates and agglomerates. The fabrication and powder characteristics of nanocrystalline 3Y-TZP powders are also described. Finally the compaction behaviour of the CuO doped 3Y-TZP nano-powder composites are discussed in this chapter.

3.2 Experimental procedure

3.2.1 Preparation of 3Y-TZP powder

A nanocrystalline powder of 3 mol% yttria stabilised tetragonal zirconia polycrystals (3Y-TZP) was prepared by a co-precipitation technique based on metal chlorides. Appropriate amounts of $ZrOCl_2 \cdot 8H_2O$ (Merck chemical, Germany) and YCl_3 (Aldrich chemical, Germany) were dissolved into water to form an aqueous mixed chlorides solution with a total metallic concentration of around 1.2 M (pH~2). The chlorides solution was then added with the aid of a peristaltic pump to a concentrated aqueous ammonia (pH ~ 14) solution, which was present in a Teflon coated steel vessel. The ammonia solution was stirred vigorously and continuously with a top-mounted turbine stirrer. In order to increase the agitation of stirring, a Teflon coated fan was placed in the vessel along the wall. More details of the precipitation setup and operation are given in [34]. The resulting wet gel was washed with copious amounts of water/ammonia mixtures, until the decanted clear liquid no longer became turbid upon addition of 0.1 M $AgNO_3$, which means that the system was chloride-free. Subsequently the precipitate was washed with ethanol to remove water. Ethanol washing was undertaken until the density of the decanted liquid was lower than 0.79 $g \cdot cm^{-1}$, implying the water content is less than 5 %. After part of the liquid in the suspension was filtered out, the remaining wet gel was oven-dried overnight at 100 ºC. The resulting amorphous yttrium-zirconium hydroxide powder was ground and sieved through a 180 μm sieve, and subsequently calcined at 550 ºC in stagnant air for 2 hours. The calcined powder was sieved again and stored in a desiccator.

3.2.2 Preparation of CuO powder

A copper oxalate precipitation method was used to prepare the nanocrystalline copper-oxide powders. $Cu(NO_3)_2 \cdot 3H_2O$ (Merck Chemical, Germany) and oxalic acid ($H_2C_2O_4 \cdot 2H_2O$, Merck Chemical, Germany) were separately dissolved into ethanol or water to form a 0.5 M solution. In order to make sure that all Cu^{2+} ions can precipitate, an excess of 5 mol% oxalic acid was used. The copper nitrate solution was added to the oxalic acid solution with the aid of a separation funnel or a peristaltic pump. While a separation funnel was used, the dropping speed of the Cu solution was controlled to be 10~15 drops per minute (roughly 1~1.5 mL·min^{-1}) and the oxalic acid solution was stirred with a magnetic stirrer. When a peristaltic pump was used, addition of Cu solution was carried out in a set-up the same as used for preparation of 3Y-TZP powder, and an adding speed of 3.5 mL·min^{-1} was used. The stirring in the latter case was much stronger than that in the former one because here a type of turbine reactor was used.

During the addition, a light blue complex precipitate of copper oxalate was formed. After all the Cu solution was added, the suspension was stirred for an extra 30 minutes. The suspension prepared in ethanol was then directly oven-dried at 100 ºC for 24 hours. The suspension prepared in water was washed with water and ethanol prior to drying (100 ºC for 24 hours). For comparison, part of the suspension prepared in water was dried without further washing. The dried cakes were ground slightly in a plastic mortar and sieved through a 180 μm sieve. Copper oxide powders were obtained by thermal decomposition of those sieved copper oxalate powders at 250, 300 and 450 ºC respectively for 2 hours. The resulting copper oxide powders were sieved again and stored in a desiccator prior to use.

3.2.3 Characterisation

X-ray diffraction (XRD, X'pert_APD, PANalytical, Cu-K$_{\alpha 1}$, λ=1.542 Å) technique was used to analyse the crystalline structure of the 3Y-TZP and CuO powders and the primary crystallite size of those powders. The volume fraction of the monoclinic zirconia phase was calculated using the relationship proposed by Toraya et al. [35]. The relative amount of CuO, Cu$_2$O and Cu-metal phase in the copper-oxide powders were estimated by the relative intensity ratio of the peaks of the XRD patterns. The primary crystallite size of these powders (D_{XRD}) was calculated X-ray line broadening technique (XRLB), according to the Scherrer equation:

$$D_{XRD} = \frac{K \cdot \lambda}{\beta \cdot \cos\theta}$$ (Eq. 3.1)

where K is the Scherrer constant; λ is the wavelength of the X-ray in nm; β is the line broadening; θ is the Bragg angle. A high-temperature XRD measurement was conducted on the as-dried yttrium-zirconium hydroxide powder in order to obtain an indication of the temperature at which amorphous zirconia-yttria phase transforms to crystalline 3Y-TZP.

Specific surface areas of all 3Y-TZP and CuO powders were determined by the BET method (ASAP 2400, Micromeritics). From the BET surface area an equivalent spherical particle diameter was calculated by:

$$D_{BET} = \frac{6}{S_{BET} \cdot \rho}$$ (Eq. 3.2)

where S_{BET} is the BET surface area and ρ is the theoretical density of the material.

Thermal decomposition behaviour of the copper oxalate powders was determined by thermal gravimetric and differential scanning calorimetric technique (TGA/DSC, Setaram Setsys 16) in air. The overall composition and purity of the 3Y-TZP powder was analysed by X-ray fluorescence spectrometry (XRF, PW 1410, Philips). Micro-morphology of the copper oxalate and CuO powders were observed by a scanning electron microscopy (SEM-EDX, Thermo NORAN Instruments).

3.2.4 Compaction tests

3Y-TZP powders were mixed with 8 mol% CuO with D$_{BET}$ particle sizes of respectively 20 and 50 nm by milling in a polyethylene bottle for 24 hours, with ethanol and zirconia balls as milling media. The milled suspension was ultrasonically vibrated for 5 min and then oven-dried at 100 °C for 24 hours. After grinding and sieving the powder mixture was stored in a desiccator prior to use. Pure 3Y-TZP (milled as well as unmilled) and the mixture powders were compacted by isostatic pressing at

various pressures in a range between 10 and 400 MPa. The density of the green compacts pressed at each compaction pressure was measured according to Archimedes principle in mercury.

3.3 Results and discussion

3.3.1 Characteristics of 3Y-TZP powder

The chemical composition of the 3Y-TZP powders prepared by co-precipitation technique as determined by XRF is given in Table 3.1. This 3Y-TZP powder is denoted as CP 3Y-TZP powder hereafter. Chemical composition of the commercial Tosoh 3Y-TZP powder as reported by the manufacturer is also listed in Table 3.1 for comparison. These two 3Y-TZP powders show similar contents of yttria and zirconia as well as the main impurity, HfO_2. This small amount of HfO_2 impurity (around 2 wt%) in both powders should be introduced from the starting zirconia precursors for powder synthesis, i.e. $ZrOCl_2 \cdot 8H_2O$ in for the CP powder. As can be seen in the chemical periodical Table Ti, Zr and Hf are belonging to the same group. These elements always co-exist in raw materials, e.g. Hf is difficult to be removed entirely from zirconia minerals. However the presence of these small amounts of TiO_2 and HfO_2 is not expected to influence the properties of the 3Y-TZP materials.

Table 3.1 Chemical composition of 3Y-TZP CP and Tosoh powder

Powder	Ti_2O wt%	Y_2O_3 wt%	ZrO_2 wt%	HfO_2 wt%
CP	0.002	5.10	93.13	1.77
Tosoh	-	5.1±0.4	92.65	2.0±0.2

Fig. 3.1 shows the XRD patterns of the yttrium-zirconium hydroxide powder calcined at various temperatures. As revealed by high-temperature XRD, the powder was amorphous after drying and started to crystallise at around 500 ºC. Calcination at 550 ºC for 2 hours was adopted by our preparation procedure in order to make sure that the obtained 3Y-TZP powder is fully crystallised and to prevent significant growth of crystallites at further heating. As indicated by the XRD pattern the CP 3Y-TZP powder exhibits a pure tetragonal crystal structure. Crystallite size of the CP 3Y-TZP powder can be calculated from the T(111) reflection of tetragonal zirconia by using X-ray line broadening method (XRLB), which is denoted as D_{XRD} in this thesis. D_{XRD} value represents the primary crystallite diameter of a polycrystalline powder. It was calculated that the obtained CP 3Y-TZP powders have a D_{XRD} of 8 nm.

A particle diameter of the 3Y-TZP powder can also be calculated from the BET surface area (D_{BET}) by using equation 3.2. As shown in literature the D_{BET} value in relation with the D_{XRD} is an indication of the degree of aggregation of the primary crystallites [36]. For the CP 3Y-TZP powder D_{BET} value is around 10 nm. The good agreement between the values of D_{XRD} and D_{BET} indicates that the powder is almost 'aggregate-free'.

Detailed analysis of aggregate structure of CP 3Y-TZP powders can be referred to Theunissen's work [26]. In that work it was demonstrated that the primary crystallites in the CP 3Y-TZP powders are arranged in strings with small aggregates at the intersections of these strings. Each aggregate contains only about 5-6 primary crystallites so that no closed pore (intra-aggregate pores) exists. While this CP

3Y-TZP is used for fabrication of ceramic materials, these small aggregates are not expected to give rise of large inhomogeneities in the materials.
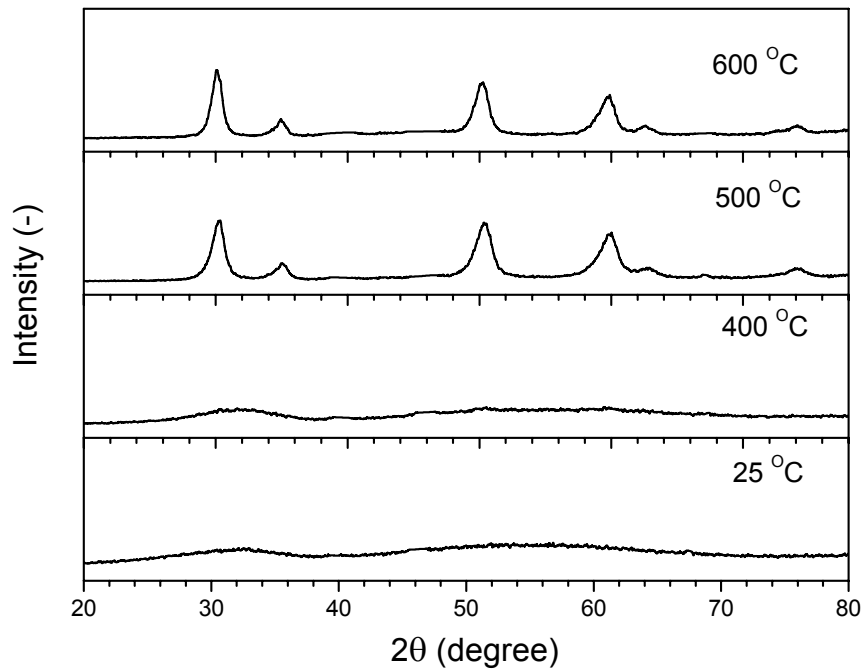
Fig. 3.1 XRD patterns of yttrium-zirconium hydroxide powder calcined at various temperatures.

3.3.2 Thermal decomposition of copper oxalate

All the copper oxalate powders produced in different ways show identical thermal decomposition behaviour as measured by TGA/DSC (Fig. 3.2). The copper oxalate powder loses about 3 % of its weight between 30 and 250 ºC due to desorption of adsorbed water and gases. Between 250 and 300
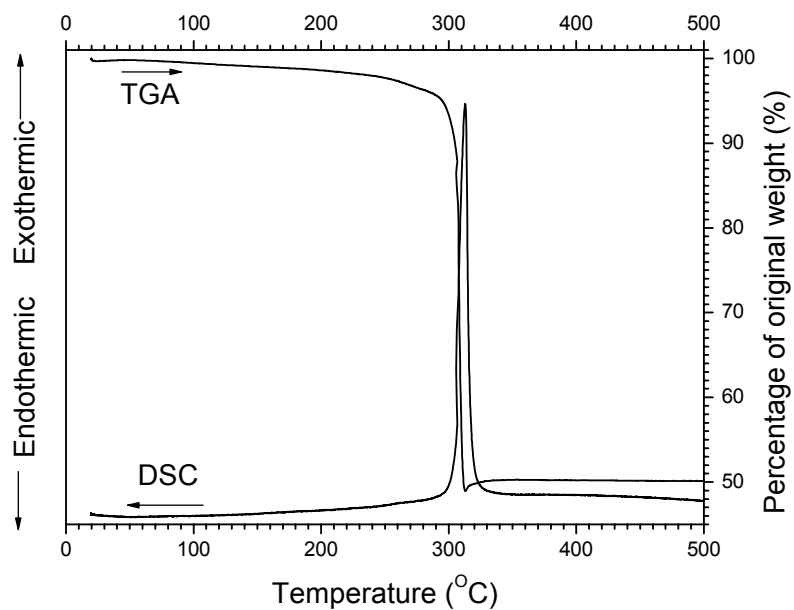
Fig. 3.2 Thermal decomposition behaviour of CuC_2O_4 as measured by TGA and DSC

ºC a sudden weight loss of more than 50 wt % is observed, combined with a sharp exothermic signal in DSC. Obviously this exothermic reaction is the decomposition of copper oxalate by release of CO and CO_2. It is known from literature that in this temperature range copper oxalate decomposes into copper metal by a stepwise cation reduction ($Cu^{2+} \rightarrow Cu^+ \rightarrow Cu^0$) [33, 37], which causes the large weight loss (>50%). The weight loss is immediately followed by a weight gaining, indicating that the Cu resulted from the decomposition of copper oxalate powder starts to re-oxidise to CuO.

It is important to point out that during the thermal analysis a relative high heating rate (10 ºC·min^{-1}) was used so that the apparent reaction temperatures (e.g. decomposition and re-oxidation) can be increased because of the delay of signal caused by thermal diffusion. If heated at lower heating rate, the decomposition and re-oxidation reactions can be finished at slightly lower temperatures.

3.3.3 Calcination dependence of crystalline and aggregate size in CuO powders

Several techniques were used to characterise the copper-oxide powders prepared by means of oxalate precipitation. Table 3.2 shows several data of powders prepared by calcining copper oxalate powders prepared from ethanol solutions. Calcination was conducted in a room furnace except the one marked as 250^a, which was conducted in an open tubular furnace. The powders are classified based on the particle diameter calculated from BET surface area (D_{BET}).

As can be seen from this table the calcination procedure has a strong influence on the characteristics of the resulting copper oxide powder. First of all the crystallite size (as determined by XRLB technique, D_{XRD}) grows remarkably with increasing calcination temperature. D_{XRD} of the 450 °C calcined copper oxide powder is more than 3 times as large as that of the 250 °C calcined one (respectively 50 and 15 nm). The particle diameter as calculated from BET surface area (D_{BET}) shows an even stronger dependence on calcination temperature. When calcination temperature increases from 250 to 450 °C the D_{BET} of resulting copper-oxide powder increases more than 6 times (50 for the 250 °C calcined compared to 360 nm for the 450 °C calcined). The difference in furnace type also shows some influence on the powder characteristics. When an open tubular furnace is used for calcination, a CuO powder with smaller D_{XRD} (12nm) and D_{BET} (20 nm) was obtained by calcining the powder at 250 ºC.

Different from the CP 3Y-TZP powder, all CuO powders show considerably larger value of D_{BET} than the D_{XRD} value. This difference between D_{BET} and D_{XRD} values can be explained by the fact that in

Table 3.2.   Powder characteristics of CuO prepared via decomposition of copper oxalate

ID	Calc. T (°C)	D_{XRD} (nm)	D_{BET} (nm)	n	q	$Dagg$(nm)
CuO-360	450	50	360	200-210	85-90	280-300
CuO-60	300	n.m.	60	-	-	-
CuO-50	250	15	50	45-50	22-25	45-50
CuO-20	250^a	12	20	20-25	12-15	30-35

Calc. T: Calcination temperature;
D_{XRD}: Crystallite size determined by XRLB;
D_{BET}: BET equivalent particle size;
n.m.: Not measured;
n: number of necks in aggregate;
q: number of particles in aggregate;
D_{agg}: average size of aggregates;
250^a: the powder was calcined at 250 °C in a tubular furnace.

these CuO powders the primary crystallites are clustered and form aggregates. In the aggregates some space, for instance, the closed pores and the very narrow space close to the neck of two crystallites, are not accessible for the adsorbent used in the BET experiments (N_2 in the current case). Thus the adsorbent can not cover the crystallite surface completely. The difference between D_{BET} and D_{XRD} values gives an indication of the degree of powder aggregation. According to Avery and Ramsay [26,36] the size and structure of aggregate are determined by the number of necks:

$$n = \frac{2D_{XRD}}{D_{N_2}}(1 - \frac{S_{BET}}{S_T})$$
(Eq. 3.3)

where n is the number of necks; D_{N_2} is the diameter of the adsorbent molecule used in BET measurement, i.e. 0.43 nm of N_2 molecule; S_{BET} is the measured BET surface area; and S_T is the theoretical surface area when it is assumed that each individual crystallite can be completely covered with adsorbent. From the number of necks the average number of crystallites per aggregate, q, and therefore the average size of the aggregates (D_{agg}) can be estimated. However the crystallite number depends on the structure of packing in the aggregates. Here a simple cubic packing of crystallites in the aggregates of all CuO powder is assumed. Theoretical analysis revealed that a cubic packing of spherical particles results in a porosity (p) of 0.476. An aggregate size (D_{agg}) can be estimated by assuming that all aggregates are spherical-shaped with a uniform diameter and consist of q crystallites with a diameter of D_{XRD}:

$$D_{agg} = (\frac{q}{1-p})^{1/3} \cdot D_{XRD}.$$
(Eq. 3.4)

Considering the possible error of D_{BET} and D_{XRD}, a range of each of those values are given in Table 3.2.

As revealed by the n, q and D_{agg} values, the copper-oxide powder calcined at 450 °C in a room furnace shows a very significant degree of aggregation. Aggregates in this powder consist of more than 80 primary crystallites and have an average diameter close to 300 nm. For the powder calcined at 250 °C in a room furnace the degree of powder aggregation is remarkably reduced, as indicated by the D_{agg} of 45-50 nm and q of 22-25. When calcining the copper oxalate in an open, tubular furnace at 250 °C, the aggregation is even more inhibited (D_{agg}=30-35nm; q=12-15). It can be easily calculated that the volume aggregates in the CuO-360 is around 1000 times larger than that in CuO-20.

The difference in crystalline size and aggregation degree between the powders calcined in different furnaces is likely to be caused by the actual cooling rate. Although a cooling rate of 2 ºC·min^{-1} was set in the ramp program, the room furnace cooled down much slower than the tubular furnace (~0.2 ºC·min^{-1} compared with 1 ºC·min^{-1}) in the beginning of cooling. Therefore the powder was kept at relatively high temperature for longer time, which means more crystallite and aggregate growth of the powder in a room furnace.

The degree of aggregation in the powder is important for ceramic fabrication. During compaction, the presence of large aggregates in the starting powder results in large voids and poor uniformity in the green powder compact [8, 27]. These large voids and poor uniformity can give a significant decrease in sinterability and result in a ceramic containing several voids [27]. From this point of view, calcination at 250 °C in an open tubular furnace is the optimal procedure.

The agglomerate properties are also an important factor from ceramic fabrication point of view. Fig. 3.3 shows SEM images of agglomerates in the copper-oxide powder calcined at 250 °C in an open tubular furnace (CuO-20 in Table 3.2). As can be seen in Fig. 3.3-a the powder consists of uniform agglomerates with a size of several micrometres. These agglomerates exhibit a very porous packing of small primary particles of only ~ 10 nm in diameter (see Fig. 3.3-b). The large porosity implies a weak strength of these agglomerates. It is expected that these weak agglomerates in the CuO-20 powder can easily be broken down to primary particles or smaller aggregates by ball-milling or ultrasonic treatment. Neither large voids nor significant inhomogeneity would be caused by these weak agglomerates when the CuO-20 powder is used for fabrication of ceramic composite materials.
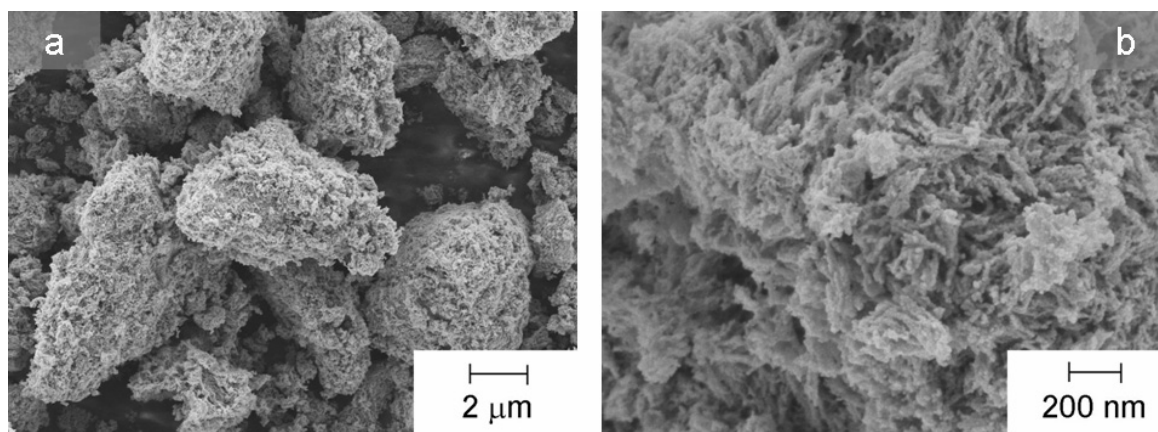
Fig. 3.3 SEM images of CuO powder produced by calcining the CuC_2O_4 synthesised in ethanol. The calcination was carried out at 250 °C for 2 hours in a tubular furnace, with a heating and a cooling rate of 2 °C·min^{-1}. a) lower magnification, b) higher magnification

3.3.4 Influence of calcination procedure on phase composition of CuO powders

The phase composition of copper-oxide powders calcined under different conditions was determined by XRD (see Fig. 3.4). Phase contents were quantitatively estimated on the basis of the intensity ratios of the most intense XRD signal peak of each phase (see Table 3.3). While calcined at 250 ℃ in a room furnace, the copper oxide powder consists of 50 vol% of Cu_2O and 3 vol% of metallic Cu because of the incomplete re-oxidation process (see Fig. 3.4). Calcination at 450 ℃ in a room furnace improves the oxidation reaction but still small amounts of Cu_2O and Cu phase are left. However, when an open furnace is used, the CuO exhibits a pure CuO after calcination at 250 °C for 2 hours. In the case of calcination in an open furnace, the powder is obviously accessible for more fresh air if compared with the case in a room furnace. It can be concluded that exposing the powder to fresh air during calcination is more favourable for obtaining a pure CuO phase composition.

Table 3.3 Phase composition of CuO prepared by decomposition of copper oxalate

ID	Calc. T (°C)	Phase composition (vol %)		
		CuO	Cu_2O	Cu
CuO-360	450	93	6	1
CuO-50	250	47	50	3
CuO-20	250[a]	100	0	0
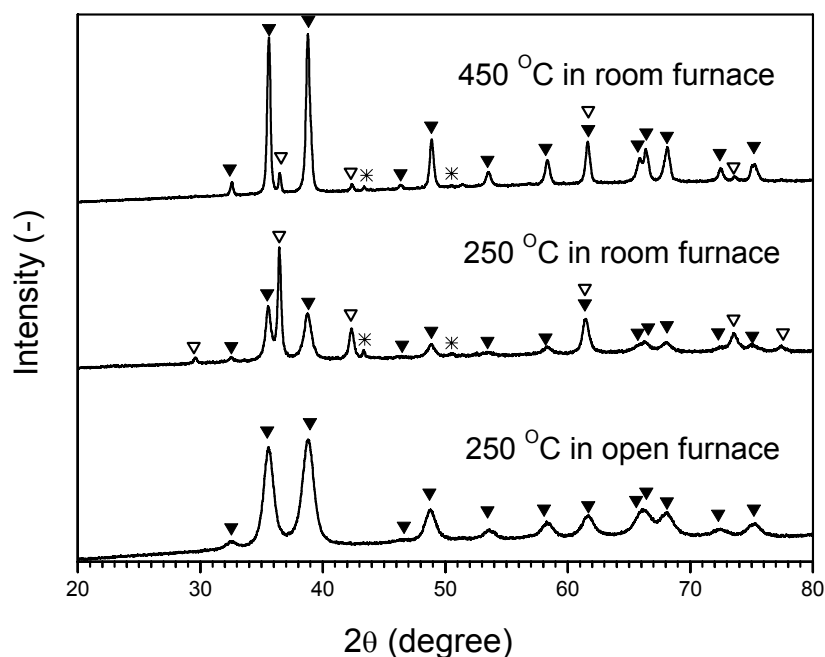
Fig. 3.4 XRD patterns of CuO powders calcined under different conditions

▼: CuO; ▽: Cu_2O; ✳: Cu

3.3.5 Influence of precipitation and washing medium on CuO powder characteristics

The influence of other process parameters on the final characteristics of the CuO powder was also investigated. The way of adding the $Cu(NO_3)_2$ solution to the oxalic acid solution during precipitation (by using either a separation funnel or a peristaltic pump) does not show significant influence on the properties of the final powder. However a peristaltic pump would be recommended for a better control in precipitation and for large scale preparation.

Table 3.4 shows the D_{BET} of the CuO powders prepared with different solvents in which the precursors were dissolved (water or ethanol). Part of the oxalate precipitated in water was washed with ethanol to replace the liquid medium before drying. All the powders were calcined in a tubular furnace at 250 °C for 2 hours with heating and cooling rate of 2 °C·min^{-1}.

Table 3.4 D_{BET} of CuO powder prepared with different precipitation and washing media

ID	Precipitation Solvent	Drying Solvent	Calcination	Furnace	D_{BET} (nm)
CuO-E	Ethanol	Ethanol	250°C×2h	Tubular	20
CuO-W	Water	Water	250°C×2h	Tubular	120
CuO-WE	Water	Ethanol	250°C×2h	Tubular	20

As can be seen in Table 3.4, the CuO powder possesses a D_{BET} of 120 nm when water is used as solvent during copper oxalate precipitation and no ethanol washing is applied. In contrast, if the copper oxalate prepared in water is washed thoroughly with ethanol, the CuO powder exhibits an identical D_{BET} after calcination as the one prepared by using ethanol as solvent during the whole process (20 nm, CuO-20). This result clearly suggests that aggregation/agglomeration is only influenced by the washing procedure of the oxalate precipitation. Reduction in aggregate size and/or

agglomerate strength as caused by ethanol washing was also observed for other powder systems [27]. This phenomenon was generally ascribed to a lower surface tension of ethanol than that of water, which causes a lower particle packing during the drying process [38,39]. In the case of CuO nanocrystalline powder as studied here, it is proven that the washing procedure also plays an important role in aggregation and agglomeration of the powder.
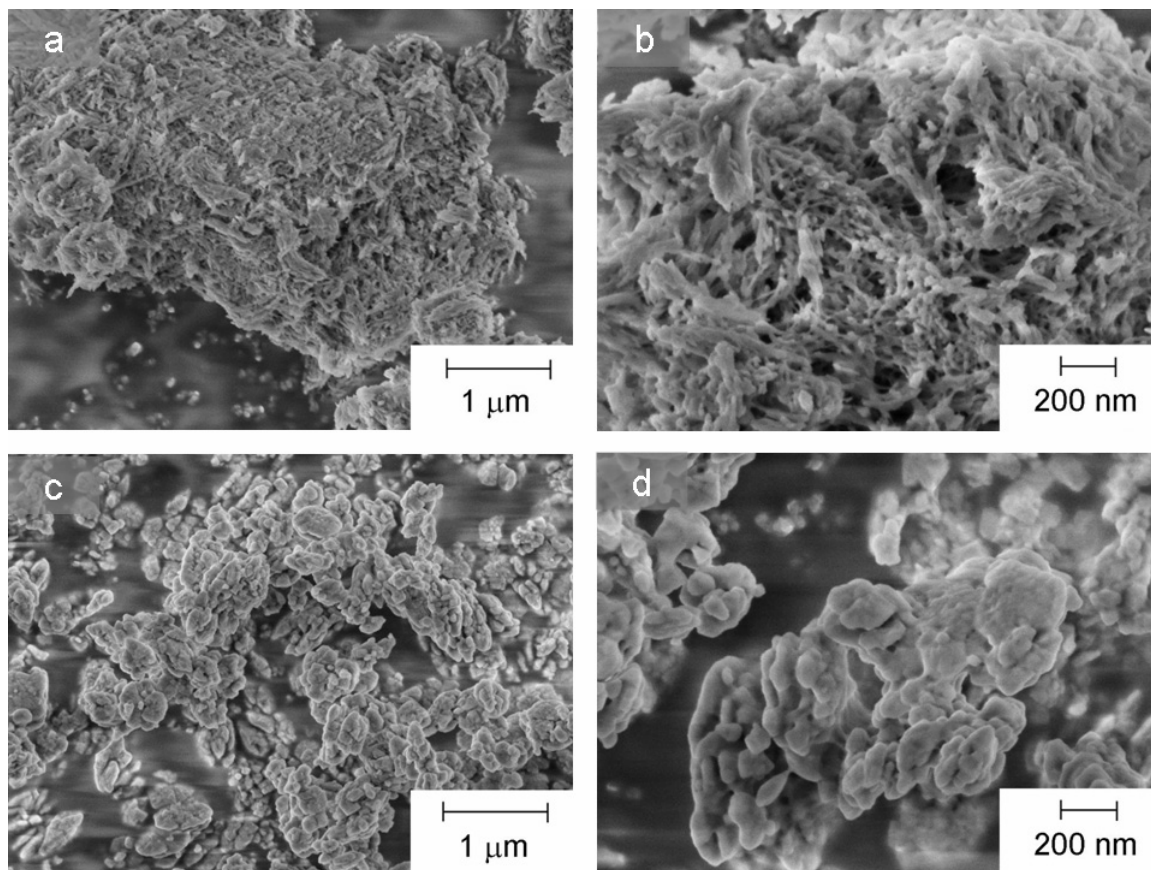
Fig. 3.5 SEM images of dried CuC_2O_4 powders, precipitated in water

a) and b): washed in ethanol; c) and d): Precipitated in water without ethanol washing

SEM images of dried copper oxalate powders prepared by precipitation in water with (Fig. 3.5-a and -b) and without (Fig. 3.5-c and -d) subsequent ethanol washing confirm the strong washing medium dependence of agglomerate structure. The ethanol washed copper oxalate powder exhibits a highly porous agglomerate structure, whereas, the un-washed one shows dense agglomerates containing closely packed aggregates. After calcination of the ethanol-washed oxalate precipitate the CuO powder shows an identical agglomerate structure as the one prepared without involving water (see Fig. 3.3). In contrast CuO resulting from calcination of the copper oxalate powder as precipitated in water without subsequent ethanol washing gives a much denser agglomerate structure as shown in Fig. 3.6, implying a stronger agglomerate strength in this powder.

The larger aggregates and the stronger agglomerates in the CuO powder produced without the ethanol washing step would be difficult to break down during wet-milling or ultrasonic vibration. If the CuO powder is used for ceramic fabrication, large voids or significant inhomogeneities in the material could arise from the presence of the aggregates and agglomerates. Therefore it is necessary to remove water as the liquid medium, at least before the drying step.
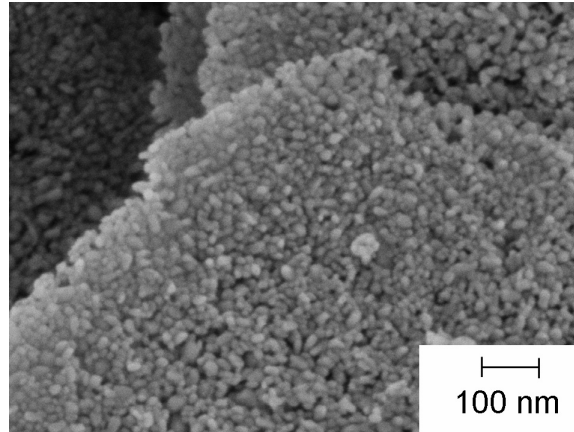
Fig. 3.6 SEM image of calcined CuO powder produced from CuC_2O_4 precipitated in water without subsequent ethanol washing. The calcinations was carried out at 250 °C for 2 hours in a tubular furnace, with a heating and a cooling rate of 2 °C·min-1.

3.3.6 Compaction behaviour of CuO doped 3Y-TZP composite powders

For producing a ceramic material, a bulk compact with certain shape and dimensions is normally needed. Dry pressing is one of the more straightforward operations to produce such a powder compact. The characteristics of the powder compact are of importance because of their significant effects on sintering and final product quality [26]. While dry pressing is used, compaction behaviour of powders strongly depends on particle size, particle morphology, and agglomeration. On the other hand, compaction behaviour can also be regarded as a way to analyse powder characteristics, especially the agglomeration status.

Compaction behaviour of nanocrystalline CP 3Y-TZP powders with and without doping of 8 mol% of CuO-20 were investigated by stepwise isostatic pressing. For the undoped CP 3Y-TZP, both as-calcined (550 °C, un-milled) and wet-milled (in the same way used for CuO doping) were measured. Fig. 3.7 shows the relative density of these powders a function of the logarithm of compaction pressure. All the curves show two linear parts with a point of intersection at pressure P_j. Below P_j the increase in density is lower than the case above P_j. According to the model as developed by van de Graaf [40], P_j is a measure of agglomerate strength. When pressed at around P_j the agglomerates are gradually fragmented, whereas they are only rearranged at pressures below P_j. Above P_j the compaction curve (part 2 in Fig. 3.7) can be described by the empirical equation [40]

$$\rho - \rho_j = m \cdot \ln(P/P_j)$$ (Eq.3.4)

where m is the slope of the curve. A large m value might be an indication of a large density distribution in the green compact, which could lead to inhomogeneity in the material or even fracture the specimen during unloading, especially when a large piece of ceramic is being made [40].

It can be seen in Fig. 3.7 that the as-calcined and unmilled CP 3Y-TZP powder exhibits much lower densities, especially at lower pressures. A P_j value of around 40 MPa and a steep slope (m) are observed in the case of un-milled CP 3Y-TZP. After wet-milling, compaction of the CP powder starts from a higher density. However the P_j value increases to 70 MPa and the m value is lower. It is indicated by the compaction behaviour that the wet-milling apparently enhances the strength of agglomerates, but a more homogeneous density distribution in the green compact is expected, which
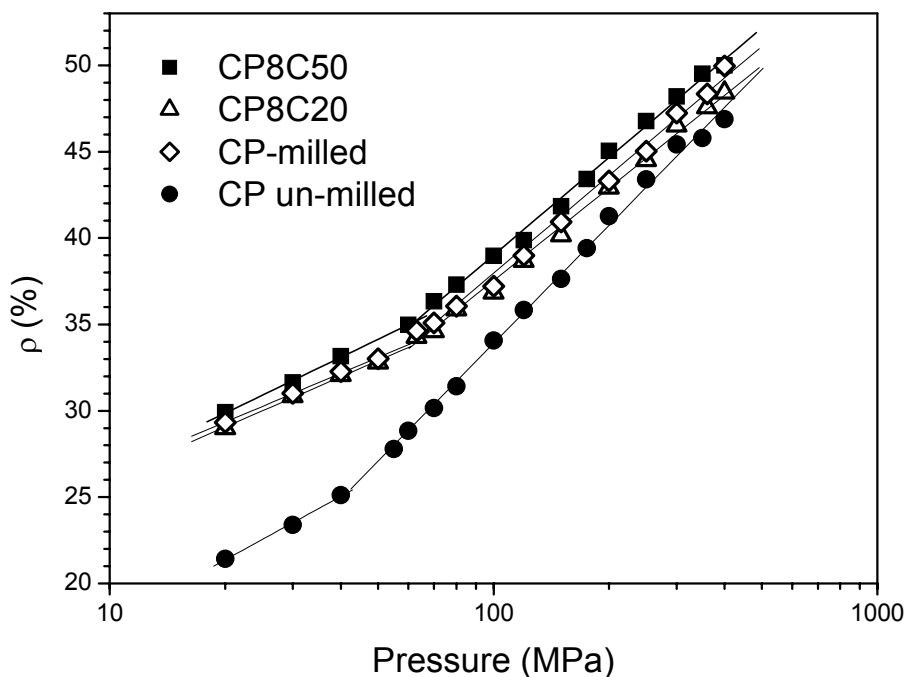
Fig. 3.7 Green compact density as a function of logarithm of compaction pressure.
CP un-milled: as-calcined CP 3Y-TZP powder
CP-milled: CP 3Y-TZP powder wet-milled in ethanol for 24 hours
CP8C20: CP 3Y-TZP powder mixed with 8 mol% CuO-20 by wet-milling for 24 hours
CP8C20: CP 3Y-TZP powder mixed with 8 mol% CuO-50 by wet-milling for 24 hours

can result in a beneficial influence on sintering and final properties of the product. So it can be concluded that wet-milling is favourable in this case.

As indicated by the identical compaction behaviour of all the milled powders (CP milled, CP8C20 and CP8C50 in Fig. 3.7), doping of CuO (8 mol%) does not give any observable influence on agglomerate strength or homogeneity in the CP 3Y-TZP powder. This implies that the doped CuO particles are uniformly dispersed in the matrix of 3Y-TZP by wet-milling for 24 hours followed by ultrasonic treatment for 5 min. This uniform dispersion of CuO particles is necessary for producing a homogeneous composite ceramic of 3Y-TZP doped with CuO.

3.4 Conclusions

Nanocrystalline CuO powders were produced by precipitation of copper oxalate followed by a thermal decomposition. The size of crystallites, aggregates and agglomerates in the produced CuO strongly increase with higher calcination temperature. Type of furnace used for the calcination slightly influence the aggregates size and strongly affect the phase composition in the CuO powder. In order to obtain a CuO powder with weak aggregates and agglomerates, calcination at 250 °C in an open tubular furnace is recognised as the optimal thermal decomposition procedure. The medium in which the copper oxalate precipitate is washed plays an important role in the size and strength of aggregates and agglomerates. It is necessary to use ethanol as washing medium prior to drying for reducing aggregation and agglomeration if the CuO powder.

37

Wet-milling prior to powder compaction is favourable for the CP 3Y-TZP powder. Uniform dispersion of CuO (8 mol%) with D_{BET} of respectively 20 and 50 nm in the CP 3Y-TZP powder can be simply achieved by ball-milling for 24 hours followed by an ultrasonic treatment for 5 min.

References

1. Burggraaf, A.J., "Stuijts Memorial Lecture 1991: Some new developments in ceramic science and Technology", *J. Eur. Ceram. Soc.*, 1992, **9**, 245-250.
2. Burggraaf, A.J., Winnubst, A.J.A. and Verweij, H., "Dense and porous nanostructured ceramics and composites"; pp. 561-576 in: Third Euroceamics, Vol. 3, Engineering ceramics. Edited by P. Duran and J.F. Fernandez. Faenza Editrice Iberica, S.L. Castellon de la Plana, Spain, 1993, Proc. 3rd Eur. Ceram. Soc. Conf. Madrid, Spain, September 12-17, 1993.
3. Turnbull, D. "Metastable structures in metallurgy", *Met. Trans.*, 1981, **12A**[5], 695-708.
4. Groza, J.R., "Nanosintering", NanoStructured Materials, 1999, **12**, 987-992.
5. Theunissen, G.S.A.M., Winnubst A.J.A. and Burggraaf, A.J., "Sintering kinetics and microstructure development of nanoscale Y-TZP ceramics", *J. Eur. Ceram. Soc.*, 1993, **11**[4], 315-324.
6. Duran, P., Villegas, M., Fernhndez, J.F., Capel, F. and Moure, C., "Theoretically dense and nanostructured ceramics by pressureless sintering of nanosized Y-TZP powders", *Mater. Sci. Eng. A*, 1997, **232,** 168-76
7. Zhu, Q. and Fan, B., "Low temperature sintering of 8YSZ electrolyte film for intermediate temperature solid oxide fuel cells", *Solid State Ionics*, 2005, **176,** 889-894.
8. Garvie, R. C., Hannink, R. H. J. and Pascoe, R. T., "Ceramic Steel", *Nature*, 1975, **258,** 703-704.
9. Lange, F.F., "Transformation toughening: Part 1 Size effects associated with the thermodynamics of constrained transformations", *J. Mar. Sci.*, 1982, **17**, 225-234.
10. Wakai, F., Sakaguchi, S. and Matsuno, Y., "Superplasticity of Yttria-Stabilized Tetragonal ZrO_2 Polycrystals", *Adv. Ceram. Mat.*, 1986, **1,** 259-263.
11. Boutz, M.M.R., Winnubst, A.J.A., Burggraaf, A.J. and Carry, C.," Low temperature superplastic flow of yttria stabilized tetragonal zirconia polycrystals", *J. Eur. Cer. Soc.*, 1994, **11**, 103-111.
12. Nieh, T.G., and Wadsworth, J., in "Ceramics Today-Tomorrow's Ceramics", edited by P. Vincenzini (Elsevier Science, Amsterdam, 1991) p. 1527.
13. He, Y. Winnubst, A.J.A. and Burggraaf, A.J., "Grain-Size Dependence of Sliding Wear in Tetragonal Zirconia Polycrystals", J. Am. Ceram. Soc., 1996, **79**[12], 3090-3096.
14. Muto, H., Matsuda, A. and Sakai, M., "Superplastic joining of 3Y-TZP", *J. Eur. Ceram. Soc.*, 2006, **26**, 379-384.
15. Kerkwijk, B., Garcia, M., Van Zyl, W.E., Winnubst, A.J.A., Mulder, E.J., Schipper D.J., and Verweij, H., "Friction behaviour of solid oxide lubricants as second phase in Al_2O_3 and stabilised ZrO_2 composites", *Wear*, 2004, **256**, 182-189.
16. Pasaribu, H.R., Sloetjes, J.W. and Schipper, D.J., "Friction reduction by adding copper oxide into alumina and zirconia ceramics", *Wear*, 2004, **255**, 699-707.
17. Kerkwijk, B., "Wear and friction of nanostructured zirconia and alumina ceramics and composites", Ph.D. thesis, University of Twente, the Netherlands, 1999.
18. Pasaribu, H.R., "Friction and wear of zirconia and alumina ceramics doped with CuO", Ph.D. thesis, University of Twente, the Netherlands, 2005.

19. Cannon, W.R., Danforth, S.C., Flint, J.H., Haggerty, J.S. and Marra, R.A., "Sinterable Ceramic powders from Laser-Driven Reaction: I, Process Description & Model", *J Am. Ceram. Soc.*, 1982, **65**, 324-330.

20. Vollath, D., Sickafus, K.E., "Synthesis of nanosized ceramic oxide powders by microwave plasma reactions", *Nano. Mat.*, 1992, **1**, 427-437.

21. Messing, G.L., Zhang, S.C., and Jayanthi, G.V., "Ceramic powder synthesis by spray pyrolysis", *J Am. Ceram. Soc.*, 1993, **76**[11], 2707-2726

22. Skandan, G., "Processing of nanostructured zirconia ceramics", *Nano. Mat.*, 1995, **5**[2], 111-126.

23. Winnubst, A.J.A., Groot Zevert, W.F.M., Theunissen, G.S.A.M. and Burggraaf, A.J., "Microstructure characteristics of ultra-fine ZrO_2-Y_2O_3 ceramic powders", *Mat. Sci. Engr.*, 1989, **A109**, 215-219.

24. Groot Zevert, W.F.M., Winnubst, A.J.A., Theunissen, G.S.A.M. and Burggraaf, A.J., "Powder preparation and compaction behaviour of fine-grained Y-TZP", *J. Mat. Sci.*, 1990, **25**, 3449-3455.

25. Mayo, M.J. "Synthesis and applications of nanocrystalline ceramics", *Materials & Design*, 1993, **14**[6], 323-329.

26. Theunissen, G.S.A.M., "Microstructure, fracture toughness and strength of (ultra)fine-grained tetragonal zirconia ceramics", PhD Thesis, University of Twente, The Netherlands, 1991.

27. Sagel-Ransijn, C.D., "Nanostructured zirconia ceramics by gel-precipitation, processing, microstructure and mechanical properties", PhD Thesis, University of Twente, The Netherlands, 1996.

28. Kingery, W.D. and Francois, B., "The sintering of crystalline oxides, I. Interactions between grain boundaries and pores", pp. 471-498 in Sintering and related phenomena. Ed. by G.C. Kuczynski, N.A. Hooton and C.F. Gibbon. Gordon Breach, New York, 1967.

29. Ran, S., Winnubst, A.J.A., Wiratha, W. and Blank, D.H.A., "Sintering behavior of 0.8 mol%-CuO-doped 3Y-TZP ceramics", *J. Am. Ceram. Soc.*, 2006, **89**[1], 151-155.

30. Seidensticker, J.R., and Mayo, M.J., "Adsorption as a method of doping 3-mol%-yttria-stabilized zirconia powder with copper oxide", *J. Am. Ceram. Soc.*, 1993, **76**[7] 401-406..

31. Hayakawa, M., Inoue, T., Pee, J.-H., Suematsu, H. and Yamauchi, H., "Liquid phase sintering of Y-TZP with CuO and $Y_2Cu_2O_5$ dopants", *Mater. Sci. Forum*, 1999, **304-306**, pp. 465-70.

32. Qin, Y., Zhang, Q., and Cui, Z., "Effect of synthesis method of nanocopper catalyst on the morphologies of carbon nanofibers prepared by catalytic decomposition of acetylene", *J. Catal.*, 2004, **233**, 389-94..

33. Jongen, N., Hofmann, H., Bowen, P., Lemaitre, J., "Calcination and morphological evolution of cubic copper oxalate particles", *J. Mater. Sci. Lett.*, 2002, **19**, 1073-1075.

34. van Zyl, W.E., Winnubst, L., Raming, T.P., Schmuhl, R. and Verweij, H., "Synthesis and characterisation of dual-phase Y-TZP and RuO_2 nanopowders: dense electrode precursors," *J. Mater. Chem.*, 12 708-13 (2002).

35. Toraya, H., Yoshimura, M. and Somiya, S., "Quantitative Analysis of Monoclinic-Stabilized Cubic ZrO_2 Systems by X-Ray Diffraction", *J. Am. Ceram. Soc.*, 1984, **67** [9], C183-C184.

36. Avery, R.G. and Ramsay, J.D.F, "The sorption of nitrogen in porous compacts of silica and zirconia powders", *J. Colloid & Interface Sci.*, 1973, **42**[3], 597-606.

37. Mohamed, M. A. and Galwey, A. K., "A kinetic and mechanistic study of the thermal decomposition of copper(II) oxalate", *Thermochimica Acta*, 1993, **217**, 263-276.

38. Horn, R.G., "Particle interactions in suspensions", pp. 58-101 in: Ceramic processing. Edited by R.A. Terpstra, P.P.A.C. Pex and A.H. de Vries, Chapman and Hall, London, 1975.

39. Lyklema, J., "Interfacial electrochemistry of disperse systems", pp. 1-24 in: Emergent process methods for high-technology ceramics, Vol. 17, Edited by R.F. Davis, H. Palmour III and R.L. Porter, Plenum Press, New York, 1984.

40. Van de Graaf, M.A.C.G., Ter Maat J.H.H., Burggraaf, A.J., "Microstructure and sintering kinetics of highly reactive ZrO_2-Y_2O_3 ceramics", *J. Mat. Sci.*, 1985, **20**, 1407-1418.

Chapter 4

Reactions during sintering of 3Y-TZP doped with CuO nano-powder composites

Abstract

This chapter describes the investigation on reactions during sintering of CuO doped 3Y-TZP nano-powder composites. 3Y-TZP and CuO nano powders were prepared by co-precipitation and copper oxalate precipitation techniques respectively. During heating a mixture of these powders it is revealed that a strong dissolution of CuO in the 3Y-TZP matrix occurs below 600 °C, resulting in significant enrichment of CuO in the 3Y-TZP grain boundaries with a thickness of several nanometres. Solid state reaction between CuO and yttria as segregated to the 3Y-TZP grain boundaries occurs at around 850 °C and forms $Y_2Cu_2O_5$. These reactions can have significant influence on sintering behaviour and microstructure evolution of the material.

4.1 Introduction

CuO doped yttria stabilized tetragonal zirconia polycrystals (Y-TZP) ceramic composites have recently drawn great interest due to their special properties such as superplastic deformation and low friction under dry sliding conditions [1-3].These properties extend the materials' potential applications into near net shape forming of ceramics [1] and as moving parts to operate in unlubricated environment [2,3].

During sintering of CuO doped Y-TZP system several reactions can occur [4-5]. These reactions have profound influences not only on sintering but also on microstructure of the final ceramic. It is observed that these reactions retard densification [5, 6] or result in a tetragonal to monoclinic zirconia phase transformation during sintering [5-9]. The material can even crack during sintering if these reactions are not well controlled [5, 9]. A sound knowledge of the reactions between CuO and 3Y-TZP during sintering is important for understanding and controlling the sintering process and microstructure evolution of the material.

The reactions between submicron CuO and 3Y-TZP (Tosoh) powders have been investigated previously [4,7,10]. Seidensticker et al. [4] performed DTA and TGA analysis on a 3 mol% CuO doped Tosoh 3Y-TZP powder prepared by an adsorption technique in air. In this system copper species are supposed to be homogeneously covering the 3Y-TZP particles as multi-layer adsorbents. Several reactions such as dissociation of CuO at 1030 °C and melting of Cu_2O at 1140 °C are clearly identified by Seidensticker [4]. The authors also claimed that an $Y_2Cu_2O_5$ phase is formed at 1200 °C due to the reaction between the molten Cu_2O and yttria as segregated to the 3Y-TZP grain boundaries. Mayo et al. reported a HR-TEM analysis on the CuO doped Tosoh 3Y-TZP systems and claimed that a small amount (< 0.3 mol%) of CuO can be dissolved into the 3Y-TZP grains by forming a Cu-rich grain boundary layer with a thickness of several nm [10]. Hayakawa and his colleagues investigated

reactions in 3Y-TZP doped with various amounts of CuO prepared by traditional mixing technique [7]. Differently from Seidensticker's results, these authors concluded that in their systems the formation of $Y_2Cu_2O_5$ occurs at around 850 °C during heating and CuO dissolves in the 3Y-TZP matrix at around 1200 °C. The discrepancy between Seidensticker's and Hayakawa's work is probably caused by the different characteristics of the powders they used.

The CuO and 3Y-TZP powders used in the present work both possess a nano particle size. Thus the characteristics of the composites powders are significantly different from those as studied by Seidensticker and Hayakawa and the behaviour of the reactions between CuO and 3Y-TZP can also be remarkably different. In this chapter reactions in CuO doped 3Y-TZP nano-powder composites were studied by thermal analysis, XPS and high-temperature XRD.

4.2 Experimental procedure

4.2.1 Powder preparation

A powder of 3 mol% yttria stabilised tetragonal zirconia polycrystals (CP 3Y-TZP) with 10 nm D_{BET} and a CuO powder with 50 nm D_{BET} (CuO-50) were prepared by co-precipitation and copper oxalate precipitation techniques, as described in chapter 3. Composites of CP 3Y-TZP doped with 8 mol% of CuO, were prepared by milling proper amounts of 3Y-TZP and CuO powders for 24 hours in a polyethylene bottle, using ethanol and zirconia balls as milling media. The milled suspension was ultrasonically dispersed for 5 min and then oven-dried at 100 ºC for 24 hours. After slightly ground in a plastic mortar, the composite powders were sieved through a 180 μm sieve and stored in a desiccator prior to use. Characterisation of these powders was performed using XRD, BET and compaction techniques (for details see chapter 3).

A mixture of fine Y_2O_3 and CuO powder with a Y/Cu atomic ratio of 1 was prepared by citrate synthesis. This powder mixture was used for high-temperature XRD analysis to detect the reaction between Y_2O_3 and CuO. Appropriate amounts of CuO (Aldrich Chemicals, Germany) and Y_2O_3 (Merck Chemicals, Germany) were separately dissolved in nitric acid (HNO_3, 38%, Merck Chemicals, Germany). Stirring and heating (80 °C) were employed to assist the dissolution. After mixing the two warm solutions, citric acid monohydrate ($C_6H_6O_7 \cdot H_2O$, Merck chemicals, Germany) was added into at the ratio acid/ (Cu+Y)=1/1. The pH value of the solution was adjusted carefully to a range between 6.5 and 7.0 by adding ammonia solution ($H_3N \cdot H_2O$, 65%, Merck Chemicals, Germany), while the whole solution was kept warm and stirred. A pH meter was used to monitor the pH value of the solution during the addition of ammonia solution. Then the solution (around 150 mL in volume) was immediately transferred to a 2L beaker and heated on a hotplate to evaporate the solvent. It is important to avoid any precipitation and violent boiling during the evaporation procedure, otherwise the stoichiometry is lost. While most of the solvent was removed the solution became a dark-blue viscous slurry. While further heating the slurry swelled and suddenly a strong combustion was ignited, leaving a foam-like brown powder. After slightly ground in a plastic mortar the resulting powder was used for the high-temperature XRD measurements.

4.2.2 Thermal analysis

In order to detect the reactions, which occur during sintering thermogravimetric analysis (TGA) and differential scanning calorimetric measurement (DSC) were carried out on compacts of CuO doped 3Y-TZP composites using a Setaram Setsys 16. The composite powders were isostatically pressed into

green compacts at 400 MPa for 5 min. The green compacts were crushed into pieces. For each TGA/DSC measurement around 25 mg compacted pieces were used.

Two different temperature programmes were used for the thermal analysis, i.e. a single heating programme and a cycled programme. During single heating the powder compact was heated at 15 °C·min^{-1} to 1100 °C (without measurements during dwelling and cooling). In the single heating experiments a platinum cup was used as sample holder. It was found that the sample reacts with the platinum cup at high temperatures (>1100 °C), which results in non-desired reactions and contamination of the equipment. Therefore the cycled measurements were conducted using an alumina cup as sample holder. For the cycled temperature programme, the sample was first heated at 15 °C·min^{-1} to 1150 °C and held at the maximum temperature for 30 min. After cooled at 5 °C·min^{-1} to 600 °C the sample was reheated to 1150 °C followed by a dwell for 30 min. Finally the sample was cooled at 15 °C·min^{-1} to room temperature. Because sintering of the nano-powder composites was carried out in an oxygen flow (see chapter 5), all thermal analysis experiments were carried out in an (90% O_2 + 10% N_2) atmosphere for obtaining an almost similar environment as that used for sintering studies.

4.2.3 XPS analysis

The reactions during sintering of the CuO doped 3Y-TZP nano-powder composites were further analysed by a series of X-ray Photoelectron Spectroscopy analysis (XPS, Quantera, Physical Electronics). For these experiments the 8 mol% CuO doped 3Y-TZP composites were used to obtain spectra of all elements. Powder compacts of 2~3 mm in thickness and 6~7 mm in diameter were prepared by isostatic pressing at 400 MPa for 5 min. One XPS analysis was conducted on the fractured surface of a green compact. The other green compacts were sintered in oxygen at 600, 700 and 850 °C respectively for 30 min, with a heating rate of 15 °C·min^{-1} and a cooling rate of 5 °C·min^{-1}. XPS spectra were measured for both freshly fractured and finely polished (with diamond paste as polishing media) surfaces of these sintered samples. Elemental composition of the measured surfaces was calculated on the basis of the measured spectra. Depth profiles of elemental concentration were also measured by step-wise sputtering the measured sample surfaces with argon plasma. It is estimated that 1-2 nm material was removed by the sputtering for each minute. Carbon signals measured in all cases are assumed to be caused by contamination and taken only as an internal reference for signals positions.

4.2.4 High-temperature XRD

High-temperature X-ray diffraction analysis (XRD, X'Pert_MPD, PANalytical, The Netherlands, with Cu-K$_{\alpha 1}$ radiation, λ=1.542 Å, as X-ray source) was performed on the mixture of CuO and Y_2O_3 ultra-fine powders prepared by citrate synthesis to characterise the reaction between CuO and Y_2O_3. The data were collected in the 2θ range of 10-40° with a step size of 0.02°. During the measurement the sample was heated at 5 °C·min^{-1} to the measuring temperature and held at that temperature for 15 min before the measurement started.

4.3 Results and discussion

4.3.1 Thermal analysis on CuO doped 3Y-TZP nano-powder composite

Thermal analysis was first conducted on the undoped and various amounts of CuO-50 doped CP 3Y-TZP samples by using TGA and DSC. Differing from Seidensticker's work [4], we used pressed

powder compacts instead of loose powders. In a pressed compact the particles are in better contact so that the reactions proceed in a way more comparable to that in sintering of a powder compact.

Fig. 4.1 shows the TGA/DSC result of the 8 mol% CuO-50 doped CP 3Y-TZP sample (CP8C50) measured with a single heating programme. A large broad exothermic peak appears between 100 and 400 °C, accompanying by a total weight loss of around 3%. This strong exothermic peak and the corresponding weight loss were observed on all DSC/TGA scans for undoped and CuO doped CP 3Y-TZP samples and was attributed to desorption of adsorbed water.

With increasing temperature a sharp exothermic peak without any weight change appears at around 850 °C on the DSC curve of the CP8C50 sample, whereas no signal was observed in this temperature range for the case of undoped CP 3Y-TZP. This exothermic peak clearly points to a reaction between CuO and the 3Y-TZP. At around 1100 °C an endothermic reaction seems to start as indicated by the quick dropping on the DSC curve in the end of this measurement. This endothermic reaction was confirmed by other DSC experiments which will be discussed later.
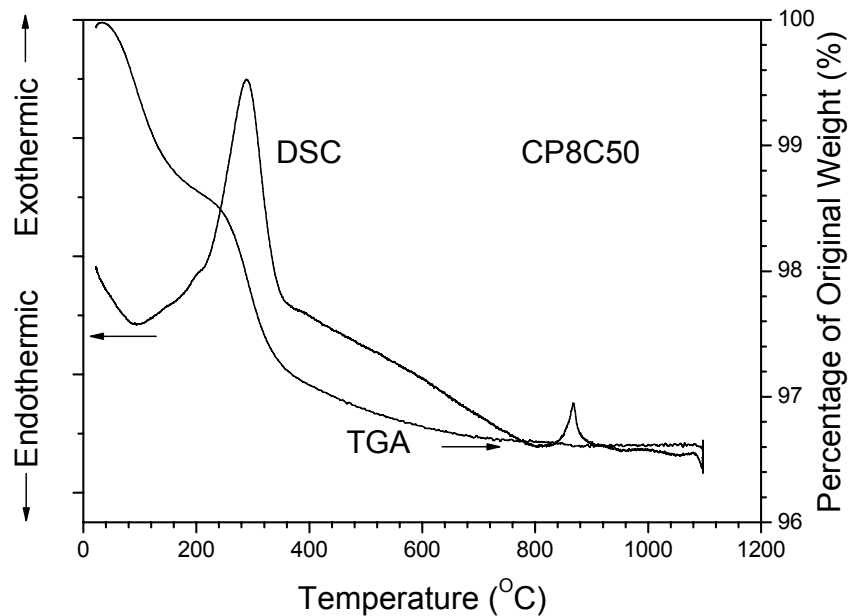
Fig. 4.1 Single heating TGA and DSC curves for CP8C50, heated in 90% O_2 + 10% N_2.

Thermal analysis with a cycled temperature programme was conducted for further characterisation of reactions during sintering of the CP8C50 sample. These results are shown in Fig. 4.2 and 4.3. The signal at 850 °C is less intense, which is likely caused by the lower thermal conductivity of the alumina cup compared to the platinum cup as used for the experiment as depicted in Fig. 4.1. An important feature of the reaction at 850 °C, as figured out by this cycled thermal analysis, is its irreversibility. As can be seen in Fig. 4.2 the DSC peak at 850 °C does not appear upon reheating.

Since in these thermal cycling experiments the maximum temperature was increased to 1150 °C the endothermic reaction at around 1100 °C can completely be observed in the cycled thermal analysis (see Figs. 4.2 and 4.3). Associated with the endothermic reaction at 1100 °C a small amount of weight loss (around 0.3 %) is observed on the TG curve. A calculation indicates that the weight loss is very likely to be caused by releasing of O_2 due to reduction of Cu^{2+} to Cu^+. During cooling the weigh was regained completely and an accompanying exothermic peak was observed on the DSC curve,
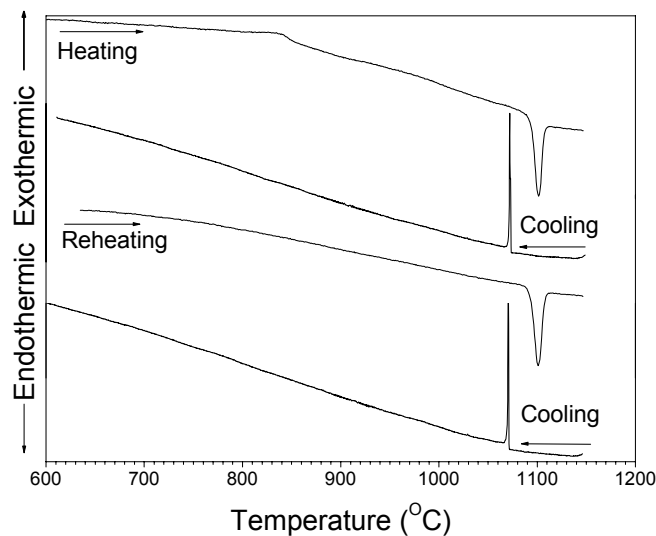
Fig. 4.2 Cycled DSC curve for CP8C50, heated in 90 % O_2 + 10 % N_2; sample

contained in an alumina cup.
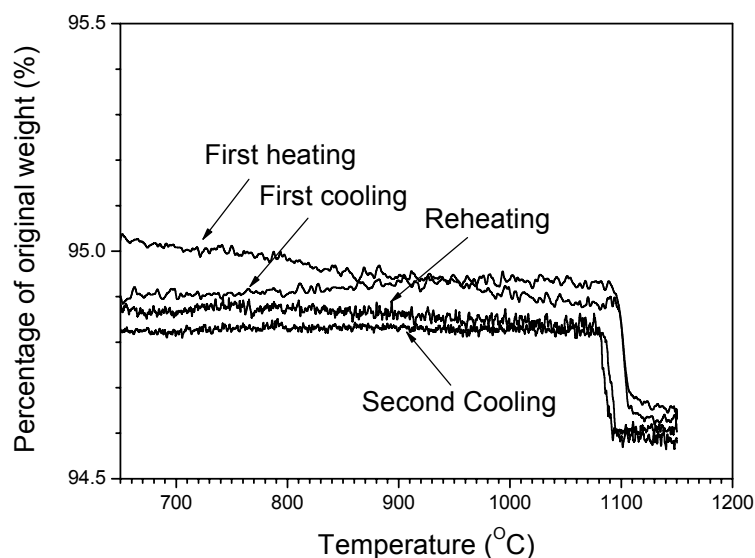
Fig. 4.3 Cycled TG curve for CP8C50, heated in 90 % O_2 + 10 % N_2; sample

contained in an alumina cup.

indicating an oxidation of the Cu^+ to Cu^{2+}. In the second round of heating and cooling the reaction at 1100 °C occurred in exactly the same way. These results suggest that the reduction/oxidation between Cu^{2+} and Cu^+ is completely reversible. It should be noticed that in our case this reduction/oxidation of Cu was observed at a considerably higher temperature (1100 °C) than in Seidensticker's work [4] who performed thermal analysis in air (1030 °C). As discussed in chapter 2 of this thesis the Cu valence change can be prevented by higher oxygen partial pressure. The higher temperature of Cu valence change shown in Fig. 4.2 should be caused by the higher oxygen partial pressure (0.9 bar) used in our cases. Additionally, melting of Cu_2O at around 1130 °C was observed in Seidensticker's work [4], however is absent in our case (until 1150 °C). This phenomenon implies that higher oxygen partial pressure inhibits the melting of Cu_2O as well.

4.3.2 XPS analysis on CuO doped 3Y-TZP nano-powder composite

Table 4.1 gives the Cu, Y and Zr elemental composition of the fractured and polished surfaces of several CP8C50 samples sintered at respectively 600, 700 and 850 °C. The data of a fractured surface of the as-pressed CP8C50 compact is also shown in Table 4.1 as a reference. For the materials as investigated in this work, it is observed by SEM that all samples fracture along the grain boundaries. It is further assumed that the polished cuts pass through the grains. Thus the elemental composition of the fracture and polished surfaces should well represent the composition of grain boundaries and grain bulk respectively.

Table 4.1 Elemental composition of fractured and polished surfaces of CP8C50 as analysed by XPS

ID	Sintering T (°C)	Measured surface	% metallic elements		
			Cu (2p3)	Y (3d)	Zr (3d)
a	Unsintered	Fractured	8.6	7.3	84.1
b	600	Fractured	23.0	5.0	72.0
c	600	Polished	3.2	5.4	91.4
d	700	Fractured	26.2	4.5	69.3
e	700	Polished	1.8	5.5	92.7
f	850	Fractured	14.8	8.0	77.2
g	850	Polished	2.9	5.6	91.5

The composition of the as-pressed compact as analyzed by XPS is in good agreement with the overall composition, implying a uniform dispersion of CuO in the 3Y-TZP matrix. The fractured surfaces of samples sintered at 600 and 700 °C show a Cu content of 23 and 26.2 atom% respectively, which are both much higher than the nominal composition. On the contrary the polished surfaces of these samples contain much less Cu (only 3.2 and 1.8 mol% for 600 and 700 °C sintered samples) if
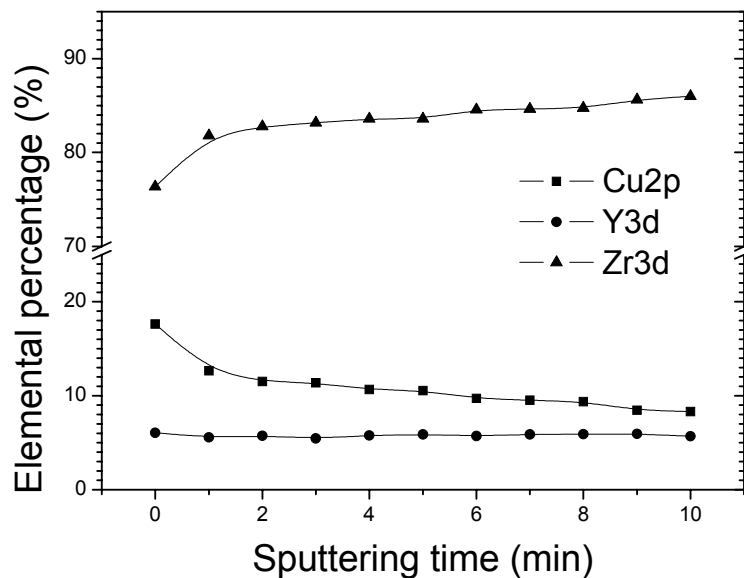
Fig. 4.4 Metallic elements composition on a fractured surface of CP8C50 sintered at 600 °C as a function of sputtering times.

compared with the as-pressed sample. With further heating to 850 °C the Cu content decreases to 14.8 mol% whereas that of the polished surface increases a bit if compared with the material sintered at 700 °C.

More information on copper distribution on the fractured surfaces of the sintered samples is given by depth profile analysis. As shown in Fig. 4.4, the Cu-signal of a material sintered at 600 °C decreases very rapidly after a short sputtering time. The same phenomenon was observed for the 700 °C and 850 °C sintered specimens. These results reveal that copper enrichment is present in a few nm thin layer of the fractured surfaces.

A detailed XPS analysis of the Cu $3p_{3/2}$ signal was performed in order to shed more light on the reactions, which result in the copper enrichment at the grain boundaries during sintering. In Fig 4.5 the result is given for a sample sintered at 600 °C (measured on a fractured surface). Samples sintered at 700 or 800 °C show the same result. An interesting observation is that for these sintered samples only one peak appears at a BE of 933 eV without the satellite at higher BE, whereas the Cu $2p_{3/2}$ spectra as measured on the unsintered specimen clearly showed a shakeup satellite peak at around 943 eV. The presence of shakeup satellite peak combined with the Cu $2p_{3/2}$ main line at 934 eV is a typical feature of Cu with oxidation state (II). This special feature of Cu $2p_{3/2}$ spectrum as described here will be further discussed later.
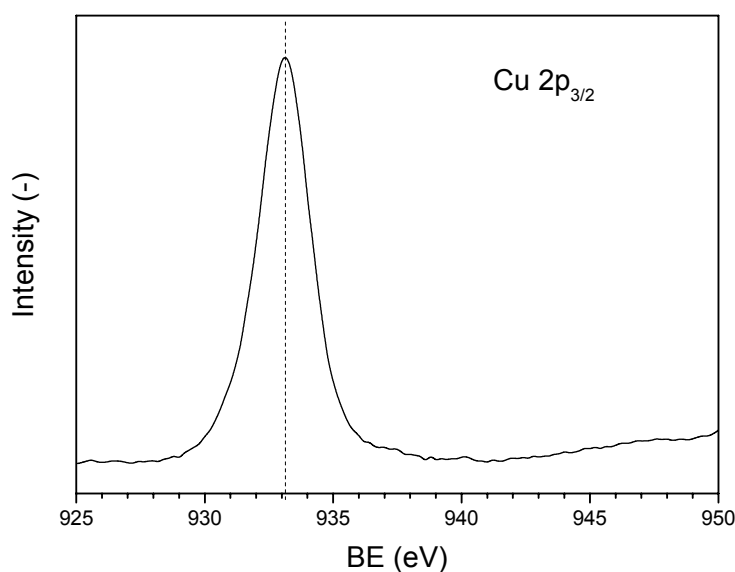
Fig. 4.5 Cu$2p_{3/2}$ spectrum of CP8C50 sintered at 600 °C.

4.3.3 Reaction between CuO and Y_2O_3

According to the pseudo-binary phase diagram of the Y_2O_3-CuO system in air [13] a reaction between Y_2O_3 and CuO takes place above 900 ºC, resulting in the formation of an yttria-copper-oxide phase. On the other hand the yttria in the Y-TZP solid solution tends to segregate to the grain boundaries at elevated temperatures ($\geq$ 800 °C) [14-15]. It was proposed in literature that the reaction can also occur between CuO and yttria as segregated to 3Y-TZP grain boundary, to form the yttria-copper-oxide, during sintering of a CuO doped 3Y-TZP system [4,7,8,10]. This reaction could be of importance for the sintering behaviour and microstructure evolution of the material. However, detailed characteristics of this reaction were not clearly reported yet.

High-temperature XRD measurements were performed on a representative system, a powder mixture of Y_2O_3 and CuO to investigate this reaction. The reactions in the powder mixture of CuO and Y_2O_3 as prepared by the citrate synthesis route is well representing the reactions between CuO and yttria as segregated to the 3Y-TZP grain boundary in our nano composite.

Fig. 4.6 shows the XRD patterns of the powder mixture at various temperatures. The starting powder can be characterised well as a mixture of CuO and Y_2O_3 powders. All signals on the pattern can be indexed to reflections of CuO and Y_2O_3, except a minor peak at around 2θ of 31°. This signal can be ascribed to a small amount of $Y_2Cu_2O_5$ which was formed by pyrolysis during the citrate synthesis. As indicated by the broad width of the peaks, both CuO and Y_2O_3 particles in this mixed powder are very
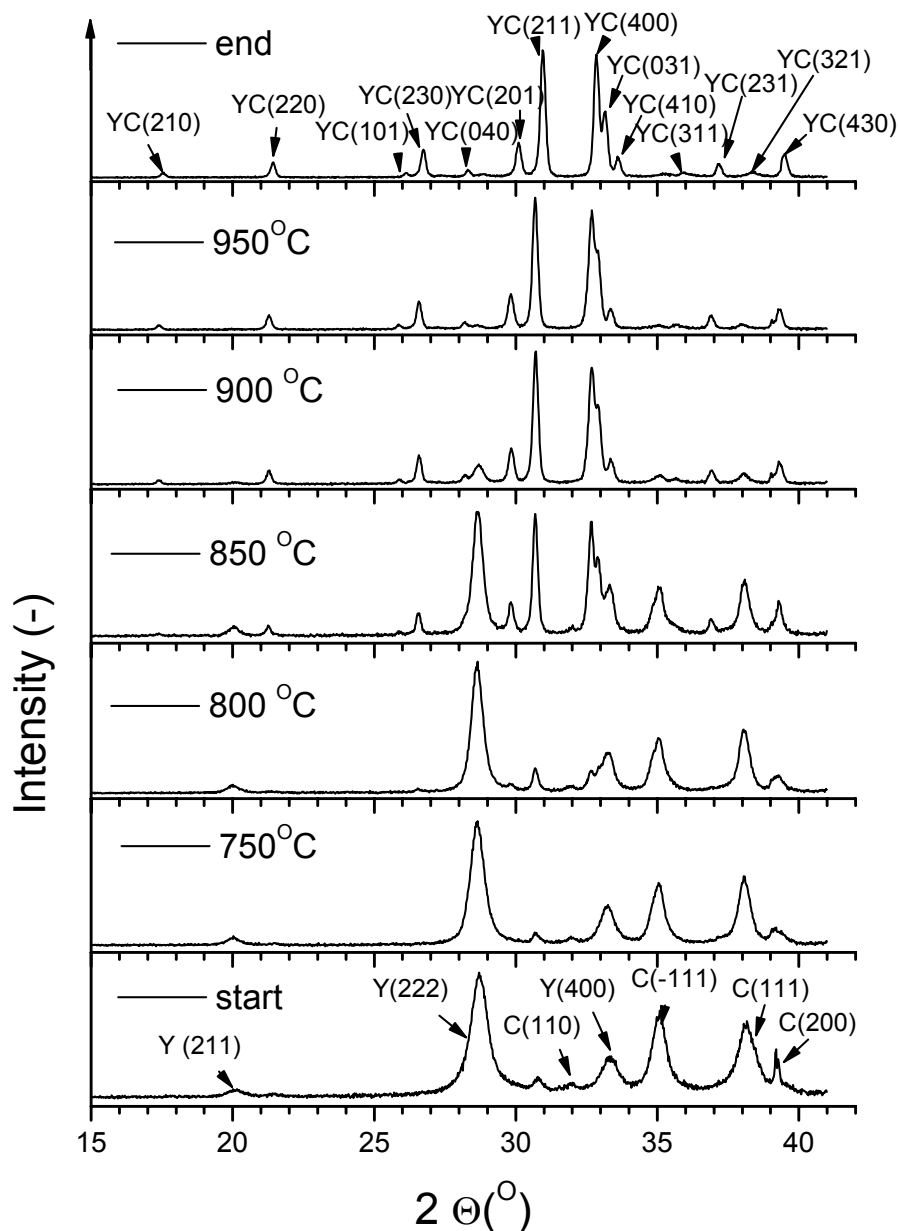
Fig. 4.6 XRD patterns of Y_2O_3+CuO powder mixture at various temperatures.

Remarks Y, C and YC denote reflections of Y_2O_3, CuO and $Y_2Cu_2O_5$ respectively; Patterns marked as "start" and "end" are measured at room temperature before heating and after cooling down respectively.

fine. While heating the pattern does not change until 750 °C except a slight shift of the peaks towards lower 2θ due to thermal expansion of the lattices. However, at 800 °C the peaks of both CuO and Y_2O_3 start to decrease and the signals of $Y_2Cu_2O_5$ appear (at 2θ of around 29.8, 30.6 and 32.6° respectively), although with very small intensities. This clearly indicates that a solid state reaction starts around 800 °C resulting in the formation of $Y_2Cu_2O_5$. At further heating the $Y_2Cu_2O_5$ signals more $Y_2Cu_2O_5$ is formed, while at 950 °C only $Y_2Cu_2O_5$ can be observed, indicating the completion of the reaction. When the sample is cooled down the sample shows an identical XRD pattern as that at 950 °C, revealing the irreversibility of the formation of $Y_2Cu_2O_5$.

4.4. Reactions during sintering of CuO-doped 3Y-TZP nano composite powder compacts

As described in the previous section several reactions occur during sintering of the CuO-doped 3Y-TZP nano-composite powder compacts. Those reactions will be discussed now.

The XPS results as shown in Table 4.1 and Fig. 4.4 indicate a strong enrichment of Cu in the 3Y-TZP grain boundary layer after sintering at 600 °C, which must be caused by a reaction between CuO and 3Y-TZP. Furthermore a change in the Cu $2p_{3/2}$ XPS spectrum (disappearing of shakeup satellite peak) was observed after sintering at 600 °C. This observation gives more insight on the reaction resulting in the CuO-enrichment in the grain boundaries. One possible explanation of the absence of a shakeup signal is the reduction of Cu^{2+} to Cu^{1+}, i.e. dissociation of CuO to Cu_2O [11]. However this reduction only occurs above 1100 °C for the investigated case as shown by thermal analysis (see Fig. 4.2). Additionally the BE of the Cu $2p_{3/2}$ main line (around 933 eV) indicates that the oxidation state of copper species should nevertheless be essentially Cu(II), because it is remarkably higher than that of Cu (I) (931 eV) [12]. Thus the special Cu $2p_{3/2}$ XPS spectrum of the 600 °C sintered specimens is more likely to be associated with another reaction like the dissolution of CuO in the 3Y-TZP matrix. Dongare et al. [12] reported that this shakeup feature disappears if Cu^{2+} is substituted on Zr^{4+} sites in the zirconia lattice and that the BE of Cu $2p_{3/2}$ shifts to a slightly lower value (933.4 eV) due to the association between Cu $2p_{3/2}$ and electron holes created by oxygen vacancies in the zirconia lattice (3Y-TZP lattice in this case). The authors also reported that the dissolution has already occurred when the CuO doped ZrO_2 system is calcined at 600 °C. The good similarity between our results and Dongare's observation proves that dissolution of CuO in the 3Y-TZP lattice occurs in our CP8C50 system when it is sintered at 600 °C. However the signal of this reaction can not be identified on the TGA/DSC curve, which might be due to the fact that its thermal effect is too small to be detected.

It is obvious that the CuO dissolution starts at the contact area between CuO and 3Y-TZP grains and the dissolved copper species further diffuse over the 3Y-TZP grains driven by chemical concentration gradients, which lead in a redistribution of copper species in the system. However, the grain boundary region is normally expected to be more kinetically (and also probably thermodynamically) favourable than the grain bulk region for copper species to occupy. As a result the grain boundary region contains much more copper than the grain bulk.

The solubility limit of CuO in the 3Y-TZP matrix in this case is difficult to determine. Seidensticker reported that in a Y-TZP matrix of submicron size (0.4 μm in grain size) a maximum amount of only 0.3 mol% can be dissolved [4,10]. These authors showed that the CuO dissolution occurs by forming a thin layer containing enriched Cu covering the 3Y-TZP grains, which is also observed in the present work. Thus the solubility of the CuO in the 3Y-TZP matrix is strongly influenced by the volume of

grain boundaries in the material. In our CP8C50 composite the 3Y-TZP grain size is less than 30 nm (see chapter 6 of this thesis) when the dissolution reaction has started (< 600 °C). The grain boundary volume in the CP8C50 composite (sintered at 600 °C) is more than 150 times larger than that of the system as studied by Seidensticker. Thus the CuO solubility in 3Y-TZP in our case is expected to be much higher than 0.3 mol%. Dongare reported that for a CuO doped pure ZrO_2 nano-ceramic prepared by a sol-gel technique up to 20 mol% can be dissolved in ZrO_2 matrix [12]. Although in our case the equilibrium status is probably not reached for the materials due to the short reaction time (30 min), it is expected that at least several mol % CuO has dissolved in the Y-TZP matrix at 600 °C.

While sintered at higher temperatures, the solubility of CuO in the 3Y-TZP matrix can be changed by either microstructural changes or the occurrence of other reactions. The reduction of Cu enrichment in the grain boundary at 850 °C (see Table 4.1), which is likely implying a decrease in CuO solubility, can be caused by the reaction as indicated by DSC analysis (see Fig. 4.1). On the other hand the decrease in grain boundary volume due to grain growth can also be a reason for a decrease in solubility.

The exothermic signal at 850 °C (See Figs 4.1 and 4.2) is clearly caused by an irreversible reaction between CuO and the 3Y-TZP grains. A similar irreversible exothermic signal was also observed by Seidensticker [4] and Hayakawa [7] on their study of CuO doped 3Y-TZP systems. Seidensticker did not assign any reaction to this signal. Hayakawa attributed this signal to the reaction between CuO and yttria resulting in the formation of $Y_2Cu_2O_5$. However these authors did not provide any additional proof of this reaction. Comparing the DSC and high-temperature XRD results as shown in Fig. 4.1 and 4.6 respectively, it can be seen that the reaction between Y_2O_3 and CuO starts at 850 °C in the CP8C50 composite and matches perfectly with the formation of $Y_2Cu_2O_5$. Thus it is proven that formation of $Y_2Cu_2O_5$ in the CP8C50 composite occurs at 850 °C during sintering, which is in a good agreement with Hayakawa's [7] conclusion.

In the case of the CP8C50 composite as studied in the present work both 3Y-TZP and CuO grains are on nanometre scale, which means large amounts of contact area between CuO and 3Y-TZP grains are present in the material. The dissolution of CuO in the 3Y-TZP grain boundaries can also improve the contact between Cu and Y species. Additionally it was reported that strong yttria enrichment in the grain boundaries also takes place after heating pure 3Y-TZP at 850 °C [14, 15]. As a consequence of these factors, this formation of $Y_2Cu_2O_5$ proceeds much faster and more intensively in the CP8C50 composite then in a coarse-grained CuO doped 3Y-TZP composite as described by Seidensticker [4] and Hayakawa [7]. It is also expected that this reaction takes place mainly in the 3Y-TZP grain boundary region.

The reactions discussed in this chapter have significant influences of sintering and microstructure evolution of the CuO doped 3Y-TZP system. These influences will be studied in chapter 5 and 6 respectively.

4.5 Conclusions

The several reactions, which occur during sintering of CuO doped 3Y-TZP nano-powder composites were investigated. A strong dissolution of CuO in the 3Y-TZP matrix below 600 °C, which results in an enrichment of Cu in the 3Y-TZP grain boundaries was proven by XPS analysis. An irreversible reaction between CuO and yttria as segregated to the 3Y-TZP grain boundaries at around 850 °C leading to a formation of $Y_2Cu_2O_5$ was clarified by combination of thermal analysis and high temperature XRD analysis. A fully reversible oxidation-reduction of Cu in the material system occurs at around 1100 °C in an O_2-rich atmosphere (90%).

Acknowledgement

References

1. Hwang, C.M.J., and Chen, I-W., "Effect of a liquid phase on superplasticity of 2-mol%-Y_2O_3-stabilized tetragonal zirconia polycrystals", *J. Am. Ceram. Soc.*, 1990, **73**[6], 1626-1632.
2. Kerkwijk, B., García, M., van Zyl, W. E., Winnubst, L., Mulder, E. J., Schipper, D. J. and Verweij, H., "Friction behaviour of solid oxide lubricants as second phase in α-Al_2O_3 and stabilised ZrO_2 composites", *Wear*, 2004, **256**[1-2], 182-189.
3. Pasaribu, H. R., Sloetjes, J. W. and Schipper, D. J., "Friction reduction by adding copper oxide into alumina and zirconia ceramics", *Wear*, 2003, **255**[1-6], 699-707.
4. Seidensticker, J.R. and Mayo, M.J., "Thermal analysis of 3-mol%-yttria-stabilized tetragonal zirconia powder doped with copper oxide", *J. Am. Ceram. Soc.*, 1996, **79**[2], 401-406.
5. Ran, S., Winnubst, A.J.A., Wiratha, W. and Blank, D.H.A., "Sintering behavior of 0.8 mol%-CuO-doped 3Y-TZP ceramics", *J. Am. Ceram. Soc.*, 2006, **89**[1], 151-155.
6. Ramesh, S., Gill, C., Lowson, S., "The effect of copper oxide on sintering, microstructure, mechanical properties and hydrothermal ageing of coated 2.5Y-TZP ceramics", *J. Mat. Sci.*, 1999, **34**, 5457-5467.
7. Hayakawa, M., Inoue, T., Pee, J.-H., Suematsu, H. and Yamauchi, H., "Liquid phase sintering of Y-TZP with CuO and $Y_2Cu_2O_5$ dopants", *Mater. Sci. Forum*, 1999, **304-306**, pp. 465-470.
8. Lemaire, L., Scholz, S.M., Bowen, P., Dutta, J., Hofmeister, H. and Hofmann, H., "Effect of CuO additives on the reversibility of zirconia crystalline phase transitions", *J. Mater. Sci.*, 1999, **34**, 2207-2215.
9. Kimura, N., Okamura, H. and Morishita, J., "Preparation of low-Y_2O_3-TZP by low-temperature sintering", *Adv. Ceram.*, 1988, **24**, 183-191.
10. Mayo, M.J., Seidensticker, J.R., Hauge, D.C. and Carim, A.H., "Surface chemistry effects on the processing and superplastic properties of nanocrystalline oxide ceramics", *Nanostructured Mater.*, 1999, **11**[2], pp. 271-282.
11. "Handbook of X-Ray photoelectron spectroscopy: a reference book of standard spectra for identification and interpretation of XPS data", Ed. by J. Chastain, Eden Prairie, Minnesota, USA, 1992.
12. Dongare, M.K, Dongare, A.M., Tare, V.B., Kemnitz, E., "Synthesis and characterization of copper-stabilized zirconia as an anode material for SOFC", *Solid State Ionics*, 2002, **152-153**, 455-462.
13. Gadalla A.M. and Kongkachuichay, P., "Compatible phases of the Y_2O_3–CuO–Cu_2O system in air", *J. Mater. Res.*, **6** 450-454 (1991).
14. Burggraaf, A. J., van Hemert, M., Scholten, D. and Winnubst, A. J. A., "Chemical composition of oxidic interfaces in relation with electric and electrochemical properties", pp. 797-802 in Reaction of Solid, Ed. by P. Barret and L.C. Dufour, 1985.
15. Theunissen, G.S.A.M., Winnubst A.J.A. and Burggraaf, A.J., "Segregation aspects in the ZrO_2-Y_2O_3 ceramic system", *J. Mater. Sci. Lett.*, 1989, **8**[1], 55-57.

Chapter 5

Sintering behaviour of CuO doped 3Y-TZP: influences of reactions and optimisation via control of these reactions

Abstract

Ceramic composites were prepared by mixing 3Y-TZP (10 nm) and various CuO (20, 50, 360 nm) nano-powders. Sintering behaviour of those nano-powder composites were measured by using a dilatometer. Dependence of sintering behaviour on CuO content and particle size of the added CuO powder was investigated. It has been revealed in chapter 4 that several reactions occur during sintering of CuO doped 3Y-TZP composites. The influences of those reactions on sintering were recognised. Dissolution of CuO in the 3Y-TZP grain boundaries occurs below 600 °C increases grain boundary diffusivity and consequently promotes sintering in the initial and intermediate stages to a very large extent. The formation of $Y_2Cu_2O_5$ at 800 - 950 °C inhibits sintering. Influences of the reactions on sintering, both beneficial and detrimental ones, are dependent on the CuO content as well as the CuO particle size. Based on those observations, a solution for optimising sintering of a CuO doped 3Y-TZP system, by controlling of reactions during sintering, was proposed. By choosing proper content (1.6 mol%) and particle size (20 nm) of added CuO powder, sintering of CuO doped 3Y-TZP nano-powder composite is optimised. The optimal material can be fully densified by just heating to 1000 °C at 15 °C·min^{-1} in oxygen.

5.1 Introduction

Zirconia based ceramic materials have obtained extensive interest in the past decades due to their advanced mechanical and electrical properties. The high fracture toughness and strength of 3 mol % yttria stabilised tetragonal zirconia polycrystals (3Y-TZP) make this material an important candidate for many structural applications [1-2]. It was also reported that fine-grained Y-TZP ceramics exhibit a superplastic deformation property, which has opened up the possibility of using ceramics in ductile near net shape forming operations [3]. Recently low dry sliding friction was obtained with CuO doped 3Y-TZP ceramics [4-5], implying a possibility of engineering applications of these materials without lubricants.

Sintering, a treatment of the powder compact at elevated temperatures, is an important step in ceramic processing. This step is basically for obtaining a high density, a good strength and a proper microstructure of the ceramic material. A sound knowledge of sintering behaviour is always necessary for manufacturing a ceramic material with desired properties.

Powder characteristics like particle size and agglomerate strength have profound influence on sintering behaviour of the material. In general smaller particles give higher sintering activity because of their larger interface energy, which results in higher driving force for sintering at lower temperature [6].

However the sintering of nano powder presents additional challenges if compared with sintering of regular powders due to stronger particle agglomeration, higher reactivity and inherent contamination, etc [7, 8].

For a composite ceramic, reactions between the components while heating can strongly influence sintering behaviour. It was reported that addition of coarse-grained CuO into a submicron 3Y-TZP powder (Tosoh) strongly inhibits densification and results in a tetragonal to monoclinic zirconia phase transformation during sintering, which are actually caused by the reactions between CuO and the Y-TZP matrix [9]. However, the influence of these reactions on sintering can also be altered by choosing other powder characteristics, like grain sizes in the nanometre meter range.

In this chapter the sintering behaviour of CuO doped 3Y-TZP nano-powder composites is described. The influences of reactions during sintering as described in chapter 4 are recognised. Optimisation of sintering of CuO doped 3Y-TZP via controlling the reactions during sintering by choosing the content and particle size of added CuO powder will be discussed.

5.2 Experimental procedure

5.2.1 Powder synthesis

A nanocrystalline powder of 3 mol% yttria stabilised tetragonal zirconia polycrystals (CP 3Y-TZP) was prepared by a co-precipitation technique of metal chlorides, as described in chapter 3. A copper oxalate complexation-precipitation technique was applied to prepare CuO powders with various BET equivalent particle sizes (20, 50 and 360 nm with code CuO-20, CuO-50 and CuO-360 respectively, see chapter 3). Composites of CP 3Y-TZP doped with 0.8, 1.6, 3.2 and 8 mol% of CuO powders were prepared by milling the proper amounts of 3Y-TZP and CuO powder for 24 hours in a polyethylene bottle, using ethanol and zirconia balls as milling media. The milled suspension was ultrasonically dispersed for 5 min and then oven-dried at 100 ºC for 24 hours. The dry cake of the composite powder was lightly ground in a plastic mortar and sieved through a 180 μm sieve. The resulting powder was stored in a desiccator prior to use.

Characterisation of these powders was performed using XRD, BET and compaction techniques as described in chapter 3.

5.2.2 Dilatometer measurements

Cylindrical green compacts of CP 3Y-TZP powder (ball-milled in the same way as used for composite powders) and the composite powders were prepared by cold isostatic pressing (CIP) at 400 MPa for 5 min. The diameter and length of the green compacts were 7~8 mm and 12~15 mm respectively. The green densities (measured according to Archimedes principle in mercury) of the compacts were 44~46 % of the theoretical density of tetragonal zirconia. The sintering behaviour of the compacts was studied using a Netzsch 402E dilatometer in an oxygen flow of 20.0 mL·min^{-1}. For all dilatometer measurements, a three segment temperature program was applied, including heating from room temperature at 15 °C·min^{-1}, holding at 1130 °C for 1 hour, and cooling to room temperature at 5 °C·min^{-1}. Linear shrinkage was recorded as a function of time and temperature. The density as a function of temperature was calculated from the green density and the observed linear shrinkage of the specimens and corrected for thermal expansion of the sample using equation 2.1 in chapter 2. Anisotropic densification was not taken into account. The good agreement between the final density

values as calculated in this way and as measured according to Archimedes principle (in mercury) confirms that anisotropic densification is negligible in call the cases.

5.3 Results and discussion

5.3.1 Sinterability of nanocrystalline and coarser-grained 3Y-TZP powders

As shown in chapter 3, the CP 3Y-TZP powder possesses a pure tetragonal crystal structure. The almost identical particle diameter values as determined by XRD and BET techniques (8 and 10 nm respectively) imply that the powder is almost aggregate-free. Compaction measurements show that the powder is weakly agglomerated.

Fig. 5.1 compares densification behaviour (density, ρ, and densification rate, $d(\Delta L/L_0)/dt$, as a function of temperature) of CP and commercially available Tosoh 3Y-TZP powder compacts during heating at 2 ºC·min^{-1}. As can be seen from Fig. 5.1, the green density of CP powder compact is lower that that of the Tosoh powder compact. However densification of CP powder started and finished at much lower temperatures (around 200°C lower) if compared with the Tosoh powder. The influence of powder properties (including crystallite size, agglomeration and aggregate structure and etc.,) on compaction and sinterability of 3Y-TZP ceramics have been investigated extensively by Theunissen [10] and Sagel-Ransijn [11]. A general conclusion drawn from their work is that nano-sized crystallites and weak agglomerates/aggregates, as is the case for the CP powder, can significantly improve sinterability. The dilatometer measurement results as shown in Fig. 5.1 are in good agreement with these conclusions.
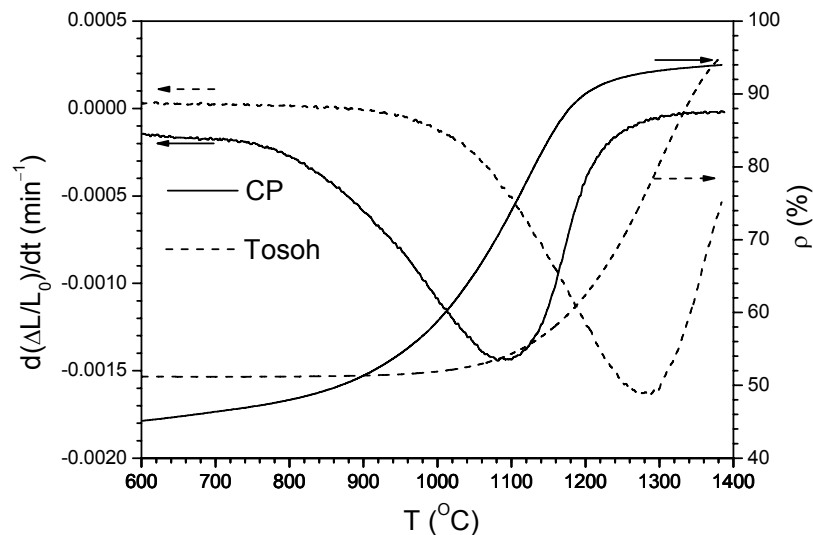
Fig. 5.1 Density and linear shrinkage rage of CP and Tosoh 3Y-TZP powder compacts as a function of temperature during heating at 2 °C·min^{-1} in air.

5.3.2 Sintering behaviour of 8 mol% CuO-50 doped CP 3Y-TZP

Fig. 5.2 shows the relative density (corrected for weight loss and thermal expansion) and the linear densification rate $(d(\Delta L/L_0)/dt)$ of the CP8C50 nano-composite as a function of temperature, during heating in an oxygen flow. The data of undoped 3Y-TZP (sintering at 15 °C·min^{-1}) are also shown in

this figure for comparison. As can be seen in Fig. 5.2 the addition of nanocrystalline CuO drastically changes the sintering behaviour of nanocrystalline 3Y-TZP. In general it can be stated that sintering of the CuO doped 3Y-TZP composite can be divided into 3 stages, e. g. stage I (700 ~ 900 ºC), stage II (900 ~ 1020 ºC) and stage III (1020 ~ 1100 ºC).
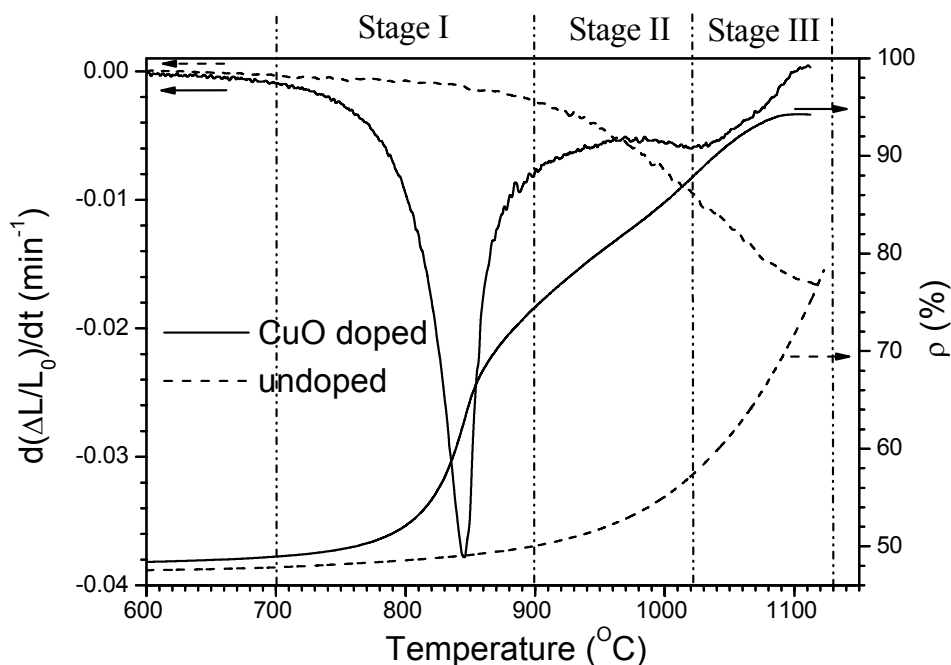
Fig. 5.2 Density and linear shrinkage rate of CP8C50 as functions of temperature during heating at 15 °C·min^{-1} in oxygen. Three sintering stages are recognised and marked by the vertical lines.

In stage I it is shown that the addition of CuO decreased the onset temperature of densification of 3Y-TZP from 850 °C (undoped) to 700 °C (CuO doped). Shortly after the start of densification, the composite sample showed a drastic increase in densification rate until 850 ºC. Within the next 50 ºC temperature range (around 3 minutes of heating) densification slowed down rapidly. During this sintering stage the density of the 8 mol% CuO-50 doped CP 3Y-TZP (CP8C50) sample was increased from 50 % to 75 %, while densification of the undoped 3Y-TZP did hardly started in the same temperature range.

In sintering stage II densification of CP8C50 proceeded at a relatively low rate. However, the contribution in this stage to the total densification is also significant (an increase from 75 % to 90 %), indicating that sintering has almost been finished after heating CP8C50 at 15 ºC·min^{-1} to around 1000 ºC. In contrast, densification of the undoped 3Y-TZP sample just started in this temperature range and the density is only below 60 %.

The densification of the CuO doped sample slowed down gradually in stage III since densification is almost finished in stage II. After the dilatometer experiment the CuO doped 3Y-TZP had a relative density of 96 % (the presence of 80 vol% monoclinic zirconia phase in the sintered sample is taken into account for the calculation of theoretical density, see chapter 6 of this thesis).

5.3.3 Influence of reactions on sintering

It has been revealed in chapter 4 that during sintering several reactions occur in the CuO doped Y-TZP systems. Those reactions have shown profound influence on densification behaviour of coarse-grained 0.8 mol% CuO doped 3Y-TZP ceramics [12] and as discussed in chapter 2 of this thesis. Basically the difference between sintering behaviour of undoped and CuO doped nanocrystalline 3Y-TZP systems as shown in Fig. 5.2 can also be interpreted in terms of reactions occurring during heating.

The first effect of CuO addition on the sintering behaviour of 3Y-TZP is the decrease in onset temperature for densification. The low onset temperature can be attributed to the dissolution of CuO in the Y-TZP matrix which starts below 600 °C, leading to a strong enrichment of CuO in the grain boundary region. This dissolution of CuO in the zirconia lattice (as discussed in chapter 4) results in an increase in lattice defects as well as the formation of a cubic zirconia phase, in grain-boundary area [12-13]. Both these phenomena as well as the dissolution process of Cu in the zirconia phase itself can significantly increase cation mobility or ion diffusivity in the 3Y-TZP grains, especially in the grain boundary region [12-15]. As grain boundary diffusion normally plays an important role in densification during sintering [16], it can be concluded that the increased ion mobility or ion diffusivity results in an enhanced initial and intermediate sintering and consequently leads to a lower on set temperature.

The extremely fast densification rate of the CP8C50 composite observed in sintering stage I is a very unique phenomenon. To our knowledge Y-TZP systems did not exhibit significant densification at such low temperatures (<900 °C), when only solid-sate diffusion is the densification mechanism. In chapter 4 it was confirmed by DSC that no melting occurs during this sintering stage. Therefore liquid-phase sintering, normally a reason of lower densification temperatures does not occur in this case. As discussed above the dissolution of CuO in the 3Y-TZP matrix strongly activates sintering by increasing grain-boundary diffusivity. This dissolution mainly takes place in the grain boundary region. Therefore the 3Y-TZP/CuO contact area per unit volume is important for the dissolution and consequently for the activation of the sintering process. In the composite studied here grain sizes of both Y-TZP and CuO are on a nano scale. Assuming the CuO grains are uniformly distributed among the 3Y-TZP matrix, a very large amount of Y-TZP/CuO contact area per unit volume can be expected. Consequently large amounts of 3Y-TZP grains are strongly activated for sintering by the dissolution of CuO in Y-TZP matrix in sintering stage I and correspondingly an extremely fast densification is achieved.

The strong decrease in densification rate as observed at 850 °C should also be caused by some reaction between CuO and the 3Y-TZP because the densification is far from complete at that temperature ($\rho <$ 70%). As revealed in chapter 4 the formation of $Y_2Cu_2O_5$ occurs at 850 °C. This formation leads to a tetragonal to monoclinic zirconia phase transformation, which is associated with a volume expansion (see chapter 6). However the drastic decrease in densification rate as observed at 850 - 950 °C can not be completely explained by the limited volume expansion (< 0.1%) caused by the t-m transformation in the corresponding temperature range. The formation of $Y_2Cu_2O_5$ itself must be responsible for the reduction in densification rate at 850 °C. The inhibition in densification, as arises from the formation of $Y_2Cu_2O_5$ in the 3Y-TZP grain boundary region, was also observed in a coarse-grained composite of 3Y-TZP (Tosoh) doped with 0.8 mol% CuO (Aldrich) as described in chapter 2. This reaction attracts the Cu solutes out of the 3Y-TZP lattice and, consequently, this might reduce the grain boundary ion diffusivity (mobility). On the other hand, assuming that the formed $Y_2Cu_2O_5$ is present as a thin grain boundary layer partly or completely covering the 3Y-TZP grains, the interface free energy (driving

force of sintering) can be decreased due to the change of grain boundary chemical composition. Additionally this layer can act as a barrier to retarding the diffusion between Y-TZP grains, which is also detrimental to densification.

5.3.4 Dependence of CuO particle size and/or concentration on densification.

The dependence of sinterability of CuO doped 3Y-TZP nano-powder composites on CuO particle size is best illustrated by comparing the dilatometer results of CP 3Y-TZP doped with a small amount (0.8 mol%) of CuO-20, CuO-50 and CuO-360 powders. In Figs. 5.3 -a and -b the density and linear shrinkage rate of the CP.8C20, CuO-50 and CuO-360 composites during heating are shown.

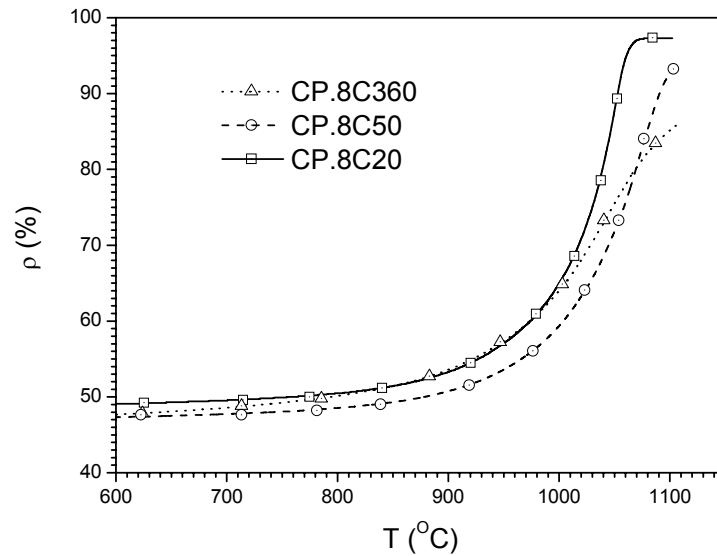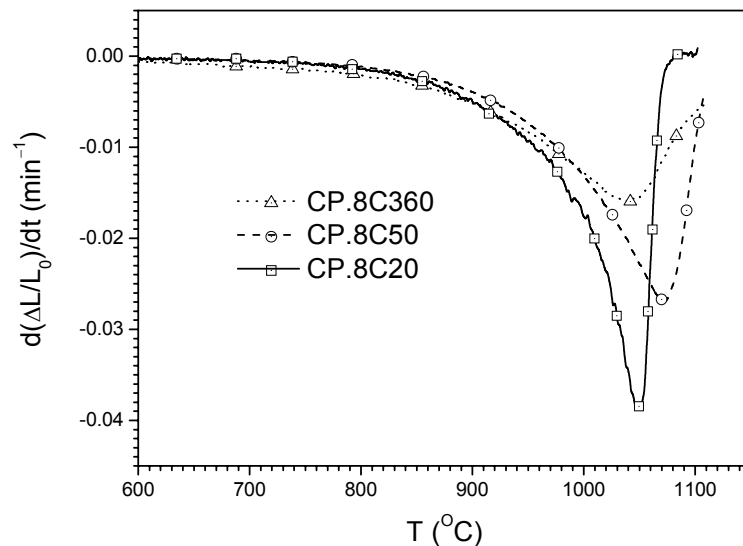Fig. 5.3-a Density of CP.8C20, CP.8C50, CP.8C360 as a function of temperature during heating at 15 °C·min^{-1} in oxygen.

Fig. 5.3-b Linear shrinkage rate of CP.8C20, CP.8C50, CP.8C360 as a function of temperature during heating at 15 °C·min^{-1} in oxygen.

In general it can be seen in Fig. 5.3-a that all CuO doped 3Y-TZP samples show significantly enhanced densification during sintering if compared with the undoped one (see Fig. 5.1). This is obviously caused by the dissolution of CuO in the 3Y-TZP matrix. The onset temperature of densification of all samples is similar (around 850 °C) and densification is identical in the initial stage (<950 °C). However with further heating the samples clearly behaved differently in the intermediate sintering stage. The densification of CuO-20 doped sample (CP.8C20) shows a maximum in shrinkage rate at around 1040 °C while a density of 87 % was reached. The densification curve of the CuO-50 doped sample (CP.8C50) is similar to that of the CP.8C20 but the maximum densification rate shifts towards a slightly higher temperature (1080 °C compared with 1040 °C of CP.8C20), associated with a density of 85% at that temperature. For these two samples the maximum in densification rate is obviously caused by the completion of the intermediate sintering stage. Before the dwell segment started, these two samples have densified to 96 % and 94 % for CP.8C20 and CP.8C50 respectively. The inhibition in densification rate arising from the formation of $Y_2Cu_2O_5$ at 850 °C as observed for CP8C50 does not appear. The absence of this densification inhibition will be further discussed more in later section of this chapter.

The CuO-360 doped sample (CP.8C360) shows a maximum in densification rate around 1050 °C, while the magnitude of maximum densification rate is much lower than that of CP.8C20 and CP.8C50. Additionally the density at its maximum densification rate is only 75%, implying that densification decreases before the intermediate sintering stage has completed. At the end of the heating segment during the dilatometer experiment the density of the CP.8C360 sample was only 88 %. It can be said that the CP.8C360 experienced an inhibition in densification if compared with CP.8C20 and CP.8C50, or a less enhancement in densification if compared with an undoped CP powder compact.

The influence of CuO content on sintering behaviour of the CuO-20 and CuO-50 doped 3Y-TZP nano-powder composites is shown in Figs. 5.4 and 5.5 (density and shrinkage rate of CPxC50 and CPxC20 respectively, x = 0.8, 1.6, 3.2 and 8). Generally it can be stated that with increasing CuO content both temperatures of on set as well as the maximum densification rate shift towards a lower temperature, implying an enhancement in sinterability in initial and intermediate sintering stage. Again it is revealed that with the same CuO content the material doped with smaller CuO particles (CuO-20) experiences more enhancement in sinterability.

For the materials with a CuO content ≤ 1.6 mol% the densification inhibition caused by the formation of $Y_2Cu_2O_5$ is not clearly visible. These samples smoothly densify until the final sintering stage starts (> 90% in density, see Figs. 5.4-a and 5.5-a). However when the CuO content exceeds 3.2 mol% (CP3.2C20, CP8C20, CP3.2C50 and CP8C50), a strong densification inhibition arises from the formation of $Y_2Cu_2O_5$. Moreover, with smaller CuO particle size this densification inhibition starts at lower temperatures and proceeds in a stronger degree.

All these influences of particle size and amount of the CuO on sintering behaviour of the composites can actually be interpreted in terms of reactions, which have an effect on sintering, i.e. the CuO dissolution and $Y_2Cu_2O_5$ formation. The degree of these two reactions is dependent on CuO content as well as the specific contact area between CuO and 3Y-TZP grains. The latter factor can be strongly enhanced by a decrease in the CuO particle size while assuming that in all cases the CuO particles are uniformly dispersed in the 3Y-TZP matrix. Obviously higher CuO content and smaller CuO particle size promote the degree of the reactions between CuO and 3Y-TZP, and therefore the influences of those reactions on sintering become more pronounced, both the beneficial (promotion of sintering due to dissolution of CuO) and the detrimental (inhibition of sintering due to formation of $Y_2Cu_2O_5$) one.
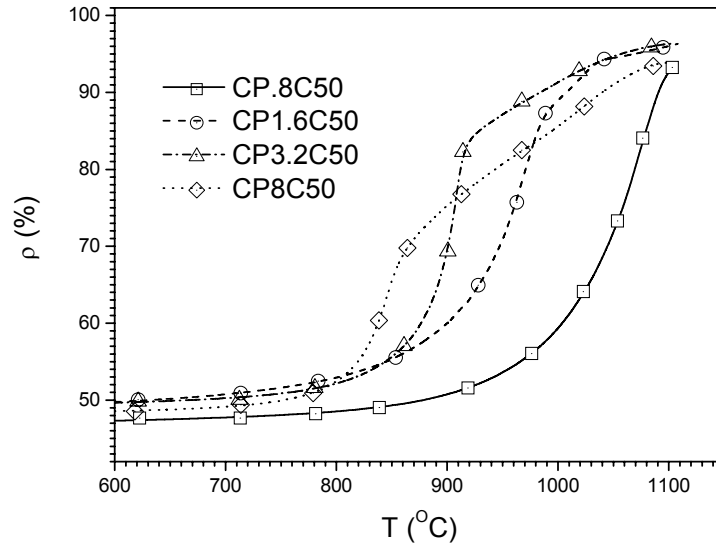
Fig. 5.4-a Density of CP 3Y-TZP doped with 0.8-8 mol% CuO-50 as a function of temperature during heating at 15 °C·min^{-1} in oxygen.
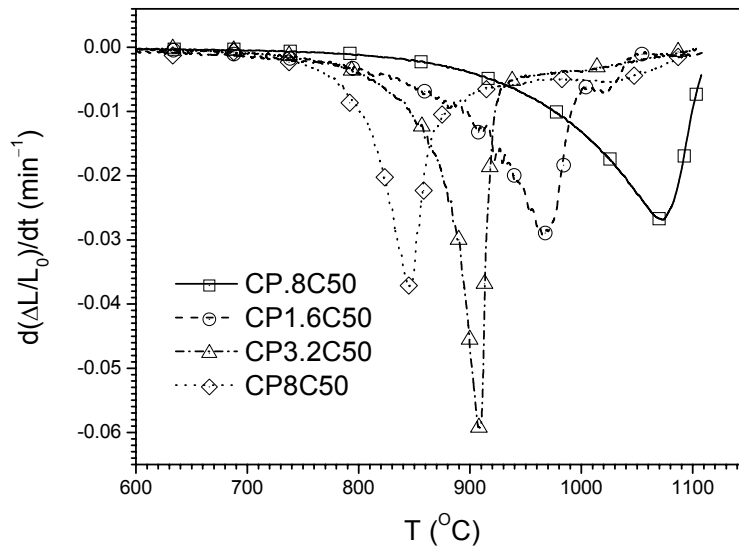
Fig. 5.4-b Linear shrinkage rate of CP 3Y-TZP doped with 0.8-8 mol% CuO-50 as a function of temperature during heating at 15 °C·min^{-1} in oxygen.

An interesting phenomenon, on which attention should be paid, is that densification inhibition due to $Y_2Cu_2O_5$ formation was observed in the case of coarse-grained 0.8 mol% CuO (CuO) doped 3Y-TZP (Tosoh) composite (see chapter 3), however, was absent in the cases of nanocrystalline CP.8C20 and CP.8C50. This seems to indicate that the degree of $Y_2Cu_2O_5$ formation in the former case is higher than that in the later cases, but in fact the reverse is true. The absence of densification inhibition for the nano composites should actually be explained by more significant promotion in sintering due to the use nanocrystalline 3Y-TZP and CuO powders. At the moment that $Y_2Cu_2O_5$ is formed in the nanocrystalline composite a higher density is already achieved if compared with the coarse-grained system and consequently the detrimental effect of the formation of $Y_2Cu_2O_5$ is effectively suppressed while sintering the nano composite.
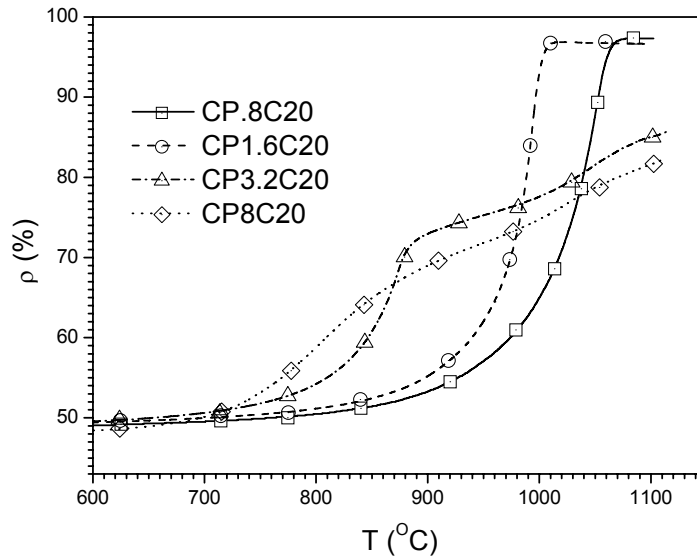
Fig. 5.5-a Density of CP 3Y-TZP doped with 0.8-8 mol% CuO-20 as a function of temperature during heating at 15 °C·min^{-1} in oxygen.
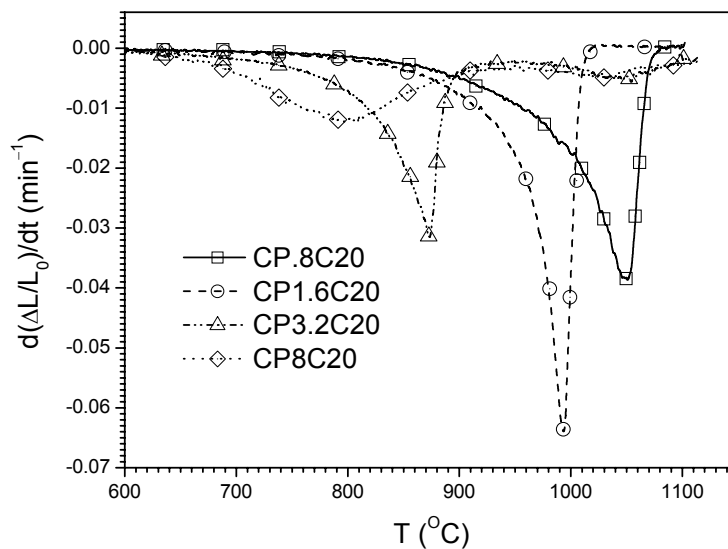
Fig. 5.5-b Linear shrinkage rate of CP 3Y-TZP doped with 0.8-8 mol% CuO-20 as a function of temperature during heating at 15 °C·min^{-1} in oxygen.

5.3.5 Optimising sinterability via control of reactions during sintering

As described in chapter 4 of this thesis several reactions occur during sintering of a CuO doped 3Y-TZP system: a) dissolution of CuO in the 3Y-TZP grain boundaries, b) formation of $Y_2Cu_2O_5$, and c) dissociation of CuO to Cu_2O. It is observed in this work that these reactions have a profound influence on sintering, some are beneficial, and some are detrimental. In summary: a) the dissolution of CuO in the 3Y-TZP matrix starting at a low temperature (< 600 °C) can increase the grain boundary ion mobility/diffusivity to a large extent, and therefore significantly promote the initial and intermediate sintering. b) In the temperature range between 800 and 950 °C a reaction between CuO

and yttria as segregated to the 3Y-TZP grain boundaries takes place and results in the formation of $Y_2Cu_2O_5$. This formation of $Y_2Cu_2O_5$ strongly slows down the sintering. c) As shown in chapter 2 of this thesis, dissociation of CuO occurs at high temperatures (> 1030 °C in air [17]) can also give a detrimental influence on sintering. Furthermore it is also observed that those reactions are strongly dependent on CuO content, particle size of CuO and 3Y-TZP powders, or sintering atmosphere (see chapter 4)

Based on the observations as summarised above, we propose a straightforward solution for optimising sintering of CuO doped 3Y-TZP systems, that is, promoting the beneficial reactions (i.e. reaction a) combined with preventing the detrimental ones (i.e. reactions b and c).

In this work the optimisation of sinterability is implemented by controlling sintering atmosphere, CuO content and particle size of the starting powders. Considering the preventing effect of a high oxygen particle pressure on reaction c) [15], a pure oxygen flow was used as the sintering atmosphere. It is confirmed by DSC/TGA analysis that the dissociation of CuO is shifted to a higher temperature (> 1100 °C) by increasing the oxygen particle pressure to 0.9 bar (0.21 bar in air). Reducing the 3Y-TZP particle size (to 10 nm) also helps to prevent the detrimental effect of this reaction. The sintering temperature significantly decreases by using 10 nm 3Y-TZP (see Fig. 5.1) so that the material get more chance to be fully densified before reaction c) takes place.

As to the reactions a) and b), both of them proceed mainly in the grain boundary region. Tuning of the CuO content and specific 3Y-TZP/CuO contact area is important for controlling these two reactions. It is shown that sintering in the initial and intermediate stages can be promoted to a very large extent by enhancing reaction a) via reducing CuO particle size and increasing CuO content. By doing so an incredibly fast densification at relatively low temperatures can be achieved. On the other hand reaction b) can also be enhanced by higher CuO content as well as smaller CuO particle size. But fortunately when the CuO content is low ($\leq$ 1.6 mol%) the detrimental effect of the reaction b) can be effectively suppressed. However if too much CuO ($\geq$ 3.2 mol%) is added reaction b) will be too pronounced to be suppressed and remarkably retard sintering. So a proper CuO particle size and CuO content should be chosen to enhance the reaction a) to the most degree when the reaction b) can still be fairly prevented. From this point of view, the composite with a CuO content of 1.6 mol% and a CuO particle size of 20 nm (CP3.2C20), among the materials studied here, exhibits the optimal sinterability. This material can be fully densified by just heating to 1000 °C at 15 °C·min^{-1} in oxygen.

5.4 Conclusions

In this chapter influences of reactions as revealed in chapter 4 on sintering of CuO doped 3Y-TZP nano-powder composites were recognised. The dissolution of CuO in the 3Y-TZP grain boundaries occurs below 600 °C increases the grain boundary diffusivity and consequently promotes sintering in the initial and intermediate stages to a very large extent. The formation of $Y_2Cu_2O_5$ at 800 - 950 °C strongly inhibits sintering.

Influences of the reactions on sintering, both beneficial and detrimental ones, are dependent on the CuO content as well as the CuO particle size. By choosing proper content (1.6 mol%) and particle size (20 nm) of added CuO powder, sintering of CuO doped 3Y-TZP nano-powder composite is optimised. The optimal material can be fully densified by just heating to 1000 °C at 15 °C·min^{-1} in oxygen.

References

1. Garvie, R.C., Hannink, R. H. J. and Pascoe, R. T., "Ceramic Steel", *Nature*, 1975, **258,** 703-704.

2. Garvie, R.C., "Structural applications of ZrO_2-bearing materials", pp.465-479 in Advances in Ceramics, vol.12: *Science and Technology of Zirconia II*, ed. by Claussen N., Ruhle M., and Heuer A.H., The American Ceramic Society, Columbus, Ohio, 1984.

3. Wakai, F., Sakaguchi, S. and Matsuno, Y., "Superplasticity of Yttria-Stabilized Tetragonal ZrO_2 Polycrystals", *Adv. Ceram. Mat.*, 1986, **1,** 259-263.

4. Kerkwijk, B., García, M., van Zyl, W. E., Winnubst, L., Mulder, E. J., Schipper, D. J. and Verweij, H., "Friction behaviour of solid oxide lubricants as second phase in α-Al_2O_3 and stabilised ZrO_2 composites", *Wear*, 2004, **256**[1-2], 182-189.

5. Pasaribu, H.R., Sloetjes, J.W. and Schipper, D.J., "Friction reduction by adding copper oxide into alumina and zirconia ceramics", *Wear*, 2003, **255**[1-6], 699-707.

6. Raj, R., "Analysis on the sintering pressure", *J. Am. Ceram. Soc.*, 1987, **70**[9], C-210-C-211

7. Groza, J.R., "Nanosintering", *NanoStructured Materials*, 1999, **12**, 987-992.

8. Mayo, M., "Processing of nanocrystalline ceramics from ultrafine particles", *Int. Mater. Rev.*, 1996, **41**, 85-115.

9. Ran, S., Winnubst, A.J.A., Wiratha, W. and Blank, D.H.A., "Sintering behavior of 0.8 mol%-CuO-doped 3Y-TZP ceramics", *J. Am. Ceram. Soc.*, 2006, **89**[1], 151-155.

10. Theunissen, G.S.A.M., "Microstructure, fracture toughness and strength of (ultra)fine-grained tetragonal zirconia ceramics", PhD Thesis, University of Twente, The Netherlands, 1991.

11. Sagel-Ransijn, C.D., "Nanostructured zirconia ceramics by gel-precipitation, processing, microstructure and mechanical properties", PhD Thesis, University of Twente, The Netherlands, 1996.

12. Mayo, M.J., Seidensticker, J.R., Hauge, D.C. and Carim, A.H., "Surface chemistry effects on the processing and superplastic properties of nanocrystalline oxide ceramics", *Nanostructured Mater.*, 1999, **11**[2], pp. 271-282.

13. Dongare, M.K, Dongare, A.M., Tare, V.B., Kemnitz, E., "Synthesis and characterization of copper-stabilized zirconia as an anode material for SOFC", *Solid State Ionics*, 2002, **152-153**, 455-462.

14. Ran, S., Winnubst, A.J.A., Wiratha, W. and Blank, D.H.A., "Synthesis, sintering and microstructure of 3Y-TZP/CuO nano-powder composites", *J. Eur. Ceram. Soc.*, 2006, **26,** 391-396.

15. Raming, T.P., Winnubst, A.J.A., van Zyl, W.E. and Verweij, H., "Densification of zirconia-hematite nanopowders", *J. Eur. Ceram. Soc.*, 2003, **23**[7], p. 1053-1560.

16. Luo, X-M., Wu, P., Kershaw, R., Dwight, K. and Wold, A., "Preparation and characterization of members of the systems Cu(II)/MgO and Cu(II)/ZrO_2", *Mat. Res. Bull.*, 1988, **23**, 1719-1925.

17. Seidensticker, J.R. and Mayo, M.J., "Thermal analysis of 3-mol%-yttria-stabilized tetragonal zirconia powder doped with copper oxide", *J. Am. Ceram. Soc.*, 1996, **79**[2], 401-406.

Chapter 6

Microstructure evolution of CuO doped 3Y-TZP nano-powder composites during sintering

Abstract

Microstructure evolution during sintering of CuO doped 3Y-TZP nano-powder composites was extensively investigated by using SEM, TEM, EDX and high-temperature XRD. These microstructural changes were interpreted on the basis of reactions occurring while sintering. It is revealed that strong growth in the final sintering stage at 1130 °C is caused by the presence of CuO. If sintering procedure is well controlled, a dense 8 mol% CuO doped 3Y-TZP ceramic with an average grain size of 120 nm can be obtained. The formation of $Y_2Cu_2O_5$ at around 850 °C as a result of the reaction between CuO and yttria as segregated to the 3Y-YZP grain boundaries leads to a t-m zirconia phase transformation during heating. As a consequence 80 vol% of monoclinic zirconia is present in the sintered nano-powder composite when the final sintering temperature is reached and remained after cooling. A strong CuO enrichment on the sample surface was observed for the CuO doped 3Y-TZP nano-powder composites sintered at 1130 °C. This surface enrichment of CuO results from migration of CuO solutes in the 3Y-TZP grains caused by the decrease in CuO solubility associated with grain growth.

6.1 Introduction

Microstructural characteristics of ceramics, such as phase composition, grain size, defects, impurity distribution etc., are of great importance for the final properties of the products. In tetragonal zirconia polycrystals (TZP) a combination of high strength and toughness can be achieved when the microstructure is finely tuned so that the tetragonal zirconia phase is retained at room temperature and only transforms to the monoclinic structure when an external load is applied [1-7]. These excellent mechanical properties are related to a stress-introduced martensitic transformation of the metastable tetragonal to the monoclinic phase [2-5]. This improvement in toughness is called phase-transformation toughening. As will be discussed in the following sections, the retention of tetragonal zirconia phase is not only influenced by chemical composition, but also other microstructural features including matrix constraint, grain size and grain boundary characteristics.

The grain size of ceramics significantly affects the final properties. Winnubst et al. [8] reported that the fracture energy of yttria stabilised zirconia exhibits a Hall-Petch relationship with grain size when fracture of the material takes place mainly in a trans-granular manner. It was found by He [9] et al. that the wear resistance of Y-TZP ceramics also shows a Hall-Petch relationship at an average grain size $d < 0.7$ μm. When $d > 0.9$ μm, the wear resistance of Y-TZP ceramics is proportional to the reciprocal of the average grain size. More interestingly, some special properties of ceramics can be obtained by controlling of the grain size. It was shown that a high superplastic deforming rate can be

achieved by using ultra-fine grained Y-TZP, which opens the opportunities of ceramic near-net shaping techniques for industrial applications [10, 11].

The presence and distribution of impurities in ceramics also strongly affects its properties. Adding small amounts of CuO or Al_2O_3 to fine-grained 3Y-TZP systems while forming an impurity-rich grain boundary layer significantly enhances superplastic deformation rates [12-14]. However, the presence of a relatively thick grain boundary layer can easily result in the formation of cracks at grain boundaries and provides a faster crack propagation, which means a decrease in strength and toughness of the material [15].

The objective of this chapter is to investigate the microstructure evolution of CuO doped 3Y-TZP nano-powder composites during sintering, including impurity segregation, crystal structure development and grain growth. The observation of the microstructure evolution will be interpreted on the basis of reactions, which occur during sintering as revealed in chapter 4 of this thesis.

6.2 Theory of crystal structure development in zirconia

Zirconia can exist in three well-defined crystal structures: monoclinic (m), tetragonal (t) and cubic (c), depending on dopant concentration, crystallite size, temperature and other parameters. For pure zirconia, the monoclinic structure is thermodynamically stable at room temperature and transforms to the tetragonal structure at 1170 °C. Tetragonal zirconia can be kept (meta)stable to room temperature by a combination of adding stabilisers such as CeO_2 and Y_2O_3, fine tuning the microstructure and applying matrix strain. The dependence of tetragonal zirconia's stability on factors such as dopant concentration, grain size and matrix strain can be well understood by analysing the free energy change ($\Delta G_{t \to m}$) of the t-m phase transformation on cooling through the transformation temperature, which is given by [16]:

$$\Delta G_{t \to m} = (G_c^m - G_c^t) + (G_{se}^m - G_{se}^t) + (G_s^m - G_s^t) \qquad \text{(Eq. 6.1)}$$

where G_c is the chemical free energy, G_{se} is the (dilatational) strain free energy and G_s is the surface free energy. The superscripts m and t denote the monoclinic and tetragonal phase, respectively. The metastable tetragonal zirconia structure can only exist when $\Delta G_{t \to m}$ is kept positive (>0). At room temperature the first term on the right hand side of the equation 6.1 is always negative due to the chemical nature of the m and t structure. However the adding dopants like Ce or Y in zirconia lattice to form a solid solution can make this term less negative.

The second term on the right hand side of equation 6.1 is also negative while no extra stress is applied.

According to strain energy analysis [16], in the presence of a tensile stress $(G_{se}^m - G_{se}^t)$ gives a negative value, which makes the tetragonal less stable. In contrary a compressive stress applied on the grains increases tetragonal zirconia tetragonal stability. This explains why zirconia grains constrained by a stiff alumina matrix can be better stabilised in the tetragonal structure. Moreover, this relationship between stress and phase transformation offers an origin of the phase transformation toughening mechanism of tetragonal zirconia based ceramic materials.

The third term on the right hand side of equation 6.1 plays a very important role to the stability of the tetragonal zirconia structure at room temperature. Without strain contribution tetragonal structure can only exist while the third term is positive and larger than the sum of the first two terms. This term can be written as:

$$G_s^m - G_s^t = \frac{6(\gamma^m - g^s \gamma^t)}{D} \qquad\qquad (Eq.6.2)$$

$$g^s = \frac{A^t}{A^m} \qquad\qquad (Eq.6.3)$$

where γ^m and γ^t are the specific interfacial surface energy of tetragonal and monoclinic phase (i.e. the interfacial surface energy before and after transformation), D is the grain size, A^t and A^m are interface surface areas of tetragonal and monoclinic zirconia (before and after transformation, $g^s <1$). It has been shown that the specific surface energy of monoclinic zirconia is larger than that of tetragonal zirconia ($\gamma^m > \gamma^t$) [17]. Therefore a larger molar surface area or, in other words, a smaller size of zirconia grains gives large positive value of the third term. Many researches have proven that tetragonal zirconia structure can be obtained at room temperature while the grain size is smaller than a critical value (D_c), which varies from 0.3 to 0.8 μm depending on dopants and stain conditions [16].

For the materials studied in this thesis, i.e. CuO doped 3Y-TZP nano-powder composites, all the factors as given in equation 6.1 must be taken into account. In summary, the tetragonal zirconia structure can be destabilised by reduction of yttria content in zirconia grains, changes in surface and grain-boundary free energy and the applied tensile stresses.

6.3 Theory of grain growth

In general grain growth is mainly dominated by grain-boundary migration. In that case the grain growth rate $d\overline{D}/dt$ is directly proportional to the instantaneous average grain boundary migration rate $\overline{u}_b$ [18]:

$$d\overline{D}/dt \propto \overline{u}_b \qquad\qquad (Eq.\ 6.4)$$

with $\overline{D}$ the average grain size. The term $\overline{u}_b$ can, in turn, be represented in terms of a force-mobility product:

$$\overline{u}_b = M_b \cdot F \qquad\qquad (Eq.\ 6.5)$$

where F is the net driving force of grain-boundary migration, and M_b is an assembly of all factors arising from the mechanism of migration of matter. For ceramics F is most commonly derived from the pressure gradient, ΔP, across the boundary arising from its curvature:

$$\Delta P = 2\gamma(\frac{1}{r_1} + \frac{1}{r_2}) \qquad\qquad (Eq.\ 6.6)$$

where γ is the grain boundary energy and r_1 and r_2 are the two radii of curvature of the boundary surface (for a spherical particle $r_1 = r_2$).

From these general equations one can simply conclude that the grains with smaller size (which means smaller boundary curvature radius) and higher grain boundary energy (γ) have higher driving force for grain growth.

This relative simple model can however not be used for most practical cases. Grain growth is actually a very complicated phenomenon, especially when solutes or impurities are present. Several mechanisms of grain-growth control have been suggested in literature.

Lee et al. [19] proposed a grain-growth model based on intrinsic properties such as grain boundary energy and diffusion coefficients which affect ΔP and $\bar{u}_b$. It was revealed by dihedral angle measurements that the grain-boundary energy of cubic zirconia is 1.6 times larger than that of tetragonal zirconia. This difference in grain boundary energy can partly explain the faster grain growth rate of cubic zirconia than that of tetragonal zirconia.

Another mechanism for grain growth control was reported based on the concept of solution drag, called the impurity-drag mechanism [20]. The drag effect arises from any preferred segregation of an impurity (solute) to the grain boundary area, which means the impurities can find energetically favourite sites in the grain boundary. The breaking of grain boundary from this impurity cloud results in an increase in free energy of the system. Thus the grain boundary tends to drag the cloud of impurities along with it and this will retard grain growth. It has been well proven by Theunissen [21,22] and Sagel-Ransijn [23] that grain growth in yttria doped zirconia system is significantly determined by impurity drag. However the impurity drag mechanism is not always applicable for every cation-doped zirconia system. Grain growth analysis on various cation doped zirconia, as carried out by Allemann et al. [24], showed that the size, valence and amounts of the cation dopants significantly affects on grain growth. When the added cations are smaller than Zr^{4+} the grain growth is strongly enhanced instead of inhibited.

A third mechanism of grain growth control is the mechanism of phase partitioning as proposed by Lange [25]. Phase partitioning can be described as a phenomena where an originally (metastable) single phase structure develops into a more stable multiphase structure during sintering. Lange observed that only slow grain growth occurred within the apparent two phase (tetragonal + cubic) region of the ZrO_2 rich part of the ZrO_2-Y_2O_3 binary system. This phenomenon was explained on the basis of the difference in lattice parameters of adjoining grains, which will produce strain energy and therefore inhibit the grain growth.

It is important to point out that the dominant mechanism of grain growth in a ceramic can alter in different sintering stages. Boutz et al. [26] observed that the grain growth of a porous system (porosity >35%) is limited by surface diffusion. It was also reported by Brook [18] that even a small amount of porosity can influence grain growth kinetics.

6.4 Theory of impurity segregation

Segregation of impurities ions to grain boundaries or surfaces is a common phenomenon observed at high temperature, especially when the amount of impurity is above its solubility in matrix. As discovered by Winnubst [27,28] solutes such as yttrium and cerium in zirconia grains tends to segregate to grain boundaries to form a thin (~2nm) solute-enriched grain boundary layer at temperatures above 850 °C. Mechanisms of segregation has been briefly summarised by Burggraaf and Winnubst [29]. Driving forces for dopant segregation can arise from 1) surface tension differences and (surface) interaction effects; 2) Strain energy (relaxation); 3) electrostatic potential and charge compensation and 4) Spread in Madelung potentials.

6.5 Experimental procedure

6.5.1 Sample preparation

Nanocrystalline 3Y-TZP (CP) and CuO powders were prepared by means of co-precipitation and oxalate precipitation respectively as described in Chapter 3. CuO powders with several equivalent BET-spherical diameter of 20, 50 and 360 nm were used, respectively denoted as CuO-20, CuO-50 and CuO-360. Composites of CP 3Y-TZP doped with 0.8, 1.6, 3.2 or 8 mol% of CuO were prepared by ball-milling the powders in ethanol using zirconia balls as milling mediate. The milled suspension was ultrasonically dispersed for 5 min and oven-dried at 100 ºC for 24 hours. After grinding and sieving, the composite powders were pressed into cylindrical green compacts by isostatic pressing at 400 MPa for 5 min.

All compacts were sintered in a Netzsch dilatometer at 1130 °C for 1 hour at a heating rate of 15 ºC·min^{-1} and a cooling rate of 2 ºC·min^{-1}. Also one 8 mol% CuO-50 doped CP 3Y-TZP sample was sintered at 960 °C for 20 hours with a heating rate of 20 ºC·min^{-1} (denoted as CP8C50-2). Oxygen flow was introduced into the dilatometer while sintering. The densification behaviours of these materials are discussed in chapter 5 of this thesis.

The compacts (0.8 mol% CuO doped) used for non-isothermal grain growth study were heated at 5 ºC·min^{-1} to a certain temperature (750, 850, 950, or 1050 ºC) in a room furnace. Once the temperature was reached, the sample was taken out of the furnace immediately and quenched in air to room temperature. It is assumed that the grain size does not change during this quenching process.

6.5.2 Microstructure and elemental distribution analysis

Scanning electron microscopy (SEM, Thermo NORAN Instruments) and transmission electron microscopy (TEM, CM30 Twin/STEM, Philips) were used for microstructure analysis. Energy depressive X-ray analysers (EDX, Thermo Noran), attached to SEM and TEM were used for elemental distribution analysis.

SEM analysis on the fully sintered samples was carried out on polished cross-sections. Prior to SEM experiments the samples sintered at 1130 °C were thermally etched at 1000 ºC for 0.5 hour. For the CP8C50-2 sample sintered at 960 °C the thermal etching was carried out at 850 °C for 1 hour. Average grain size was determined by the linear intercept technique based on the SEM images of the polished and thermally etched surfaces by using the Mendelson's line intercept technique [30]:

$$D = 1.56L \qquad\qquad\text{(Eq. 6.7)}$$

where L is the average linear intercept.

For the non-isothermally sintered samples for grain growth study, SEM image on the fractured surfaces were taken. The Mendelson's method for average grain size calculation is not fully applicable for the fractured surfaces. The grain size of the non-isothermally sintered samples was roughly estimated by observation of the SEM images.

6.5.3 Zirconia phase analysis

Slices of 3Y-TZP and 8 mol% CuO-50 doped CP 3Y-TZP composites with dimensions of 10×8×0.5 mm were prepared by isostatic pressing at 400 MPa followed by careful polishing with sand papers

(silicon carbide paper, P# 1000). These slices were used for X-ray diffraction (XRD, X'Pert_MPD, PANalytical) analysis at various temperatures in order to investigate possible zirconia phase changes during sintering. During the XRD experiments, the samples were heated at 5 °C·min^{-1}. The slices were held at each measuring temperature for 15 minutes before measurement started. The volume fraction of monoclinic zirconia phase (V_m) was calculated based on the peak intensities of $M[111]$, $M[\bar{1}11]$ and $T[111]$ XRD signals using the relationship as proposed by Toraya et al. [31]:

$$V_m = \frac{1.311 X_m}{1 + 0.311 X_m}$$
(Eq. 6.8)

$$X_m = \frac{I_m(\bar{1}11) + I_m(111)}{I_m(\bar{1}11) + I_m(111) + I_t(111)}$$
(Eq. 6.9)

with I is the XRD peak intensity and where the subscripts m and t represent the monoclinic and tetragonal phases respectively. In this study presence of cubic zirconia phase was not taken into account.

6.6 Results and discussion

6.6.1 General Microstrcutural feature

Fig. 6.1 shows SEM images of polished and thermally etched surfaces of undoped CP 3Y-TZP, which was sintered at 1150 °C for 2 hours, and 0, 0.8 and 8 mol% of CuO-50 (50 nm CuO particles) doped
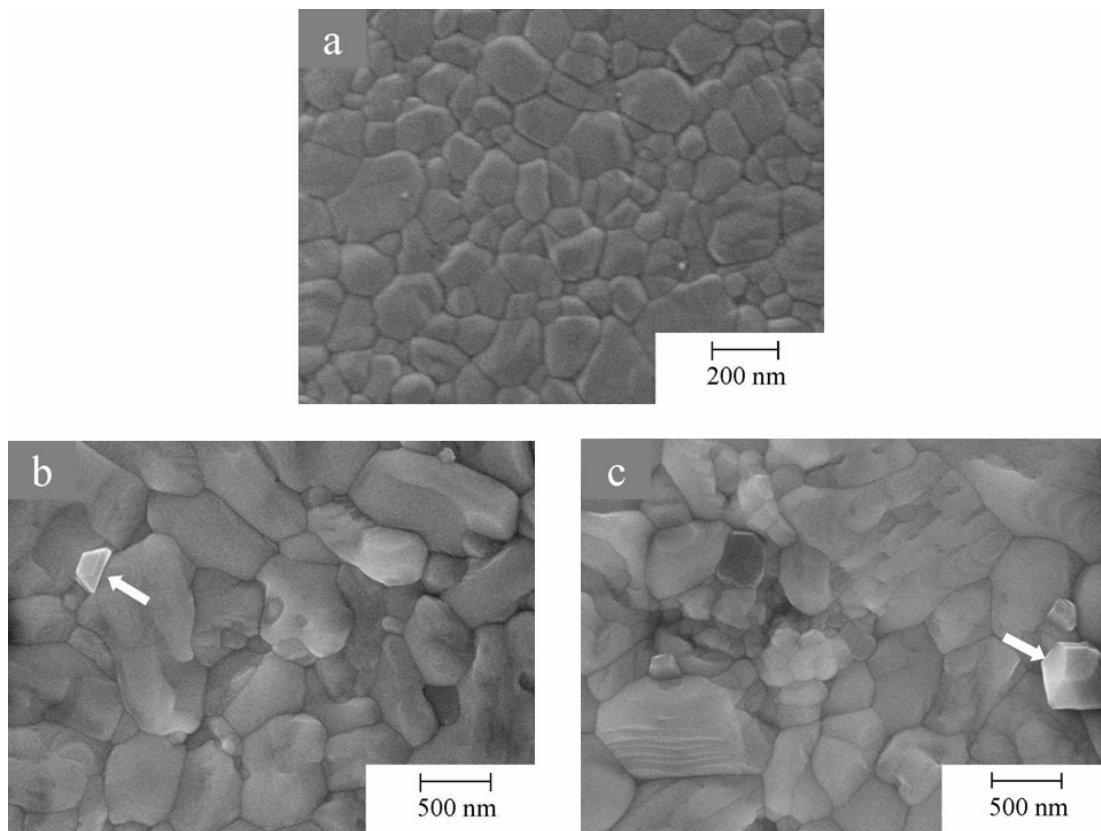

Fig. 6.1 Cross-section SEM images of (a) undoped CP sintered at 1150 °C for 2 hours; (b) CP0.8C50 and (c) CP8C50 sintered at 1130 °C for 1 hour in oxygen.

CP 3Y-TZP after sintering at 1130 °C for 1 hour. All these samples show a dense structure. However, whereas the fact that the undoped 3Y-TZP exhibits a uniform microstructure containing grains with an average size of 150nm, the CuO doped samples, no matter how much CuO added, possess a very non-uniform microstructure showing very large irregularly shaped grains up to several µm surrounded by much smaller grains with a size of around 200 nm. With increasing CuO content, the amount of large grains increases. The CuO-20 doped 3Y-TZP samples show the same microstructural feature. Obviously a strong grain growth during sintering was introduced by the addition of CuO nano-powders. On the detected cross-sections of CuO doped 3Y-TZP samples several brighter faceted grains (as pointed by white arrows in Figs. 6.1-b and -c) can be found. EDX analysis reveals that these well crystallised particles almost only consist of CuO. These surface CuO grains are probably formed by segregation of CuO to the surface as will be discussed in later section.

Fig. 6.2 shows a TEM image of the sintered 8 mol% CuO-50 doped 3Y-TZP composite. A non-uniform grain size distribution is shown again in this TEM image. It is also revealed that the grain boundaries are clean, meaning that no amorphous phase can be observed in the grain boundary region or triple junctions of the grains. This is in accordance with the absence of liquid phase during sintering (see the thermal analysis in chapter 4). An EDX mapping analysis combined with TEM was conducted to detect the elemental distribution in the bulk of the sample (see Fig. 6.3). As can be seen on the mapping images some small grains with diameter varying from 10 to 100 nm, as marked by white circles in Fig. 6.3-a, show a strong copper content. Seemingly these particles consist of almost pure CuO.
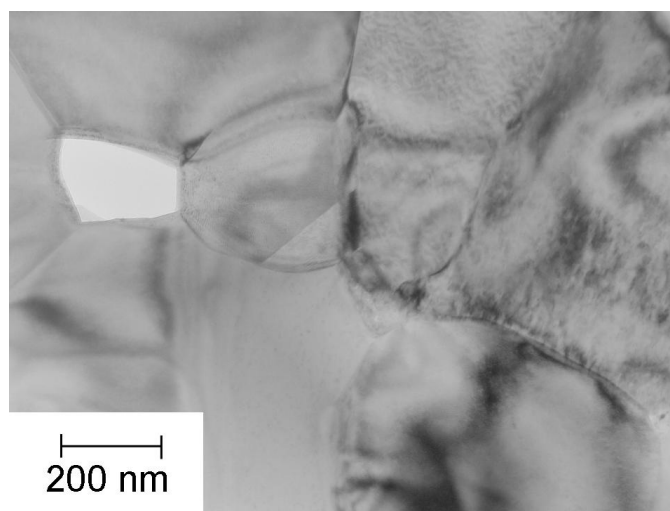
Fig. 6.2 TEM image of CP8C50 sintered at 1130 °C for 1 hour in oxygen.

As shown in chapter 5, the nano-composite of 3Y-TZP doped with 8 mol% CuO-50 (CP8C50) shows a very fast densification at a relatively low temperature (<900 °C). Based on this knowledge, we performed a sintering test of a CP8C50 composite at 960 °C for 20 hours, with a heating rate of 20 °C·min^{-1}. With this low maximum temperature plus long dwell sintering procedure the composite was densified to 96% in density (corrected for the presence of monoclinic zirconia). Figs. 6.4 and 6.5 show the SEM and TEM images of this material respectively. Interestingly the material exhibits a real nano-structured microstructure consisting of uniformly small grains with an average diameter of 120

nm (see Fig. 6.4). This result clearly shows that a dense CuO doped 3Y-TZP ceramic without significant grain growth is successfully obtained by well controlling the sintering procedure.

No bright faceted particle was observed in the SEM image of this CP8C50-2, indicating that segregation of CuO to the surface does not significantly take place at the (thermal) etching temperature (850 °C). Grain boundaries of the material are rather clean (see Fig. 6.5).
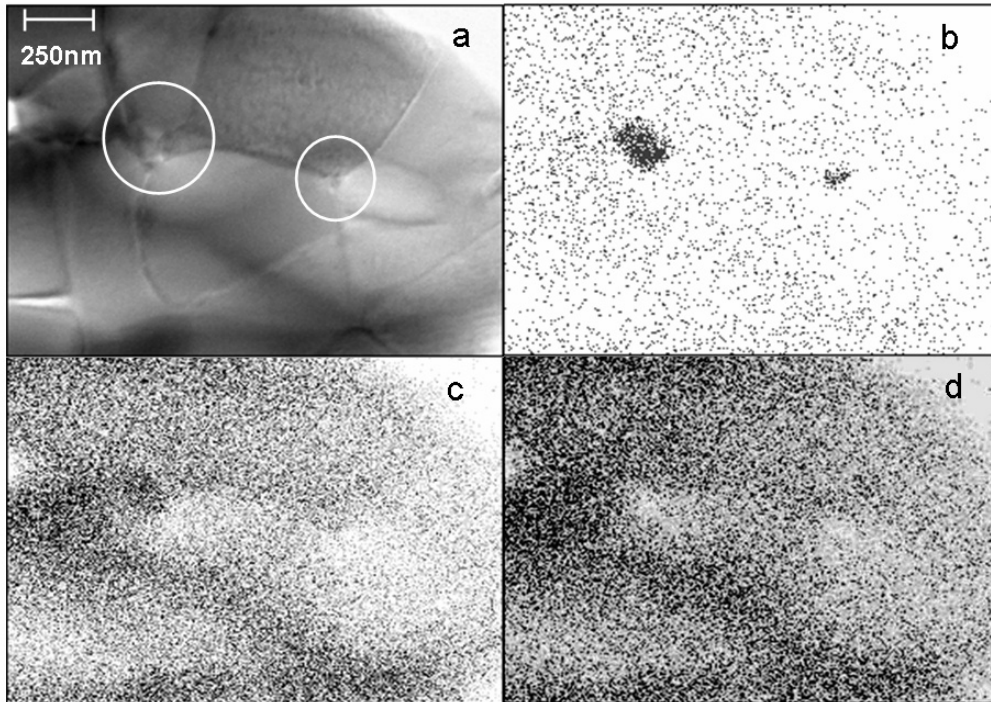
Fig. 6.3 EDX mapping CP8C50 sintered at 1130 °C for 1 hour in oxygen.

    a) TEM image of the EDX- mapped area;   b) Cu distribution

    c) Y distribution;   d) Zr distribution
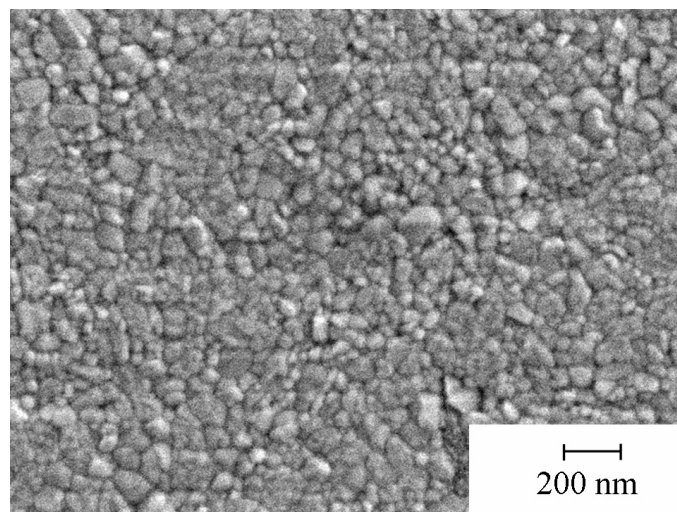
Fig. 6.4 SEM image of polished and thermally etched cross-section of CP8C50 sintered at 960 °C for 20 hours in oxygen.
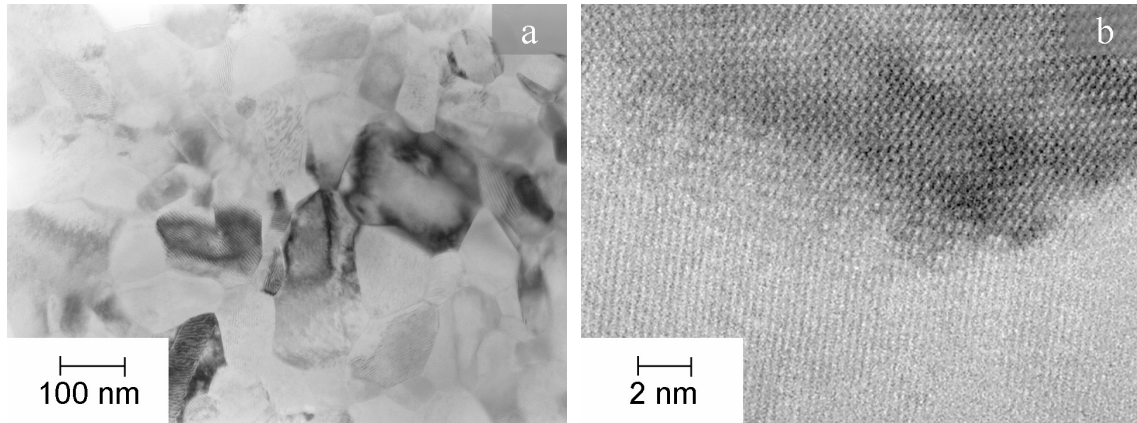
Fig. 6.5 TEM image of Cu8C50 sintered at 960 °C for 20 hours in oxygen.

a) lower magnification;   b) higher magnification

6.6.2 Grain growth during non-isothermal sintering

For a further investigation of microstructure evolution SEM analysis on fractured surfaces of 0.8 mol% CuO-20 doped 3Y-TZP (CP.8C20) samples quenched from various temperatures was conducted (see Fig. 6.6).
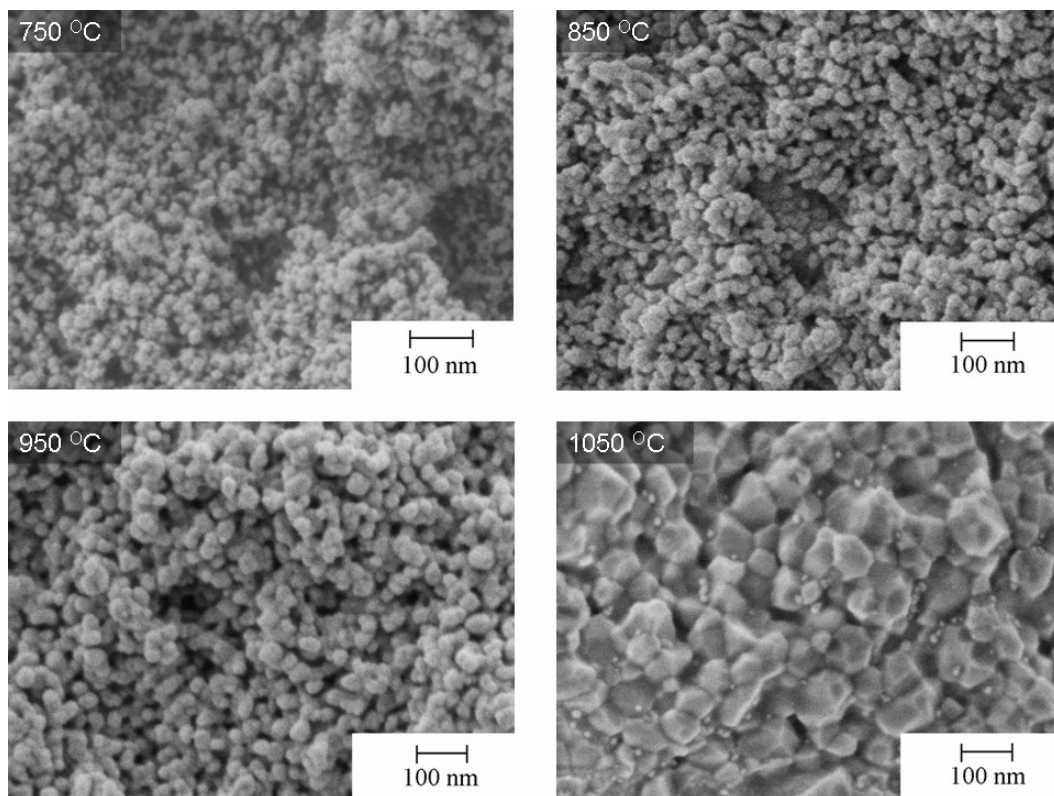
Fig. 6.6 SEM image of fractured surfaces of CP.8C20 composite sintered at various temperatures.

It can be seen in Fig. 6.6-a that the sample quenched from 750 °C shows a very porous structure consisting of aggregated rounded grains around 20 nm in diameter. When heated to 850 and 950 °C, the porosity of the sample significantly decreases and the aggregates get denser with the boundaries of the primary grains getting blurred (see Figs. 6.6-b and -c). This indicates that the sintering has entered the intermediate stage at 950 °C, which is in a good agreement with the dilatometer results as shown in chapter 5. The grain growth in this sintering stage is limited (average grain size is less than 40 nm). At 1050 °C the CP.8C20 sample shows a quite dense structure consisting faceted grains with an average size of around 100 nm (see Fig. 6.6-d), which is remarkably larger than that of the undoped 3Y-TZP sintered at the same temperature (50 nm, see [22]). During further sintering the grains grow very fast and reach a size of several micrometres after sintering at 1130 °C for 1 hour, whereas the undoped 3Y-TZP fully sintered at 1150 °C for 2 hours shows an average grain size of only 150 nm [22]. It is clearly revealed that the strong grain growth as introduced by addition of CuO mainly takes place in the final sintering stage, starting around 1050 °C.

As revealed in chapter 4 a Cu-rich grain boundary layer is formed in the 3Y-TZP matrix grains after heating at 600 °C or more. These Cu impurities in the grain boundaries do not result in the impurity drag effect for inhibiting growth of the 3Y-TZP grains. It is probably due to the smaller size of Cu^{2+} ion than that of the Zr^{4+} ion. This is in a good agreement with the Allemann's [24] model of impurity influence on grain growth. On the other hand, it was shown in chapter 5 that the CuO dissolution can strongly enhance the grain boundary diffusivity of the 3Y-TZP. This enhanced grain boundary diffusivity might increase the velocity of the grain boundary motion ($\overline{u}_b$ in equation 6.4) and so that lead to a further acceleration of grain growth in the final sintering stage.

6.6.3 Zirconia crystal structure evolution during sintering

Crystal structure of the sintered CuO doped CP 3Y-TZP nano-powder composites were analysed by XRD. All the samples used for XRD experiments were sintered to >93% dense (corrected for the presence of monoclinic zirconia). Because the zirconia phase transformation can be caused by external stresses, the XRD measurement was conducted on as-sintered sample surfaces. Fig. 6.7 shows the XRD patterns measurement on CP 3Y-TZP doped with 0~8 mol% of CuO-20.

Generally it can be seen in Fig. 6.7 that the undoped CP 3Y-TZP sample shows a pure tetragonal crystal structure after sintering. On the contrary all CuO doped 3Y-TZP samples show a large amount of monoclinic zirconia phase. The formation of monoclinic zirconia phase was also observed in the case of submicron 0.8 mol% CuO (Aldrich) doped 3Y-TZP (Tosoh) composites as shown in chapter 2. It is obvious that t-m phase transformation or, in another word, destabilisation of the tetragonal zirconia phase, is caused by addition of CuO during sintering. Besides the zirconia peaks, some other impurity peaks (at the 2θ remarked by the arrows on the top x axis in Fig. 6.7) can clearly be observed when the CuO content >1.6 mol%. These impurity peaks will be treated in the next section. In this section only the zirconia crystal structure is discussed.

Assuming the zirconia grains are randomly distributed on the measured surfaces, the volume fraction of monoclinic zirconia phase V_m in the samples can be calculated from the XRD peak intensities by using Toraya's method [31]. The calculated results for different CuO doped 3Y-TZP composites are listed in Table 6.1.
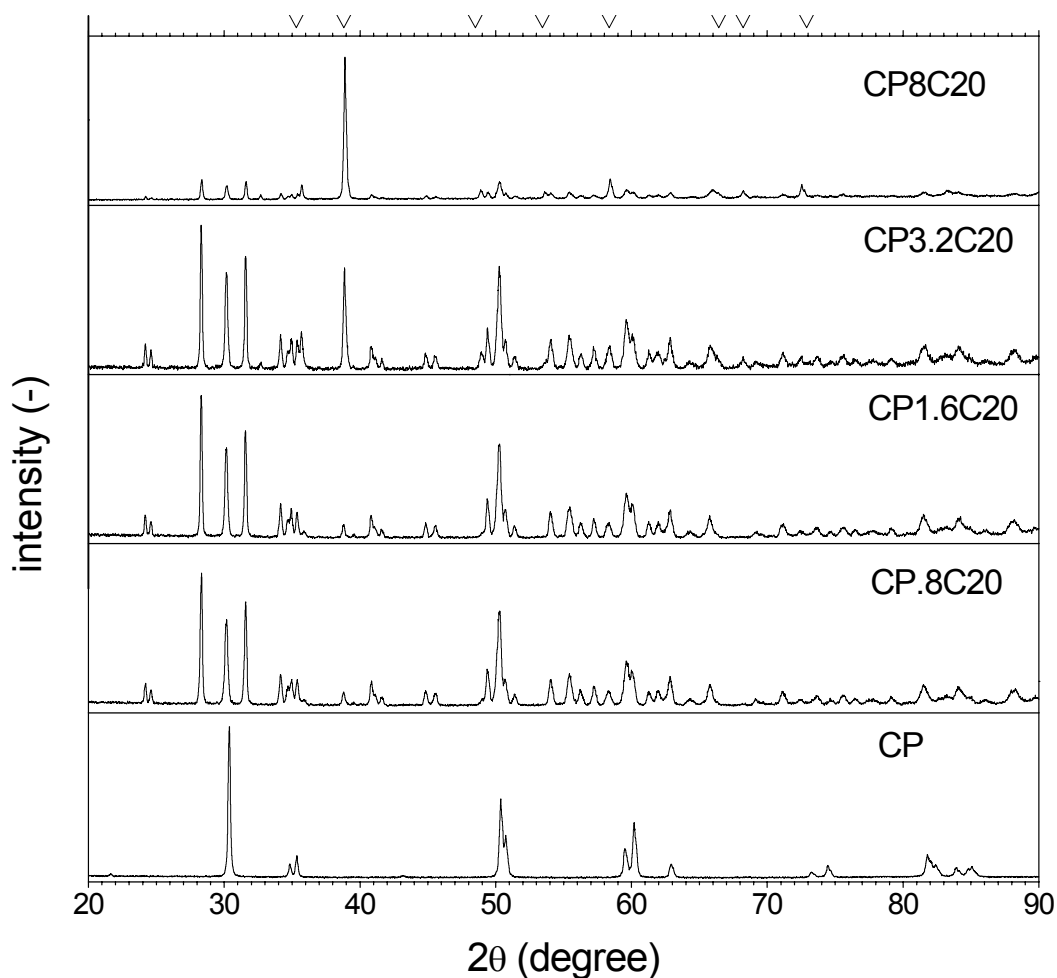
Fig. 6.7 XRD pattern of as-sintered surface of CP (sintered at 1150 °C for 2 hours) CP.8C20, Cp1.6C20, CP3.2C20 and CP8C20 (sintered at 1130 °C for 1 hour in oxygen). Arrows on the top x axis point out the position of CuO signals.

All CuO-doped samples as listed in Table 6.1 contain around 80 vol% of monoclinic zirconia phase after sintering. Only when 0.8 mol% of CuO with BET equivalent particle size of 50 and 360 nm is added, the amount of monoclinic zirconia is less. As indicated by the equation 6.2 tetragonal zirconia can be destabilised by growth of grain size. However the fact that two CuO-50 doped samples with extremely different grain size (several μm of CP8C50-1 compared with 120 nm of CP850-2) possess the same monoclinic zirconia content clearly indicates that the grain size effect does not account for the t-m zirconia phase transformation in the case of CuO doped 3Y-TZP nano-powder composites. It must be caused by the interaction between CuO and the 3Y-TZP grains. It was shown in chapter 4 that the contact area between CuO and the 3Y-TZP grains plays an important role in the reactions between CuO and 3Y-TZP. Lower CuO amount as well as larger CuO particle size result in a decrease in the contact area and therefore leads to less interaction between CuO and 3Y-TZP gains. Consequently the t-m phase transformation of zirconia can be less pronounced.

Table 6.1 Volume fraction of monoclinic zirconia phase in CuO doped 3Y-TZP composites

Sample ID	Type of CuO added	CuO content (mol%)	Sintering procedure*	Vm (%)
CP	-	0	15-1150×2h-2	0
CP.8C360	CuO-360	0.8	15-1130×1h-2	61
CP.8C50	CuO-50	0.8	15-1130×1h-2	68
CP.8C20	CuO-20	0.8	15-1130×1h-2	79
CP1.6C20	CuO-20	1.6	15-1130×1h-2	79
CP3.2C20	CuO-20	3.2	15-1130×1h-2	78
CP8C20	CuO-20	8	15-1130×1h-2	79
CP8C50-1	CuO-50	8	15-1130×1h-2	80
CP8C50-2	CuO-50	8	20-960×20h-2	79

*Sintering procedure is denoted as 'heating rate in °C·min^{-1}'-'maximum temperature in °C'×'dwell time in hours'-'cooling rate in °C·min^{-1}', e.g. "15-1130×1h-2" means the sample was sintered at 1130 °C for 1 hour at a heating and cooling rate of 15 and 2 °C·min^{-1}, respectively.

In order to figure out the zirconia crystal structure evolution process during sintering, high-temperature XRD analysis on a CP8C50 powder slice was carried out. In Fig. 6.8 the V_m as calculated by using Toraya's method is plotted as a function of temperature during heating. V_m of the undoped 3Y-TZP is also shown in Fig. 6.8 as a reference. Both CuO doped and undoped 3Y-TZP samples showed considerable amounts of monoclinic zirconia phase before heating started. This presence of monoclinic zirconia phase should be purely caused by the tensile stresses introduced by polishing. With increasing temperature the monoclinic zirconia phase was reduced in both cases due to

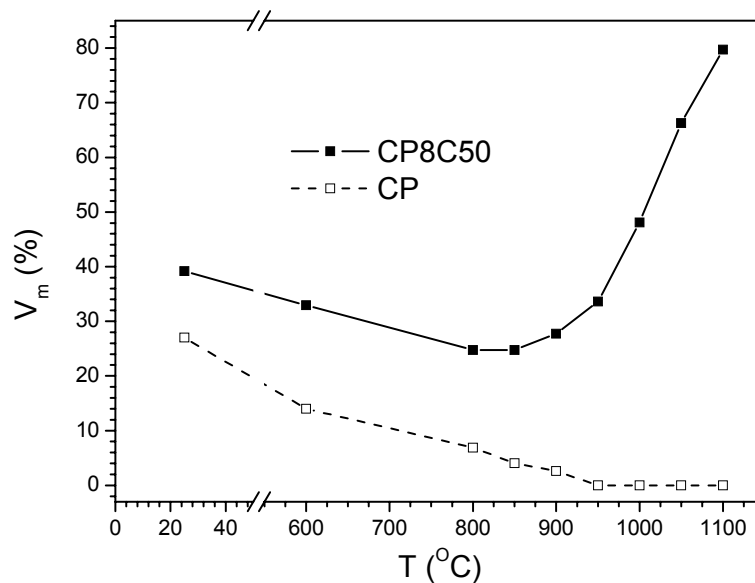Fig. 6.8 Volume fraction of monoclinic zirconia phase in CP8C50 as a function of temperature during heating.

relaxation of stresses. In the case of undoped CP 3Y-TZP the amount of monoclinic zirconia continuously decreases until it disappeared at around 950 °C, whereas, the V_m of the CuO doped 3Y-TZP composite started to increase at 850 °C. In the temperature range between 900 °C and 1100 °C the monoclinic zirconia increases drastically from 30 % to 80 %. During cooling the CuO-doped sample showed no further phase transformation, indicating that the zirconia phase transformation has been completed during heating process. This result is in excellent agreement with those in Table 6.1 (after cooling to room temperature the material contains 80 vol% monoclinic zirconia).

Tetragonal to monoclinic zirconia phase transformation introduced by addition of CuO was also observed by other researchers [32,33]. However in the literature reported before the t-m phase zirconia transformation is only recognised to occur during cooling. Lemaire et al. [32] attributed the t-m phase zirconia phase transformation to the depletion of yttria from the bulk of Y-TZP grains due to reaction between the added CuO and yttria as segregated to the grain boundaries, which forms a liquid phase during sintering. The depletion of yttria in the Y-TZP grains actually means the loss of tetragonal stabiliser and so that the first term in equation 6.1 turns to be more positive. Seidensticker et al. [34] also claimed the formation of an yttria-copper-oxide, which melted at around 1200 °C. Seemingly this observation supports Lemaire's conclusion. Hayakawa et al. [33] found that addition of $Y_2Cu_2O_5$ also leads to a formation of significant amounts (60 vol% for 1 mol% $Y_2Cu_2O_5$ doped) of monoclinic zirconia during cooling, while no extra $Y_2Cu_2O_5$ was formed during sintering. Thus depletion of yttria in the zirconia grains should not occur in this case. This result clearly is in disagreement with Lemaire's model. Hayakawa explained the t-m zirconia phase transformation by dissolution of copper in the 3Y-TZP matrix.

For the CP8C50 nano-powder composite, as studied in the present work, it has been clarified in chapter 4 of this thesis that the dissolution of CuO takes place < 600 °C and the formation of $Y_2Cu_2O_5$ at around 850 °C. The temperature of the latter reaction matches perfectly with the temperature at which the t-m phase transformation starts. So the destabilisation of tetragonal zirconia is likely to be attributed to the formation of $Y_2Cu_2O_5$ rather than the dissolution of CuO.

However Lemaire's [32] model, i.e. depletion of yttria from the 3Y-TZP grains associated with the formation of $Y_2Cu_2O_5$, seems not to be the proper explanation of the t-m zirconia phase transformation in our cases. Hayakawa has confirmed that addition of $Y_2Cu_2O_5$ can also results in formation of monoclinic zirconia phase. Additionally a CP.8C20 sample sintered at 1000 °C, which possesses an average grain size around 100 nm, shows a monoclinic zirconia content of 70 vol%. Assuming that all CuO has reacted with yttria of the 3Y-YZP matrix, in overall 2.6 mol% of yttria should still be in the Y-TZP matrix. This amount of yttria is sufficient to keep most of the Y-TZP grains in tetragonal phase [16].

The following explanation is proposed of t-m zirconia phase transformation as caused by the addition of CuO to Y-TZP. The presence of $Y_2Cu_2O_5$ as a thin layer covering the 3Y-TZP grains, which is formed by the reaction between CuO and yttria in our case, changes the specific interfacial energies (γ^t and γ^m in equation 6.2) of the 3Y-TZP, which makes the third term in equation 6.1 $(G_s^m - G_s^t)$ less positive. As a consequence the value of $\Delta G_{t \to m}$ decreases and the tetragonal zirconia phase is destabilised. This explanation fits the observation made by Lemaire and Hayakawa as well.

It is noticeable that Lemaire [32] and Hayakawa [33] observed a sudden t-m zirconia phase transformation during cooling of their submicron CuO doped 3Y-TZP systems. For the submicron 0.8 mol% CuO doped 3Y-TZP as studied in chapter 2, the sudden phase transformation during cooling was also observed, whereas, for the nano-powder composites as studied here this does not occur. This

discrepancy can be simply explained by the difference in sintering temperature. The submicron powder composites normally require higher sintering temperature (>1400 °C) for obtaining a dense ceramic. Because the tetragonal crystal structure becomes thermodynamically stable for zirconia at temperatures above 1200 °C, the submicron composites must exhibit a pure tetragonal structure after dwell at the maximum sintering temperature, although the tetragonal destabilisation mechanism as described above has occurred during heating. When the sample cooled to a certain temperature (often at 600 ~ 700 °C) the destabilised zirconia grains can no longer retain their metastable tetragonal structure and then transform to monoclinic phase. On the contrary the nano-powder composites studied here were sintered at temperatures ≤ 1130 °C, which is lower than the thermodynamically stable temperature for tetragonal zirconia. During heating all the destabilised zirconia grains have already transformed to monoclinic phase so that no extra t-m phase transformation occurs during cooling. This explanation is confirmed by another high-temperature XRD measurement of CP8C50 composite performed with a maximum temperature of 1250 °C, which shows a m-t zirconia phase transformation above 1200 °C during heating combined with a t-m transformation during cooling.

It is important to point out that the large stresses created by the sudden t-m phase transformation during cooling often results in microcracking, and in some cases, can even break the materials. This microcracking, as caused by a sudden phase transformation during cooling, was observed in the coarse-grained 0.8 mol% CuO doped 3Y-TZP system sintered in air, as described in chapter 2. For the nano-composites studied here the t-m phase transformation occurs only gradually during heating and the stresses created by the phase transformation can be released during the dwell period. The risk of microcracking or breaking arising from the t-m zirconia phase transformation is then avoided. Thus better mechanical properties of those materials can be expected.

6.6.4 Segregation of CuO to the sample surface

It has been shown by XRD that a impurity phase is present on the surfaces of the CuO doped 3Y-TZP nano-powder composites sintered at 1130 °C (see Fig. 6.8). A careful analysis of the XRD signals reveals that this phase is CuO with a highly preferred orientation as indicated by the strong intensity of the (111) reflection. The intensity of this Cu (111) peak significantly increases with increased CuO contents in the materials. However the polished surfaces of those samples do not give any CuO XRD peak. These results clearly indicate the segregation of an impurity phase to the sample surface. An EDX line-scanning from bulk to surface of a cut CP8C20 sample confirms the presence of Cu-rich layer of around 10 μm in thickness on the sample surface.

This enrichment of CuO on the sample surface shows a dependency on both starting powders and sintering temperatures. It can not be observed for the submicron powder composite of 3Y-TZP (Tosoh) doped with 8 mol% CuO (Aldrich) sintered at 1500 °C. The nano-powder composites sintered at temperatures below 1000 °C (CP8C50-1) does not show this surface CuO enrichment either.

This CuO enrichment of CuO is related to some reactions between CuO and the 3Y-TZP matrix. As revealed by XPS analysis a certain amount of CuO can be dissolved into the 3Y-TZP within a grain boundary layer of several nm when a nano-powder composite is sintered at 600 °C (see chapter 4). Assuming the CuO dissolution occurs only in the 3Y-TZP grain boundary region and the solubility of CuO in a unit volume of grain boundary layer is constant during the whole sintering process, then the overall solubility of CuO in the 3Y-TZP matrix strongly depend on the specific grain-boundary volume of the material system. This specific grain boundary volume is actually determined by the

grain size. For a nano-powder composite, for instance CP8C20, the size of 3Y-TZP grains is less than 20 nm when the dissolution of CuO occurs (<600 °C). This means a large volume of grain boundary region is available and a relatively high overall solubility of CuO in this sintering stage can be expected. However when the sample was sintered at 1130 °C the grain size has evolved to several micrometers (see Fig. 6.1). The overall CuO solubility in the 3Y-TZP matrix significantly reduces due to the decrease in grain boundary volume, and results in a "squeezing out" of CuO solutes from the 3Y-TZP matrix. These squeezed-out CuO migrates via grain boundary diffusion (which has been highly accelerated at high temperatures) to the sample surface to find energetically favourable locations and re-crystallise in a preferred orientation. As a consequence, a Cu-rich surface layer is formed for the nano-powder composites sintered at 1130 °C. This mechanism is confirmed by the absence of Cu-rich surface layer in the CP8C50-2 sample, in which no significant grain growth occurs during sintering.

As to the submicron powder composites, i.e. Tosoh 3Y-TZP doped with Aldrich CuO, the change in grain boundary volume during sintering is much less pronounced than the case of nano-powder composites. Additionally the dissolution of CuO during sintering is expected to occur in a much lower degree due to the smaller grain-boundary volume and contact area between CuO and the 3Y-TZP grains. No significant squeezing out of CuO is expected to take place in this case and so that Cu-rich surface layer was not formed.

6.7 Conclusions

Microstructure evolution of CuO doped 3Y-TZP nano-powder composites during sintering was extensively investigated. The microstructure evolution phenomena observed were interpreted on the basis of several reactions, which occur during sintering as revealed in chapter 4.

Strong grain growth of CP 3Y-TZP was introduced by addition of CuO when the composites sintered at 1130 °C. Dissolution of CuO in the 3Y-TZP grain boundaries accelerates the grain growth in the final stage. By sintering the material at 960 °C for 20 hours, a dense 3Y-TZP doped with 8 mol% CuO with an average grain size of 120 nm can be obtained.

Zirconia phase transformation from tetragonal to monoclinic in CuO doped 3Y-TZP composites during heating is caused by reactions between CuO and yttria as segregated to the 3Y-TZP grain boundaries at 850 °C, which results in the formation of $Y_2Cu_2O_5$. A large amount of monoclinic zirconia phase (80 vol%) is formed after sintering at 1130 °C for 1 hour. The formation of $Y_2Cu_2O_5$ occurs mainly in the 3Y-TZP grain boundary region and destabilises the tetragonal zirconia by affecting the specific interfacial energy. For the CuO doped 3Y-TZP nano-composites sintered below 1130 °C the t-m phase transformation occurs mainly during heating so that the risk of microcracking and fracture of the material is avoided.

A CuO-rich layer was observed on the sample surface for the CuO doped 3Y-TZP nano-powder composites sintered at 1130 °C. The formation of a CuO-rich surface layer is related to the CuO dissolution in the 3Y-TZP and grain growth during sintering. At low temperatures (< 600 °C) a large amount of CuO dissolves in the 3Y-TZP grain-boundary region. The overall CuO solubility significantly reduces with decrease in grain boundary volume, which is caused by strong grain growth in the final sintering stage. The "squeezed-out" CuO solute migrates to the sample surface and re-crystallise there with a highly preferred orientation and leads to the formation of CuO-rich surface layer.

References

1. Garvie, R.C., Hannink, R.H.J. and Pascoe, R.T., "Ceramic Steel", *Nature*, 1975, **258,** 703-704.

2. Rühle, M. and Evans, A.G., "High toughness ceramics and ceramic composites", *Prog. Mater. Sci.*, 1989, **33**[2], 85-167.

3. Heuer, A.H., "Transformation Toughening in ZrO_2-Containing Ceramics", *J. Am. Ceram. Soc.*, 1987, **70**[10] 689-98.

4. Evans, A.G. and Cannon, R.M., "Toughening of brittle solids by martensitic transformations", *Acta Metall.*, 1986, **5**, 761-800.

5. Evans, A.G., "Perspective on the development of high-toughness ceramics", *J. Am. Ceram. Soc.*, 1990, **73**[2], 187-206.

6. Basu, B., Vleugels, J., Van der Biest, O., "Toughness tailoring of yttria-doped zirconia ceramics", *Mat. Sci. Eng.*, **A380** (2004) 215-221.

7. Ruiz, L; Readey, M.J., "Effect of Heat Treatment on Grain Size, Phase Assemblage, and Mechanical Properties of 3 mol% Y-TZP", *J. Am. Ceram. Soc.*, 1996, **79**[9] 2331-40.

8. Winnubst, A.J.A., Keizer, K. and Burggraaf, A.J., "Mechanical properties and fracture behaviour of ZrO_2-Y_2O_3 ceramics", *J. Mar. Sci.*, 1983,**18**, 1958-1966.

9. He, Y., Winnubst, L., Burggraaf, A.J., "Grain-Size Dependence of Sliding Wear in Tetragonal Zirconia Polycrystals", *J. Am. Ceram. Soc.*, 1996, **79**[12], 3090-3096.

10. Wakai, F., Sakaguchi, S. and Matsuno, Y., "Superplasticity of Yttria-Stabilized Tetragonal ZrO_2 Polycrystals", *Adv. Ceram. Mat.*, 1986, **1,** 259-263.

11. Boutz, M.M.R., Winnubst, A.J.A., Burggraaf, A.J. and Carry, C.," Low temperature superplastic flow of yttria stabilized tetragonal zirconia polycrystals", *J. Eur. Cer. Soc.*, 1994, **11**, 103-111.

12. Hwang, C.M.J., and Chen, I-W., "Effect of a liquid phase on superplasticity of 2-mol%-Y_2O_3-stabilized tetragonal zirconia polycrystals",*J. Am. Ceram. Soc.*, 1990, **73**[6], 1626-1632.

13. Mayo, M.J., Seidensticker, J.R., Hauge, D.C. and Carim, A.H., "Surface chemistry effects on the processing and superplastic properties of nanocrystalline oxide ceramics", *Nanostructured Mater.*, 1999, **11**[2], pp. 271-282.

14. Sakka, Y., Suzuki, T.S., Morita, K., Nakano, K., Hiraga, K., "Colloidal processing and superplastic properties of zirconia- and alumina-based nanocomposites", *Scripta mater.*, 2001, **44**, 2075–2078.

15. Krell, A. and Blank, P., "Inherent reinforcement of ceramic microstructure by grain boundary engineering", *J. Eur. Ceram. Soc.*, 1992, **9,** 309-322.

16. Lange, F.F., "Transformation toughening: Part 1 Size effects associated with the thermodynamics of constrained transformations", *J. Mar. Sci.*, 1982, **17**, 225-234.

17. Garvie, R.C., "The occurrence of metastable tetragonal zirconia as a crystallite size effect", *J. Phy. Chem.*, 1965, **69**[4], 1238-1243.

18. Brook, R.J., "Controlled grain growth", pp. 331-364, in: Treatise of Materials Science and Technology, **Vol. 9**, edited by F.F.Y. Wang, Academic Press, New York, 1976.

19. Lee, I.G. and Chen, I.-W., "Sintering and grain growth in tetragonal and cubic zirconia", pp. 340-345 in: Sintering '87. Edited by Somiya et al., Elsevier applied science, London, 1987.

20. Lücke, K. and Detert, K., "A quantitative theory of grain-boundary motion and recrystallization in metals in the presence of impurities", *ACTA Metall.*, 1957, **5**, 628-637.

21. Theunissen, G.S.A.M., "Microstructure, fracture toughness and strength of (ultra)fine-grained tetragonal zirconia ceramics", PhD Thesis, University of Twente, The Netherlands, 1991.

22. Theunissen, G.S.A.M., Winnubst, A.J.A. and Burggraaf, A.J., "Sintering kinetics and microstructure development of nanoscale Y-TZP ceramics", *J. Eur. Cer. Soc.*, 1993, **11**, 315-324.

23. Sagel-Ransijn, C.D., "Nanostructured zirconia ceramics by gel-precipitation, processing, microstructure and mechanical properties", PhD Thesis, University of Twente, The Netherlands, 1996.

24. Allemann, J.A., Michel, B., Marki, H.-B., Gauckler, L.J. and Moser, E.M., "Grain Growth of Differently Doped Zirconia", *J. Eur. Cer. Soc.*, 1995, **15**, 951-958.

25. Lange, F.F., "Controlling grain growth", pp. 497-508 in: Ceramic microstructures '86: Role of interfaces, Materials Science Research Volume 21, Edited by J. A. Pask and A. G. Evans, Plenum Press, New York, 1987.

26. Boutz, M.M.R., "Nanostructured tetragonal zirconia ceramics, microstructure, sinter forging and superplasticity", PhD Thesis, University of Twente, The Netherlands, 1993

27. Winnubst, A.J.A., Kroot, P.J.M. and Burggraaf, A.J., "AES/STEM Grain Boundary Analysis of Stabilized Zirconia Ceramics", *J. Phys. Chem. Solids*, 1983, **10**, 955-960.

28. Theunissen, G.S.A.M., Winnubst, A.J.A. and Burggraaf, A.J., "Surface and grain boundary analysis of doped zirconia ceramics studied by AES and XPS", *J. Mar. Sci.*, 1992, **27**, 5057-5066.

29. Burggraaf, A.J., Winnubst, A.J.A., "Segregation in oxide surfaces, solid electrolytes and mixed conductors"; pp. 449-77 in: Surface and near surface chemistry of oxide materials. Edited by J. Nowotny and L.-C. Dufour, Elsevier Science Publishers B. V., Amsterdam, 1988.

30. Mendelson, M.I., "Average grain size in polycrystalline ceramics", *J. Am. Ceram. Soc.*, 1969, **52**, 443-446.

31. Toraya, H., Yoshimura, M. and Somiya, S., "Calibration Curve for Quantitative Analysis of the Monoclinic-Tetragonal ZrO_2 System by X-Ray Diffraction", *J. Am. Ceram. Soc.*, 1984, **67**[6] C119-C121.

32. Lemaire, L., Scholz, S.M., Bowen, P., Dutta, J., Hofmeister, H. and Hofmann, H., "Effect of CuO additives on the reversibility of zirconia crystalline phase transitions", *J. Mater. Sci.*, 1999, **34**, 2207-2215.

33. Hayakawa, M., Inoue, T., Pee, J.-H., Suematsu, H. and Yamauchi, H., "Liquid phase sintering of Y-TZP with CuO and $Y_2Cu_2O_5$ dopants", *Mater. Sci. Forum*, 1999, **304-306**, pp. 465-70.

34. Seidensticker, J.R. and Mayo, M.J., "Thermal analysis of 3-mol%-yttria-stabilized tetragonal zirconia powder doped with copper oxide", *J. Am. Ceram. Soc.*, 1996, **79**[2], 401-406.

Chapter 7

Spark Plasma Sintering of CuO doped 3Y-TZP nano ceramics

Abstract

A nano-powder composite of 3Y-TZP doped with 8 mol% CuO was processed by spark plasma sintering (SPS) technique. SPS is proven to be a very efficient method for densifying the nano-powder composite to a dense ceramic. A 96 % dense composite ceramic with an average grain size of 70 nm was obtained by applying the SPS process at 1100 °C and 100 MPa for 1 min. During the SPS process the reactions between CuO and 3Y-TZP were suppressed and the CuO phase was reduced to metallic Cu. One of the consequences is that the 3Y-TZP phase was remained almost purely tetragonal after the SPS process. Annealing after SPS process results in grain growth and tetragonal to monoclinic zirconia phase transformation. The grain size and monoclinic zirconia phase content are strongly dependent on the annealing temperature. By combining all the processing techniques studied in this work, including traditional pressureless sintering (as shown in chapter 5 and 6), SPS process and the following annealing, properties of the composite ceramic can be tuned via manipulation of microstructure. Tuning the mechanical properties of dense 8 mol% CuO doped 3Y-TZP composite ceramic by utilising different processing technique is shown as an example.

7.1 Introduction

CuO doped 3Y-TZP composite ceramics are of interest for advanced mechanical applications due to their special properties such as large superplasticity [1, 2] and low friction under dry sliding conditions [3, 4]. Good processing and microstructure control are important for the potential applications of this class of materials. It has been shown in chapter 5 that the sinterability of CuO doped 3Y-TZP nano-powder composites can be successfully optimised by means of choosing proper concentration and particle size of the CuO powder, when conventional pressureless sintering is used. In chapter 6 it was shown that a good grain size control of this composite material can be achieved by adjusting the sintering conditions. However, the formation of large amounts of monoclinic zirconia is proven to inevitably be caused by the reaction between CuO and 3Y-TZP during conventional sintering.

Spark plasma sintering (SPS) is a recently developed processing technique, also known as field assisted sintering technique (FAST) [5-8]. In stead of using an external heating source, the SPS employs a pulsed DC current passing through the electrically conducting pressure die and, in appropriate cases, also through the sample. This implies that the die itself acts as a heating source and that the sample is heated from both outside and inside [7, 8]. The SPS technique provides several engineering advantages, including very fast heating rate and short processing time, no need for additives or pre-compaction [6, 7]. These advantages give more possibilities to control the microstructure evolution during the sintering process and so to improve mechanical, electronic or optical properties of the materials [8-11].

Processing the CuO doped 3Y-TZP composite ceramic with some advanced techniques, such as SPS, other than traditional pressureless sintering, is very attractive. It is especially interesting to see the possibility to manipulate the microstructure more extensively and therefore to the properties of the material. This chapter describes the processing of nano powder composite of 3Y-TZP powder doped with 8 mol% CuO powder. Densification behaviour and microstructure evolution are presented. The dependence of microstructure on the SPS processing and the following annealing treatment is investigated. The possibility of tuning material properties by means of utilising various processing techniques is presented via an example of adjusting mechanical properties of the 8 mol% CuO doped 3Y-TZP ceramic.

7.2 Experimental procedure

7.2.1 Powder preparation

Nanocrystalline 3Y-TZP (CP) and CuO-50 powders were prepared by means of co-precipitation and oxalate precipitation respectively as described in Chapter 3. Composites of CP 3Y-TZP doped 8 mol% of CuO were prepared by ball-milling the powders in ethanol using zirconia balls as milling mediate. The milled suspension was ultrasonically dispersed for 5 min and then oven-dried at 100 °C for 24 hours. After grinding and sieving, the composite powders were ready for spark plasma sintering.

7.2.2 SPS processing

SPS experiments were performed on a FCT FAST device (Type HP D 25/1, FCT System, Rauenstein, Germany), which is an electronic field assistant furnace equipped with a 250 kN uniaxial-press. The power supply can provide a pulsed DC up to 8000 A at a voltage up to 10 V and the process chamber can be evacuated down to 0.05 Pa. Proper amount of CuO doped 3Y-TZP powder was placed in a graphite die with an inner diameter of 20 mm. The inner wall of the die and the surfaces of the lower and upper punches were protected from contamination by 1 mm thick graphite paper. Graphite protection plates were placed between the punches and the water cooled electrodes, which transfer electric current as well as pressure to the die set. During the SPS process, temperature program was generated by controlling the current cycles. The temperature was measured by a pyrometer with focus point at the bottom of the central borehole of the graphite set-up, 2.88 mm from the bottom of the upper punch and 5.125 mm from the centre of a 4.25 mm thick sample inside the die.

In the present work the CuO doped 3Y-TZP nano-powder composites were SPS processed with a maximum pressure of 100 MPa and a maximum temperature of 1000, 1050 and 1100 °C respectively denoted as SPS-1, SPS-2 and SPS-3 respectively. Each sintering cycle contains the following segments:

I) at a pressure of 16 MPa (a load of 5 kN), a constant DC current was applied until the central pyrometer reached its onset temperature (450 °C);

II) after a dwell at 450 °C for 1 min, the temperature was linearly increased to 850 °C at a heating rate of 400 °C·min^{-1};

III) dwell at 850 °C for 1 min while the pressure was increased linearly to 100 MPa;

IV) heating to the maximum sintering temperature at a rate of 100 °C·min^{-1}, The maximum temperature for the SPS-1, SPS-2 and SPS-3 specimens are 1000, 1050 and 1100 °C respectively;

V) dwell at the maximum temperature for a fixed time. The dwell time at the maximum temperature for the SPS-1, SPS-2 and SPS-3 specimens are 5 min, 3 min and 1 min respectively;

VI) unloading the pressure and current and free cooling down to room temperature of the die set.

During SPS processing, travel distance of the piston was recorded as a function of time. This piston travel distance (ΔL) relative to the piston position at the starting of the process represents the linear axial shrinkage, and therefore shows the densification behaviour of the specimen. After the SPS process, all specimens were polished with grinding papers to remove the outmost layers, which are contaminated with carbon.

7.2.3 Characterisation

The density was measured according the Archimedes method in mercury. Microstructural features of the materials were investigated by scanning electron microscopy (SEM, Thermo NORAN Instruments) analysis on the fractured surfaces. Transmission electron microscopy (TEM, CM30 Twin/STEM, Philips) was also used for microstructure characterisation of SPS-3 specimen. X-ray diffraction (X'pert_APD, PANalytical, using Cu-K$_{\alpha 1}$, λ =1.542 Å) was performed for phase analysis on cut and polished SPS-3 samples. One of the samples obtained a temperature treatment at 500 °C in air for 2h to release the residual surface stresses created by polishing. Data were collected in a 2θ range between 20 and 80 ° with a step size of 0.02°. The volume fraction of monoclinic zirconia phase is determined by Toraya's method [12].

The influence of annealing on grain size and zirconia crystal structure was performed on sample SPS-3. Specimen were cut and polished with diamond paste (3 μm grade) and annealed at 850, 900, 950, and 1000 °C, respectively, in an oxygen flow for 1 hour with a heating and a cooling rate of 15 and 2 °C·min^{-1} respectively. The annealed cuts were then analysed by XRD and SEM. Average grain size was determined by using the Mendelson's line intercept technique [13]. Elemental distribution was analysed by an Energy depressive X-ray analyser (EDX, Thermo Noran) attached to the SEM.

7.2.4 Mechanical test

Vickers hardness and fracture toughness were determined by means of indentation test (Indentation hardness tester, Model FV-700, Future-Tech Corp., Tokyo, Japan). The Vickers hardness, H_V, was measured at an indentation load of 98.1 N. Five indentations were made for each sample. The fracture toughness, K_{IC}, was obtained from the radial crack pattern of the indentations and calculated from the Shetty formula [14]:

$$K_{IC} = 0.089(H_V P / 4L)^{1/2}$$

where P is the load (98.1N), H_V is the Vickers hardness and L is the length of the crack initiated at the edge of the indent. It is important to point out that the fracture toughness data varies largely depending the determine technique and the formula for calculation. This Shetty formula is chosen because it was derived for the Palmqvist type crack (0.25 < L/a < 0.5, where a is the half diagonal of the Vickers indent) in ceramics [14-16], which is the case in our study. Nevertheless, the K_{IC} data determined by this method should only be used for comparison between the cases presented in this work.

7.3 Results and discussion

7.3.1 Densification during SPS process

The densification behaviour through segment II to V (see the experimental section) is shown in Fig. 7.1. A specimen with a relative density of 96% of the tetragonal zirconia system was obtained after SPS processing at 1100 °C under 100MPa for only 1 min (SPS-3). In this figure the piston position at dwell 450 °C (pressure = 16 MPa) is taken as a reference for the calculation of relative piston movement distance (ΔL). It can be seen in Fig. 7.1 that no significant densification is visible in segment II. Upon loading of pressure a large piston movement is achieved (segment III). In segment IV, when a pressure of 100 MPa has been achieved, the piston movement shows a linear dependence of temperature. During the dwell at 1100 °C (segment V) the densification saturates quickly within 20 seconds.
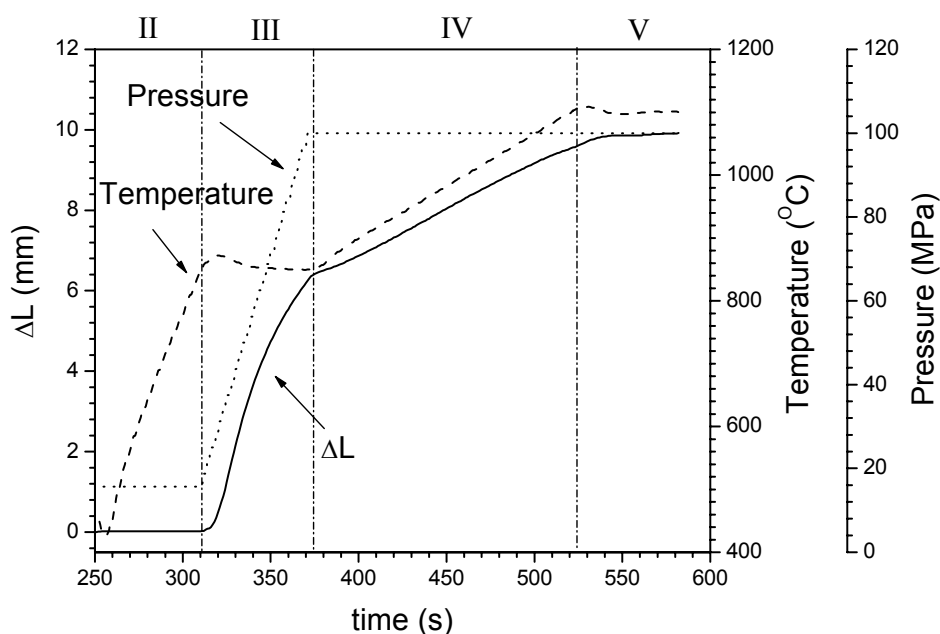
Fig. 7.1 Densification behaviour of CP8C50 powder composite of sample SPS-3.
Piston position at the start of segment II is set as starting point for piston movement distance calculation.

Table 7.1 shows the final density of SPS processed specimen with different maximum temperature and dwell time. Only 50 °C decrease in maximum temperature results in a significant lower density (final density reduces to 85% and 76% in cases of SPS-2 and SPS-1 respectively). Longer dwell time does not effectively compensate the reduction in densification due to the lower temperature.

On the basis of the densification behaviour as described above, SPS is proven to be a very efficient technique for producing a dense ceramic from the CuO doped 3Y-TZP nano composite powder (CP8C50). In the case of SPS-3 process, the specimen was fully densified within 4 min (assuming densification starts segment III). In the case of traditional pressureless sintering, it at least takes hours to obtain a fully dense CP8C50 ceramic (see chapter 5). Furthermore, the temperature sensitivity of the final density implies that the densification procedure under SPS conditions is highly temperature-driven.

Table 7.1 Density of 8 mol% doped 3Y-TZP nano-powder composites processed by SPS

Code	Max. T (°C)	Dwell Time (min)	ρ (%)
SPS-1	1000	5	76
SPS-2	1050	3	85
SPS-3	1100	1	96

7.3.2 Microstructure characterisation

Fig. 7.2 shows the microstructure of the fractured surfaces of the SPS processed CP8C50 ceramics with different maximum temperatures. The SPS-1 specimen (sintered at 1000 °C for 5 min) shows a porous structure consisting of aggregates of uniform small rounded grains with an average diameter of around 40 nm (see Fig. 7.2-a). Besides the small pores with a size of about 10 - 40 nm, several large irregular voids with a size up to 0.5 μm are present. A 50 °C increase in maximum temperature (i.e. SPS-2) not only results in a denser microstructure, but also in an almost disappearance of the large voids. No significant grain growth is observed if compared with the SPS-1 specimen. The SPS-3 specimen shows a very dense microstructure, which is in accordance with the high density as measured by Archimedes method. This material consists of uniform faceted grains with a slightly larger size than that of the SPS-1 and -2 samples. However, most of the grains in SPS-3 are still smaller than 100 nm, indicating only mild grain growth. Fig. 7.3 shows TEM images of the SPS-3
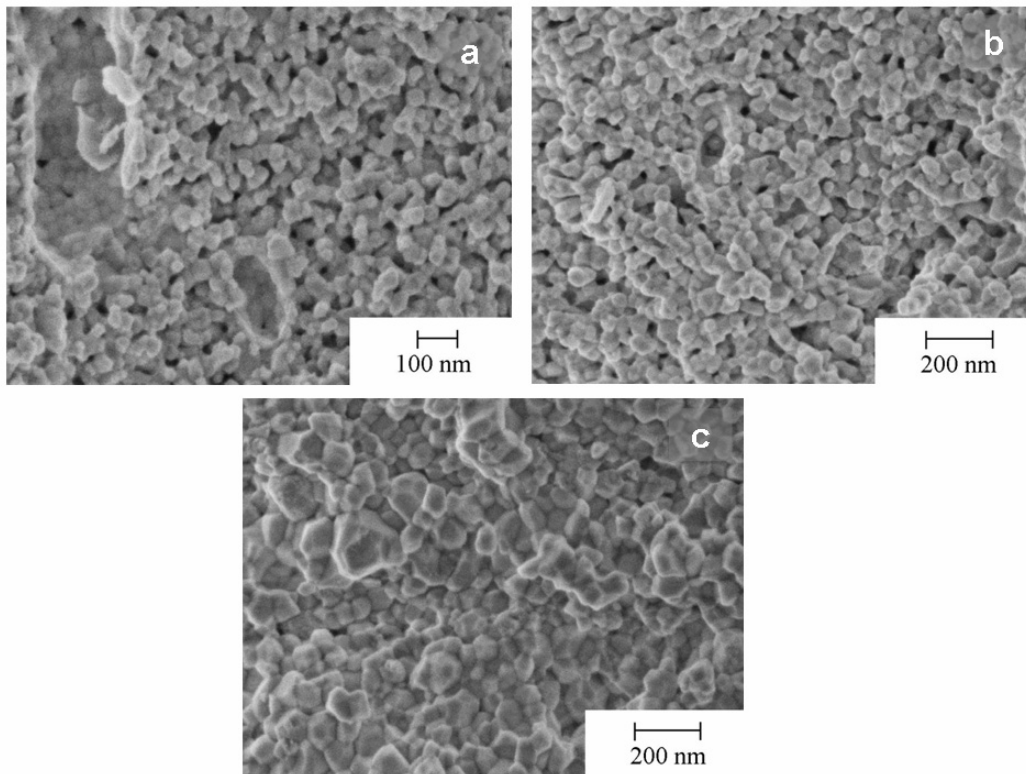

Fig. 7.2 SEM images of fractured surfaces of CP8C50 SPS processed at
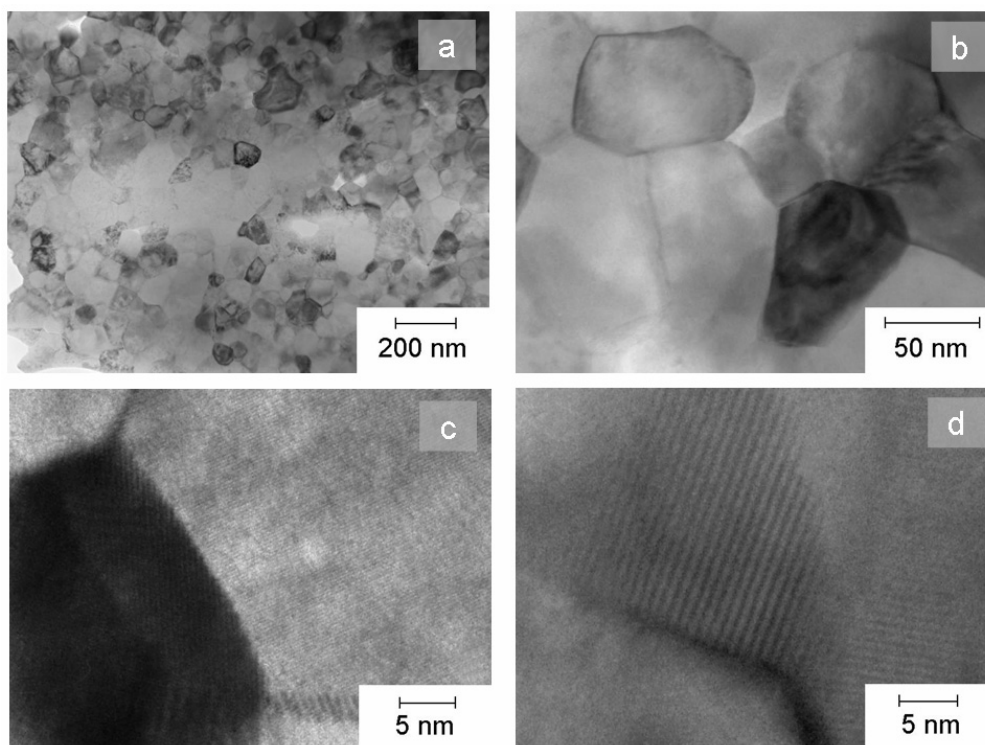a) 1000 °C (SPS-1); b) 1050 °C (SPS-2) and c) 1100 °C (SPS-3)

Fig. 7.3 TEM images of SPS-3 sample taken with different magnification

specimen. Again a dense microstructure consisting of uniform grains with a size of around 70 nm is revealed (see Figs. 7.2-a and -b). TEM images with higher magnification shows that the grain boundaries are clean and absent of any amorphous phase.

The microstructure characteristics as observed by the SEM pictures in Fig. 7.2 shed more light on the densification procedure of the CP8C50 nano-composite during SPS processing. The disappearance of the large voids (which are present in the SPS-1 specimen) after the SPS-2 process, without accompanying significant grain growth, suggests a fast rearrangement of grains in the temperature range of 1000 and 1050 °C. It is thus illustrated that in this temperature range under the applied pressure grain boundary sliding is strongly activated, and correspondingly grain rearrangement under the high external pressure (100 MPa) gives the most important contribution to densification. The mild grain growth between 1050 and 1100 °C (see Figs. 7.2-b and -c) indicates another mechanism of densification, i.e. grain boundary diffusion, as is activated in this temperature range and gives the main contribution to densification.

A comparison between microstructure of SPS processed and conventionally (pressureless) sintered CP8C50 composites is of interest. As shown in chapter 5 and 6, the average grain size for a dense ceramic of conventionally sintered CP8C50 composites (120 nm and several micrometres for 960 and 1130 °C sintered samples respectively) is significantly larger that of the SPS-3 (which is only 70 nm) . So it can be concluded that the SPS processing effectively suppresses grain growth during densification of the CuO doped 3Y-TZP nano-powder composite. This inhibition of grain growth, which is believed to be associated with extremely fast heating rate in combination with high external pressure, is considered as a distinguished advantage of the SPS process [5-8].

Fig. 7.4 shows the XRD pattern of an as-polished and a 500 °C annealed SPS-3 specimen. For the as-polished specimen the main phase can be identified as tetragonal zirconia. It is important to point

out that residual stresses are present in the as-polished specimen so that the XRD peaks are broadened and the intensity ratios between peaks are slightly different from standard references. After annealing at 500 °C in air the XRD signals get more narrow and the intensity ration between the t-ZrO$_2$ signals are in good agreement with the value provided by the standard references. This change in pattern feature should be attributed to the effective release of residual surface stresses in the specimen, which was introduced by cutting and polishing. At 2θ about 28° a minor peak of monoclinic zirconia is observed after annealing. From this XRD pattern an amount of less than 3 vol% monoclinic zirconia is estimated by Toraya's [12] method. This small amount of monoclinic zirconia is probably also present in the as-polished sample but is difficult to be observed because of the broadening of peaks. Nevertheless, it can be stated that the SPS-3 material contains almost only tetragonal zirconia. This result is in a very remarkable contrast with the large amounts (80 vol %) of monoclinic zirconia phase in the conventionally sintered CP8C50 composites. The tetragonal to monoclinic zirconia phase transformation arising from reactions between CuO and the 3Y-TZP as described in chapter 6 is prevented in the case of SPS processing.
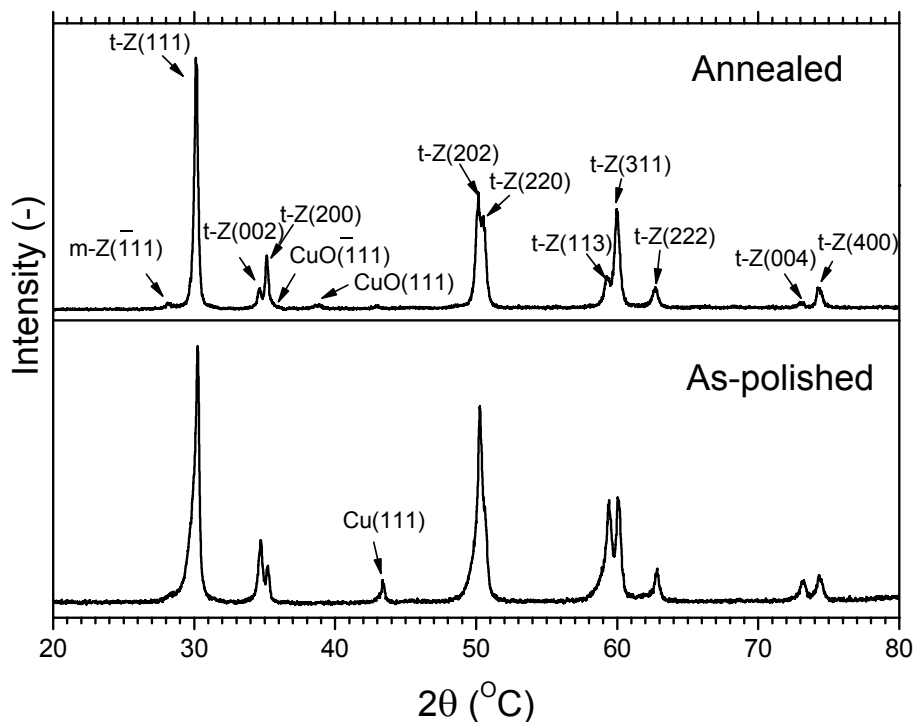
Fig. 7.4 XRD pattern of as-polished and 500 °C annealed SPS-3 samples

t-Z, m-Z, CuO and Cu denote signals of tetragonal zirconia, monoclinic zirconia, Cu(II)

oxide and   metallic copper respectively.

In the XRD pattern of the as-polished SPS-3 a relative small peak, ascribed to metallic Cu, is observed at 2θ of 43.5°. After annealing at 500 °C the metallic Cu signal significantly reduces, while CuO($\bar{1}$11) and CuO(111) reflections appear. These phenomena clearly indicate that the CuO phase in the starting CP8C50 powder is reduced to a metallic phase during the SPS-3 process and re-oxidises by annealing in air. During the SPS processes a vacuum was applied to protect the graphite dies from oxidation, while additionally the powder was put in a graphite die with adjacent graphite sheets (for protection of the die from contamination). So a strong reductive environment is expected during the SPS process, where Cu (II) can easily be reduced to Cu(0) at elevated temperatures.

In summary, it can be concluded that a nano-structured ceramic consisting of tetragonal zirconia and metallic Cu is obtained by SPS processing of CP8C50 composite nano powder.

7.3.3 Influence of SPS on the reactions between CuO and 3Y-TZP

During conventional pressureless sintering of CP8C50 several reactions, including dissolution of CuO in the 3Y-TZP grain boundaries below 600 °C and formation of $Y_2Cu_2O_5$ at around 850 °C, take place (see chapter 4) and show a profound influence on sintering and microstructure evolution. The dissolution reaction increases grain boundary diffusivity and results in a fast densification in the lower temperature range of (750 - 850 °C) (see chapter 5) as well as a strong grain growth in the final sintering stage (see chapter 6). The latter reaction inhibits densification (see chapter 5) and causes a strong tetragonal to monoclinic zirconia phase transformation during heating (see chapter 6). The influence of SPS processing on the reactions as described in chapter 4 and the consequences of densification and microstructure will now be discussed.

In general it can be said that both reactions as observed during pressureless sintering are significantly suppressed by the extremely fast heating rate (400 °C·min^{-1} from 450 to 850 °C and 100 °C·min^{-1} from 850 to 1100 °C), or, in another words, the very short processing time (in total around 7 min) of the SPS-3 process. It may be simply due to that those reactions do not have sufficient time to occur to a considerable extent. Several consequences of this inhibition of the reactions can be seen in the SPS-3 sample. First the densification in the temperature range of 750 - 850 °C is totally negligible (segment II in Fig. 7.1), whereas a significant densification as activated by CuO dissolution was observed in the corresponding temperature range in the case of pressureless sintering (see chapter 5). Secondly strong grain growth as occurring above 1050 °C is effectively prevented. Finally the phase transformation from tetragonal to monoclinic zirconia during sintering is prevented when the SPS procedure was applied.

The reduction of CuO to metallic Cu, as revealed by XRD analysis (see Fig. 7.4), can also contribute to the retention of tetragonal of zirconia in the SPS-sample. As describe in chapter 4, the formation of $Y_2Cu_2O_5$ is a result of the reaction between CuO and yttria as segregated to the 3Y-TZP grain boundaries. Assuming Cu does not react with Y_2O_3, the reduction of CuO obviously results in the removal of a reactant for this reaction and consequently prevents the formation of $Y_2Cu_2O_5$. As a consequence the t-m phase transformation does not occur. This explanation is supported by the observation of Lemair et al [17]. These authors annealed a 0.45 wt% CuO doped 3Y-TZP coarse-grained composite, which contains significant amounts of monoclinic zirconia phase after sintering, in a H_2 flow at 1200 °C. After this annealing it is revealed by TEM analysis that the Cu species has been reduced to metallic phase, and that the monoclinic zirconia phase completely disappears.

7.3.5 Microstructure development during annealing of the SPS-3 material

Fig. 7.5 shows SEM images of polished cross-sections of SPS-3 after annealing at various temperatures. The XRD patterns of the annealed sample are shown in Fig. 7.6. The volume fraction of monoclinic zirconia phase in the samples as determined by Toraya's method is listed in Table 7.2 and compared with CP8C50 produced by conventional pressureless sintering. In general it can be seen that the microstructure significantly changes during annealing.
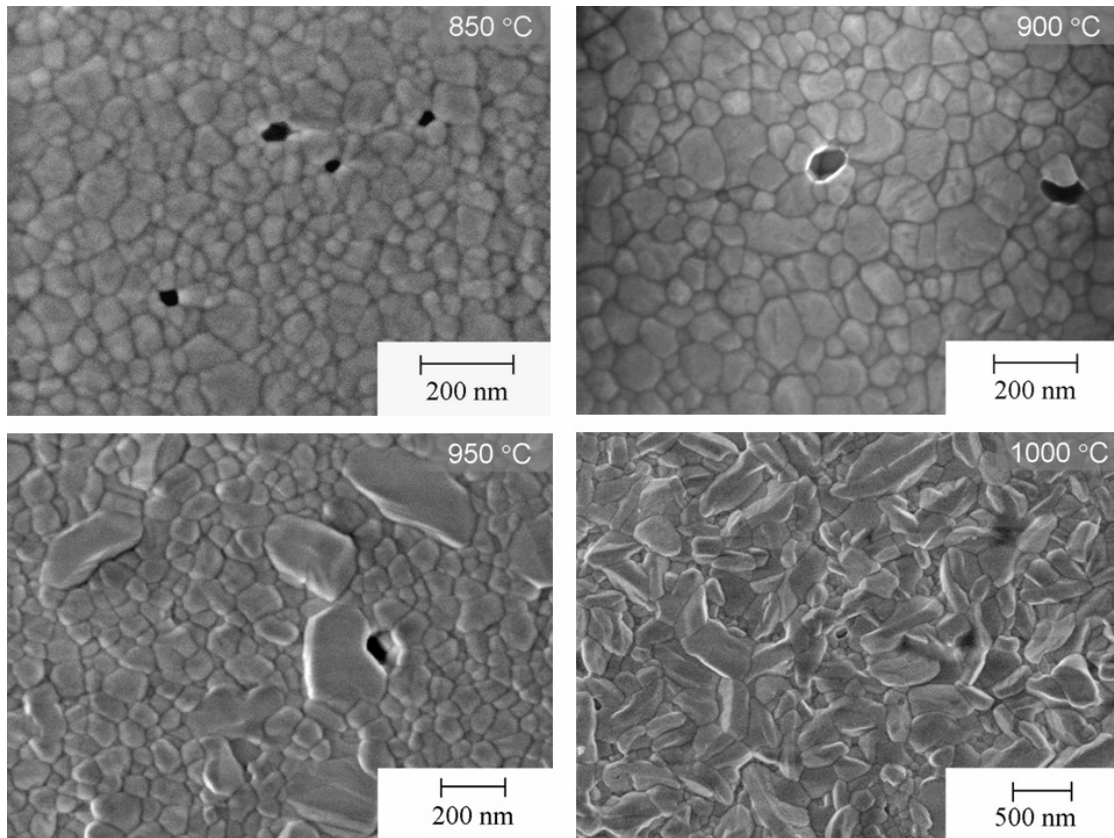
Fig. 7.5 SEM images of SPS-3 samples annealed at various temperatures in an oxygen flow.

After annealing at 850 °C the sample consists of grains with uniform sizes. The average grain size as determined by the line intercept technique is 70 nm, which is identical with the as-sintered sample. This sample also shows the same XRD pattern as that of the as-sintered SPS-3 material. Therefore it can be concluded that the microstructure of the SPS-3 material does not change during annealing at 850 °C. For the sample annealed at 900 °C for 1 hour, the only difference in microstructure from the SPS-3A-1 sample is the slightly larger average grain size (110 nm). It can be said that annealing the SPS-3 below 900 °C has almost no visible influence on the microstructure of the SPS-3 material except the slight uniform grain growth.

Table 7.2 Density of 8 mol% doped 3Y-TZP nano-powder composites processed by SPS

Code[*]	ρ (%)	Vm (vol%)	d	H_V (GPa)	K_{IC}
PS1130	95	80	>1 μm	8.7±0.2	3.7±0.1
PS960	96	79	120 nm	10.9±0.2	3.7±0.1
SA850	96	0	70 nm	11.4±0.9	4.3±0.4
SA900	96	0	110 nm	11.8±0.2	5.4±0.7
SA950	96	30	120 nm	10.5±0.5	3.1±0.3
SA1000	96	77	500 nm	9.3±0.1	3.8±0.1

[*] PSx: Pressureless sintered at x°C; SAx: SPS-3 sample annealed x °C.
ρ: relative density; Vm: volume fraction of m-ZrO$_2$; d: average grain size;
H_V: Vickers hardness; K_{IC}: fracture toughness

Fig. 7.6 XRD patterns of SPS-3 sample after annealing at various temperatures

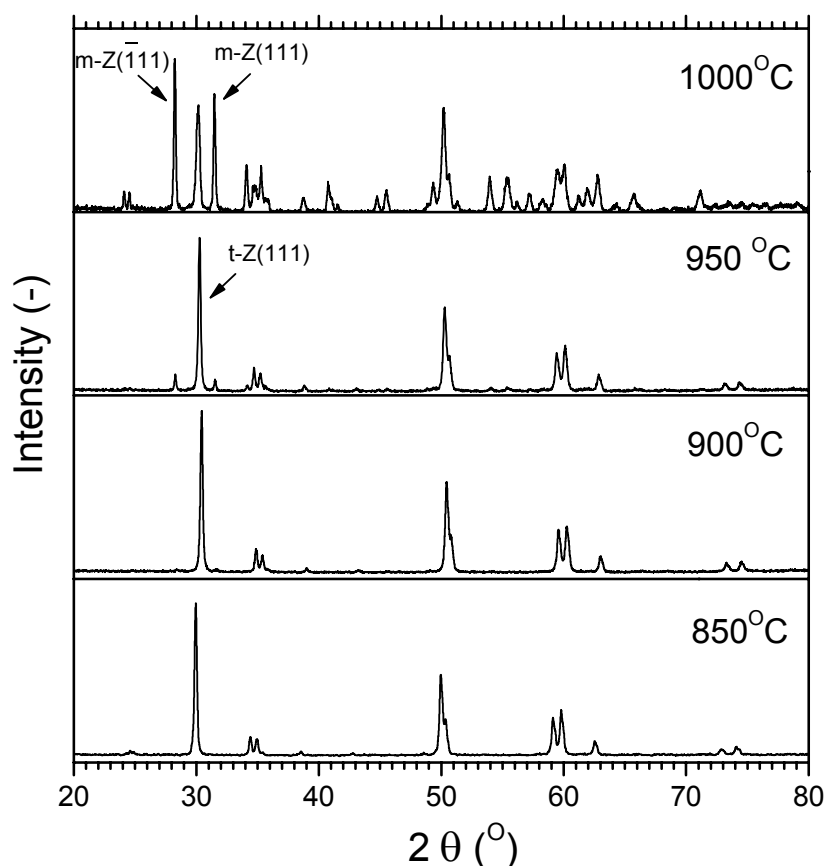In contrast with the negligible microstructure development during annealing $\leq$ 900 °C, some remarkable changes in microstructure of the SPS-3 material are observed after annealing $\geq$ 950 °C. The sample annealed at 950 °C shows a non-uniform grain size distribution. A significant amount of large grains with a size of more than 200 nm and an elongated shape are visible in the cross-section image (Fig. 7.5-950 °C). However the average size of the grains surrounding the large ones is only 120 nm. This result implies that a strong grain growth starts. It is also revealed by XRD analysis that around 30 vol% of monoclinic zirconia phase was formed during the annealing at 950 °C (see Figs. 7.6 and Table 7.2). After annealing at 1000 °C for 1 hour almost all the grains became elongated. The length of these grains is as large as 500 nm. Accompanying with this drastic microstructure evolution, 77 vol% of monoclinic zirconia phase was formed.

The significant microstructure evolution during annealing above 950 °C can be explained by the reactions between CuO and 3Y-TZP grains. As discussed above, the reactions as observed during conventional pressureless sintering are effectively suppressed during the SPS process due to the extremely fast heating rate as well as the strongly reducing atmosphere. During annealing above 950 °C the Cu phase has re-oxidised and reactions between 3Y-TZP and CuO can occur, i.e., CuO dissolution in the 3Y-TZP grain boundaries and the formation of $Y_2Cu_2O_5$ are re-activated. Therefore the consequences of these reactions to the grain growth and t-m zirconia phase transformation are observed after annealing.

7.3.6 Adjusting microstructure and properties by control of the sintering process

Properties of ceramic materials strongly depend on microstructure characteristics, e.g. grain size, phase composition, etc. For dense CuO doped 3Y-TZP ceramics produced by means of pressureless sintering, it has been shown in chapter 6 that the grain size can be well controlled by adjusting sintering temperature and dwell time. CP8C50 sintered at 960 °C for 20 hours exhibits a gain size of 120 nm, whereas, the one sintered at 1130 °C for 1 hour gives a grain size up to several micrometres. However the formation of large amounts (80 vol%) of monoclinic zirconia phase is always inevitable when conventional sintering is used. When the CuO doped 3Y-TZP nano-powder composite (CP8C50) is processed by the SPS technique, as described in this chapter, an even smaller grain size (70 nm) is given and more importantly, the tetragonal zirconia phase is well maintained during processing. Additionally, the grain size and phase composition of the material can be further adjusted by annealing after SPS processing. Combining all these techniques, including pressureless sintering, SPS processing and annealing, one has largely extended tools to manipulate the microstructure of the CuO doped 3Y-TZP composite ceramic, and, moreover, to adjust properties of the material.
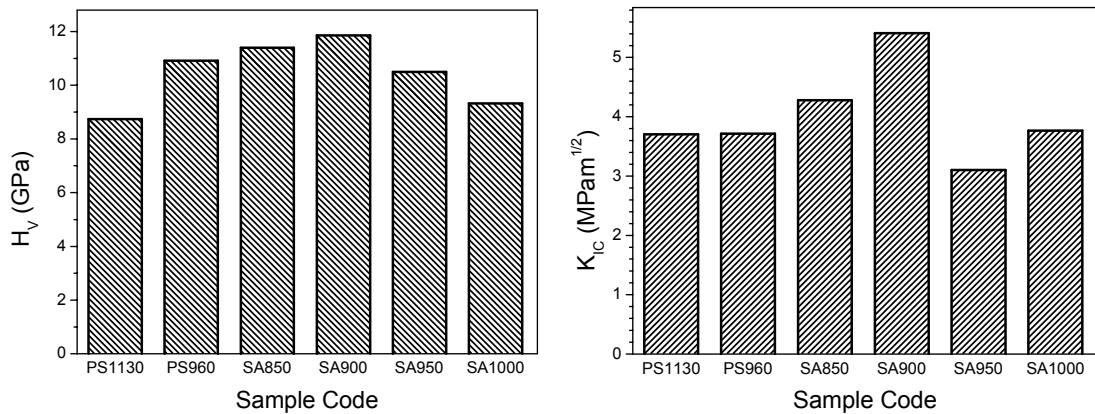

Fig 7.7 Vickers hardness and fracture toughness of pressureless sintered CP8C50 and SPS-3 sample annealed at various temperatures. For explanation of sample codes see table 7.2

As an example of adjusting properties by means of microstructure manipulating, hardness and fracture toughness of the CP8C50 ceramics are presented in Table 7.2 and Fig. 7.7. All these CP8C50 ceramics possess a relative density of more than 95% (presence of monoclinic zirconia phase is taken into account for theoretical density calculation). The dependence of hardness (H_V) on grain size is clearly revealed for the CP8C50 ceramic composites. The materials with small grain sizes exhibit remarkably higher hardness ($H_V \geq 10.5$ GPa when $d < 200$ nm) than the coarse-grained materials ($H_V \leq 9.5$ GPa when $d > 500$ nm). On the other hand, fracture toughness (K_{IC}) shows a remarkably dependence on the combination of the monoclinic zirconia content and grain size. All materials containing 80 vol% of monoclinic zirconia phase show similar fracture toughness ($K_{IC} \approx 3.7$ MPa·m$^{1/2}$). The SPS-3 sample annealed at 850 °C (SA850), which possessed no monoclinic zirconia phase and an average grain size of 70 nm, gives a slightly higher fracture toughness ($K_{IC} \approx 4.3$ MPa·m$^{1/2}$). If the tetragonal zirconia phase is maintained and a slight increase in grain size is achieved, i.e. after annealing at 900 °C for 1 hour (SA900), a remarkable improvement in fracture toughness ($K_{IC} \approx 5.4$ MPa·m$^{1/2}$) is observed. However, generating 30 vol% monoclinic zirconia in the material by annealing at 950 °C (SA950) significantly decreases the fracture toughness ($K_{IC} \approx 3.1$ MPa·m$^{1/2}$) although the grain size is remained

the same. It is concluded that SPS processing followed by annealing at 900 °C for 1 hour is the optimal producing procedure for the 8 mol% CuO doped 3Y-TZP ceramic from a mechanical point of view.

For a thorough understanding of the microstructure influence on mechanical properties of the CuO doped 3Y-YZP ceramics, more research is of course required. Nevertheless, the results as presented here have clearly shown that microstructure and properties of material can be adjusted to a significant extent by utilising various processing techniques.

It is important to note that microstructure normally matters for many properties of a ceramic material. In this sense some other functional properties of the CuO doped 3Y-TZP composite ceramic, e.g. (super)plastic tribological and electrical properties can also be tuned by utilising different processing techniques, including pressureless sintering, SPS process and annealing. Tuning mechanical properties of the composite ceramic is shown here just as an example. More investigation on tuning other properties of CuO doped 3Y-TZP composite ceramic (and other materials) by manipulation of microstructure, via control of processing, is of great interest.

Conclusions

SPS is proven to be a very efficient technique for producing a dense nano-structured ceramic (with an average grain size of 70nm) from the CuO doped 3Y-TZP nano composite powder (CP8C50). The composite material prepared by SPS processing shows a significantly different microstructure from the one produced by conventional pressureless sintering. The SPS composite possesses a phase composition of purely tetragonal zirconia with metallic Cu, whereas, 80 vol% of monoclinic zirconia phase is always present in conventionally sintered composites. This difference in microstructure is caused by the extremely fast heating rate as well as the strongly reducing atmosphere associated with the SPS processing.

The presence of metallic Cu in the SPS composite is caused by the reduction of CuO due to the reaction atmosphere. Because of the fast heating rate of SPS process (400 °C·min^{-1} and 100 °C·min^{-1} when the temperature is below and above 850 °C respectively) and the reduction of CuO, the reactions between CuO and 3Y-TZP as observed during pressureless sintering of CuO doped 3Y-TZP system are effectively suppressed. As one of the consequences, the t-m zirconia phase transformation caused by formation of $Y_2Cu_2O_5$, as observed in the case of conventional sintering, is totally suppressed.

The microstructure characteristics of the SPS composite can be effectively adjusted by annealing at different temperatures. Combining all the processing techniques as described in this work, including pressureless sintering, SPS and the following annealing steps, properties of the CuO doped 3Y-TZP composite can be tuned via manipulation of microstructure. Tuning the mechanical properties of dense 8 mol% CuO doped 3Y-TZP composite ceramic by utilising different processing technique is shown as an example.

Acknowledgement

References

1. Mayo, M.J., Seidensticker, J.R., Hauge, D.C. and Carim, A.H., "Surface chemistry effects on the processing and superplastic properties of nanocrystalline oxide ceramics", *Nanostructured Mater.*, 1999, **11**[2], pp. 271-282.

2. Hwang, C.M.J. and Chen, I.-W., "Effect of a liquid phase on superplasticity of 2-mol%-Y_2O_3-stabilized tetragonal zirconia polycrystals", *J. Am. Ceram. Soc.*, 1990, **73**[6], 1626-1632.

3. Kerkwijk, B., García, M., van Zyl, W.E., Winnubst, L., Mulder, E.J., Schipper, D.J. and Verweij, H., "Friction behaviour of solid oxide lubricants as second phase in α- Al_2O_3 and stabilised ZrO_2 composites", *Wear*, 2004, **256,** 182-189.

4. Pasaribu, H.R., Sloetjes, J.W. and Schipper, D.J., "Friction reduction by adding copper oxide into alumina and zirconia ceramics", *Wear*, 2003, **255**[1-6], 699-707.

5. Groza, J.R., Zavaliangos, A., "Sintering activation by external electrical field", *Mat. Sci. Eng.*, 2000, **A287**, 171-177.

6. Groza, J.R. "Field assisted sintering", In: ASM handbook; *Powder Metall*, 1998, **7**, p. 583-589.

7. Vanmeensel, K. Laptev, A. Hennicke, J, Vleugels, J., Van der Biest, O., "Modelling of the temperature distribution during field assisted sintering", *ACTA Mat.*, 2005, **53**, 4379-4388.

8. Shen, Z., Nygren, M., "Microstructural prototyping of ceramics by kinetic engineering: application of spark plasma sintering", *The Chem. Record*, 2005, **5**, 173-184.

9. Shen, Z., Zhao, Z., Peng, H., Nygren, M., "Formation of tough interlocking microstructures in silicon nitride ceramics by dynamic ripening", *Nature*, 2002, **417,** 266-269.

10. Khor, K.A., Cheng, K.H., Yu, L.G., Boey, F., "Thermal conductivity and dielectric constant of spark plasma sintered aluminium nitride", *Ma. Sci. Eng.*, 2003, **A347**, 300-305.

11. Su, X., Wang, P., Chen, W., Shen, Z., Nygren, M., Yibing, C., Yan, D., "Effects of composition and thermal treatment on infrared transmission of Dy-a-sialon", *J. Eur. Ceram. Soc.*, 2004, **24**, 2869-2877.

12. Toraya, H., Yoshimura, M. and Somiya, S., "Calibration Curve for Quantitative Analysis of the Monoclinic-Tetragonal ZrO_2 System by X-Ray Diffraction", *J. Am. Ceram. Soc.*, 1984, **67**[6], C119-C121.

13. Mendelson, M.I., "Average grain size in polycrystalline ceramics", *J. Am. Ceram. Soc.*, 1969, **52**, 443-446.

14. Shetty, D.K., Wright, I.G., Mincer, P.N. and Clauer, P.N., "Indentation fracture of WC-Co cermets", *J. Mat. Sci.*, 1985, **20**, 1873-1882.

15. Niihara, K., Morena, R., Hasselman, D.P.H., "Evaluation of$K$ Ic of brittle solids by the indentation method with low crack-to-indent ratios", *J. Mat. Sci. Lett.*, 1982, **1**, 13-16.

16. Niihara, K., "A fracture mechanics analysis of indentation-induced Palmqvist crack in ceramics", *J. Mat. Sci. Lett.*, 1982, **2**, 221-223.

17. Lemaire, L., Scholz, S.M., Bowen, P., Dutta, J., Hofmeister, H. and Hofmann, H., "Effect of CuO additives on the reversibility of zirconia crystalline phase transitions", *J. Mater. Sci.*, 1999, **34**, 2207-2215.

Chapter 8

Microstructure and its effect on tribological and mechanical properties of coarse-grained CuO doped 3Y-TZP ceramics

Abstract

Dense 8 mol% CuO doped 3Y-TZP ceramics were prepared by pressureless sintering at 1500 and 1550 ºC respectively. TEM revealed that the ceramic sintered at 1500 ºC exhibits grain boundaries free of any amorphous phase, while crystalline copper-oxide grains were found in the zirconia matrix, whereas the one sintered at 1550 ºC contains a Cu-rich amorphous grain boundary layer. The tribological behaviour of these materials was tested under dry sliding conditions using a pin-on-disc tribometer. The material sintered at 1500 ºC showed self lubrication resulting in a low friction coefficient (f) of 0.2~0.3 and low specific wear rate (k) $<< 10^{-6}$ mm^3·N^{-1}·m^{-1}. In contrast the material sintered at 1550 ºC showed poor tribological behaviour (f=0.8~0.9; k>>10^{-6} mm^3·N^{-1}·m^{-1}) under the same conditions. The difference in tribological behaviour of those two materials was interpreted on the basis on mechanical properties and microstructure characteristics.

8.1 Introduction

In engineering applications wear and friction need to be minimized to avoid large energy costs and fast damage of machine components. At present liquid lubricants, which are mainly organic substances, are widely used to reduce wear and friction. However, due to economic and environmental reasons, the usage of liquid lubricants is more and more unfavourable. Additionally, under some special circumstances, such as in high vacuum and at high temperatures, liquid lubricants can not be used. Therefore it is increasingly interesting to develop new engineering materials, which can be used in dry contact sliding situations. It is now generally recognised that materials suitable for unlubricated tribo-applications should fulfil the following two criteria: the specific rate, k, is less than 10^{-6} mm^3·N^{-1}·m^{-1}; and the friction coefficient, f, is lower than ≤ 0.2 [1]

Specific properties of ceramics like high hardness, chemical inertness and high thermal stability, make these materials increasingly interesting for engineering applications, especially as materials for tribological systems. Extensive research on tribological properties of various ceramics systems have been carried out in the past decades [2-7]. As indicated by these researches, high wear resistance can be obtained with ceramic tribosystems under dry contact situations. However, friction coefficient of those dry sliding ceramic tribosystems generally varies in a range of 0.5~1.0, which is unacceptable for real applications.

Ideas of self-lubricating composites were introduced by Alexeyeve [8] in order to reduce friction and wear of tribological systems in dry sliding situations. A self-lubricating composite is essentially a material containing relatively small amounts of a soft solid phase uniformly dispersed in a matrix of a hard phase. During sliding of this composite against a hard counter body, it is expected that the soft

phase in the surface zone is deformed and squeezed out over the surface by the counter body to form a soft and smooth film between the contacting surfaces. This interfacial soft film can reduce wear and friction of the sliding pair as a (solid) lubricant. An advantage provided by self-lubricating composites is the fact that the friction-reducing film can be created continuously during sliding so that low friction coefficient can be sustainably achieved.

This self-lubricating mechanism was also implemented by Kerkwijk [9] by adding various soft oxides (CuO, MgO, MnO$_2$, ZnO or B$_2$O$_3$) into alumina or zirconia ceramics. Tribology tests under dry sliding conditions revealed that among these soft oxides only the addition of CuO could significantly reduce the friction coefficient. Pasaribu et al. [10] investigated the friction behaviour of various amounts of CuO doped alumina and zirconia ceramics, showing again that addition of CuO results in remarkable reduction of friction of alumina and zirconia under certain dry sliding conditions. However, microstructure properties and wear mechanisms responsible to this friction reduction are not clear yet.

In the present work, two self-lubricating ceramic composites of 8 mol% (5 wt%) CuO doped 3Y-TZP were prepared from commercial starting powders by conventional mixing and isostatic pressing followed by pressureless sintering at 1500 and 1550 ºC respectively. Tribology tests were carried out using a pin-on-disc tribometer under dry sliding conditions, using an alumina ball as counter material. Microstructure characteristics were investigated in detail by XRD, SEM and TEM. Mechanical properties were also studied by 4-point bending and SENB techniques. The significant different tribological behaviours of these two materials will be interpreted on the basis of mechanical properties and microstructural characteristics.

8.2 Experimental procedure

8.2.1 Sample preparation

Ceramic discs of Y-TZP doped with 8 mol% CuO were prepared from commercial 3Y-TZP (TZ3Y, Tosoh, Japan) and CuO (Aldrich, Germany) starting powders. Appropriate amounts of powders were mixed by wet-milling for 24 hours in a polyethylene bottle, using ethanol and zirconia balls as milling media. The milled suspension was oven-dried at 80 ºC for 24 hours and at 120 ºC for 8 hours successively. The dry cake was ground slightly in a plastic mortar and then sieved through a 180 μm sieve. Green compact discs of the composite powder with a diameter of 50mm and a thickness of around 5 mm were prepared by uniaxial pressing at 30 MPa followed by isostatic pressing at 400 MPa. These discs were sintered for 8 hours in stagnant air at 1500 (denoted as sample A hereafter) or 1550 ºC (denoted as sample B hereafter) respectively. The heating and cooling rate used were both 2 ºC·min^{-1}. The densification during sintering was analysed by dilatometer measurement using a Netzsch 402E dilatometer. The final density of the sintered discs was measured using Archimedes' technique in mercury. The sintered discs were polished to a surface roughness (R$_a$) of 0.1 μm using diamond paste. The polished discs were ultrasonically cleaned in ethanol and then annealed at 850 ºC for 2 hours to remove carbon contamination and release surface stresses.

8.2.2 Microstructure characterization

Phase composition of the CuO doped 3Y-TZP ceramics was determined by X-ray diffraction (XRD, X'pert_APD, PANalytical). The volume fraction of the monoclinic zirconia phase was determined on the basis of peak intensity ratio of M[111], M[$\bar{1}$11] and T[111] XRD peaks using the relationship proposed by Toraya et. al.[11]. Morphologies of fractured surfaces of the sintered ceramics and of

wear tracks after sliding for a certain distance were observed by scanning electron microscopy (SEM, JSM5800, JEOL). Transmission electron microscopy (TEM, CM30 Twin/STEM, Philips) combined with an energy dispersive X-ray analyzer (EDX, Thermo Noran) was also used to investigate the microstructure of the ceramics.

8.2.3 Tribology test

Dry sliding tribological tests were performed on a pin-on-disc tribometer (CSEM, Switzerland), using the ball on disc geometry (Fig. 8.1). The ceramic disc was mounted on a holder, which is driven by a motor for controlled sliding speed and sliding distance. A commercial alumina ball (Gimex Technische Keramiek b.v., the Netherlands) of 10 mm in diameter was used as counter material. The normal load is applied by placing a corresponding mass on top of the pin. In order to obtain constant test conditions the tribometer was placed in a controlled environment with the temperature set at 23°C and the relative humidity at 40%. For each test a normal load of 5N (maximum Hertzian pressure = 0.9 GPa) and a sliding velocity of 0.1 m·s^{-1} were applied. The sliding distance was at least 1 km.
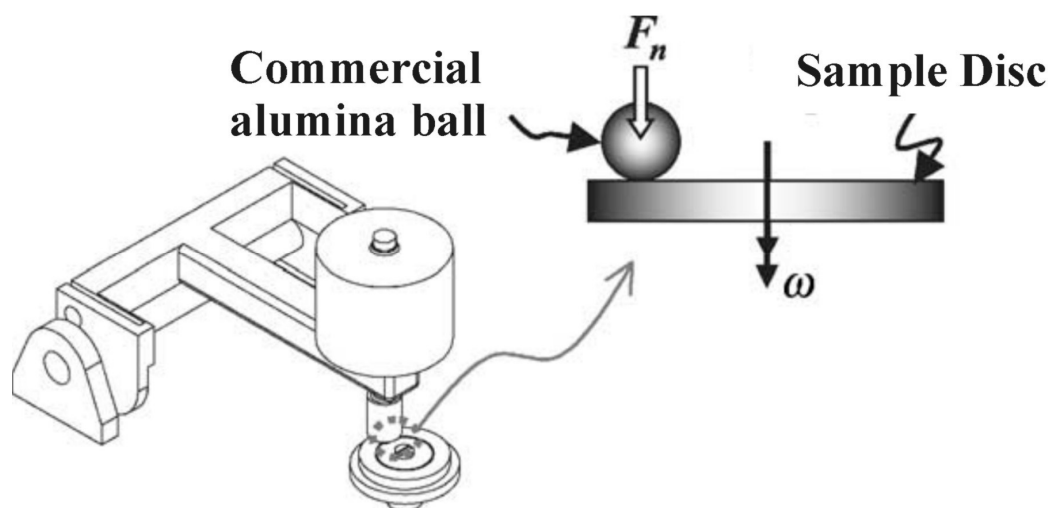
Fig. 8.1 Schematic presentation of pin-on-disc tribometer.

8.2.4 Mechanical tests

Mechanical properties of the ceramics materials were analysed using a universal testing machine (OverDyn S220) at room temperature. Bending strength was measured by a 4-point bending technique with an inner and outer span of 10 and 20 mm, respectively. The samples for the bending strength measurements were cut into bars of 26×5×2 mm^3 and polished at the side which is opposite to the loading piston and comes under tensile stress during tests. The polished surface represents the composition and microstructure of the bulk of the ceramic. In order to eliminate the influence of surface residual stresses introduced by cutting and polishing, all samples were annealed at 750 °C for 2 hours before bending test, using a heating and a cooling rate of 2 °C·min^{-1}. During the bending tests a crosshead speed of 0.7 mm·min^{-1} was used. The strength value (σ_f) was calculated using the general equation:

$$\sigma_f = \frac{3PL}{bW^2} \qquad (8.1)$$

where P is the load at fracture, L is half of the difference between the inner and outer span, b is the sample width (5 mm) and W is the sample height (2 mm). For each material system 9 specimens were measured and the average of the calculated data was taken as the resulting value.

Fracture toughness was measured by a 3-point Single-Edge-Notched-Beam (SENB) technique with a span of 12 mm. The samples for SENB tests were cut into bars of $15 \times 3 \times 1$ mm^3 and a notch with a width and depth of 50 and 450 μm was cut on one edge. The real dimension of the notch of each specimen was measured under a light microscopy. No precracking was performed. Prior to the test all samples were annealed in the same way as mentioned above to remove surface residual stresses. During tests a crosshead speed of 0.3 mm·min^{-1} was used. The toughness values (K_{1C}) were calculated using the general equation [12]:

$$K_{1C} = \frac{3PSY\sqrt{a}}{2bW^2} \qquad (8.2)$$

where P is the load at fracture, S is the span width, b is the sample width (1 mm) and W is the sample height (3 mm) and a is the depth of the notch. Y is a dimensionless correction factor based on the ratio of the notch depth and the sample height and is calculated by:

$$Y = 1.93 - 3.07 \cdot (\frac{a}{W}) + 14.53 \cdot (\frac{a}{W})^2 - 25.11 \cdot (\frac{a}{W})^3 + 25.80 \cdot (\frac{a}{W})^4 \qquad (8.3)$$

For each material system 12 specimens were measured and the average of the calculated data was taken as the resulting value.

8.3 Results and discussion

8.3.1 Sintering

Relative densities of 8 mol% CuO doped and undoped 3Y-TZP as calculated on the basis of green density and linear shrinkage data recorded by a dilatometer are plotted in Fig. 8.2 as a function of temperature during heating. It can be seen clearly that in this case addition of 8 mol % CuO strongly inhibits densification so that a higher sintering temperature ($\geq$1500 °C) is necessary for obtaining dense samples. The retardation of densification can be explained by several reactions occurring during sintering, which have been discussed in one of our previous papers [13] and in chapter 2 of this thesis.

The samples sintered at slightly different temperatures (1500 °C and 1550 °C; resp. sample A and B) show similar densities and crystallite phase composition. XRD analysis shows that both sample A and B contain around 70 vol% of monoclinic zirconia phase after sintering, although pure tetragonal 3Y-TZP powder was used as starting material. Cu-containing phases in these two samples are too less to be distinguished on XRD patterns. As discussed in chapter 2 and 6, the formation of monoclinic zirconia can be interpreted in terms of the reaction between CuO and yttria as segregated to grain boundaries during sintering, which causes destabilization of tetragonal zirconia. Taking into account the presence of monoclinic zirconia phase, both samples reached a relative density $> 97\%$ after sintering for 8 hours at the temperatures indicated.
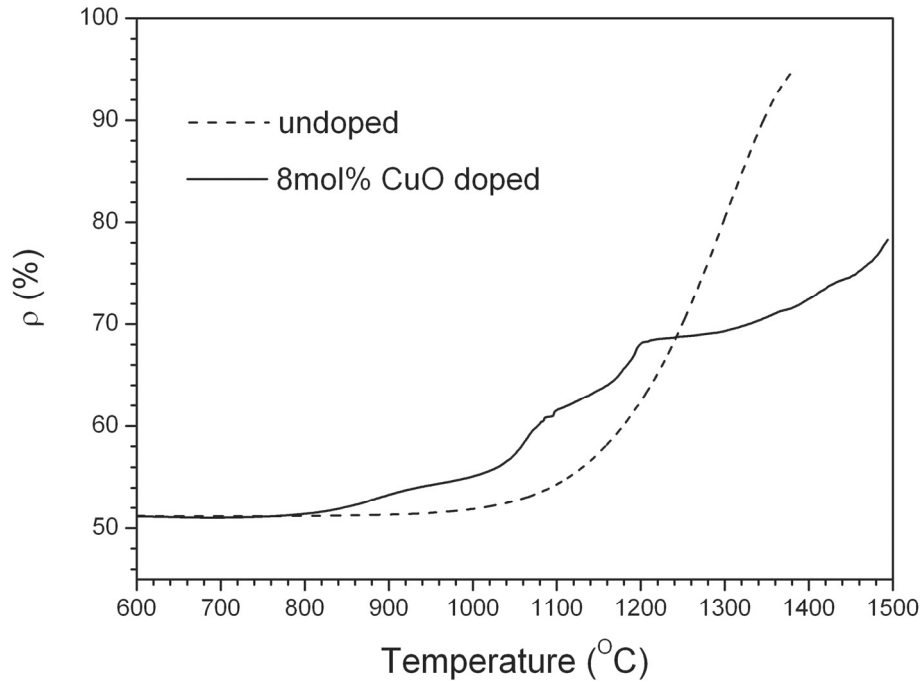
Fig. 8.2 Density of undoped 3Y-TZP (dashed line) and 8 mol% CuO doped 3Y-TZP (solid line) as a function

of temperature during heating (2 °C/min).

8.3.2 Microstructure

Scanning electron microscopic (SEM) images of fractured surfaces of sample A and B are shown in Fig. 8.3. Both samples show a relative dense microstructure, which is in accordance with the high density of those materials. The average grain size in both samples appears to be around 2 μm, indicating that strong grain growth during sintering is introduced by addition of CuO. The undoped 3Y-TZP systems sintered at these temperatures only show a grain size of about 0.6 μm [14]. Especially, the fractured surface of sample B mainly consists of faceted grains with uniform size of 2 μm. In contrast, sample A exhibits of small amounts of small rounded grains (<500nm)
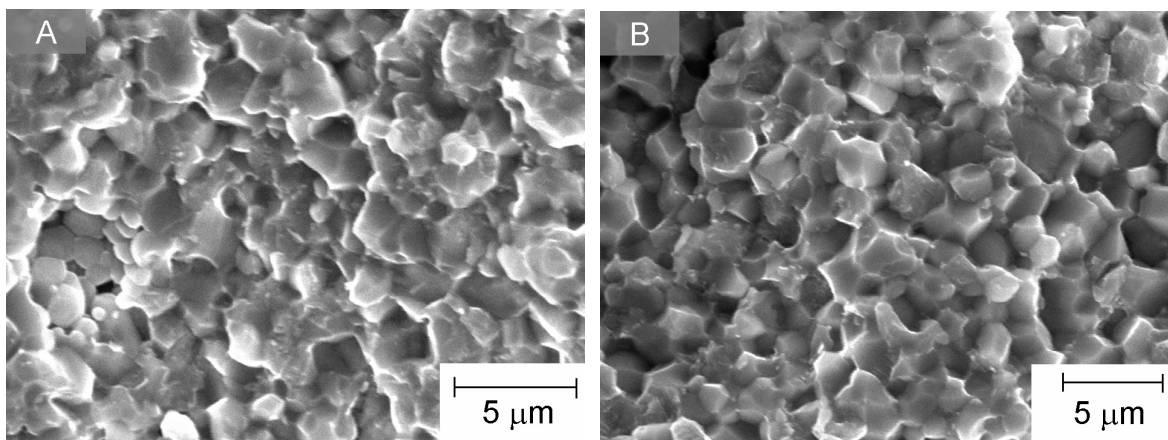
Fig. 8.3 SEM images of fractured surfaces of 8 mol% CuO doped 3Y-TZP sintered at

(A) 1500 ºC and (B) 1550 ºC.

homogeneously dispersed within a matrix of large grains (~2μm). In addition, the SEM images further reveal a difference in fracture mode between sample A and B. Sample B shows a pure intergranular fracture behaviour, while a mixed trans/inter-granular fracture can be observed in sample A.

For further investigation of the microstructure transmission electron microscopy (TEM) of the bulk region of these two samples was conducted (Fig. 8.4). Significant differences in microstructure between sample A and B are clearly visible on TEM images and can be distinguished in two terms: grain boundary morphology and Cu distribution. Sample B clearly exhibits an amorphous grain-boundary layer of a few nanometre thickness, while sample A shows a rather clean grain boundary and amorphous grain boundary layer, if any, can not be observed, even at higher magnification (see Fig. 8.4-c). As revealed by EDX analysis, the crystalline grains of a few hundred nm in diameter (as shown in the white circle in Fig. 8.4-A), mainly consist of copper-oxide. These small copper-oxides grains as observed by TEM/EDX probably correspond to the small rounded grains as found on the SEM image of sample A (see Fig. 8.3-A). In sample B copper species are mainly distributed in the amorphous grain boundary layer along the Y-TZP grain boundaries.
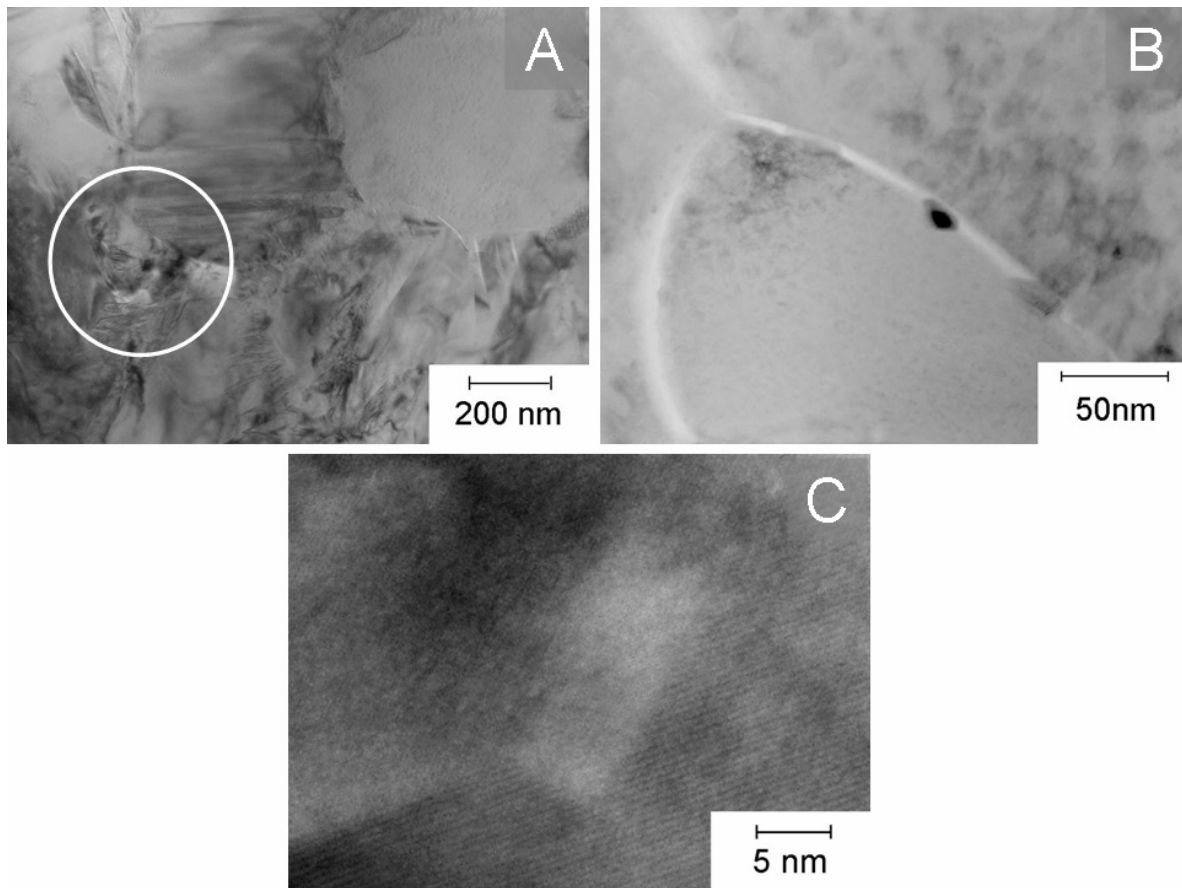
Fig. 8.4 TEM images of 8 mol% CuO doped 3Y-TZP sintered at A) 1500 ºC and B) 1550 ºC. C) image of a triple-grain junction in sample A with a higher magnification

The amorphous grain boundary layer in sample B is likely to be related to a liquid phase formed during sintering. In CuO doped 3Y-TZP systems, there are several possible origins of liquid phase formation during sintering. Thermal analysis on 3 mol% CuO doped 3Y-TZP system as carried out by Seidensticker [15] has shown that Cu_2O (as a result of dissociation of CuO) melts around 1140 °C. In

addition, according to the binary phase diagram of yttria-copper-oxide [16], the CuO or Cu_2O can react with yttria as segregated from zirconia grains to form a new yttria-copper-oxide phase, which also melts at temperatures above 1100 °C. Both origins of liquid phase formation during sintering will lead to an enrichment of Cu species in the liquid phase. The difference in grain boundary morphology and Cu identity distribution between sample A and B could be explained by the different characteristics of the Cu-rich liquid phase at different temperatures. The viscosity of a molten oxide can be very sensitive to temperature. In our cases the samples sintered at 1550 °C significantly bent after sintering whereas almost no bending of the 1500 °C sintered samples was observed. This phenomenon might be an evidence of the much lower viscosity of the liquid phase at 1550 °C than at 1500 °C. During the dwell at 1550 °C, the less viscous Cu-rich liquid phase can easily flow and spread along 3Y-TZP grains. With this liquid phase flow the Cu species, which were present as clusters (or grains) in a matrix of 3Y-TZP grains in the starting compact, re-distribute completely. As a result a solid amorphous phase enriched with Cu is formed along the 3Y-TZP grain boundaries during cooling. In contrast, this liquid phase flow seems not to occur in the case of sample A, probably because of the higher viscosity of the Cu-rich liquid phase at 1500 °C.

8.3.3 Tribological behaviour and mechanical properties

Tribological behaviour of the CuO-doped 3Y-TZP was measured by a pin-on-disc tribometer under dry sliding conditions. Friction coefficients as a function of sliding distance are shown in Fig. 8.5. Fig. 8.6 shows SEM images of wear tracks on sample A and B after sliding for a distance of about 200 m. Friction coefficient data of undoped 3Y-TZP ceramic sintered at 1400 ºC, tested under the same conditions as used for sample A and B (normal load = 5N, sliding velocity = 0.1 m·s^{-1}), are also plotted in Fig. 8.5 as a reference.
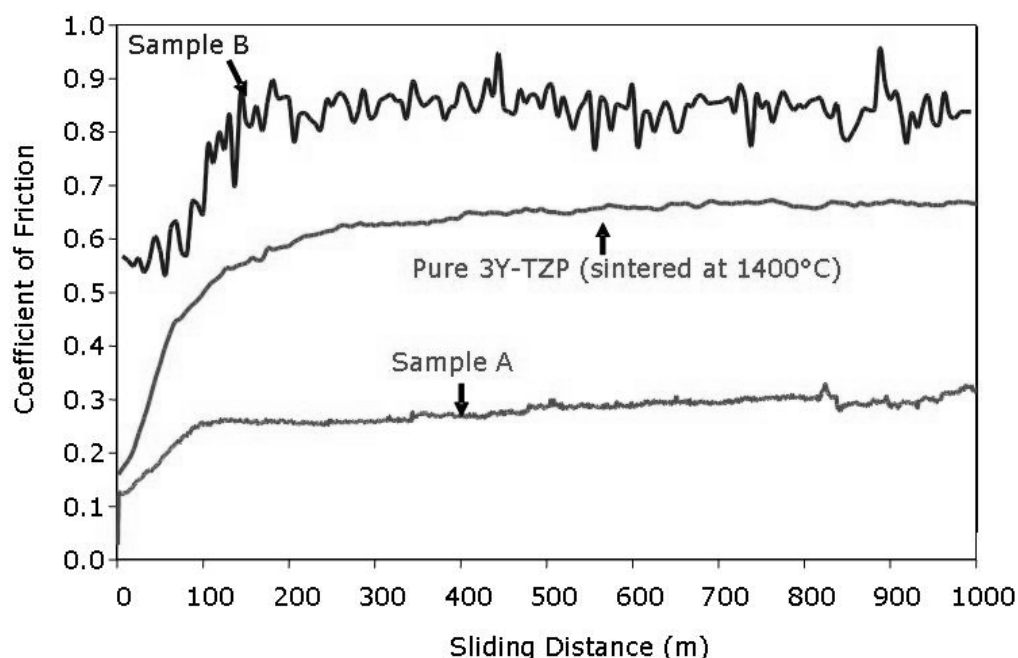

Fig. 8.5 Coefficient of friction as a function of sliding distance for 8 mol% CuO doped 3Y-TZP ceramics

sintered at 1500 ºC (Sample A) and 1550 ºC (Sample B) and undoped 3Y-TZP sintered at 1400 ºC.
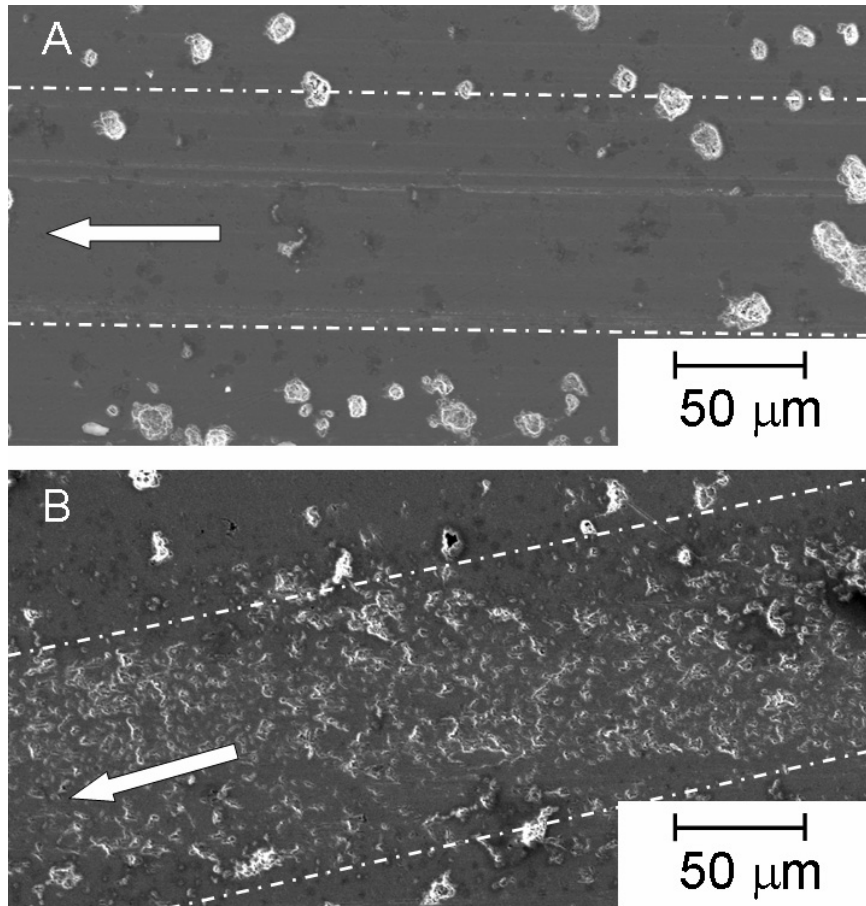
Fig. 8.6. SEM images of wear tracks (between white dashed lines) of 8 mol% CuO doped 3Y-TZP
sintered at (A) 1500 ºC and (B) 1550 ºC, after 200 m sliding

From the results as shown in Figs. 8.5 and 8.6 one can see that only 50 °C difference in sintering temperature (1500 °C for sample A vs. 1550 °C for sample B) leads to a tremendous difference in tribological properties of 8 mol% CuO doped 3Y-TZP ceramics. Within 1 km sliding distance sample A shows a nicely low coefficient of friction of 0.2~0.3, which is only half of the value obtained with undoped 3Y-TZP. This result clearly indicates that the addition of CuO does remarkably reduce the coefficient friction of 3Y-TZP systems. Combined with this low friction coefficient, only mild wear occurs in this sliding stage, leaving a "polished" smooth wear track surface (see Fig. 8.6-A). The specific wear rate is much less than 10^{-6} mm^3·N^{-1}·m^{-1} within the tested sliding distance (1 km), indicating a good wear-resistance of this material.

Whereas sample A shows promising tribological properties, sample B exhibits undesired tribological properties under the same test conditions. In the case of sample B, the coefficient of friction rises to 0.8~0.9 (Fig. 8.5), which is 3 times the value of sample A. This friction coefficient value is even higher then that of an undoped 3Y-TZP ceramic. A rather rough wear track (see Fig. 8.6-B) showing many surface pores left by pulling-out of surface grains was observed after only 200 m of sliding, indicating the occurrence of severe wear. Correspondingly a specific wear rate much higher than 10^{-6} mm^3·N^{-1}·m^{-1} was measured, showing a rather poor wear-resistance of sample B. The results clearly reveal that the sintering temperature is very critical for tribological properties of the CuO doped 3Y-TZP ceramics as studied in the present work.

Mechanical properties of the CuO doped 3Y-TZP ceramics were also measured. Table 6.1 shows the bending strength (σ_f) and fracture toughness (K_{IC}) results. These techniques measure the bulk properties of the materials. Generally it can be said that addition of CuO results in significant decrease in both bending strength and fracture toughness if compared with the values of undoped 3Y-TZP ceramics reported in literature [18]. This decrease in mechanical properties can be explained by the microstructure difference between CuO doped and undoped ceramics. For the undoped 3Y-TZP ceramic, showing a pure tetragonal crystal structure, large part of the high fracture toughness is caused by the phase-transformation toughening mechanism [18]. This phase-transformation toughening strongly depends on the amount of transformable tetragonal zirconia phase in the material. As can be expected, the 8 mol% CuO doped 3Y-TZP as investigated in this work, which shows 70 vol% of monoclinic zirconia phase already after sintering, can hardly benefit from this toughening mechanism and thus the measured mechanical properties are much lower. Moreover the presence of an impurity phase (i.e. the Cu-rich phase), especially the amorphous Cu-rich grain boundary layer in sample B, can give rise to weak points and crack initiating flaws in the material and therefore decreases the toughness and strength even more. But nevertheless these CuO-doped samples have sufficient strength and toughness for structural applications.

Table 6.1 Bending strength and fracture toughness of 8 mol% doped 3Y-TZP ceramics

Sample ID	Material	Sint.T (°C)	σ_f (MPa)	K_{IC} (MPa·m$^{1/2}$)
A	3Y-TZP+8 mol%CuO	1500	310±10	1.7±0.2
B	3Y-TZP+8 mol%CuO	1550	260±10	1.7±0.1
C	3Y-TZP	1400	450±20	7.8±0.5*

* Data taken from [17]

By comparing the two CuO doped 3Y-TZP ceramics, one can see that slightly higher sintering temperature leads to a decrease in bending strength (260 MPa for sample B compared with 310 MPa for sample A), whereas the fracture toughness remains unchanged (1.7±0.1 MPa·m$^{1/2}$). As a basic principle, strength and toughness of a material can be interpreted as the resistance to respectively formation (or initiation) and propagation of (micro)cracks in the material.

Fracture toughness is regarded to be an intrinsic characteristic of the material and can be expressed as the following under plain stress conditions [19]:

$$K_{IC} = \sqrt{2\gamma_f E} \qquad\qquad (8.4)$$

where γ_f is the facture surface energy, which is necessary to create a unit area of new fracture surface; and E is the elastic modulus. The good similarity between the K_{IC} values of sample A and B suggests the small difference in sintering temperature does not change the intrinsic properties of the material.

Bending strength is a factor strongly depends on cracks, flaws or other weak points, which are sources of premature mechanical failure. According to Griffith's theory, bending strength can be expressed as:

$$\sigma_f = \frac{K_{IC}}{\sqrt{\pi c}} \qquad\qquad (8.5)$$

where c is the critical flaw length (Griffith flaw size). From the measured K_{IC} and σ_f values, the Griffith flaw size can be calculated to be 9.5 and 14 μm for sample A and B respectively. However in the materials studied here no voids or cracks with such a large size were observed (neither in the bulk

nor on the surface of the samples used for mechanical tests). The calculated Griffith flaw size in this case should more be referred as a parameter representing the mechanically weak factors possessed by the materials. Various microstructural factors, for instance, degree of interaction between defects, can be assembled into this parameter. Considering the same powder processing and identical finishing treatments of all samples used for bending tests, the larger Griffith flaw size, and therefore the lower bending strength of sample B is more likely to be only caused by the 50 °C higher sintering temperature.

8.3.4 Relations between microstructure, mechanical properties and tribological behaviour

The significant difference in tribological behaviour of sample A and B will now be discussed in terms of the different mechanical properties and microstructure.

From tribological point of view, the low friction and wear obtained in the case of sample A can be interpreted by a self-lubricating mechanism [8-10, 20]. During sliding against an alumina ball, a soft interfacial layer between the ceramic disc and alumina ball is generated. This soft interfacial layer can act as a lubricant and reduces friction. As will be revealed in chapter 9 the presence of CuO in 3Y-TZP ceramics plays an important role for the self-lubricating effect. However, this work clearly points out that not only the presence of CuO, but also a proper microstructure and good mechanical properties (strength) are very important for implementation of this self-lubricating mechanism. The dependence of tribological behaviour on microstructure and mechanical properties can be well interpreted by the wear model as recently developed by Pasaribu [20], which predicts wear severity of a ceramic tribosystem.

In general severe wear must be avoided for obtaining low wear and low friction coefficient. Once severe wear occurs the interface between the sliding materials will be quickly damaged and the roughness of the wear surface will be drastically increased. In this case neither low wear rate nor low friction can be obtained. According to the wear model of ceramic as developed by Pasaribu [21], severe wear will occur when

$$2.7 S_{C,m} + 6 \Xi \geq 16.2 \tag{8.6}$$

in which $S_{C,m}$ is the mechanical severity of a sliding circular contact defined as

$$S_{C,m} = \frac{3P(1+10f)\sqrt{c}}{2\pi a^2 K_{IC}} \tag{8.7}$$

and Ξ is the thermal severity defined as

$$\Xi = \frac{fPV}{aK_{eff}\Delta T_S} \tag{8.8}$$

where P is the applied load, f is the coefficient of friction, c is a pre-existing crack (or flaw) length, a is the radii of the circular contact area between the pin and disc, V is the sliding velocity, K_{eff} is the effective thermal conductivity, and ΔT_s is the thermal shock resistance. More details of this model can be found in the PhD thesis of Pasaribu [20]. By substituting the calculated Griffith flaw size (9.5 μm for sample A) as the pre-existing crack length and 0.25 as the friction coefficient value in equation 8.8, the $2.7 S_{c,m} + 6 \Xi$ value (equation 8.6) is calculated to be 15 in the case of tribological test of sample

A, suggesting the wear is in a mild region. However in the case of sample B the $2.7S_{c,m} + 6\Xi$ value turns to be 18 when calculated under the same conditions (also assuming the coefficient of friction = 0.25), clearly indicating that severe wear would occur event if a low coefficient of friction is present. It can be concluded that in the case of sample B, even when a low friction coefficient is present at the start of the sliding experiment, the system is already in the severe wear regime, resulting in a rapid increase in the friction coefficient value after a short sliding distance. This is in excellent agreement with the tribology test results as shown in Figs. 8.3 and 8.4.

Microstructure characteristics, especially the grain boundary morphology, also contribute to the difference in wear severity of sample A and B. It was pointed out by Krell and Blank [21] that the presence of a thick amorphous layer in the grain boundary region results in low grain-boundary strength of the material and provides an easy path for crack propagation. Considering the clean grain boundaries in sample A and the amorphous grain boundary layer in sample B, one can expect a lower grain boundary strength of sample B compared with sample A. The difference in model of fracture between sample A (mixed trans- and inter-granular) and B (pure inter-granular) as shown in Fig. 8.3 is actually a good indication of the difference in grain-boundary strength. This also explains the lower σ_f of sample B than that of sample A. During tribology tests, under the applied contact pressure (0.9 GPa) microcracks are easier to nucleate and propagate along the weak grain boundaries, leading to significant pulling-out of surface grains as indicated by the SEM image of the wear track of sample B. Corresponding to this strong pull-out of surface grains, the wear track is roughened quickly. The fast roughening of the wear track further increases wear severity. On the contrary, the clean grain boundaries of sample A seem to be sufficiently strong to avoid significant pull-out of surface grains under the test conditions and therefore mild wear and low friction can be kept for longer sliding distance.

8.4 Conclusions

Dense 8 mol% CuO doped 3Y-TZP ceramics were prepared by pressureless sintering. Reactions occurring during sintering significantly retard densification of the ceramics so that high sintering temperatures ($\geq$ 1500 ºC) are required for obtaining dense materials, while starting from relative coarse-grained powders. However the sintering temperature is a very critical factor for microstructure characteristics, mechanical properties and tribological behaviour of this material.

3Y-TZP doped with 8 mol% of CuO sintered at 1500 ºC shows amorphous-free grain boundaries as well as crystalline copper-oxide grains in a matrix of zirconia grains. In contrast materials only sintered 50 ºC higher temperatures (1550 ºC) exhibit an amorphous grain boundary layer, in which copper identities are distributed.

Here addition of CuO in 3Y-TZP also leads to a significant decrease in bending strength and fracture toughness if compared with undoped 3Y-TZP, which can be attributed to the large amount of monoclinic zirconia phase and other microstructure characteristics introduced by CuO addition. The CuO doped 3Y-TZP sintered at 1550 °C shows the same K_{IC} value but lower σ_f value if compared with the one sintered at 1500 °C.

The material sintered at 1500 ºC exhibited a good self-lubricating effect while sliding against alumina ball under dry contact conditions, showing significant reduction of friction coefficient if compared with undoped 3Y-TZP ceramic (from 0.6 to 0.2~0.3). Mild wear combined with low wear rates (k<<10^{-6} mm$^3 \cdot$N$^{-1} \cdot$m^{-1}) was also obtained for this material. An increase in sintering temperature of only

50 °C destroys the beneficial effect of CuO doping on friction as well as wear-resistance of the composite material. The relatively large flaws and amorphous grain boundary layer of the material sintered at higher temperature leads to severe wear and strong pull-out of surface grains during the tribological test. As a consequence severe wear occurs and poor tribological behaviour ($f = 0.8$-0.9; $k >> 10^{-6}$ mm$^3 \cdot$N$^{-1} \cdot$m^{-1}) was observed for this material. The relationship between microstructure, mechanical and the tribological properties as observed in this work is in excellent agreement with the model as developed by Pasaribu [20].

References

1. Czhichos, H., Klaffke, D., Santner, E. and Woydt, M., "Advances in tribology: the material point of view", *Wear*, 1995, **190**, 151-161.

2. Zum Gahr, K.-H., "Modeling and microstructural modification of alumina ceramic for improved tribological properties", *Wear*, 1996, **200,** 215-224.

3. Zum Gahr, K.-H., "Effect of grain size on friction and sliding wear of oxide ceramics", *Wear*, 1993, **162–164,** 269-279.

4. Woydt, M., Kadoori, J., Habig, K.-H., Hausner, H., "Unlubricated sliding behaviour of various zirconia-based ceramics", *J. Eur. Ceram. Soc.*, 1991, **7,** 135-145.

5. He, Y.J., Winnubst, A.J.A., Schipper, D.J., Burggraaf, A.J. and Verweij, H., "Effects of a second phase on the tribological properties of Al$_2$O$_3$ and ZrO$_2$ ceramics", *Wear*, 1997, **210**, 178-187.

6. Kong, Y., Yang, Z., Zhang, G., Yuan, Q., "Sliding friction and wear of alumina-reinforced zirconia-toughened mullite composites", *Wear*, 2002, **252**, 607-613.

7. Kerkwijk, B., Mulder, E., Verweij, H., "Zirconia–alumina ceramic composites with extremely high wear resistance", *Adv. Eng. Mater.*, 1999, **1,** 69-71.

8. Alexeyev, N., Jahanmir, S., "Mechanics of friction in self-lubricating composite materials. Part I: Mechanics of second phase deformation and motion", *Wear*, 1993, **166**, 41-48.

9. Kerkwijk, B., Garcia, M., Van Zyl, W.E., Winnubst, A.J.A., Mulder, E.J., Schipper D.J., and Verweij, H., "Friction behaviour of solid oxide lubricants as second phase in Al$_2$O$_3$ and stabilised ZrO$_2$ composites", *Wear*, 2004, **256**, 182-189.

10. Pasaribu, H.R., Sloetjes, J.W., Schipper, D.J., "Friction reduction by adding copper oxide into alumina and zirconia ceramics", *Wear*, 2004, **255**, 699-707.

11. Toraya, H., Yoshimura, M. and Somiya, S., "Calibration Curve for Quantitative Analysis of the Monoclinic-Tetragonal ZrO$_2$ System by X-Ray Diffraction", *J. Am. Ceram. Soc.*, 1984, **67**[6] C119-C121.

12. de With, G. and Hattu, N., "On the use of small specimens in the measurement of the fracture toughness for brittle materials", *J. Mat. Sci. Lett.*, 1981, **16**, 1702-1704.

13. Ran, S., Winnubst, A.J.A., Wiratha, W. and Blank, D.H.A., "Sintering behavior of 0.8 mol%-CuO-doped 3Y-TZP ceramics", *J. Am. Ceram. Soc.*, 2006, **89**[1], 151-155.

14. Munoz-Saldana, J., Balmori-Ramirez, H. and Jaramillo-Vigueras, D., "Mechanical properties and low-temperature aging of tetragonal zirconia polycrystals processed by hot isostatic pressing", *J. Mat. Res.*, 2003, **18**[10], 2415-2426.

15. Seidensticker, J.R. and Mayo, M.J., "Thermal analysis of 3-mol%-yttria-stabilized tetragonal zirconia powder doped with copper oxide", *J. Am. Ceram. Soc.*, 1996, **79**[2] 401-406.

16. Gadalla, A.M. and Kongkachuichay, P., "Compatible phases of the Y$_2$O$_3$-CuO-Cu$_2$O system in air", *J. Mater. Res.*, 1991, **6,** 450-454.

17. He, Y.J., "Tribological and mechanical properties of fine-grained zirconia and zirconia-alumina ceramics", Ph.D. thesis, University of Twente, the Netherlands, 1995.

18. Lange, F.F., "Transformation toughening: Part 1 Size effects associated with the thermodynamics of constrained transformations", *J. Mar. Sci.*, 1982, **17**, 225-234.

19. Davidge, R.W., "Mechanical behaviour of ceramics", Cambridge University Press, Cambridge, England, 1979.

20. Pasaribu, H.R., "Friction and wear of zirconia and alumina ceramics doped with CuO", Ph.D. thesis, University of Twente, the Netherlands, 2005.

21. Krell, A. and Blank, P., "Inherent reinforcement of ceramic microstructure by grain boundary engineering", *J. Eur. Ceram. Soc.*, 1992, **9,** 309-322.

Chapter 9

Self-lubrication mechanism of coarse-grained 3Y-TZP doped with 8 mol% CuO sliding against alumina ball

Abstract

Dense 8 mol% CuO doped 3Y-TZP ceramic prepared by pressureless sintering at 1500 ºC exhibits a good wear-resistance (specific wear rate $k < 10^{-6}$ mm$^3 \cdot$N$^{-1} \cdot$m^{-1}) and promisingly low friction (friction coefficient f =0.2-0.3) when sliding against an alumina ball under unlubricated conditions. The objective of this chapter is to study the main phenomenon on the reduction in friction coefficient. It was recognised that a self-lubricating mechanism is the most contribution to the reduction of friction. During operation of the tribosystem, a soft interfacial patchy layer is generated in the contact area by deposition of wear debris material. As confirmed by a calculation based on a deterministic friction model, this soft interfacial patchy layer reduces friction. It was evidenced that the presence of copper oxide in the wear debris is important for the formation of such an interfacial layer. The mechanism of the transition from mild to severe wear was also investigated. Detachment of a top layer in the wear track was proven to be the main reason for this tribological change in friction.

9.1 Introduction

Advanced materials suitable for unlubricated tribo-engineering applications are increasingly attractive since the usage of liquid lubricants becomes more and more undesirable for economic and environmental reasons. These tribological material systems should have both a sustainably low coefficient of friction, $f \leq 0.2$, and a low specific wear rate, $k \leq 10^{-6}$ mm$^3 \cdot$N$^{-1} \cdot$m^{-1} [1].

Zirconia based ceramics are one of the promising materials for tribo-engineering applications. Good wear resistance combined with high bending strength and fracture toughness were obtained on these materials [2-5]. Recently it was reported that the coefficient of friction of 3Y-TZP ceramic under unlubricated (dry sliding) conditions can be reduced to a promisingly low value (0.25) by addition of CuO [7-9]. The reduction of friction coefficient was expected to be caused by the self-lubricating effect [10] introduced by the added CuO as a soft second phase in the hard matrix of the 3Y-TZP [7-9]. In chapter 8 of this thesis it has been revealed that the microstructure properties of the CuO doped 3Y-TZP ceramic are important for obtaining the low friction coefficient. However the details of the reduction of friction coefficient have not been reported yet.

The objective of this chapter is to figure out the mechanism of the reduction in friction coefficient of the 8 mol% CuO doped 3Y-TZP ceramic as observed in chapter 8. The wear tracks after the tests were carefully analysed by using SEM, EDX, XRD and nano-indentation. Based on the results of these analysis the mechanism of reduction in coefficient of friction will be discussed in detail based on a deterministic friction model as developed by Pasaribu [9].

9.2 Experimental

9.2.1 Sample preparation

Dense ceramic discs of 8-mol%-CuO doped 3Y-TZP were prepared from commercial submicron 3Y-TZP (TZ3Y, Tosoh, Japan) and CuO (Aldrich, Germany) starting powders. Details of the sample preparation can be found in chapter 3 of this thesis. Appropriate amounts of powders were mixed by wet-milling for 24 hours in a polyethylene bottle, using ethanol and zirconia balls as milling media. After drying and grinding, the powder was sieved through a 180 μm sieve. Green compacts of the composite powder with a diameter of 50mm and a thickness of around 5 mm were prepared by uniaxial pressing at 30 MPa followed by isostatic pressing at 400 MPa. The samples were sintered in stagnant air at 1500 °C for 8 hours, with a heating and a cooling rate both of 2 °C·min^{-1}. The sintered discs were polished to a surface roughness (Ra) of 0.1 μm using diamond paste. The polished discs were ultrasonically cleaned in ethanol and then annealed at 850 ºC for 2 hours to remove carbon contamination and release surface stresses.

9.2.2 Tribology test

Dry sliding tribological tests were performed on a pin-on-disc tribometer (CSEM, Switzerland), using the ball on disc geometry. Details of tribological tests can be found in chapter 8 of this thesis. A commercial alumina ball (Gimex Technische Keramiek b.v., the Netherlands) of 10 mm in diameter was used as counter material. The tests were formed under a control environment with a temperature of 23°C and a relative humidity of 40%. For each test a normal load of 5N (maximum Hertzian pressure = 0.9 GPa) and a sliding velocity of 0.1 m·s^{-1} were applied.

9.2.3 Characterisation

Density of the materials was measured according to Archimedes principle in mercury. Scanning electron microscopy (SEM, Thermo Noran Instruments) and transmission electron microscopy (TEM, CM30 Twin/STEM, Philips) were used to characterise the microstructure of as-sintered samples (see chapter 8). Wear tracks morphologies were analysed using SEM. Energy dispersive X-ray analysis (EDX, Thermo Noran Instruments) was used to analyse chemical composition. X-ray diffraction (XRD, X'pert_APD, PANalytical) was performed to analyse phase composition inside and outside the wear tracks. Nano-indentation experiments were carried out inside and outside the wear tracks to determine hardness of the materials in the outermost region of the samples. The indentation process starts by loading a nano-indenter with an increased load at a constant rate to a certain value, held at the peak value for a preset amount of time and then decreased to zero at the same rate as that for loading. By analysing the loading-unloading curve hardness value was determined as a function of indentation depth. Details of the nano-indentation experiments are described elsewhere [9].

9.3 Results and discussion

9.3.1 Tribological test

A relative density higher than 95% was achieved for the 8 mol% CuO doped 3Y-TZP ceramic sample disc after sintering. The microstructural characteristics of the as-sintered sample are given in chapter 8 of this thesis.

Under the applied test conditions, the samples show a fiction coefficient of 0.2-0.3 within a sliding distance of 1.5 km. This friction coefficient value is significantly lower than that of an undoped 3Y-TZP measured under the same conditions (f = 0.6 when normal load of 5N and sliding velocity of 0.1 m·s^{-1} were applied). The specific wear rate associated with this low friction region is much less than 10^{-6} mm^3·N^{-1}·m^{-1}, indicating that mild wear is dominant in this region. After this low friction region, the friction coefficient value increases drastically up to 0.8. Simultaneously the wear rate turned to be much higher than 10^{-6} mm^3·N^{-1}·m^{-1}. It is obvious that a transition from mild to severe wear occurs. More details of the tribological test are given in chapter 8 of this thesis.

9.3.2 Wear track characterisation

In order to reveal the mechanism of reduction in friction coefficient, the wear tracks were analysed in detail by various techniques. Fig. 9.1 compares general features of the surface inside and outside the wear track. After around 0.2 km wear test the track had a width of approximately 250 μm. A friction coefficient of 0.25 is corresponding to this sliding region. At the surface outside the wear track a large amount of voids with a typical size of tens micrometres are present. These surface voids should be formed by pull-out of clusters of grains during polishing. By using a milder polishing procedure the formation of surface voids can be avoided. However a sample with surface voids is presented in this work because it helps to identify the mechanism of the reduction in friction. Only few pores can be observed inside the wear track, indicating elimination of the surface voids during the sliding of the sample disc against the alumina ball. The wear track shows no significant surface damage except some narrow wear grooves, which seem to be formed by ploughing effect. These features of wear track are in good accordance with the mild wear rate as observed in the corresponding wear regime. A surface profile across the wear track is shown in Fig. 9.2. As can be seen in Fig. 6.2 the roughness inside the wear track is much less than that of the area outside the wear track (as-polished surface). Additionally
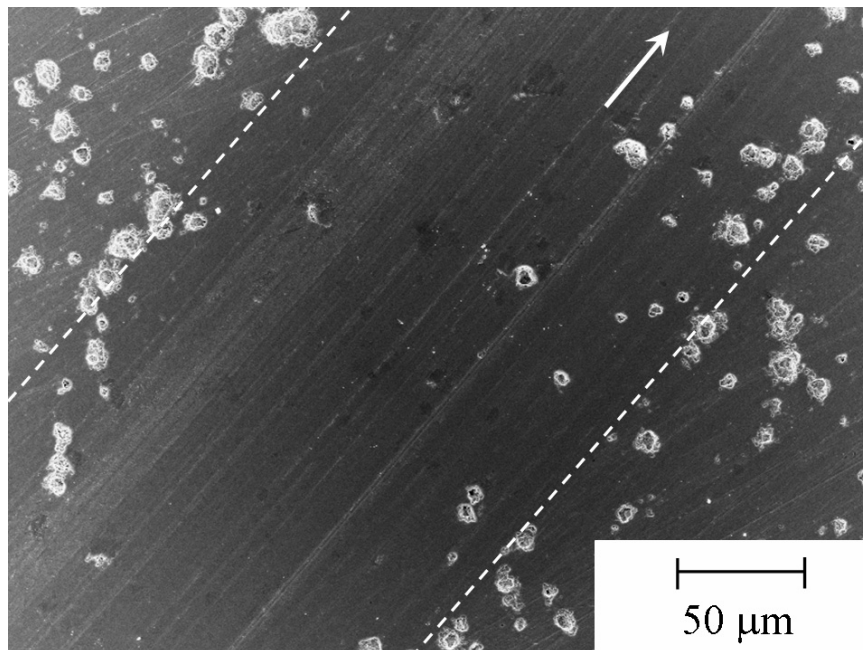

Fig. 9.1 SEM taken from a 3Y-TZP doped with 8 mol% CuO, after tribological test for around 0.2 km. The weak track is denoted within the two white dot lines and sliding direction is denoted by the white arrow.
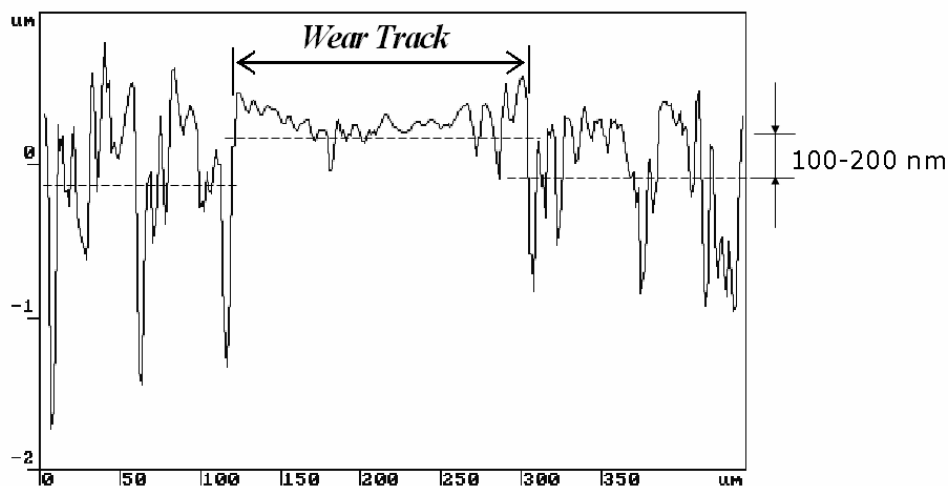
Fig. 9.2 Surface profile across the wear track

the surface of the wear track is slightly elevated. The elevation of the wear track surface is likely to be caused by deposition of wear debris materials from both the alumina ball and the tested CuO doped 3Y-TZP sample.

More details on the morphology of the wear track are shown in Fig. 9.3. Quite a few smooth dark areas with various sizes and irregular shape can clearly be observed inside the wear track (Fig. 9.3-a). These dark areas also give lower yield of back-scattered electrons on the SEM image (Fig. 9.3-b), indicating that these areas consist of elements with lower atomic number. The formation of these dark areas is best illustrated by the surface void adjacent to a large dark area as marked by the white circle in Fig. 9.3-a. It is assumed that this void already exists prior to the wear experiment and is caused by polishing of the sample. During wear test debris is generated from both the tested sample disc and the alumina ball. Under influence of the high contact pressure during sliding, wear debris is continuously pressed into the voids. This explains the elimination of surface voids in the wear track. The smooth feature of those dark areas implies that wear debris is can smoothly be smeared along the wear track.

Figs. 9.3-c and -d show enlarged morphologies of areas as marked by the white boxes I and II in Fig. 9.3-a. At area-I significant micro-fracture patterns are visible perpendicular to the sliding direction (as e.g. points by white arrows in Fig. 9.3-c), although the amount and size of these cracks is rather small. The micro-fracture pattern is a clear evidence of fatigue at that area. Adhesion wear seems to be the dominant wear mechanism at area-I. Area-II shows a very similar feature as that of the smooth dark areas as observed in Fig. 9.3-a. This suggests that area-II consists of the same material as the smooth dark areas, i.e. the wear debris. It is very likely that an outermost layer of wear debris material is deposited in area-II. But it is just too thin to be recognised by the back-scattered electron image, which normally collects signals of the region around 100 nm underneath the material surface.

It is important to note that the formation of thin patchy layer of debris material in the wear track as shown in Fig. 9.3-d is independent of the presence of surface voids. In the wear track on a better polished sample without surface voids, which shows also low friction coefficient (f = 0.25 when a normal load of 5 N and a sliding velocity of 0.1 m·s^{-1} were applied), these patchy layers were also observed. Clearly the formation of such smooth patchy layers, i.e. deposition of wear debris in the wear track, is more related to the intrinsic properties of the materials of the tribosystem (CuO doped 3Y-TZP sliding against alumina).
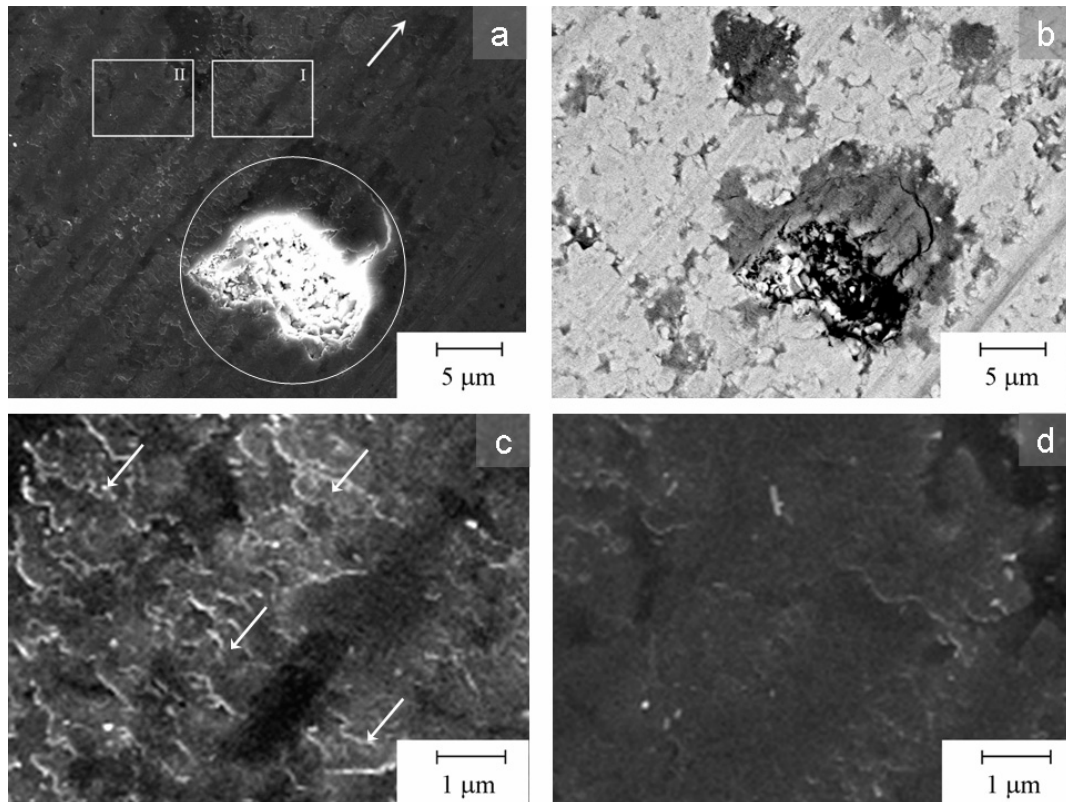
Fig. 9.3 Higher magnification SEM images of a wear track on 8mol% CuO doped 3Y-TZP sliding against an alumina ball. a) Secondary electron image, white arrow denotes the sliding direction ; b) back-scattered electron image; c) enlarged image of area I in a), white arrows denotes micro-fracture pattern; d) enlarged image of area II in a)

These patchy layers seem to play an important role to reduce the friction coefficient of the tribosystem. Therefore a sound knowledge about the characteristics of the thin patchy layer, for instance, chemical composition and mechanical properties, is important to understand the mechanism of the reduction in friction. However the chemical composition of the patchy layer is difficult to determine directly because its thickness is too small to be analysed properly by methods like EDX. A rough estimation of the thickness based on the surface profile (see Fig. 9.2) shows that it is in the range between 100 and 200 nm. Although this thickness is very sufficient for some surface sensitive analysis methods such as X-ray photoelectron spectroscopy (XPS), the imaging resolution of these methods is not sufficient to identify the patchy layer area (around 100 μm^2 as shown in Figs. 9.3-a and -d). However, the compacted wear debris in the surface voids, i.e. the dark areas in Fig. 9.3-a, give us a chance to solve this problem in an indirect way. As discussed above the patchy layer is formed by deposition of wear debris, which should have the same chemical composition as the wear debris filled in the surface voids. Fortunately the wear debris compacts in the surface voids are thick enough to be analysed by EDX attached to the SEM. This is actually the reason why the sample with surface voids is presented in this work.

Fig. 9.4 shows the elemental distribution of the same region as shown in Fig. 9.3, as measured by the EDX mapping technique. Quantitative analysis inside and outside the dark areas was performed by means of EDX point analysis (see Table 9.1). It is clearly revealed that the both Al and Cu are

enriched in the patchy layers. The presence of a copper-rich layer in the wear track is confirmed by XRD analysis inside (patchy layer) and outside (bulk material) the wear track (see Fig. 9.5). As can be seen in Fig. 9.5 the strongest peak of Cu_2O is clearly visible in the pattern of inside the wear track but is not that pronounced in the pattern of outside the wear track. These results strongly suggest that the presence of Cu (in a form of copper oxide) in the wear debris is important for the formation of the smooth interfacial patchy layer.
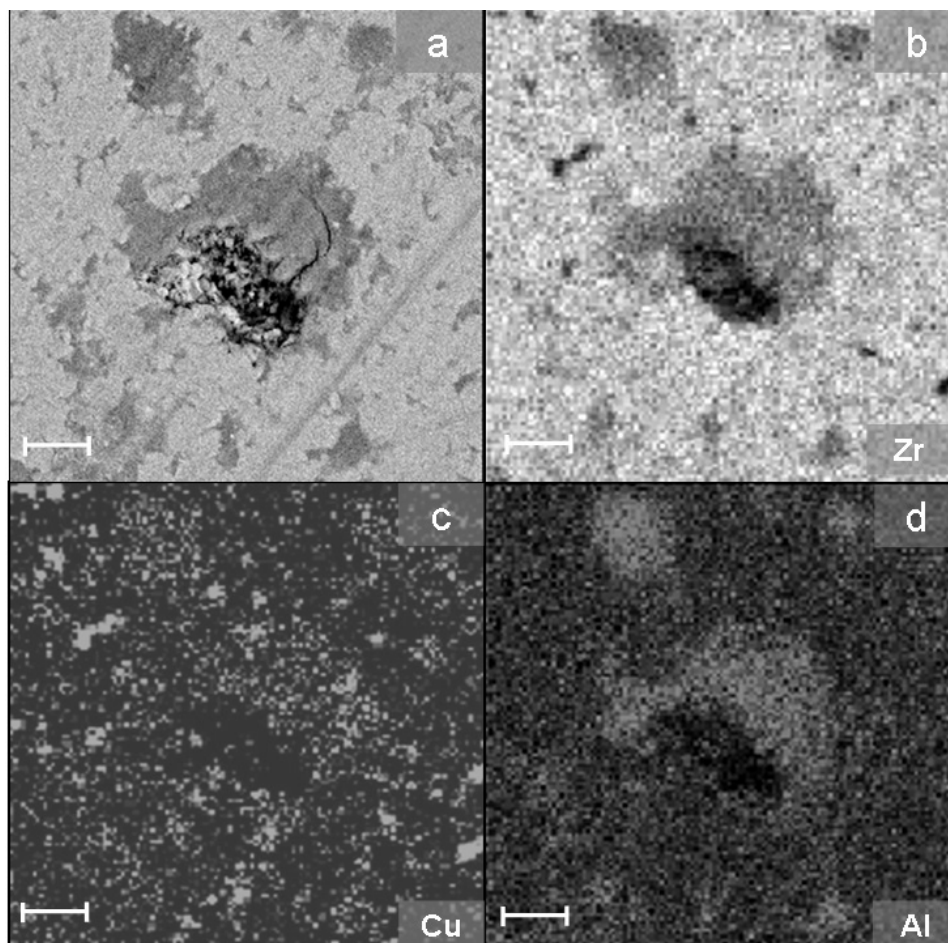
Fig. 9.4 Elemental distribution as determined by EDX mapping of a wear track of 8 mol% CuO doped 3Y-TZP sliding against an alumina ball. The bar represents 5 μm.

a) back-scattered image;   b) Zr distribution;   c) Cu distribution;   d) Al distribution.

Table 9.1 Metallic elements composition in the wear track

ID	Position	% metallic elements		
		Zr	Cu	Al
a	Inside dark area	75±1	13±1	12±0.5
b	Outside dark area	97±1	1.7±0.5	1.2±0.5
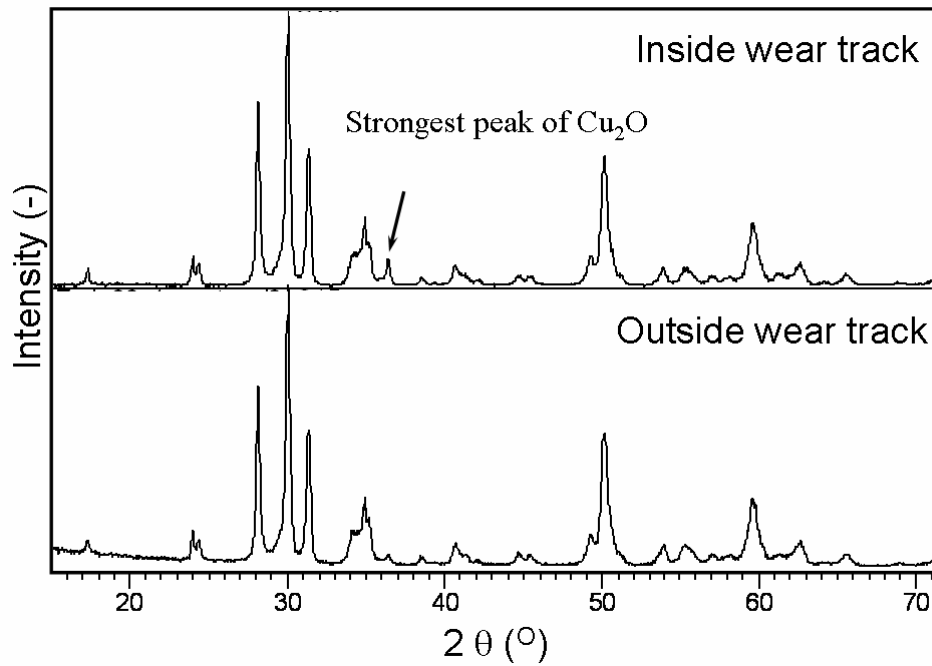
Fig. 9.5 XRD pattern measured in and out the wear track on the 8 mol% CuO doped 3Y-TZP ceramic after tribological test.

9.3.3 Mechanism of reduction in friction coefficient

As described in the previous section, during sliding a patchy layer is formed by means of deposition of Cu- and Al- rich wear debris. A mechanism of the reduction in friction coefficient by means of this layer will be discussed now.
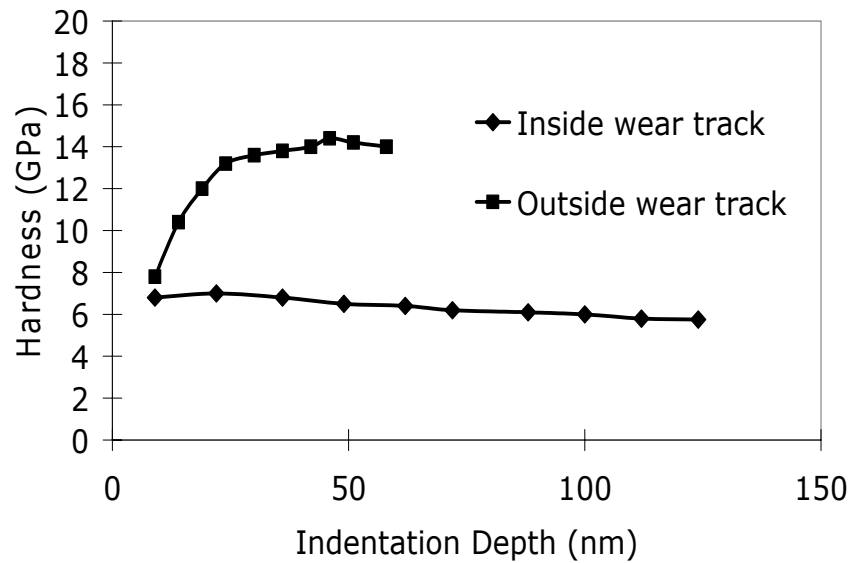
Fig. 9.6 Hardness as a function of indentation depth of CuO doped 3Y-TZP ceramic after tribological test.

Nano-indentation measurements were conducted inside and outside the wear track. The hardness values as determined by this technique are plotted as a function of the penetration depth (Fig. 9.6). As can be seen in this figure the hardness values of the surface inside the track and outside the wear track are almost the same for low indentation depths (10 nm). This might indicate that a patchy layer can already be formed during polishing. It is also possible that a thin layer of adsorption substances gives the low hardness value. With increasing indentation depth the hardness measured outside the wear track goes up quickly to 14 GPa, which is in a good agreement with the value of a bulk 3Y-TZP ceramic. However the hardness as measured in the wear track remains as low as 6 GPa at an indentation depth of 120 nm. This clearly indicates that the patchy layer inside the wear track, which is generated during sliding of the tribosystem, is significantly softer than the bulk material. Thus inside the wear track the material possess a layered surface structure, which can be characterised as a soft layer supported a hard substrate.

According the theory of Bowden & Tabor [10] the macroscopic friction coefficient of a layered surface can be calculated by using the following equation when no ploughing effect is considered:

$$f = \frac{\tau}{H} = \frac{\frac{1}{3\sqrt{3}} H_l}{H_s} . \qquad \text{(Eq. 9.1)}$$

where τ is the interfacial shear strength; H is the hardness; subscripts l and s denotes the layer and substrate. If the hardness values of the top layer and substrate in the wear track on the CuO doped 3Y-TZP ceramic are inserted in equation 9.1, a friction coefficient of 0.082 can be calculated. This value is much lower than the experimentally measured friction coefficient (0.2-0.3).

To explain the friction coefficient value as measured on our CuO doped 3Y-TZP ceramic sliding against alumina, other factors should also be taken into account. Halling [11] developed an analytical friction model of a flat layered surface sliding against a rough surface based on the adhesion theory of Bowden and Tabor [10], indicating that the friction of a layered surface varied as a function of the layer thickness. It is shown that when the layer is very thin the friction coefficient of the layered system is about the same as that of the substrate without a layer. As the thickness of the layer increases, the coefficient of friction is reduced to an optimum value after which the coefficient of friction increases again, and for a very thick layer the value of the coefficient of friction is the same as that of the layer material when used as a bulk material. This is in good agreement with the experimental observation of Bowden & Tabor on a steel rider sliding against various thicknesses of indium layers on steel [10]. In our case the thickness of the patchy layers generated during sliding is difficult to be accurately determined. It is suggested by the surface profile that the thickness of the top layer might be between 100 to 200 nm (see Fig. 9.2).

Recently Pasaribu [9] developed a deterministic friction model of a rough surface sliding against flat layered surfaces, which extends the capability of Halling's model and shows a better prediction of the coefficient of friction as a function of layer thickness. This model is used to calculate friction coefficient of the tribosystem of CuO doped 3Y-TZP sliding against alumina as studied here. Due to the soft layer in the wear track is not uniform but patchy, an additional parameter, the percentage of wear track that is covered with the soft layer (γ) is introduced in the calculation. Fig. 9.7 shows the calculated friction coefficient as a function of the thickness and coverage of the soft layer in the wear track. As shown above the measured coefficient of friction is 0.2-0.3 and the thickness of the soft layer is around 100-200 nm. According to Fig. 9.7 the value of γ can be estimated to be close to 80%. This value seems to be slightly over-estimated. Referring the SEM image of the wear track as shown in Fig.

9.2, one can see that a γ value of 50 - 60% is more reasonable. It is possible that factors other than those discussed above play a role for the friction behaviour of the tribosystem as described here. Nevertheless, the deterministic friction model as developed by Pasaribu clearly reveals the mechanism of reduction in friction of the tribosystem of CuO doped 3Y-TZP sliding against an alumina ball as follows. During sliding a thin soft patchy layer is generated by deposition of wear debris in the interface, which acts as a lubricant and reduces the friction coefficient. This mechanism is in a good agreement with the self-lubricating model as proposed by Alexeyev [12].
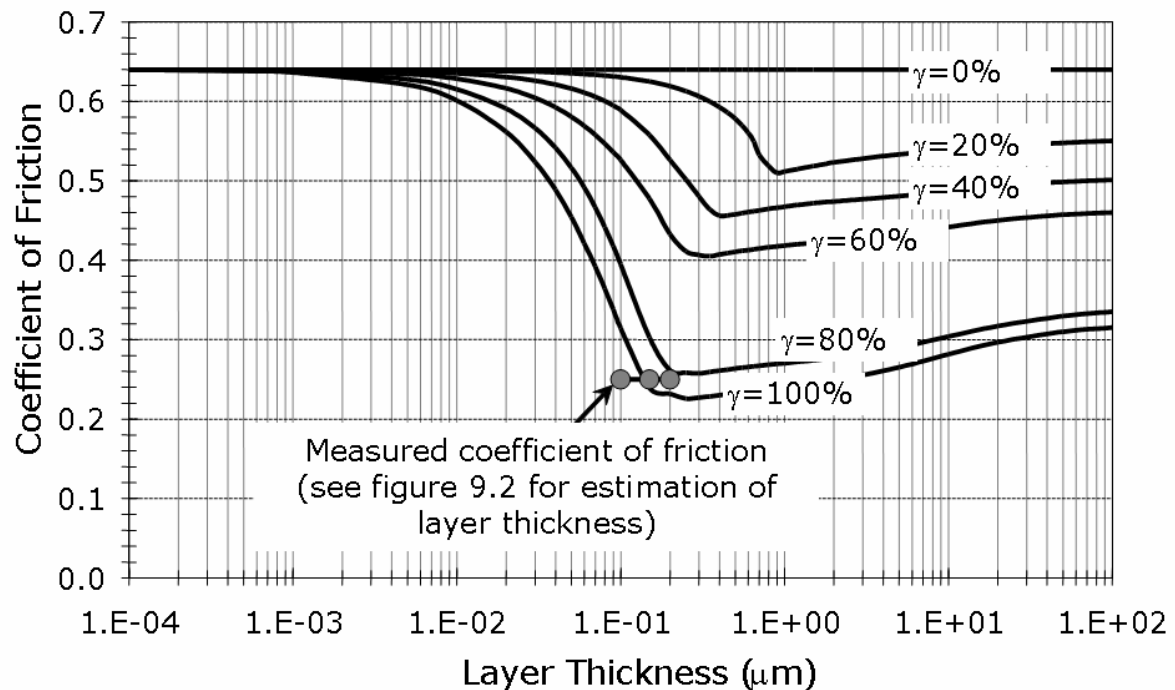
Fig. 9.7 Friction coefficient of CuO doped 3Y-TZP sliding against alumina calculated according to Pasaribu's friction model as a function of thickness and coverage of the soft layer in wear track [9].

9.3.4 Transition from low to high friction

It is shown by the tribological test (see chapter 8) that the friction coefficient increases suddenly from 0.2-0.3 to a very high value (0.8) after operation of the test for around 1.5 km. Simultaneously the wear rate drastically increases. SEM images were taken from the wear track associated with the high friction (after sliding for more than 1.5 km, see Fig. 9.8) in order to study the mechanism of the transition in tribological behaviour.

In Fig. 9.8 the detachment of the top layer is clearly visible. The wear track indicates that delamination becomes to be the dominant wear mechanism during this sliding stage (adhesion wear mechanism seems to be dominant before the transition). Obviously a quick lost of material arise from this delamination, consequently resulting in a severe wear as well as a drastic roughening of the wear track. Only high friction coefficient can be expected once such a heavy surface damage occurs.

It is interesting to have a brief speculation of the process of the wear mechanism transition. In Fig. 9.8 it can be seen that the detached top layer in the wear track exhibits a rather smooth surface feature, which is very similar with the patchy layer as show in Fig. 9.3-d. It is very likely that this detached top

layer is actually formed by the accumulation of patchy layers generated by deposition of wear debris formed during prolonged sliding. As a consequence the patchy layer gets thicker and larger. As indicated in Fig. 9.8, this layer can cover most of the area in the wear track. However, surface micro-cracks, which inevitably exist, are propagating during the sliding, as driven by the high contact pressure as well as the friction force. The crack propagation is expected to proceed preferably along the interface between the soft top layer and the hard substrate and ultimately the top layer is detached chip by chip.
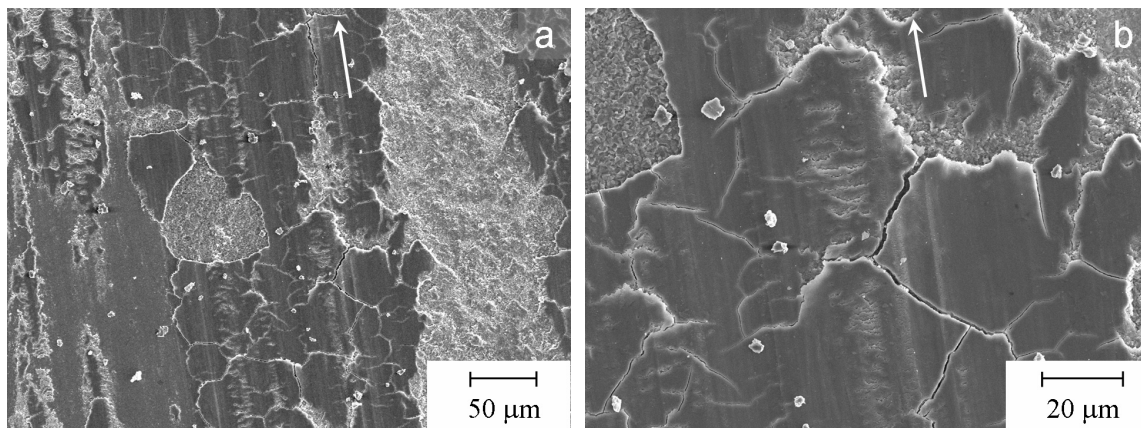

Fig. 9.8 SEM images of the wear track after tribological test for a sliding distance around 2 km. White arrows in the images denote the sliding direction.

a) with lower magnification; b) with higher magnification

9.4 Conclusions

The tribosystem of an 8 mol% CuO doped 3Y-TZP ceramic (pressureless sintered at 1500 ºC) sliding against an alumina ball shows a promising tribological behaviour (specific wear rate $k < 10^{-6}$ mm^3·N^{-1}·m^{-1}; friction coefficient f =0.2-0.3) under dry sliding conditions. Self-lubricating is recognised as the mechanism of the reduction in friction coefficient. During sliding a soft patchy layer at the interface is formed by deposition of wear debris, which reduces the friction coefficient as a lubricant. Presence of Cu in the wear debris is important for the formation of the soft interfacial patchy layer.

A transition from mild to severe wear takes place after the tribosystem operated for a long sliding distance (1.5 km). This transition in tribological behaviour is caused by detachment of top layers in the wear track.

References

1. Czhichos, H., Klaffke, D., Santner, E. and Woydt, M., "Advances in tribology: the material point of view", *Wear*, 1995, **190**, 151-161 1995.
2. He, Y.J., "Tribological and mechanical properties of fine-grained zirconia and zirconia-alumina ceramics", Ph.D. thesis, University of Twente, the Netherlands, 1995.
3. He, Y.J., Winnubst, A.J.A., Schipper, D.J., Burggraaf, A.J. and Verweij, H., "Effects of a second phase on the tribological properties of Al$_2$O$_3$ and ZrO$_2$ ceramics", *Wear*, 1997, **210**, 178-187.
4. Kerkwijk, B., Mulder, E., Verweij, H., "Zirconia–alumina ceramic composites with extremely high wear resistance", *Adv. Eng. Mater.*, 1999, **1,** 69-71.

5. Kong, Y., Yang, Z., Zhang, G., Yuan, Q., "Sliding friction and wear of alumina-reinforced zirconia-toughened mullite composites", *Wear*, 2002, **252**, 607-613.

6. Woydt, M., Kadoori, J., Habig, K.-H., Hausner, H., "Unlubricated sliding behavior of various zirconia-based ceramics", *J. Eur. Ceram. Soc.*, 1991, **7**, 135-145.

7. Kerkwijk, B., Garcia, M., Van Zyl, W.E., Winnubst, A.J.A., Mulder, E.J., Schipper D.J., and Verweij, H., "Friction behaviour of solid oxide lubricants as second phase in Al_2O_3 and stabilised ZrO_2 composites", *Wear*, 2004, **256**, 182-189.

8. Pasaribu, H. R., Sloetjes, J. W. and Schipper, D. J., "Friction reduction by adding copper oxide into alumina and zirconia ceramics", *Wear*, 2003, **255**[1-6], 699-707.

9. Pasaribu, H.R., "Friction and wear of zirconia and alumina ceramics doped with CuO", Ph.D. thesis, University of Twente, the Netherlands, 2005.

10. Bowden, F.P. and Tabor, D., "Friction and lubrication of solids", Part I, Clarendon Press, 1950.

11. Halling, J., "The rule of surface films in the frictional behavior of lubricated and dry contacts - A unifying influence in tribological theory", *ASLE Transaction*, **24**[4] 528-536 (1983).

12. Alexeyev, N., Jahanmir, S., "Mechanics of friction in self-lubricating composite materials. Part I: Mechanics of second phase deformation and motion", *Wear*, 1993, **166**, 41-48.

Chapter 10

Evaluation and recommendations

The research as described in this thesis is part of a project, sponsored by the Dutch Technology Foundation (STW), entitled "Nanoscale wear-resistant ceramic materials with low friction" (project nr.: TFC.5287). Its aim is to improve the tribological properties of zirconia and alumina ceramics and to determine the relation of tribological properties with microstructure and environmental conditions. This project was performed in close collaboration between three research groups of the University of Twente, i.e. Inorganic Materials Science (IMS), Materials Science and Technology of Polymers (MTP) and finally Surface Technology and Tribology. The research within the IMS group, on which this thesis is based, is mainly concentrated on the ceramic fabrication process and discovering a relation between microstructure and fabrication process on one hand and microstructure and tribological properties on the other hand. Composite ceramics of 3 mol% yttria stabilised tetragonal zirconia (3Y-TZP) doped with CuO, which has shown promising tribological properties [1], was chosen as the material for investigation. Modelling of tribological behaviour of ceramic materials as developed in IMS group was performed in the group of Surface Technology and Tribology by Pasaribu [2]. A "toolbox" for nanotribological measurements was developed in the group MTP by Tocha [3], which was applied in nanotribological measurements on the ceramic materials as developed in the IMS group. A combination of the research efforts of the three groups has provided more insights for improving tribological properties of ceramic materials. However further research is necessary for obtaining a solid basis for the development of novel ceramic materials, which fulfil the requirements of tribological applications in dry sliding conditions (meaning a specific wear rate $k < 10^{-6}$ mm$^3 \cdot$N^{-1}m^{-1} and a coefficient of friction $f < 0.2$).

10.1 Processing and microstructure

10.1.1 Powder preparation

Powders with uniform particle size in the nanometre range as well as small aggregates and weak agglomerates are required for the fabrication of nanocrystalline ceramics of good quality (e.g. with high density, uniformity in microstructure). The preparation of 3Y-TZP and CuO nano-powders is described in chapter 3. It is shown that an almost aggregate-free 3Y-TZP powder with an average particle size of 10 nm can be reproducibly prepared by a co-precipitation technique, which was well developed in our group [4-6]. A copper oxalate complexation/precipitation technique for the fabrication of nanocrystalline CuO powders is developed in this project. As described in chapter 3 the calcination procedure, precipitation and washing media play critical roles for crystallite size, aggregation and agglomeration control of these CuO powders. A weakly agglomerated CuO powder with a crystallite size and BET equivalent particle size of respectively 12 and 20 nm was obtained by precipitation of a copper oxalate complex in ethanol followed by calcination at 250 °C for 2 hours in an open tubular furnace. Although complexation/precipitation in water followed by ethanol washing gives the same results, precipitation directly in ethanol is recommended because of reduction in fabrication steps.

By using nanocrystalline 3Y-TZP and CuO powders prepared by the methods as described in chapter 3, the sintering temperature of the CuO doped 3Y-TZP composite ceramic (< 1130°C, see chapter 5) is largely decreased if compared with the coarse powder composites (≥ 1400 °C, see chapter 2). Reduction in sintering temperature would be very beneficial while the ceramic composite is co-fired with other materials for making a multi-component device.

10.1.2 Reactions and microstructure evolution during sintering

During sintering of ceramic composites containing reactive phases, such as CuO and 3Y-TZP, reactions between these phases profoundly influence, beneficially as well as detrimentally   densification, grain growth and further microstructural evolution,. A sound knowledge of the reactions and their influences is important for optimising sinterability and obtaining the desired microstructure. For a CuO doped 3Y-TZP nanocrystalline powder composite it is revealed that dissolution of CuO in the 3Y-TZP grain boundaries occurs below 600 °C and a formation of $Y_2Cu_2O_5$ takes place at around 850 °C (chapter 4). The former reaction strongly improves grain boundary diffusivity and consequently enhances densification in the initial and intermediate sintering stage and grain growth in the final sintering stage (chapter 5 and 6).   The latter reaction does not only retards densification but also results in a strong destabilisation of the tetragonal zirconia phase. For a coarse-grained CuO doped 3Y-TZP composite (chapter 2) the influences of these two reactions were also observed, but at higher temperatures and with lower significance. Additionally it is found that dissociation of CuO to Cu_2O at 1030 °C in air also inhibits sintering in these coarse-grained systems. This dissociation has a negative effect on densification and can be partially overcome by increase in oxygen partial pressure. Therefore sintering in an oxygen flow is recommended for the coarse-grained CuO doped 3Y-TZP system.

Based on knowledge on these reactions and their influences on sintering, improvement in sinterability can be achieved by promotion of the beneficial (i.e. CuO dissolution in the 3Y-TZP matrix) and inhibition of the detrimental (i.e. formation of $Y_2Cu_2O_5$) reactions during sintering. Particle size and content of CuO in the composites can be used as tools for adjusting the reactions. It is shown in chapter 5 that decrease in CuO particle size and increase in CuO content significantly enhance both the CuO dissolution and formation of $Y_2Cu_2O_5$ during sintering. With a combination of appropriate CuO particle size (20 nm) and CuO content (1.6 mol%) only the dissolution of CuO in the 3Y-TZP matrix, but not the formation of $Y_2Cu_2O_5$ is remarkably promoted. By doing so the sinterability is optimised. The optimised CuO doped 3Y-TZP nano-powder composite can be fully densified by just heating to 1000 °C at 15 °C·min^{-1} in an oxygen flow without dwell.

It is important to notice that the improvement in sinterability as described in this thesis does not involve liquid phase sintering. Although densification can be significantly enhanced in case of liquid-phase sintering, undesired strong grain growth and the formation of an amorphous grain boundary phase are normally inevitable. In contrast dense nanostructured ceramics without any amorphous phase can be obtained while the sinterability is remarkably improved by the powders and methods as described in chapter 5 and 6. This method of sintering optimisation, i.e. control of reactions, can be very useful for other ceramic composites involving highly reactive components, especially when nanostructured products are desired.

10.1.3 Manipulation of microstructure and tuning of properties

The microstructure can be very critical for obtaining ceramic materials with the desired properties. Tools for adjusting the microstructure of ceramic materials gives us to a large extent the possibility of tuning

material properties. In this thesis it is shown that the microstructure of CuO doped 3Y-TZP nano-powder composites, e.g. grain size and phase composition, can be largely adjusted by utilising different processing techniques including pressureless sintering, spark plasma sintering and post-treatment or annealing. In chapter 7 it is shown that the mechanical properties can be tuned by manipulation of the microstructure. It is important to note that this tuning of mechanical properties is only one example of the idea as described above. Other material properties such as superplasticity and tribological properties can also be tuned in a similar way. Moreover this idea of property tuning may also applicable for other materials.

10.2 Tribology in CuO doped 3Y-TZP ceramic composites

10.2.1 Ceramic sintering and tribological properties

Improvement in tribological properties of 3Y-TZP ceramic induced by addition of CuO, when an alumina ball is used as the counter body, has been revealed by Kerkwijk [1] and Pasaribu [3]. A promisingly low friction coefficient (f = 0.2-0.3) was achieved on the CuO doped 3Y-TZP (sintered at 1500 °C) sliding against an alumina ball in unlubricated conditions, while undoped 3Y-TZP ceramic gives a friction coefficient of 0.6 under the same tribological conditions.

In this thesis it is shown that a good control of ceramic sintering is critical for the tribological properties of the CuO doped 3Y-TZP ceramics. It is shown in chapter 8 that only an increase of 50 °C in sintering temperature (1550 °C compared with 1500 °C) results in remarkable differences in microstructure and consequently in very poor tribological properties of the material. As revealed by TEM the material sintered at 1550 °C contains a Cu-rich amorphous grain boundary phase, whereas the one sintered at 1500 °C shows clean grain boundary morphology. As a consequence of the presence of this amorphous grain boundary phase the bending strength of the material decreases and grain pull-out occurs more easily under tribological conditions. Additionally the critical flaw size (Griffith flaw size) is increased by the 50 °C higher sintering temperature. According to the wear model as developed by Pasaribu [2], which predicts wear severity, the increased critical flaw size of the material sintered at 1550 °C results in severe wear even if the system shows a low friction coefficient (e.g. f = 2.5). In contrast mild wear can be maintained under the applied tribological condition in the case when the material is sintered at 1500 °C. This model clearly explains the tremendous difference in tribological properties between the materials sintered at 1500 and 1550 °C. As illustrated by these observations, it is important to avoid amorphous grain boundary, and therefore weak grain boundaries, as well as to minimise Griffith flaw size for obtaining mild wear.

10.2.2 Mechanism of reduction in friction coefficient

A good understanding of the mechanism of the reduction in friction coefficient is important for further development of tribosystems based on advanced ceramic materials with low friction coefficient. In this thesis this mechanism is revealed in detail (chapter 9). It is clearly illustrated that a Cu- and Al-rich thin patchy layer (around 200 nm in thickness) in the contact area between the sliding bodies is formed by deposition of debris. According to the wear model as developed by Pasaribu [2] this soft patchy layer reduces the friction coefficient while acting as a solid lubricant. This mechanism is similar to the self-lubricating mechanism as proposed by Alexeyev [7].

Kerkwijk [1] observed that not only the presence of CuO but also the properties of counter body are important for obtaining the self-lubrication effect of the CuO doped 3Y-TZP ceramic based tribosystem.

A high friction coefficient (f =0.8 [1]) is exhibited when a zirconia ball is used as counter body. One possible explanation of this phenomenon relies on the hardness (H) and/or Young's modulus (E) of the counter body. The H and E values of Al_2O_3 (22 GPa and 392 GPa respectively) are much higher than those of Y-TZP (14 GPa and 210 GPa respectively). A harder and/or more rigid counter body may help to plastically deform the wear debris in contact area into a soft layer, which gives the self-lubrication effect. Additionally, the difference in hardness and Young's modulus of the counter body can change the fundamental wear and friction mechanisms as well. At present the friction model developed for the self-lubricating tribosystem does not take these parameters into account [2]. Further development of the friction model by incorporating the counter body properties is recommended.

10.2.3 CuO content and maintenance of self-lubrication during prolonged sliding

After operation of the tribosystem for a certain distance (several kilometres) the low friction and low wear rate are destroyed suddenly. It is revealed that this is caused by delamination of the thick top layer of the CuO doped 3Y-TZP ceramic (see chapter 9), which is actually formed by accumulation of the soft patchy layer giving self-lubricating effect. This delaminated layer can act as a ploughing agent for the CuO doped 3Y-TZP ceramic, which results in fatigue wear and a significant roughening of the surface. Also wear transition from mild to severe occurs and consequently this all leads to high friction and wear rate. The results as described in this thesis indicate that the thickness of the soft patchy layer formed by deposition of debris plays an important role in wear behaviour. A thin layer of 200 nm thick gives good tribological properties, whereas a much thicker layer results in high friction and wear rate. In order to prolong the distance of low friction region, it seems to be important to inhibit the increase in the layer thickness. As indicated in chapter 9, the increase in the layer thickness is actually a consequence of the accumulation of the debris in the contact area. Optimisation of the CuO content in the composite ceramic is one of the promising methods to inhibit the increase in layer thickness. Doping 3Y-ZP with 8 mol% of CuO, as employed in this work, is obviously sufficient for generation of the soft layer in the contact area resulting in a self-lubrication effect. However this amount may be too much and thus the increase in the layer thickness is too fast. If the CuO content is reduced to such an amount that a thin soft layer can still be formed on one hand and the creation and removal of debris in the contact area is reduced on the other hand, the sliding distance with low friction coefficient of the material could be significantly extended. For the coarse-grained systems as investigated in chapters 8 and 9, the optimal CuO content might be in a range between 1~3 mol%. For the nano-structured systems, more CuO can be dissolved in the 3Y-TZP matrix. In order to have sufficient CuO as second phase in these nano composites probably, more CuO content (3 ~ 5 mol %) is needed.

10.2.4 Improvement in ceramic processing for even better tribological properties

As stated in the previous section, the delaminated patchy layer can act as a ploughing agent for the CuO-doped 3Y-TZP resulting in particle or grain pull-out from the bulk of the ceramic. In order to combat this grain pull-out it is necessary to have a ceramic with e.g. higher density, small or no cracks and microflaws and/or higher fracture toughness. An improvement in the fabrication process of the ceramic might result in the desired microstructure and properties

He [8] observed that grain size and phase composition significantly influences the tribological properties of Y-TZP ceramics. It is of course important to know the dependence of grain size and phase composition on the tribological properties of the CuO doped 3Y-TZP composite ceramic. The nano-nano composite as developed in this work might be an interesting material, because higher toughness and smaller cracks are expected if compared with the coarser grained systems. However, for

the time being it was difficult to prepare these nano-nano composite with dimensions suitable for tribological tests. This was mainly caused by the poor flowability of the nano-powders which results in density gradient in the dry-pressed compact. To solve this problem either improvement of powder flowability [6] or other forming techniques such as pressure filtration must be employed.

Furthermore, it is suggested in this thesis that minimisation of the critical (Griffith) flaw size in ceramic materials is important for obtaining good tribological properties. By means of dry pressing, which is used as compaction technique in this work, relatively large flaws are easily introduced in the green compact, resulting in relative large cracks or flaws in the sintered body.

With regard to these two aspects, applying of advanced compaction techniques like slip casting and pressure filtration is recommended for the ceramic processing. These advanced compaction technique are beneficial for reduction inhomogeneities and flaws in the green compact and therefore the flaw size and concentration is reduced in the sintered ceramic as well. For minimisation of flaw size, pressure-assistant sintering technique such as sinter forging can also be helpful [5, 8]. All these methods improve the microstructure and therefore certainly have a positive effect on tribological properties.

10.2.5 Optimisation of tribological operation conditions

Tribological behaviour strongly depends on operation conditions. As revealed by the wear model developed by Pasaribu [4] the normal load (contact pressure) and sliding velocity strongly affect the wear mechanism of a tribosystem. Additionally, the formation of soft interfacial layer, which gives self-lubrication effect, should also be influenced by operation conditions.

In this work a relatively high contact pressure (0.9 GPa) and a mild sliding velocity (0.1 m·s^{-1}) were applied during the tribological test. Optimisation of the combination of normal load and sliding velocity should be helpful for further reducing wear rate and friction coefficient as well as prolonging the distance with low friction coefficient.

References

1. Kerkwijk, B., "Wear and friction of nanostructured zirconia and alumina ceramics and composites", Ph.D. thesis, University of Twente, the Netherlands, 1999.
2. Pasaribu, H.R., "Friction and wear of zirconia and alumina ceramics doped with CuO", Ph.D. thesis, University of Twente, the Netherlands, 2005.
3. Tocha, E., "Bridging length and time scales by AFM-based nanotribology: application to nanostructured ceramics and polymer surfaces", Ph.D. thesis, University of Twente, the Netherlands, 2006.
4. Theunissen, G.S.A.M., "Microstructure, fracture toughness and strength of (ultra)fine-grained tetragonal zirconia ceramics", PhD Thesis, University of Twente, The Netherlands, 1991.
5. Boutz, M.M.R., "Nanostructured tetragonal zirconia ceramics, microstructure, sinter forging and superplasticity", PhD Thesis, University of Twente, The Netherlands, 1993.
6. Sagel-Ransijn, C.D., "Nanostructured zirconia ceramics by gel-precipitation, processing, microstructure and mechanical properties", PhD Thesis, University of Twente, The Netherlands, 1996.
7. Alexeyev, N., Jahanmir, S., "Mechanics of friction in self-lubricating composite materials. Part I: Mechanics of second phase deformation and motion", *Wear*, 1993, **166**, 41-48.
8. He, Y.J., "Tribological and mechanical properties of fine-grained zirconia and zirconia-alumina ceramics", Ph.D. thesis, University of Twente, the Netherlands, 1995.

Acknowledgements

Indeed, the four-year study in the University of Twente was a very enjoyable experience, which I also attribute to my nice colleagues and friends. Very sincerely I appreciate all of them for what they have done for me.

First I wish to express my sincere appreciation to Prof. Dave Blank and Dr. Louis Winnubst for offering me this opportunity to do the research described in this thesis. Especially I am very grateful to my assistant promotor, Dr. Louis Winnubst, not only for the guidance and support in the research work, but also for the friendship we have made in these four years.

The research project which I worked on was sponsored by the Dutch Technology Foundations (STW). I gratefully acknowledge its financial support. Also I thank all the members of the users' committee for their invaluable feedback and comments.

Many people did great contributions to my research project. I do appreciate Wika Wiratha, Peter de Veen, Prof. Dik Schipper, Dr. Rihard Pasaribu, Jan-Willem Slotjes, Prof. Julius Vancso, Dr. Holger Schönherr, Dr. Ewa Tocha, for the close collaboration and the monthly meeting. I want to thank Attila Csaki, Herman Koster, Gerrit Mollenhorst, Mieke Luiten-Olieman, Henk Veldhuis, Cindy Huiskes and Dr. Emiel Speets, Dr. Enrico Keim, Mark Smithers for their help on experimental work. Special thanks should also go to Prof. Jef Vleugels and his colleagues for the SPS experiments and wonderful hospitality.

Over the past years I have enjoyed the pleasant working environment in the Inorganic Material Science group. I'm very grateful to all the (ex-) members of the group, especially my office mates, Shankho, Tijana, Ahmed and Song. Because of them, "go to work" sounds lovely.

Many of my thanks should also go to my Chinese friends, and my colleagues in the Association of Chinese Students and Scholars in The Netherlands (ACSSNL). Without them my life would not be that colourful in the past years. The enjoyable time we spent together is unforgettable.

A sincere thank to my parents, for their constant unconditional support.

Last, deepest thank goes to my wife, Yanshu, for her love, care, encouragement, and every thing. Yanshu, nobody could find a word to express how grateful I am to you.

Shen Ran

Enschede, The Netherlands

June, 2006

Curriculum Vitae

Shen Ran was born on January 26, 1975 in Shanghai, China. After graduating from high school (Kongjiang High School, Shanghai) in 1992, he started his study at the University of Science and Technology of China (USTC). In 1996 he obtained his bachelor degree of Materials Chemistry. After that he continued his studies at USTC and obtained his first Ph.D. degree of Inorganic Chemistry with a thesis entitled "Dense oxygen-permeable ceramic membrane and membrane reactors for partial oxidation of methane" in 2002. In August 2002, he joined the group of Dave H.A. Blank at the University of Twente, The Netherlands. Since then, under supervision of Dr. Louis Winnubst, he has been carrying out research on the project entitled "Nanoscale wear-resistant ceramic materials with low friction". The main results of his research work are described in this thesis.

Publications

1. Ran, S, Winnubst, A.J.A., Koster, H., de Veen, P.J. and Blank, D.H.A., "Sintering behaviour and microstructure of 3Y-TZP + 8 mol% CuO nano-powder composite", *J. Eur. Ceram. Soc.*, in press.

2. Ran, S., Winnubst, A.J.A., Wiratha, K.W. and Blank, D.H.A., "Synthesis, sintering and microstructure of 3Y-TZP/CuO nano-powder composites", *J. Eur. Ceram. Soc.*, 2006, **26**[1], 391-396.

3. Ran, S., Winnubst, A.J.A., Wiratha, K.W. and Blank, D.H.A., "Sintering behavior of 0.8 mol%-CuO-doped 3Y-TZP ceramics", *J. Am. Ceram. Soc.*, 2006, **89**[1], 151-155.

4. Pasaribu, H.R., Reuver, K.M., Schipper, D.J., Ran, S., Wiratha, K.W., Winnubst, A.J.A., and Blank, D.H.A. "Environmental effects on friction and wear of dry sliding zirconia and alumina ceramics doped with copper oxide" *Int. Refract. Met. and Mater,*. 2005, **23,** 386 – 390.

5. Winnubst, A.J.A., Ran, S., Wiratha, K.W., Blank, D.H.A., Pasaribu, H.R., Sloetjes, J-W., and Schipper, D.J., "A wear-resistant zirconia ceramic for low friction application" Proc. Euro Ceramics VIII, (Istanbul, Turkey), *Key Engin. Mater.,* 2004, **264-268,** 809-812.

6. Feng, S.J., Ran, S., Zhu, D.C., Liu, W. and Chen, C.S., "Synthesis Gas production from methane with $SrFeCo_{0.5}O_y$ membrane reactor", *Energy & Fuels,* 2004, **18,** 385-389.

7. Chen, C.S., Feng, S.J. Ran, S., Zhu, D.C., Liu, W. and Bouwmeester, H.J.M, "Conversion of Methane to Syngas by a membrane-based oxidation-reforming process", *Angew. Chem., Int. Ed.*, 2003, **42,** 5196-5198.

8. Chen, C.S., Ran, S., Liu, W., Yang, P.H., Peng, D.K. and Bouwmeester, H.J.M, "$YBa_2Cu_3O_{6+\delta}$ as an oxygen separation membrane", *Angew. Chem., Int. Ed.*, 2001, **40**, 784-786.

9. Ran, S., Zhang, X., Yang, P.H., Jinag, M., Peng, D.K. and Chen, C.S., "Oxygen transport through $SrFe_{1.125}Co_{0.375}O_y$ coupled with oxidation of Carbon monoxide", *Solid State Ionics*, 2000, **135**, 681-685.